Heat flux and hydrography at a submarine volcano: Observations and models of the Main Endeavour vent field in the northeast Pacific

Scott R. Veirs

A dissertation submitted in partial fulfillment
of the requirements for the degree of

Doctor of Philosophy

University of Washington

2003

Program Authorized to Offer Degree: School of Oceanography

University of Washington

Graduate School

This is to certify that I have examined this copy of a doctoral dissertation by

Scott R. Veirs

and have found that it is complete and satisfactory in all respects,

and that any and all revisions required by the final

examining committee have been made.

Chair of Supervisory Committee:

Russell McDuff

Reading Committee:

Russell McDuff

William Lavelle

Jeffrey Parsons

Date:

University of Washington

Abstract

Heat flux and hydrography at a submarine volcano: Observations and models of the Main Endeavour vent field in the northeast Pacific

by Scott R. Veirs

Chair of Supervisory Committee:

Professor Russell McDuff
Oceanography

This dissertation discusses hydrothermal plume hydrography and heat flux measurement at the Main Endeavour hydrothermal vent field (MEF) on the Endeavour segment (Juan de Fuca ridge, northeast Pacific). Observations are from an underwater vehicle called Autonomous Benthic Explorer (ABE), a lowered CTD, and 2 current meter moorings.

Chapter 1 contains motivating questions, terminology, plume theory, and a review of past heat flux measurements at the MEF. A new correction factor is derived relating source heat flux to plume heat flux calculated with isohaline temperature anomalies.

Chapter 2 presents setting, methodology, and an analysis of hydrography and currents near the MEF. Hydrography varies on scales as short as 10–50 m and 10–60 min, and fluid is warmer on average than at the segment ends. Oscillatory currents change from multidirectional above the ridge to rectilinear within the axial valley (Thomson *et al.* 2003). Northward mean flow of 2-5 cm/s within the valley is aligned with the rectilinear oscillations ($\sim$5 cm/s amplitude), while southwestward mean flow of 5-10 cm/s above the ridge is only intermittently aligned with the multidirectional oscillations ($\sim$5 cm/s amplitude).

Heat flux is estimated within the axial valley (Chapter 3) and above the ridge (Chapter 4). In both cases, an advection/diffusion model simulates plume distributions and characterizes heat flux statistics. The mean *horizontal* heat flux within the axial valley through

vertical control surfaces 0–100 m above bottom (mab) is $\sim$76 MW, based on warming north relative to south of the MEF and the northward mean flow. The modeled standard deviation of this horizontal flux is $\sim$114 MW. The *vertical* heat flux in plumes rising through a horizontal surface $\sim$100 mab (Stahr *et al.* 2003) is 643$\pm$116 MW. This vertical flux, previous source flux measurements, and the horizontal flux together imply that heat flux partitioning between focused and diffuse sources is $\sim$6:1, contradicting the prevalent view that diffuse sources account for 90% of the heat flux at vent fields. The net horizontal heat flux *above the ridge* through vertical control surfaces extending from $\sim$100–400 mab is 442$\pm$213 MW, consistent with the vertical flux. Past estimates of flux in plumes are higher because they are not net fluxes and likely include contributions from multiple vent fields.

TABLE OF CONTENTS

LIST OF FIGURES

LIST OF TABLES

GLOSSARY

ABE: Autonomous benthic explorer: an autonomous underwater vehicle

ADCP: Acoustic doppler current profiler

CTD: An instrument package that measures conductivity, temperature, and depth

CT PAIR: A pair of instruments measuring conductivity and temperature

GBL: Geothermal boundary layer (Thomson *et al.* 1995)

GPS: Global positioning system

MAVS: Modular acoustic velocity sensor

MAB: Meters above bottom

MAS: Meters above source

MEF: Main Endeavour (vent) field

MJD: Modified Julian day: the number of days since midnight, November 17, 1858. This chronology offers the advantage of continuous time to Endeavour researchers comparing inter-annual data sets, yet avoids the (even greater) number of digits required to express Julian days. (See Appendix B for a table of MJD, year days, and calendar dates.)

PVD: Progressive vector diagram

VOC: Vertically oscillating cast

VOT: Vertically oscillating tow

NOMEF: A group of CTD stations north of the MEF, within ~500 m along axis

SOMEF: A group of CTD stations south of the MEF, within ~500 m along axis

UTM: Universal transverse Mercator: a Mercator mapping using the equatorial cylindrical projection; UTM coordinates in this thesis are based on zone 9 and the WGS84 ellipse, and can be converted to latitude and longitude using the UNIX/LINUX utility *proj*.

ACKNOWLEDGMENTS

Initial acknowledgments go to those who offered me initial guidance: John Delaney and Marv Lilley. John helped me decide that graduate study of the oceans, and of hydrothermal systems in particular, was a logical training ground for an Earth systems scientist. I thank John for his vision, which always seems to be true in the end. Marv has been a constant presence for me, as helpful as he is quiet. I thank him, along with Geoff Lebon and the late Mary Landsteiner, for teaching me how to use the CTD safely, and for giving me unlimited access to his gas chromatography lab (where Ben Larson provided patient and efficient training).

My thesis advisor, Russ McDuff, deserves highest praise for his dedication and friendship. Russ has been a pragmatic advisor who encourages independence, motivates through both curiosity and formal assessment of progress toward goals, and catalyzes progress through consistent intellectual exchange. He has been a model for me of an innovative teacher, a strategic and rigorous research scientist, and a gentleman devoted to balancing his love of family, the outdoors, and the oceans. I thank him most for his accessibility (order 10^3 emails, 10^2 weekly meetings, and 10^1 squash games — not to mention trans-Pacific collaboration on my first paper) and for his support of my teaching interests through our involvement in REVEL cruises, my leave of absence to teach, and improvements of the TA training program. Keep on truckin' on, Russ!

I thank Bill Lavelle deeply for going beyond the call of duty as an advisor. Bill has offered his patient attention and scientific acumen during long and invariably helpful discussions about hydrothermal plumes. He graciously provided numerical simulations of MEF plumes that facilitated my interpretation of the Flow Mow hydrography. He introduced me to puff models and equations that became core parts of my thesis. He has also been a meticulous editor, both on my reading committee and as a volunteer reader of manuscript drafts, ultimately inspiring me to reconsider carefully the process of scientific writing.

The members of my supervisory committee also deserve accolades. They have been generous with their time and have graciously accommodated the logistics involved in coordinating a large committee. I thank Glenn Cannon for his flexibility, attention, and many ideas about the currents and hydrography of the Juan de Fuca ridge. Jeff Parsons has my gratitude for being a dedicated reader, for his infectious curiosity about particles in plumes, and for his help in considering lab experiments. I thank Susan Hautala (and her student Irene Garcia-Berdeal) for sharing insights and data, and for helping a geologist think more deeply about physical oceanography. Will Wilcock has my appreciation for his incisive geophysical questions, as well as for inoculating me with Matlab skills, a process that was painful during his homework assignments, but which proved invaluable my research. Finally, I would like to thank Stephen Porter for being a stalwart Graduate School Representative always ready with a refreshing geological query.

The Flow Mow experiment was accomplished at sea by an exceptional team of researchers, educators, and sailors. Special thanks to Christian Sarason Parker and Fritz Stahr for their camaraderie as students, scientists, and educators; I appreciate your advice, ideas, and white board prowess, and I look forward to further collaborations. Along with the REVEL 2000 participants, Fritz and Christian helped acquire 179 hr of CTD data in just over 2 weeks. This exceptional resolution of the MEF hydrography was also made possible by the (ABE) engineering genius of Dana Yoerger, Al Bradley, and their WHOI collaborators, as well as the captain, marine technicians, and crew of the R/V Thompson who patiently cycled the ship and CTD around the MEF control volume. Rick Thomson and his team at the Institute for Ocean Science, Canada deployed, recovered, and processed all current meter moorings and generously provided the current meter data and analysis. Throughout my graduate experience, Rick has been an inspiring presence across the northern waters. I thank him for his unending generosity, good humor, and lessons in long-distance collaboration and data exchange. Thank you also to Meg Tivey, who kindly made her MAVS data available for comparison, and to Hal Mofjeld, who provided helpful harmonic analysis of tidal records from Endeavour.

I will miss the School of Oceanography community, and thank all the individuals who have taught me, helped me, and enriched my experience as a student and scientist. I would like to acknowledge in particular the faculty and graduate students of the Hydrothermal Vents group and Marine Geology and Geophysics option. I especially thank Lisa Gilbert, Devamonie Naidoo, and my other office and class mates for being good friends and reliable sounding boards regarding all facets of graduate school.

I must also thank the tax payers of the United States. I am grateful for support during my first 3 years from a NASA Global Change Fellowship which allowed me unusual flexibility in selecting a research direction. I also acknowledge the support through the NSF grants to Russ McDuff and his collaborators, in particular NSF grant OCE-9872090. Data analysis, figure generation, modeling, and typesetting were made possible with Matlab and the most excellent open-source tools: Perl, GMT (Wessel and Smith 1991), and LaTeX.

Finally, and most importantly, I thank my family and friends. Annie, Mom, Dad, Laura, and Mila — you *are* my optimism and persistence; thank you for keeping me going, throughout. And thank you, dear friends, for both the heartfelt perspective and endless joyful distractions.

Chapter 1

MEASURING HYDROTHERMAL POWER

I begin this introductory chapter with my motivations for studying hydrothermal plumes and for obtaining accurate measurements of fluxes through hydrothermal vent systems. I then introduce the general problem of quantifying advective heat flux in the hydrothermal environment, along with some terminology and equations that will be applied in subsequent chapters. This establishes a framework within which heat flux is clearly defined and identifies some sources of uncertainty in the measurement of heat flux. I finish the chapter with a review of the history of heat flux measurements at the Endeavour segment of the Juan de Fuca ridge, emphasizing past accomplishments at the Main Endeavour hydrothermal vent field (MEF). The review of methods and results provides context and contrast for the Flow Mow study, an effort to measure the net heat flux from the MEF in the summer of 2000.

The goal of this dissertation is to investigate the relationship between the heat flux of a hydrothermal source and the heat flux measured within the associated hydrothermal plume. A secondary, related goal is to characterize hydrothermal plumes and their hydrographic impact. Both goals are accomplished through analysis of field observations and mathematical models of plumes. This thesis specifically addresses the analysis of results from the Flow Mow study, including: an overview of regional hydrography and current observations; measurements made in buoyant hydrothermal plumes; examination of hydrography and computation of horizontal fluxes *within* the axial valley, where the currents are rectilinear; and presentation of hydrography and computation of horizontal fluxes *above* the axial valley and ridge crests, where the currents are multidirectional. A major component of the Flow Mow study, the measurement of *vertical* heat flux in plumes rising from the MEF, is described in detail by STAHR *et al.* (2003); this dissertation only summarizes the vertical flux results, and then combines them with the horizontal flux estimates to infer MEF source fluxes.

1.1 Motivation

In the 25 years since hydrothermal vent systems were discovered in the deep sea, science has accumulated a stunning knowledge of them. Yet one of their most basic characteristics has remained remarkably elusive: the amount of energy flowing through them. In a surficial ecosystem powered by the sun, the influx of solar energy places an upper bound on photosynthetic productivity, and in turn, constrains the nature of the ecosytem and the degree to which it influences Earth processes. Similarly, the flux of energy through sea floor hydrothermal vents is of fundamental importance in assessing the nature of hydrothermal systems, as well as their role in the oceans and, more generally, the Earth system.

The heat flux out of a hydrothermal vent system is related to the heat flux into the system from a magma source and the circulation of fluid within the oceanic crust. The magnitude of the heat flux and its temporal evolution, both observable at or above the sea floor, are related to many questions about the less-accessible subsurface:

- What type of magma source supplies the material to build the oceanic crust, and what processes are involved in the construction? What are the mechanisms of heat exchange between the magma source and hydrothermal fluid? Is the evolution of the heat flux more consistent with the cooling of a dike (*e.g.* Cherkaoui *et al.* 1997) or the migration of a cracking front into an axial magma chamber (Lister 1974)?

- How does hydrothermal fluid circulate, and how does it distribute thermal and chemical energy within the upper crust and at the sea floor? Perhaps more importantly, from an evolutionary standpoint, how does the circulation change over time? How long do individual hydrothermal systems persist?

- Under what conditions is the crust habitable (*e.g.* McCollom and Shock 1997)? What is the extent of the subsurface biosphere (Gold 1992), and where within it did life most likely originate?

- Are there hydrothermal sources or sinks of chemical species that significantly affect ocean chemistry (*e.g.* Edmond *et al.* 1982)?

The heat flux from magma and hot rock drives convection of sea water in the oceanic crust, leading to the formation of hydrothermal plumes. The plumes enter the ocean, altering local stratification, chemical concentrations, and degree of diapycnal and lateral mixing. Heat flux measurements have been difficult to obtain, in part, because of uncertainty about how hydrothermal plumes disperse. Plumes may be distributed by currents in the hydrothermal environment, which often involve oscillations and mean flows interacting with complex topography. Plumes may also induce a circulation which also affects their distribution. The possibility that hydrothermal plumes may simultaneously be affected by and affect the ambient velocity field raises a different set of questions:

1. Which factors predominantly govern plume dynamics: source properties, turbulent mixing, ambient currents, stratification, and/or the Earth's rotation?

2. What method of measuring hydrothermal heat flux is optimal with respect to metrics like accuracy, precision, cost-effectiveness, and time-efficiency?

3. How should estimates of heat flux from the MEF be compared and how do they compare?

4. What are the effects of plumes on the hydrography of the Northeast Pacific ocean?

5. What methods (tracers, instruments, and models) are most useful for locating hydrothermal sources?

6. How do different types of plumes affect the transport and distribution of vent organisms, their larvae, or metalliferous sediments?

This thesis addresses questions 1–4 directly. Questions 5–6, as well as some aspects of the questions about the subsurface in the previous list are reconsidered in the final discussion (Chapter 5). At its core, however, this disseration focuses on 2 central issues:

- What form do plumes take in different types of cross flow?

- How can the heat flux from their sources best be determined?

There is a spectrum of processes that may govern how hydrothermal plumes enter the deep ocean. At one extreme, cross flow is negligible and rotational dynamics dominate. At the other, rotational forces have a small effect relative to cross flow. The importance of both processes is substantiated by theory, modeling, and laboratory experiments, but the relative role of cross flow and rotation in generating observed hydrothermal plume behaviors remains uncertain.

When lateral transport by deep ocean currents is low relative to the flux of fluid provided by a vent, a hydrothermal plume can accumulate above the source. In this situation, theory and numerical modeling (*e.g.* Speer 1989), as well as laboratory experiment (Helfrich and Battisti 1991; Speer and Marshall 1995) indicate that hydrothermal plumes rise into a stratification as axisymmetric conical plumes, equilibrate, and spread at a level of neutral buoyancy, rotating anticyclonically in geostrophic balance. One manifestation of this processes, the vertical spreading of isopycnals associated with the geostrophic flow, is expected from mathematical modeling (Speer 1989) and has been observed in a "megaplume" associated with seismic and hydrothermal activity near 45°N on the Juan de Fuca Ridge (Baker *et al.* 1987). The most direct evidence that such hydrothermal eddies, or vortices, form during periods of intense, episodic hydrothermal venting is a anticyclonic rotation observed in the trajectory of a RAFOS float emplaced near the equilibration depth of a megaplume (Lupton *et al.* 1998). Vorticity measured with acoustic doppler current profiler (ADCP) and current meter arrays has been offered as evidence of vortex formation above a steadily venting hydrothermal site (Joyce *et al.* 1998), but at larger scales is more consistent with opposite ridge-parallel flows along isobaths on either side of the Juan de Fuca ridge (Helfrich *et al.* 1998). These observations, all from environments with ambient mean currents, beg the question, "How slight must a cross flow be for hydrothermal plumes to exhibit the rotational dynamics observed by Helfrich and Battisti (1991), and do such conditions exist in any known hydrothermal environment?"

Deep sea currents over submarine ridges often have horizontal magnitudes comparable to the vertical velocities in the stems of hydrothermal plumes (∼1–10 cm/s), and are therefore expected to bend hydrothermal plumes over as they rise, based on theory (*e.g.* MIDDLETON and THOMSON 1986), numerical modeling (*e.g.* LAVELLE 1997), and limited laboratory experiments (HOULT *et al.* 1969). Consequently, the plumes equilibrate deeper in the stratification than in quiescent conditions and ultimately intrude into the ocean as relatively thin, streaming plumes, rather than broad, coherent, rotating volumes. Bent over plumes have been observed visually (*e.g.* M. Lilley, pers. comm.), hydrographically (LUPTON 1995), and acoustically (RONA *et al.* 1991) from submersibles during periods of cross flow. Regional-to-field scale hydrographic surveys in venting regions (*e.g.* THOMSON *et al.* 1992) have revealed plume tracer distributions that support this second view of how plumes form and spread.

Embedded within the issue of how plumes form is the second central issue related to the interaction of plumes and currents: how to measure the heat flux from vent fields and ridge segments precisely, accurately, and economically. A spectrum of ingenious methods have attempted to quantify heat flux in advected, equilibrated, hydrothermal plumes (*c.f.* 1.3.1), but most have relied on the assumption that the heat flux measured in a plume is directly related to the heat flux through a specific area of sea floor. This thesis posits that substantial uncertainties can arise from this assumption. Design of a method for measuring heat flux more precisely (as well as economically) at the field and segment scale depends on an understanding of how plumes and currents interact, and how the hydrography they influence can be related to source heat fluxes.

1.2 Defining heat flux in a hydrothermal context

The flux of heat between crust and ocean can be conceptualized over a wide range of scales, each of which may be dominated by a distinct process. One could ask how much heat is transfered by conduction from crust to ocean over an entire plate, or by convection at the axis of a spreading center, or by conduction, through only the top surface of a sulfide flange. Fundamentally, submarine hydrothermal circulation involves the heating of cold deep sea water as it circulates through the oceanic crust. The total net vertical flux of heat through hydrothermal up-flow zones in the upper crust must be equivalent to the net heat flux from rock to water along the path through the crust. But above the sea floor and even within the shallow crust heat is transfered from the up-flow zone through diverse phenomena, generally of increasing scale. For example, water is warmed in the upper crust through mixing and conduction near the high temperature up-flow zone and rises through the sea floor as low temperature vent fluid over much broader areas than the hotter vents. Also, once buoyant fluid exits the crust, it forms a hydrothermal plume, a phenomena that extends up into the overlying ocean and can be distributed widely.

No matter the scale, it is useful to establish a control volume that encompasses the heat transfer processes of interest. As long as energy is not being generated or stored within the control volume, application of the conservation of energy within the volume can clarify what questions can be answered at a particular scale. By focusing on net rather than total heat flux through the surfaces of a control volume, a potential temperature anomaly rather than potential temperature itself becomes a central variable. Defining an anomaly is especially important when a rising hydrothermal plume entrains ambient fluid that is thermally stratified.

This section focuses on the relationship between fluxes associated with hydrothermal phenomena at distinct scales: equilibrated plumes, rising plumes, entrainment, and different types of vents. I begin by defining some key terminology, discussing the concept of a control volume, and clarifying the calculation of hydrothermal heat flux. I then review the physical characteristics of hydrothermal plumes that are expected from plume theory, with an emphasis on how to relate hydrographic temperature anomalies to the source fluxes that cause them.

1.2.1 Heat and flux

Heat is energy in transit between two objects with different temperatures (*e.g.* Halliday and Resnick 1988). In addition to mechanical energy (kinetic + potential), an object has an internal energy — the sum of its thermal, chemical, and nuclear energy. In this context, thermal energy is the kinetic energy of randomly moving atoms in an object. Thermal energy changes when temperature changes, and can be changed by heat. Heating or cooling occurs through conduction, convection, or radiation.

In the geophysical literature the terms heat "flux" and heat "flow" are sometimes used interchangeably, with SI units of W or W/m^2. For example, STEIN *et al.* (1995) report heat flux in W and heat flow in W/m^2 when referring to both convection and conduction, while LITTLE *et al.* (1987) report heat flow in W/m^2 when discussing convection. This ambiguity is perhaps understandable, as "flux" means flow in Latin, but in this dissertation I use *flow* when referring to a fluid velocity. I reserve *flux* to mean the net rate at which an intensive property, with density $R(x, y, z)$ (quantity/m^3 or quantity/kg) is transported in a velocity field $\mathbf{v}$ through the open surface A with normal unit vector $\hat{\mathbf{n}}$ (SCHEY 1992). The flux is thus the surface integral:

$$\mathbf{F} = \int_A R\mathbf{v} \cdot \hat{\mathbf{n}} dA \tag{1.1}$$

with units of quantity/s. This thesis is largely concerned with the situation in which the quantity is thermal energy. While we could quantify the flux of temperature (T), if we are interested in energy fluxes then it is convenient to formulate an expression for thermal energy density, or heat concentration: $\rho c_p T$, the product of fluid density (kg/m^3), specific heat capacity (J·°C^{-1}·kg^{-1}), and temperature (°C), with overall units of J/m^3.

When the thermal energy density is substituted for R in equation 1.1, we obtain a general equation for the heat flux

$$\boldsymbol{H} = \int_A \rho c_p T \mathbf{v} \cdot \hat{\mathbf{n}} dA \simeq \int_A \rho c_p \theta \mathbf{v} \cdot \hat{\mathbf{n}} dA \tag{1.2}$$

with units of J/s, or W. (I introduce potential temperature, θ, here because the internal heating caused by adiabatic compression when water is transported vertically just a few hundred meters can cause temperature anomalies comparable to those caused by geothermal heating (EMERY and THOMSON 2001). Thus, heat flux is a power, and hydrothermal heat flux is a measure of the geothermal power transported through surface area A. When assessing the net flux through a closed surface, $\hat{\mathbf{n}}$ points outward by convention and the sign of the flux is therefore positive when $\mathbf{v}$ is directed outward.

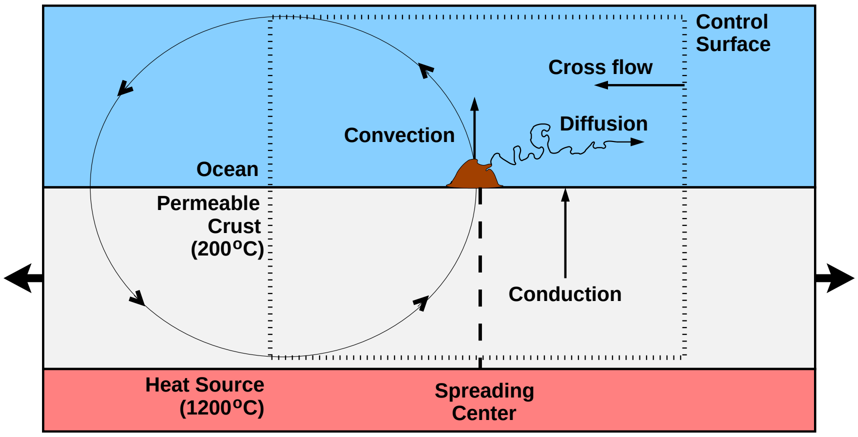

Figure 1.1: A schematic depiction of processes that transfer energy between the mantle, crust, and ocean at the axis of a spreading center. In assessing the heat flux associated with each process, the scale of the control surface over which a flux is measured will be different.

1.2.2 The heat flux budget

On the scale of a tectonic plate, heat fluxes between the crust and the ocean are dominated by conductive heat flux and low temperature convection (*e.g.* STEIN *et al.* 1995). At the scale of a hydrothermal field (Figure 1.1), heat is transfered from the crust to the ocean through convection and conduction, and is dispersed through turbulent diffusion, hydrothermal plume dynamics, and advection. One approach to measuring the heat flux associated with a particular transfer process is to establish a control volume that encompasses or intersects the process in an advantageous way. Then the fluxes through the control surfaces can be related through a heat flux budget. This section emphasizes the relative importance of advective processes within the MEF and introduces a generic method of quantifying heat flux through the surfaces of a control volume that encloses a hydrothermal vent field (Figure 1.2).

At the MEF, energy is transfered primarily through advection. At a typical high T vent, the flow of hot water results in a heat flux density of $\sim$1500 MW/m^2 (*e.g.* SCHULTZ *et al.* 1992). Given the number of such vents ($\sim$100) and the typical cross-sectional area of the vent orifices ($\sim 10^{-3}$ m^2), the total heat flux through MEF high T vents is of order 100 MW.

As discussed in this thesis, the heat flux from low temperature vents is of the same order of magnitude.

In contrast, the heat flux expected from conduction through the basaltic sea floor within the MEF is relatively minor. A recent transect through the MEF measured conductive heat flux density on unsedimented basalt with a range of 0.02–20 $\mathrm{W/m^2}$ (H. P. Johnson, pers. comm.). Multiplying this range by the approximate surface area of the entire MEF ($300 \times 700 \simeq 2 \times 10^5\,\mathrm{m^2}$) yields heat fluxes of order 10^{-3} to 1 MW. Thus, the conductive heat flux is at least 100 times smaller than the heat flux associated with hydrothermal venting.

Other types of energy transfers do occur within the submarine hydrothermal system, including chemical fluxes and reactions, electromagnetic radiation, and radioactive decay. Comparison to the heat flux densities typical of convective sources, however, indicates that most are of negligible magnitude, despite being interesting. Chemical species in hydrothermal vent fluid contain substantial chemical energy, and some (particularly, H_2 and CH_4) are oxidized quickly (Lilley *et al.* 1995) which will generate heat in the local environment. The magnitude of this heat source will be considered in Chapter 5. Infrared radiation with wavelength $\lambda \sim$1000 nm and intensity $I \sim 10^7$ photon$\cdot$m$^{-2}\cdot$s^{-1} has been observed, emanating from the high-temperature hydrothermal plumes within about a meter of the vent orifice (Van Dover and Chave 1996), but it is extremely weak, having an energy flux density Ihc/λ at the emitting surface of $\sim 10^{-12}\,\mathrm{W/m^2}$, where h and c are the Planck constant (6.6×10^{-34} J$\cdot$s$^{-1}\cdot$photon^{-1}) and the speed of light (3×10^8 m/s), respectively. Radioactive decay is ultimate power source of all hydrothermal heat fluxes, along with addition to the cooling of the Earth. Radiogenic heating and circulation in the mantle result in partial melting of the asthenosphere, a process that concentrates radioactive incompatible elements (uranium, thorium, potassium) in the crust. The decay of these isotopes within the oceanic crust generates an insignificant amount of heat, on the order of 10^{-11} W/kg of tholeiitic basalt (Turcotte and Schubert 1982). For a 6 km-thick crust, this amounts to $\sim 10^{-5}\,\mathrm{W/m^2}$.

The problem of measuring hydrothermal fluxes in the water column can be conceptualized by raising the bottom surface of the control volume in Figure 1.1 up to the sea floor, and assuming that convection, entrainment, and advection in ambient currents are the dom-

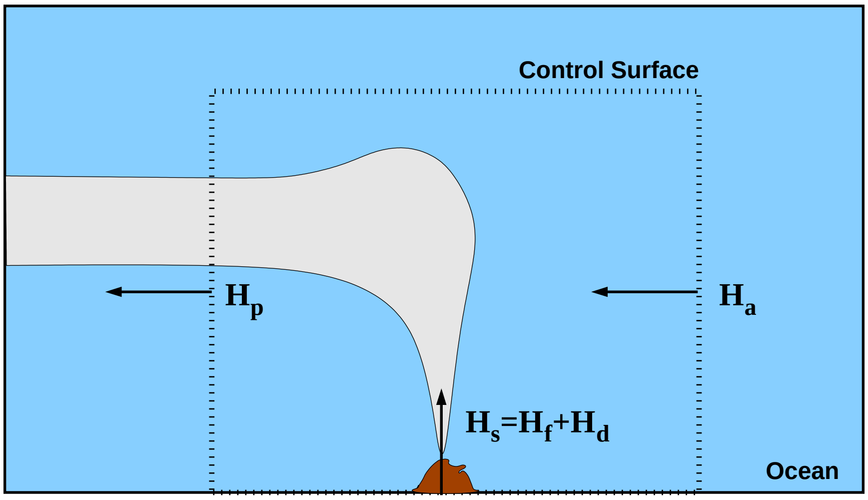

Figure 1.2: A generic control volume over a hydrothermal vent field in a steady cross flow. H_s is a source heat flux through the horizontal bottom surface. H_a is the flux of ambient heat carried by the cross flow from right to left through the vertical upstream surface. H_p is the flux through the vertical downstream surface, including ambient and plume components. Zero flux is assumed for the top surface, as well as the near and far vertical surfaces that are oriented parallel to the cross flow. H_d and H_f are the heat fluxes through diffuse and focused vents, respectively, and may generate plumes with a wide range of rise heights — not necessarily characterized accurately by the light grey schmatic plume.

inant heat transfer processes (Figure 1.2). A heat budget can be constructed with reference to the simplified schematic in Figure 1.2. The net heat flux through the bottom surface (H_s) is directed inward because of the hydrothermal source. Plume dynamics determined by background stratification and flow, rotation, convection, and turbulent mixing govern the rise of the hydrothermal plume, its entrainment of fluid, and its equilibration in the cross flow. Advection results in an inward heat flux (H_a) through the upstream surface and an outward plume-influenced heat flux (H_p) through the downstream surface. For simplicity, u is aligned with the front and back surfaces, yielding zero flux through each.

In a steady state with zero heat flux through the top surface and the non-venting sea floor, the net heat flux through the closed surface can be expressed as

$$H_p - H_a - H_s = 0. \tag{1.3}$$

Solving Equation 1.3 for H_s, expanding H_a and H_p according to Equation 1.2,calling the surface-normal horizontal and vertical velocity components u and w, respectively, and substituting potential temperature θ for T to compensate for the effect of pressure on T, Equation 1.3 becomes

$$H_s = H_p - H_a = \int_{A_p} \rho_p c_{p_p} \theta_p u_p \mathrm{d}A - \int_{A_a} \rho_a c_{p_a} \theta_a u_a \mathrm{d}A. \tag{1.4}$$

In the deep sea hydrothermal environment, θ_p is rarely more than a few °C greater than θ_a, so insignificant error is introduced by assuming $c_p = c_{p_p} \simeq c_{p_a}$. Similarly, if we assume the vertical density profiles are identical on the upstream and downstream surfaces, then $\rho = \rho_p(z) \simeq \rho_a(z)$, and both ρ and c_p can be brought outside the surface integral. Adding a final assumption, that the upstream and downstream surfaces are parallel, level, aligned, of equal area, and normal to a uniform flow field with speed $u = u_a = u_p$, the right-hand side of Equation 1.4 simplifies to:

$$H_s = \rho c_p u \int_A (\theta_p - \theta_a)\,\mathrm{d}A. \tag{1.5}$$

$\theta_p(l, z)$ and $\theta_a(l, z)$ are scalar fields, distinct functions of position on otherwise equivalent surfaces. Often, θ_a is assumed to be horizontally uniform and characterized vertically by a temperature profile acquired far upstream of a plume source at a "background" location. In this case, $\theta_p - \theta_a$ defines a depth-referenced, or *level-to-level* potential temperature anomaly, hereafter $\Delta_z\theta$ (nomenclature and symbolism from LAVELLE *et al.* (1998) and THURNHERR (2000), respectively).

When processing hydrographic observations, a common way to evaluate the right hand surface integral is to treat it as a summation of $\Delta_z\theta\mathrm{d}A$ over M area elements:

$$\int_A (\theta_p - \theta_a)\,\mathrm{d}A \simeq \sum_{i=1}^{n} \Delta_z\theta_i \mathrm{d}A_i \tag{1.6}$$

which is also equal to $\overline{\Delta_z\theta}A$ via the definition of an areal average. Similarly, in this thesis I use the definition of the areal average

$$\begin{aligned} \overline{\theta} &\equiv \frac{\int_A \theta \mathrm{d}A}{\int_A \mathrm{d}A} \\ \int_A \theta \mathrm{d}A &= \overline{\theta} A. \end{aligned} \tag{1.7}$$

to evaluate the surface integrals in individual terms of the heat budget. To calculate $\overline{\theta}$ on a surface, I average the raw data in a regular grid, using a cell size that is large enough to enclose many adjacent data points and minimize data gaps. The mean value of all cells containing data is then multiplied by an orthogonal velocity to compute the heat flux for a particular surface.

1.2.3 The source flux

From the perspective of answering questions about hydrothermal heat fluxes, the most important part of the heat budget is H_s, the flux of heat into the control volume from the source. Within the MEF, and perhaps all vent fields, H_s appears to be partitioned between 2 distinct types of venting, historically categorized as "diffuse" and "focused." In order to examine this partitioning, heat flux from diffuse sources will subsequently be labeled H_d, while heat flux from focused sources will be denoted H_f (Figure 1.2).

A key variable that helps to define diffuse and focused sources is buoyancy flux,

$$B = \frac{g(\rho - \rho_o)}{\rho_{\mathrm{ref}}} Q, \tag{1.8}$$

which depends on the density difference between the vented fluid (ρ) and the density of fluid at the same depth outside the plume (ρ_o) and the volume flux at the vent (Q), as well as two constants: the acceleration due to gravity ($g = -9.8\,\mathrm{m/s^2}$) and a reference density (taken to be $\rho_{\mathrm{ref}} \sim 10^3\,\mathrm{kg/m^3}$). The vent fluid potential temperature (θ) and salinity (S) are the primary controls on ρ, while Q is simply the product of the source area (A) and the venting velocity (w).

Table 1.1 illustrates that for typical MEF vent types, a black smokers and a tube worm patch, the high θ in the smoker fluid creates a density anomaly that is $\sim 100\times$ that of the tube worm patch. Although the patch radius has a strong control on B, in this typical case the smoker B is about 10 times the B of the 1 m radius tube worm patch. An increase in the radius of the tube worm patch from 1 to 3.3 m results in a B equal to that of the black smoker with sea water salinity, $S_{\mathrm{sw}} = 34.6\,\mathrm{psu}$.

In this thesis, "diffuse" sources are considered to be characterized by the 1 m-radius low B MEF tube worm patch, with source S =95–100%S_{sw}. Plumes from such sources are

Table 1.1: Typical hydrothermal source fluid properties. Densities at low *theta* calculated with the UNESCO International Equation of State (IES 80) (Fofonoff 1985). Densities at high θ approximated from Bischoff and Rosenbauer (1985) and verified as typical with Ginster *et al.* (1994) and Turner and Campbell (1987). $\Delta\rho = \rho(\theta, S, z)\,\mathrm{m} - \rho_o(1.8, 34.6, 2200)$, with $\rho_o = 1037.92\,\mathrm{kg/m^3}$. B calculated according to Equation 1.8.

Source	θ	S	$\Delta\rho$	r	w	Q	B
	°C	psu	kg/m^3	m	m/s	m^3/s	m^4/s^3
Sea water S smoker	350	34.6	-300	0.05	1	0.0078	0.023
Relatively fresh smoker	350	24.6	-350	0.05	1	0.0078	0.027
Tube worm patch	30	34.6	-7	1	0.01	0.031	0.002
Big tube worm patch	30	34.6	-7	3.3	0.01	0.342	0.023

expected to equilibrate $\lesssim$100 m above source (hereafter abbreviated "mas") (J.W. Lavelle, pers. comm.). In comparison, plumes from high B "focused" sources, like MEF black smokers, typically have rise heights of 100–300 mas (Speer and Rona 1989; Middleton and Thomson 1986). Unlike high B plumes that rise above the ridge crests to be advected away, the low-lying plumes contain thermal and chemical energy with a less certain fate. Their distribution may be controlled by entrainment into nearby plumes from high B sources, by lateral transport in ambient currents, or by a combination of both. Each possibility has distinct implications for the design of flux measurements and the dispersal of vent larvae and microbes.

1.2.4 Entrainment

In a stratified environment, a rising plume entrains water that is relatively dense until its buoyancy flux passes through zero (*e.g.* McDuff 1995). As its positive momentum carries the negatively buoyant plume higher, the plume entrains relatively light fluid. When it finally stops rising and begins the downward part of an oscillation around its equilibration depth, it will not sink as deep as it would have otherwise. This entrainment and oscillation continues until the plume momentum and buoyancy fluxes both go to zero and the plume attains its equilibration depth (*c.f.* Figure 1.5).

Equilibrated plumes are typically mixtures of about 1 part hydrothermal fluid and 10^4 parts entrained fluid (Lupton *et al.* 1980). In the equilibrated MEF plume, on average a ∼200 m-thick layer centered near 2000 m, the dilution inferred from the difference between source and plume temperature anomaly is 1:7000 (Lupton *et al.* 1985). The associated plume salinity anomaly indicates that more than 70% of the entrained fluid comes from below 2000 m (Lupton *et al.* 1985) and that the dilution is closer to 1:3500 in the equilibrated plume (R. McDuff, pers. comm.). In general, venting fluid is diluted by a factor of 100–1000 in the first 5–10 m of rise, and by about another order of magnitude en route to the equilibration depth of the plume (Lupton 1995). This is consistent with the theory of axisymmetric plumes (Morton *et al.* 1956) which assumes that the rate of entrainment is linearly proportional to the vertical velocity of the rising plume. Since the vertical velocity decreases with height above the source, the entrainment velocity is greatest near the source and greatly diminished high above it. In contrast, the vertical transport in the plume grows nearly linearly with elevation because the decrease in entrainment velocity is balanced by the increasing plume radius.

While the observed dilution of source anomalies demonstrates entrainment is an important hydrothermal process, the detailed nature of hydrothermal entrainment has rarely been investigated. In one experiment, dye emitted 1 m away from a high B source at the level of the orifice (0.5 m above bottom) was entrained horizontally and completely (Kim *et al.* 1994). Similar dye releases provide anecdotal evidence that entrainment may even begin below the orifice depth, through the porous matrix of the underlying sulfide structures (A. Schultz, pers. comm.). Numerical models of a hydrothermal plume in a stratified cross flow suggest that plume-induced downward recirculating flows should be expected, especially on the downstream side of the plume and within just a few plume stem diameters of the centerline (Lavelle 1994). For a control volume over a vent field it is not yet clear how much of the entrained fluid is drawn in laterally through the side surfaces versus vertically through the top surface on the periphery of the rising plumes.

Because hydrothermal plumes entrain a substantial amount of the fluid through which they rise, focused plumes have the potential to completely entrain diffuse plumes. This is attractive because it affords an opportunity to infer field-scale hydrothermal fluxes (H_f+H_d) from a measurement of H_p in an equilibrated plume, advected well above the topography (Figure 1.3). Calculating H_p in an upper level control volume with hydrography from a lowered CTD and currents from a mooring is generally more cost-effective than sampling a representative population of vents on the sea floor and summing the resultant heat fluxes to obtain $H_f + H_d$. A drawback of this approach is that it is difficult to predict or assess the degree to which H_d is entrained. If the side surfaces of the lower control volume are not monitored, any measurement of H_p will not necessarily be equal to $H_f + H_d$ because the proportion of background and hydrothermal fluid entrained within the lower control volume is uncertain. It is entirely possible that part of H_d will be entrained while the remainder is advected laterally from the lower control volume by ambient cross flow.

1.2.5 A control volume that assesses dominant processes

The relationship between H_f, H_d, and H_p can be better assessed by increase the extent of the control volume until it reaches from the sea floor to above the maximum plume rise height and contains all known low and high B sources in a field. Dividing the enlarged control volume vertically enables a vertical flux H_v to be measured at a height where rising plumes have a size and signal strength that is optimal (plume diameter is increased to ensure adequate sampling frequency, but signal-to-noise ratio is still high). With such a field-scale control volume (Figure 1.3), the heat budget for the lower control volume can be used to understand partitioning of H_s into H_f and H_d, and to address questions about entrainment. Similarly, quantifying the net H_p through the side surfaces of the upper control volume allows comparison of flux in the equilibrated plume with H_v and $H_s = H_f + H_d$.

The heat budget for the *lower control volume* is

$$\begin{aligned} H_f + H_d &= H_v + H_h \\ H_f + H_d &= \rho c_p \int_{A_v} w_v \theta_v \mathrm{d}A + \sum_{j=1}^{4} \rho c_p \int_{A_j} \mathbf{u}_j \cdot \hat{\mathbf{n}}_j \theta_j \mathrm{d}A_j. \end{aligned} \tag{1.9}$$

Here, the integral form of H_v accounts for the rising plume stem as well as the possible downward circulation driven by plume dynamics like entrainment. Numerical simulation of

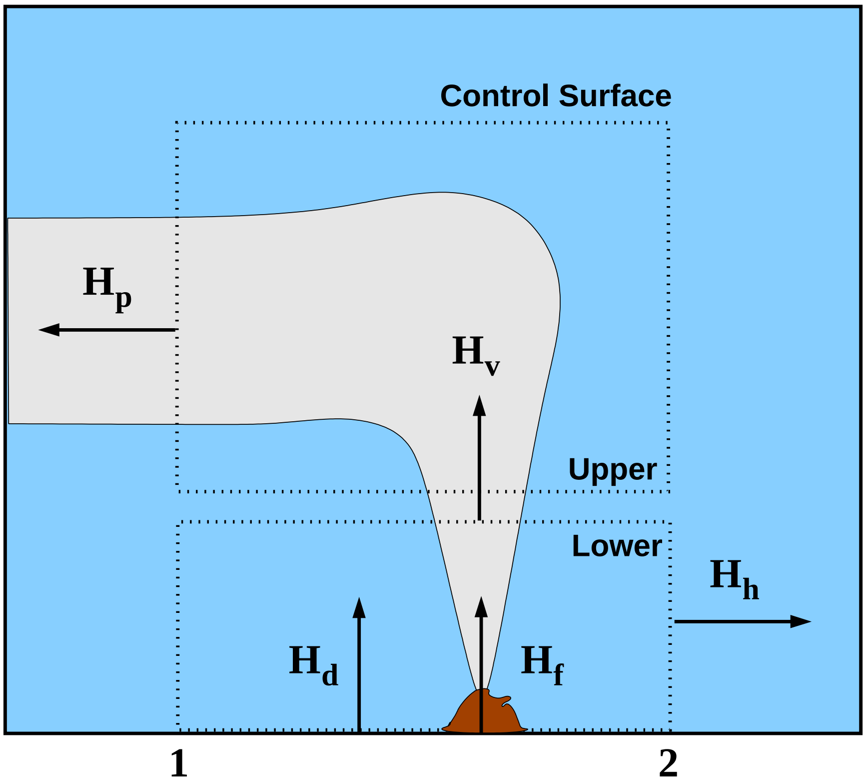

Figure 1.3: A field-scale control volume divided vertically at a height where rising plumes have a size and signal strength that is optimal for quantifying H_v, the net vertical flux through the top of the lower control volume. H_h and H_p are the *net* horizontal fluxes through the side surfaces of the lower and upper control volumes, respectively. H_f and H_d represent the source heat fluxes from focused and diffuse vents. Vertical surfaces are labeled 1 and 2; remaining side surfaces (3 & 4, not depicted) are parallel to the mean flow.

a plume from a MEF focused source in a steady cross flow indicates that such downward motion may be common near the base of the equilibrating plume, especially downstream of the plume stem (J.W. Lavelle, pers. comm.). Similarly, $\mathbf{u}$ could be any combination of ambient cross flow and plume-induced motion.

In the case where there is no cross flow, the only horizontal velocity will be that due to entrainment, $\mathbf{u_e}$. Assuming that a central source causes lateral entrainment, rather than entrainment through the top control surface, then the $\mathbf{u_e}$ field will be symmetrical and directed radially inward on all side surfaces. For studies which place control surfaces close enough to sources for the entrainment velocities to be detectable, a cylindrical control volume may be optimal. For studies like this one, in which control surfaces are more than ~100 m from typical focused sources, the entrainment velocity is expected to be undetectable. For a typical focused source, with $Q_f \simeq 0.01\,\mathrm{m}^3/$, the mean u_e over the first 10 m of rise (assuming volumetric dilution of $\sim 100 \times Q_f$ at 10 mas) will be ~0.01 cm/s at a radial distance of ~100 m. Even for a cluster of 10 such sources, the effective u_e at 100 m distance will be only ~0.1 cm/s.

In the case where a deep horizontal cross flow is aligned with the lower control volume, only entrained fluid will cross the 2 side surfaces aligned with the flow, while entrainment and the cross flow will add vectorially on the other 2 side surfaces. In the case of a cross flow $\overline{u} > u_e$ through the control volume directed normal to side surfaces 1 and 2 (from left to right in Figure 1.3, Equation 1.9 becomes

$$
\begin{aligned}
H_f + H_d &= \rho c_p \int_{A_v} w_v \theta_v \mathrm{d}A - \\
&\quad \rho c_p \Big(\int_{A_1} (\overline{\mathbf{u}} + \mathbf{u}_e) \cdot \hat{\mathbf{n}}_1 \theta_1 \mathrm{d}A_1 + \int_{A_2} (\overline{\mathbf{u}} - \mathbf{u}_e) \cdot \hat{\mathbf{n}}_2 \theta_2 \mathrm{d}A_2 + \\
&\quad \int_{A_3} \mathbf{u}_e \cdot \hat{\mathbf{n}}_3 \theta_3 \mathrm{d}A_3 + \int_{A_4} \mathbf{u}_e \cdot \hat{\mathbf{n}}_4 \theta_4 \mathrm{d}A_4 \Big) \\
&= \rho c_p \left(\int_{A_v} w_v \theta_v \mathrm{d}A - (\overline{u} + u_e)\overline{\theta}_1 A_1 + (\overline{u} - u_e)\overline{\theta}_2 A_2 - u_e(\overline{\theta}_3 A_3 + \overline{\theta}_4 A_4) \right) \\
&= \rho c_p \left(\int_{A_v} w_v \theta_v \mathrm{d}A - \overline{u}(\overline{\theta}_1 A_1 - \overline{\theta}_2 A_2) - u_e(\sum_{j=1}^{4} \overline{\theta}_j A_j) \right). \qquad (1.10)
\end{aligned}
$$

Note that Equation 1.7 was used in the transition from surface integrals to mean θ values over each surface.

The heat budget applied to the lower control volume in the Flow Mow study (*c.f.* Section 2.2) is a simplified version of Equation 1.10. Because the distance separating the control surfaces from high B MEF sources is ~100-200 m, u_e is expected to be negligible relative to the ambient tidal flow. Thus, the last term is dropped from Equation 1.10, yielding:

$$\begin{aligned} H_f + H_d &= H_v - \rho c_p \overline{u}(\overline{\theta}_1 A_1 - \overline{\theta}_2 A_2) \\ &= H_v + \rho c_p \overline{u}(\overline{\theta}_2 A_2 - \overline{\theta}_1 A_1) \\ &= H_v + \rho c_p \overline{u} A \overline{\Delta_z \theta} \\ &= H_v + \overline{H}_2 - \overline{H}_1. \end{aligned} \tag{1.11}$$

The heat budget for the *upper control volume* in the Flow Mow study is a simplified version of Equation 1.2. The net horizontal flux through the side surfaces (4 in this case) is balanced by the hydrothermal flux input from below, H_v:

$$H_v = \sum_{j=1}^{4} H_p. \tag{1.12}$$

Equations 1.11 and 1.12 will be applied to observations in Chapters 3 and 4, respectively, and can also be combined to eliminate H_v, effectively merging the upper and lower control volumes. If the situation is simplified further by assuming that the cross flow $\overline{u}$ is uniform at all depths, as opposed to being sheared as suggested in Figure 1.3, then the heat budget for the combined control volumes takes the form of Equation 1.5:

$$H_s = H_f + H_d = \rho c_p \overline{u}(\overline{\theta}_2 - \overline{\theta}_1) A, \tag{1.13}$$

in which surface 1 is still upstream of surface 2, but the surfaces have equal area A and extend from the sea floor to above the maximum plume rise height. As in Equations 1.5 and 1.6, the difference in potential temperatures is equal to the level-to-level anomaly, $\Delta_z \theta$. This general expression, along with its inherent assumptions, is at the core of the majority of past measurements of heat flux near the MEF, as well the estimates presented in this thesis.

Often, however, it proves convenient to substitute a density-referenced or salinity-referenced potential temperature anomaly for the depth-referenced one in Equation 1.13. Many past studies have utilized density-referenced anomalies; in this thesis, salinity-referenced anomalies are used. These distinct anomalies are defined and related to the calculation of heat flux in the next sections.

1.2.6 Temperature anomaly definition

While it is possible to define a level-to-level anomaly using profiles of θ and S in the deep ocean, the profiles typically have some curvature; in contrast, trends in θ–σ_θ, S–σ_θ, and θ–S space are nearly linear (*c.f.* Section 2.5.2). Because it is convenient to define an anomaly by fitting a line to the trends in these latter spaces temperature anomalies are usually defined with density or salinity as a reference. Given that modern computers have eased the task of using a non-linear trend as a reference, though, it is notable that level anomalies have rarely been utilized in analyzing hydrothermal hydrography. Some attention to level anomalies is given in Chapter 2 (*c.f.* Figure 2.21).

A "striking" deviation from a linear θ–σ_θ trend was first observed at the Endeavour by LUPTON *et al.* (1985) and can be used to define a density-referenced anomaly (hereafter *isopycnal* anomaly, $\Delta_\rho\theta$) in the hydrothermal environment. Given the slope m of the θ–σ_θ trend, as well as a point on the line $(\theta_{\text{ref}}, S_{\text{ref}})$ the anomaly is

$$\Delta_\rho\theta = \theta - \theta_{\text{ref}} - m(\sigma_\theta - \sigma_{\theta\text{ref}}). \tag{1.14}$$

If the reference point is the y-intercept, then $\theta_{\text{ref}} = \theta_o$, $\sigma_{\theta\text{ref}} = 0$, and Equation 1.14 simplifies to

$$\Delta_\rho\theta = \theta - \theta_o - m\sigma_\theta. \tag{1.15}$$

A salinity-referenced, or *isohaline* anomaly was first used by WEISS *et al.* (1977) to differentiate between hydrothermal plumes and θ "false plumes" caused by mechanical mixing or vertical excursions of their towed vehicle. The isohaline anomaly is defined given the slope of the θ–S background trend:

$$\Delta_S\theta = \theta - \theta_o - \frac{\mathrm{d}\theta}{\mathrm{d}S}S. \tag{1.16}$$

When the reference point is taken to be the background fluid level with the base of a hydrothermal plume (S_B, θ_B), the isohaline anomaly becomes

$$\Delta_S\theta = \theta - \theta_B - \frac{\mathrm{d}\theta}{\mathrm{d}S}(S - S_B). \tag{1.17}$$

The isohaline anomaly in Equation 1.17 is equivalent to the "q-ness" variable offered in McDougall (1990) as useful in relating equilibrium plume and source fluxes because, like $\Delta_\rho\theta$, it is zero for all points on the background line. This is a useful property under the assumption that all entrained fluid is background fluid, because entrained fluid will not contribute to the flux of the anomaly in the rising plume.

As the review of past MEF studies will show (*c.f.* Section 1.3), it is common practice to use isopycnal, rather than level, temperature anomalies in the calculation of H_p. In analyzing the hydrothermal hydrography in this thesis (Section 2.5.2), all 3 types of anomalies are considered.

1.2.7 Relating source and plume anomalies and fluxes in rising plumes

In calculating heat fluxes with anomalies, however, it is critical to understand how the different anomalies are related. How is H_p, calculated with a particular anomaly, related to the source heat flux H_s calculated with a level anomaly?

One way to study how different types of temperature anomalies evolve as a plume rises from its source is to utilize a 1-dimensional "MTT" model (Morton *et al.* 1956; Speer and Rona 1989; McDuff 1995). The MTT model of an axisymmetric turbulent plume in a quiescent, stratified background is comprised of equations that conserve mass, vertical momentum, heat, and salt. As mentioned before, entrainment velocity is assumed proportional to vertical velocity in the plume. The 4 coupled 1-dimensional equations were solved numerically in an axisymmetric geometry for specific source fluxes and linear profiles of background temperature and salt.

The implementation of the MTT model in Matlab by R. McDuff utilized here is initialized with background profiles specific to the MEF vicinity,

$$\begin{aligned} S(z) &= S_B + \frac{\mathrm{d}S}{\mathrm{d}z}z = 34.64 - 9.29 \times 10^{-5}z, \\ \theta(z) &= \theta_B + \frac{\mathrm{d}\theta}{\mathrm{d}z}z = 1.8 + 5 \times 10^{-4}z, \end{aligned} \tag{1.18}$$

and initial source conditions typical of a MEF focused source ($\theta_o = 350°$C, $w_o = 1$ m/s, $r_o = 0.05$ m, and variable S_o). The model yields vertical profiles of θ, S, w, and r within the plume as a function of elevation above the source up to the height of maximum rise (Figure 1.4). Each value of θ in the plume is associated with a value for S, ρ, and z that can be used in Equations 1.16, 1.14, or 1.18 to calculate the isohaline, isopycnal, and level temperature anomaly. For the modeled case depicted in Figure 1.5 the source salinity was 30 psu, about the mean value for MEF high B sources.

Within the rising plume, the isohaline, isopycnal, and level anomalies differ in magnitude (Figure 1.5). The difference is most pronounced near the equilibration depth, where the isohaline anomaly is about a factor of 2 greater than the other anomalies. This discrepancy has been noted at the equilibration depth in both observations and theory by many investigators. For example, observations of hydrothermal plumes near low B vents on basement outcrops east of the Endeavour segment in the Cascadia basin had a mean ratio, $\Delta_S\theta/\Delta_\rho\theta = 1.54 \pm 0.04$ (Thomson *et al.* 1995). This is consistent with the value of 1.52 predicted by Thurnherr (2000) from his Equation 6.5:

$$\frac{\Delta_S\theta}{\Delta_\rho\theta} = 1 - \frac{\alpha}{\beta}\left(\frac{\partial\theta}{\partial S}\right) = 1 - R_\rho, \tag{1.19}$$

in which α and β are the coefficients of thermal expansion and haline contraction evaluated for conditions near 2600 m, and the observed ambient slope is $\frac{\partial\theta}{\partial S} = -5.51 \pm 0.05$ (Thomson *et al.* 1995). Using values appropriate for MEF plumes equilibrating near 2000 m ($\alpha = 1.5 \times 10^{-4}{}^\circ\mathrm{C}^{-1}$, $\beta = 7.8 \times 10^{-4}\,\mathrm{psu}^{-1}$, $\frac{\partial\theta}{\partial S} = -5.1$), R_ρ becomes -1.0 (McDuff 1995) and the ratio in Equation 1.19 becomes about 2. While this value is consistent with the modeled anomalies near the equilibrium depth, the profiles converge at greater depths, implying that in rising plumes the same ratio of anomaly magnitudes should not necessarily be expected.

The vertical profiles of temperature anomaly, vertical plume velocity w, and plume radius r can be combined to compute the vertical heat flux, $H_v(z) = \rho c_p\left(\theta_v(z) - \theta(z)\right) w(z)\pi r(z)^2$. Dividing $H_v(z)$ by the source heat flux, $H_s = \rho c_p(\theta_o - \theta_B)w_o\pi {r_o}^2$ yields a correction factor (the "McD" parameter in Figure 1.5) that indicates how the vertical heat flux calculated with temperature anomaly measurements from a particular height should be corrected to estimate H_s. Note that this correction factor is similar to the inverse of the f_θ factor

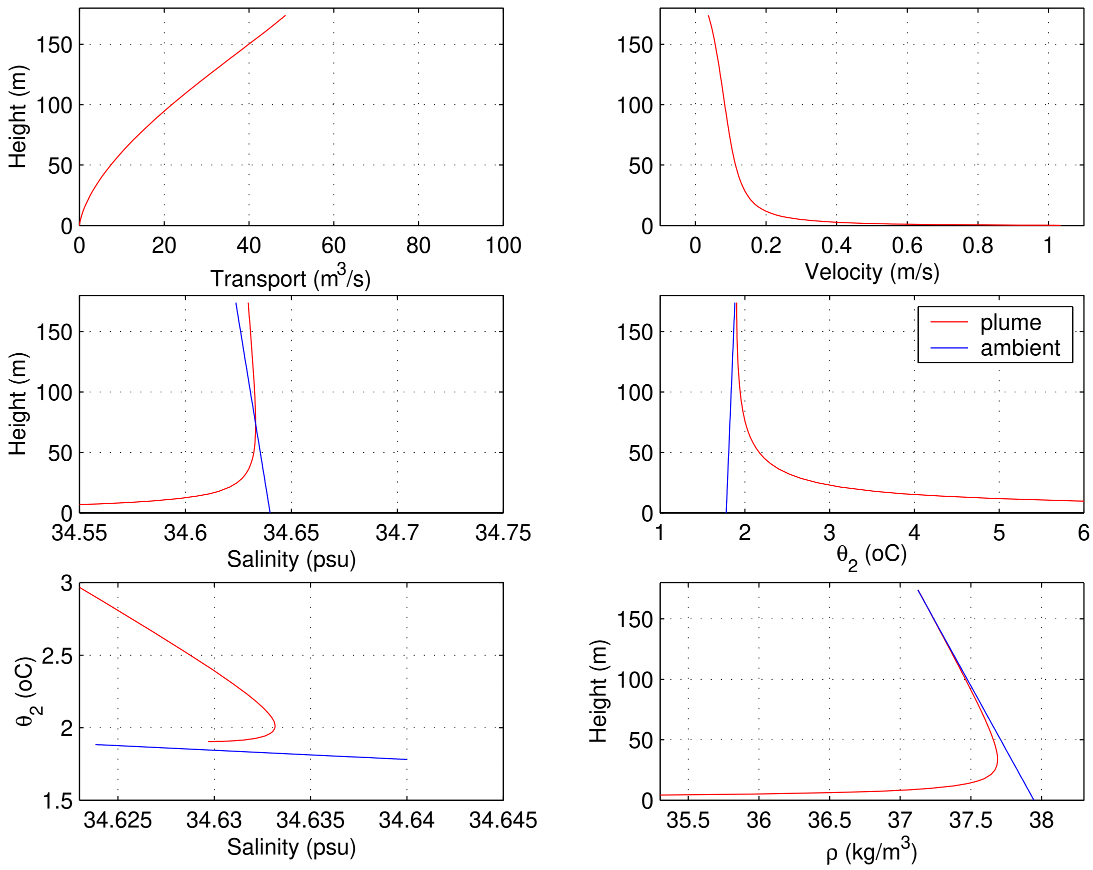

Figure 1.4: Modeled plume properties for a source with θ_o =350°C and S_o = 30 psu, and ambient θ and S profiles typical of the deep northeast Pacific. All panels are depth profiles of ambient and in-plume conditions except the lower left θ–S diagram. Proceeding counter-clockwise from lower right panel, profiles are of density, potential temperature, vertical velocity, vertical transport, and salinity.

tabulated in (LAVELLE *et al.* 1998), though the f_θ factor was derived for an equilibrated megaplume and may not apply in the rising plume stem (J.W. Lavelle, pers. comm.).

Both $\Delta_\rho\theta$ and $\Delta_z\theta$ lead to H_v estimates that are lower than the source flux H_s at all depths, except at the source depth, where H_v based on $\Delta_z\theta$ equals H_s. The correction factor associated with isopycnal and level anomalies is $\sim$0.8 near 100 mas, and about ~ 0.5 when the plume B first goes to zero. For $S_o = 30$ psu the H_v calculated with $\Delta_S\theta$ requires a small correction directly above the source (factor of $\sim$0.9), but no correction near the equilibrium depth. This is consistent with the correction factor of 1 applied in MCDOUGALL (1990) at the equilibration depth, but is a special case. Experimentation with the plume model over a wide range of source salinities demonstrates that the correction factor varies greatly for H_v based on $\Delta_S\theta$, and significantly for H_v based on $\Delta_\rho\theta$ or $\Delta_z\theta$ (Figure 1.6).

Heat fluxes calculated with the isohaline anomaly in plumes originating from sources with S_o close to sea water salinity at the vent depth, S_{sw}, require the smallest correction factor ($\lesssim$0.005 at 100 mas). Such sources include the saltier northern MEF sources with $S_o \approx 30$ psu, and probably all diffuse sources found in the MEF. High B sources in the southern MEF have $S_o \approx 20$ to 27 psu and lead to H_v estimates that need correction factors of 0.72–0.90. The few diffuse sources which have been sampled have $S_o \approx 0.99 S_{\mathrm{sw}}$ (D. Butterfield, pers. comm.), but represent dilutions of focused flow and should therefore be corrected with a factor related to the focused end member from which they were derived.

Over the same range of MEF S_o, a heat flux based on isopycnal or level anomalies needs to be corrected by factors of 0.80–0.90 at 100 mas. The range of modeled correction factors near equilibrium, 0.20–0.65, is the same as the range tabulated in Table III of MCDUFF (1995) calculated using Equation 22 of MCDOUGALL (1990) for $S_o = 0$ to $200\% S_{\mathrm{sw}}$:

$$\frac{Q_{\mathrm{eq}}\Delta_\rho\theta_{\mathrm{eq}}}{Q_o\Delta_z\theta_o} = -\frac{1}{R_\rho - 1}\left(1 - \frac{R_\rho}{R_{\rho_o}}\right) \tag{1.20}$$

in which the eq subscript represents the equilibrium values, and the density anomaly in the source fluid, $R_{\rho_o} = \frac{\alpha\Delta_z\theta_o}{\beta\Delta_z S_o} = (1.5 \times 350)/(7.8 \times \pm 35) = \pm 1.9$.

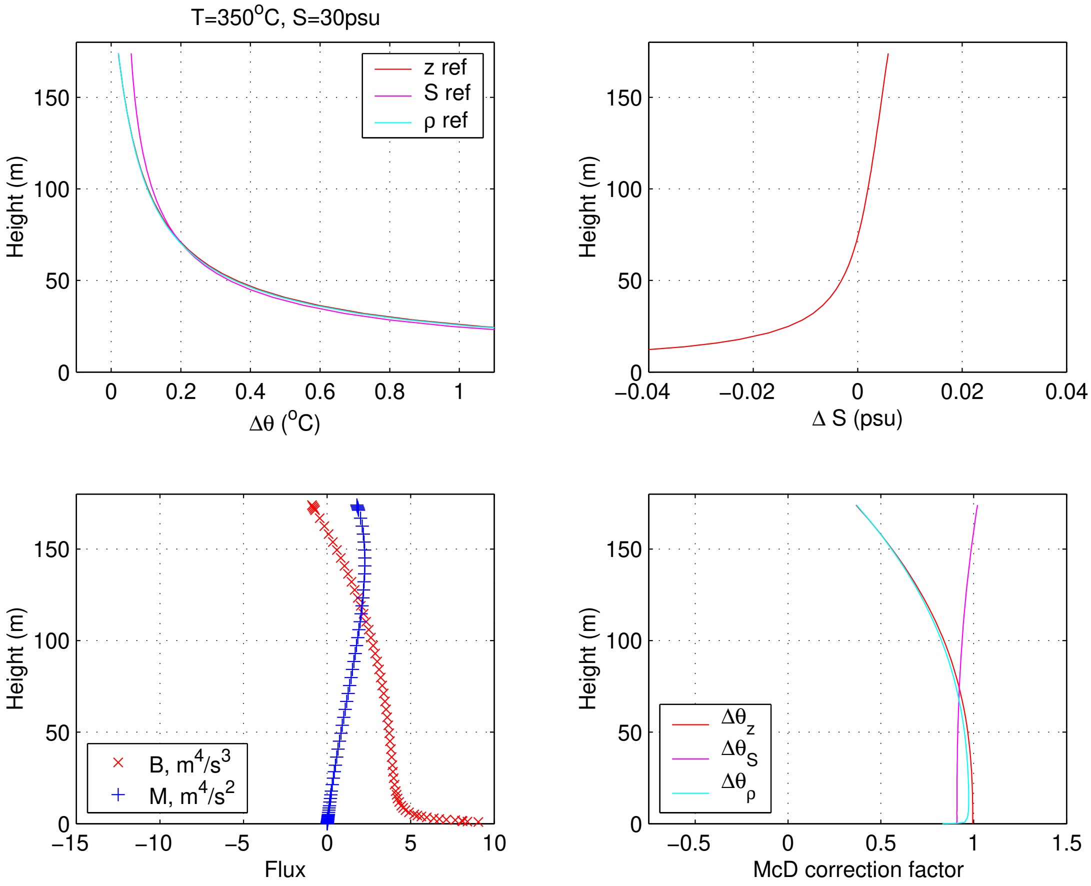

Figure 1.5: Modeled properties of a rising hydrothermal plume. Upper left panel shows profiles of temperature anomalies, referenced to depth, density, and salinity. Note that the level anomaly is slightly larger than the isopycnal anomaly over this depth range; they are distinct immediately above the source at very large anomaly values (not shown). Upper right panel shows profile of level salinity anomaly. Lower left panel illustrates how buoyancy flux, B and momentum flux M change as the plume rises to its maximum height. Lower right panel depicts the profile of McD factor, the ratio of vertical to source heat flux, for different temperature anomalies used to calculate the vertical flux.

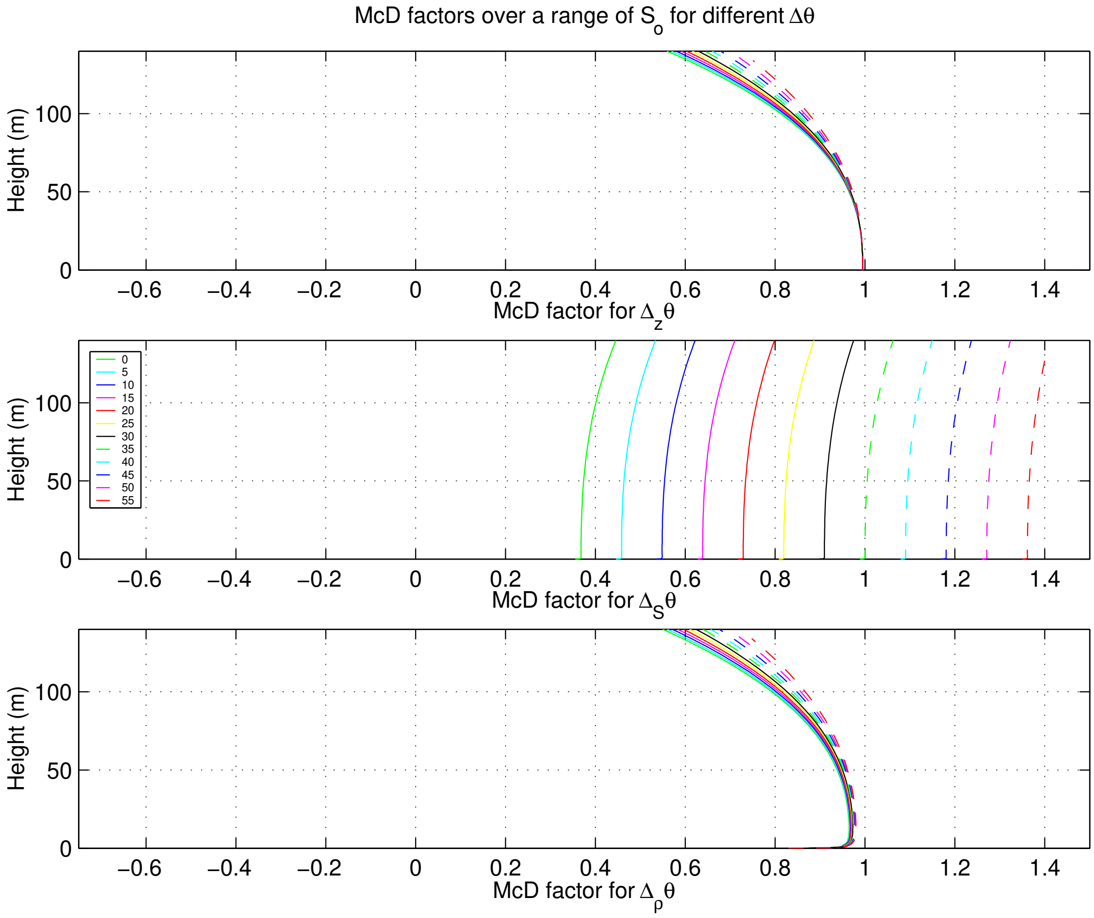

Figure 1.6: Correction factors for modeled vertical heat flux calculated with different types of temperature anomalies. Upper to lower panels show correction profiles for level, isohaline, and isopycnal temperature anomalies, respectively. Note that profiles are truncated at 130 meters above bottom in order to emphasize the evolution of properties within the first 100 m of rise.

1.2.8 General relationship between isohaline anomaly and source heat flux

This section describes a more general relationship between the source heat flux and a net heat flux out of the control volume calculated using isohaline anomaly. The MTT model applies to plumes rising without a cross flow and provides a correction factor numerically for any height during the plume ascent to equilibration depths. Here, a correction factor is derived without reliance on the MTT model and with a more general situation in mind, one that could include cross flow and asymmetric plume distributions.

In analogy to the derivations that relate isopycnal and level anomalies in Lavelle *et al.* (1998), I specify 3 points in space: a point P within a hydrothermal plume, a point L at the same level as P, and a point H outside the plume at a depth where the salinity is equal to that at point P. Defining the potential temperature at each point as θ_P, θ_L, and θ_H, and beginning with the assumption that for any H and L points on a linear θ–S background trend (described by $\gamma = \mathrm{d}\theta/\mathrm{d}S \equiv (\theta_\mathrm{L} - \theta_\mathrm{H})/(S_\mathrm{L} - S_\mathrm{H})$), the isohaline and level anomalies can then be related by

$$\begin{aligned}
\Delta_S\theta &= \theta_\mathrm{P} - \theta_\mathrm{H} \\
&= \theta_\mathrm{P} - \theta_\mathrm{L} + \theta_\mathrm{L} - \theta_\mathrm{H} \\
&= \Delta_z\theta + \gamma(S_\mathrm{L} - S_\mathrm{H}) \\
\Delta_S\theta &= \Delta_z\theta - \gamma\Delta_z S. \qquad (1.21)
\end{aligned}$$

The last step is made through substitution of $\Delta_z S \equiv S_\mathrm{P} - S_\mathrm{L}$ and $S_\mathrm{P} = S_\mathrm{H}$.

Multiplying each term in Equation 1.21 by ρc_p (again taken to be constant for all parts of the plume) and a generic velocity u, and then integrating over a *bounding* surface A yields a heat flux equation relating the isohaline heat flux H_isoS to the level-to-level fluxes of heat and salt, H and F:

$$\begin{aligned}
\int_A \rho c_p u \Delta_S\theta \mathrm{d}A &= \int_A \rho c_p u \Delta_z\theta \mathrm{d}A - \int_A \rho c_p u \gamma \Delta_z S \mathrm{d}A \\
H_\mathrm{isoS} &= H - \rho c_p \gamma F \qquad (1.22)
\end{aligned}$$

The divergence theorem holds that the flux of salt F through the bounding surface A must be equal to the source salt flux $F_o = \int_{A_o} u\Delta S_o \mathrm{d}A$ through the input surface A_o, where the level anomaly of salt is ΔS_o. Similarly, the outward flux of heat H must equal the input heat flux $H_o = \int_{A_o} u\Delta\theta_o \mathrm{d}A$. Dividing these 2 expressions leads to an expression that links the fluxes and the source anomalies:

$$\begin{aligned} \frac{H}{F} &= \frac{H_o}{F_o} = \frac{\rho c_p \Delta\theta_o}{\Delta S_o} \\ F &= H\left(\frac{\Delta S_o}{\rho c_p \Delta\theta_o}\right). \end{aligned} \tag{1.23}$$

Substituting this expression for F into Equation 1.22 and solving for net level heat flux H, or equivalently input heat flux H_o, leads to

$$\begin{aligned} H_{\mathrm{isoS}} &= H - \gamma H\left(\frac{\Delta S_o}{\Delta\theta_o}\right) \\ H = H_o &= \left(\frac{1}{1 - \frac{\mathrm{d}\theta \Delta S_o}{\mathrm{d}S \Delta\theta_o}}\right) H_{\mathrm{isoS}}, \end{aligned} \tag{1.24}$$

in which the parenthetical term is the correction C that must be made to relate isohaline heat flux to level heat flux. Note that in this derivation γ need not be a linear function relating S and θ.

For typical MEF stratification and focused source properties ($\mathrm{d}\theta/\mathrm{d}S \sim 5\,^\circ$C/psu, $\Delta\theta_o \sim 350\,^\circ$C, $\Delta S_o \sim 0$ psu to -20 psu), C ranges from 1.0 to 1.40, respectively. For the average $\Delta S_o \sim -10$ psu in the MEF, $C = 1.17$; H or H_o is 17% larger than H_{isoS}. When $\Delta S_o \sim -5$ psu, $C = 1.08$; H or H_o is only 8% larger than H_{isoS}.

This relatively small correction to isohaline heat flux needed to obtain estimates of source heat flux over the range of MEF source salinities (Figure 1.6) motivates me to use isohaline temperature anomalies in this thesis. Henceforth, the isohaline anomaly is referred to using the generic symbol $\Delta\theta$. Unless otherwise noted, all figures that follow in this thesis and that involve potential temperature anomalies will display observed $\Delta_S\theta$. All fluxes calculated with these anomalies are "isohaline heat fluxes" but are presented generally as "heat flux estimates" with the understanding that this is a loose use of the term "heat flux" relative to its definition in Equation 1.2. Towards the end of the thesis, isohaline heat flux estimates are corrected using $C = 1.17$, the correction factor associated with the average ΔS_o in MEF vents, to yield a "best estimates" of level heat flux. The Flow Mow best estimates will be compared in Chapter 5 with the historical estimates of heat flux that are reviewed in the next section.

1.3 History of MEF heat flux measurement

Despite compelling scientific motivations, accurate measurements of hydrothermal heat flux at the field scale have proven surprisingly difficult to obtain. In this thesis I focus on understanding the source of the difficulty and determining methods that improve the accuracy and precision of flux estimates in the hydrothermal environment. In preparation for describing a new method used in the Flow Mow study (Chapter 2), this section reviews past measurements of H_f, H_d, and H_p (Figure 1.3) at the MEF and the methodological issues that affected their accuracy and precision. The results of each study provide context for the MEF heat fluxes presented in this thesis. Each study also provides an opportunity to apply Equation 1.2 in order to clarify what was measured and to identify potential sources of uncertainty.

1.3.1 Heat flux measured in equilibrated MEF plumes

Baker and Massoth 1987

Measurements of horizontal current were first incorporated into estimates of H_p near the MEF by Baker and Massoth (1987). This study is exceptional in that it also quantified an upstream, ambient heat flux, H_a, with a vertically oscillating CTD tow (VOT), rather than assuming that the upstream θ field was defined by a single, distant hydrocast. Over a period of ~3 days in June, 1985, ~40 hr of CTD and transmissometer data were acquired during 5 VOTs that assessed the upstream control surface as well as 6 control surfaces downstream of the MEF. The navigated tows were designed to intersect the plume equilibration depths along vertical surfaces oriented normal to the anticipated southwestward mean current.

Current measurements were recorded by an Aanderaa meter at 2127 m depth on a mooring deployed near 47°58.7'N, 129°05.2'W, roughly centered in the axial valley and between the High Rise and Salty Dawg vent fields (Franks 1992). The observed value of $\overline{u}$ during the survey was 2.1±1.2 cm/s at 205° true, very nearly aligned with the 020° true strike of the ridge axis. (This mean was calculated by S. Roth Franks and the theoretical RMS error estimate was derived by Baker and Massoth (1987, page 70); it is unclear, however, whether the mean value indeed derives from the moored meter, or from a different 8-day deployment during the same cruise using the Alvin, as suggested by Thomson *et al.* (1990, page 7262). Over a 27 day period prior to and including the survey, $\overline{u}$ measured at the moored meter was 1.5 cm/s at 170° (Baker and Massoth 1987, page 67), a direction that is more consistent with the 337 day progressive vector diagram for the same meter, which indicates southeastward mean flow at 135° (Franks 1992, Figure II.39). Re-examination of the low-pass filtered records of along- and across-axis velocity components (Franks 1992, Figure II.14, Julian Day 540–542) suggests that the mean flow during the hydrographic survey was initially 2.2 cm/s at 145°, peaked mid-survey flowing 3.2 cm/s at 183°, and finally decreased to 2.0 cm/s at 200°. The along-axis components of these velocities are all within the estimated error and therefore would not not alter the range of heat flux estimates. The $\overline{u}$ magnitude published in Baker and Massoth (1987) appears to have been computed by S. Roth Franks from the unfiltered time series.

Vertical oscillation of the CTD from 1800–2400 m depth and a tow speed of 0.5–1 m/s resulted in hydrographic samples being horizontally separated along-track by 200–2000 m. Retrospective analysis of the hydrographic sections that were approximately normal to the $\overline{u}$ direction of 205° generated 1 upstream and 6 downstream sections, depicted schematically in Figure 1.7 relative to the along-axis distribution of hydrothermal fields known today. Temperatures on each section were expressed as isopycnal anomalies ($\Delta_\rho\theta$). The downstream plume core $\Delta_\rho\theta$ varied ±0.01°C around a typical value of ∼0.05°C, but did not decrease monotonically. In contrast, particle concentrations decreased rapidly downstream in the Endeavour plume (Baker and Massoth 1987).

The integral in Equation 1.2 was evaluated on the upstream and downstream surfaces as a summation, $\sum_i A_i\Delta_\rho\theta_i$. While the method of summation is not explicit, it appears to have involved contouring the VOT data on each section, measuring the area A_i belonging to each non-zero contour, and multiplying by the $\Delta_\rho\theta_i$ value of that contour. Baker and Massoth (1987) acknowledge a potentially large source of uncertainty when they note that some of the cross-ridge sections had $\Delta_\rho\theta$ contours that did not close on the western edge,

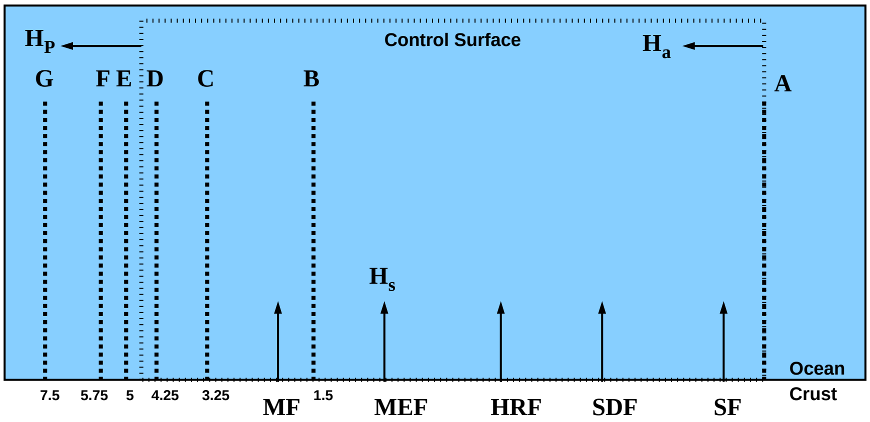

Figure 1.7: Schematic of the Baker and Massoth (1987) measurement of heat flux in advected equilibrated plumes above the Endeavour segment. Approximate along-axis positions of known vent fields are depicted as source fluxes (vertical arrows) along with axis-perpendicular CTD transects (dotted lines A–G, with distance from MEF noted in km for downstream sections, B–G). Field names are abbreviated as in Figure 2.1; other annotations are consistent with Figure 1.2.

suggesting that a portion of the plume was not sampled. Additional sources of uncertainty in the summation are the possibilities that the cross-ridge sections had different areal extents, and that the contouring algorithm misrepresented the real spatial distribution of $\Delta_\rho\theta$.

The net horizontal heat flux through the control volume was estimated by first subtracting the upstream summation from downstream summation, and multiplying by $\rho c_p = 4.2\,\mathrm{MJ{\cdot}m^{-3}{\cdot}^\circ C^{-1}}$. The resultant values for the 6 downstream sections were then averaged, obtaining a mean of $7.9{\pm}2.6{\times}10^4$ MJ/m which was finally multiplied by $\overline{u}$ =0.021±0.012 m/s to yield H_s =1700±1100 MW. As Figure 1.7 illustrates, it is not clear whether H_s represents the heat flux from the MEF, from another field within the control volume, or from some combination of them. Because the effective control volume happened to contain *all* of the major fields known today, the H_p estimate of Baker and Massoth (1987) justifiably constitutes an estimate of the heat flux from the entire Endeavour segment, although it is has primarily been attributed to the MEF alone in the literature. Because the western edge of the plume was not well-defined, H_s from this study is likely an underestimate of the segment-scale heat flux.

The Baker and Massoth (1987) estimate of H_s is adjusted upward by a factor of 2 in Ginster *et al.* (1994, page 4948), based on the premise that temperature anomalies calculated "with respect to ambient temperature at the same depth… neglected the effect of entrainment of colder bottom water into the rising plume." This adjustment can be refined slightly in 2 ways. First, although it is not stated explicitly in Baker and Massoth (1987), they used $\Delta_\rho\theta$, not $\Delta_z\theta$ (E. Baker, pers. comm.). While it is generally important to be clear about temperature anomaly definition, in this case the plumes can safely be assumed to be at equilibrium depth where the heat flux correction factor factor is the same for fluxes based on $\Delta_\rho\theta$ and $\Delta_z\theta$ (*c.f.* Figure 1.6). Secondly, if it is assumed that the surveyed plume was in a steady state and connected to MEF sources, then H_s should be adjusted according to Equation 1.20 with characteristic MEF R_ρ and R_{ρ_o}, rather than Equation 1.19. For the MEF range of S_o the correction factor is 0.20–0.95, not necessarily 0.50. However, this intermediate correction factor is reasonable, and changes the original estimate of Baker and Massoth (1987) to 3400±2200 MW.

Rosenberg et al. 1988

After noting that the position of the plume near the MEF varied during their 23 day study, Rosenberg *et al.* (1988) present hydrographic and chemical data collected over 5 days within what they believe to be a "snapshot" of the plume. Based on 4 VOTs and 5 vertical casts, they mapped $\Delta_\rho\theta$ in a plume extending ~15 km west-southwest from the MEF vicinity. The assumption of a steady-state plume was based on the similarity of radon concentrations at 2 stations near the MEF, one of which was occupied on day 1, the other on day 5. They offer no information about the horizontal homogeneity of the plume, but divide the plume into central and outlying zones in which $\Delta_\rho\theta$ ranges from 0.005 to 0.05°C. Sub-zones are then assigned the maximum observed $\Delta_\rho\theta$ observed within each. Depth profiles of radon concentration and $\Delta_\rho\theta$ were acquired in each of 4 sub-zones in the central plume zone about ~1, 3, 8, and 12 km west-southwest of the MEF, and at a background station ~5 km east of the MEF.

Figure 1.8 illustrates the method by which Rosenberg *et al.* derived a heat flux with measurements of $\Delta_\rho\theta$ and ^{222}Rn, a radioisotope with a 3.85 day half life. The basic premise is that the flux of radon through the bottom surface of a control volume (F) will equal the rate at which radon atoms decay within the volume ($\mathrm{d}N_{Rn}/\mathrm{d}t$). One important underlying assumption is that the *thermal* plume is steadily entering the bottom of the volume and exiting a side, while the steady radon influx decays completely before the hydrothermal plume crosses the downstream surface. This means the control volume is large enough to contain the entire "standing crop" of radon. By assuming the bottom surface flux is dominated by rising plumes with mean vertical transport Q and mean radon concentration [Rn], the general flux equation (Equation 1.1) can be used to calculate the upward flux of radon, $F = Q[\mathrm{Rn}]$. This expression, when combined with the definition of exponential decay, $\mathrm{d}N_{\mathrm{Rn}}/\mathrm{d}t = -\lambda N_{\mathrm{Rn}}$, yields a radon budget:

$$F = Q[\mathrm{Rn}]_v = -\lambda \int_V [\mathrm{Rn}]_p \mathrm{d}V \tag{1.25}$$

in which the subscripts v and p are associated with the vertical transport and the plume enclosed by the control volume, respectively. The volume integral is computed in Rosenberg *et al.* by assigning a vertically-integrated Rn concentration to each plume zone, multiplying it by the area of the associated zone and a plume thickness that is assumed to be uniform, and summing over all zones. The concentrations for the central zones are computed from the measured data above 2100 m; for the outlying zones, the concentrations are extrapolated from the adjacent central value according to the temperature ratio between the zones. The method of estimating $[\mathrm{Rn}]_v$ is explained below, during the evaluation of Equation 1.27.

Setting the size of the control volume to encompass the entire radon plume is a central issue in the Rosenberg *et al.* flux determination. A potentially large source of uncertainty arises from delineating the perimeter of the outlying zones so the encompassed area has $\Delta_\rho\theta$ equal to 1/2 the central $\Delta_\rho\theta$. This means that the areas of the outlying zones are somewhat arbitrary, with the plume edge being defined by a range of $\Delta_\rho\theta$ thresholds, from 0.005 to 0.025 °C. If radon concentrations are assumed to be proportional to observed $\Delta_\rho\theta$, as was done by Rosenberg *et al.*, then to ensure all radon is inventoried the plume edge should be defined by a consistent, minimum, near-zero $\Delta_\rho\theta$ contour, and the volume integration should continue out to that contour level. As implemented, the volume integration underestimates

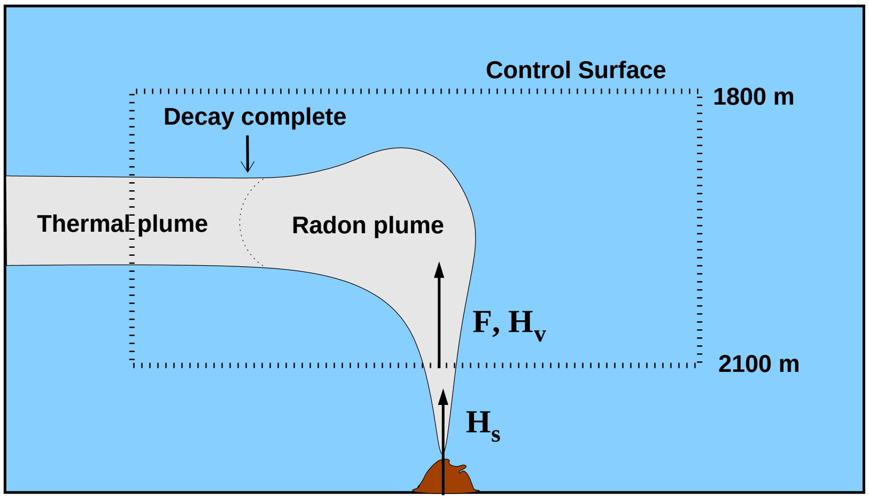

Figure 1.8: Schematic of the ROSENBERG *et al.* (1988) measurement of radon flux F and heat flux H_v through the 2100 m isobath near the MEF. Note that H_s does not necessarily equal H_v.

the standing crop of radon because it misses regions of positive $\Delta_\rho\theta$ surrounding the outlying zones (A*, B*, C* in Figure 4 of ROSENBERG *et al.* (1988)). Similarly, despite extending ~15 km downstream, the hydrographic survey and control volume failed to include the downstream edge of the last central zone (D). For comparison, a minimal mean flow above the ridge of 1 cm/s would extend the radon plume ~3.3 km downstream during a single 3.82 day half-life.

The vertical heat flux through the bottom of the control volume H_v is

$$H_v = \rho c_p \Delta_\rho \theta_v Q. \tag{1.26}$$

Solving Equation 1.25 for Q and substituting it into Equation 1.26 yields H_v as a function of the decay rate $\lambda = 2.1\times10^{-6}\,\mathrm{s}^{-1}$ and the ratio $\Delta_\rho\theta_v/[\mathrm{Rn}]_v$:

$$H_v = \rho c_p \left(\frac{\Delta_\rho \theta_v}{[\mathrm{Rn}]_v}\right)\left(-\lambda \int_V [\mathrm{Rn}]_p \mathrm{d}V\right) \tag{1.27}$$

Under the assumption that $[\mathrm{Rn}]_v$ and $\Delta_\rho\theta_v$ must be greater than or equal to the peak anomaly values in the equilibrated plume, ROSENBERG *et al.* (1988) assign to both variables the peak values observed within the plume core near 2000 m in the 2 profiles taken closest to MEF. They use radon anomalies measured in disintegrations per minute (dpm) relative to the background abundance (30 dpm) to evaluate $[\mathrm{Rn}]_v$ and then adjust $\Delta_\rho\theta_v$ upward, apparently arbitrarily, from 0.05°C to 0.07°C to account for entrainment of deeper colder water between the source and the 2100 m isobath. Then, with $\rho c_p = 4.2 \times 10^6\,\mathrm{J{\cdot}m^{-3}{\cdot}{}^\circ C^{-1}}$, $\lambda = 2.1 \times 10^{-6}\,\mathrm{s^{-1}}$, $[Rn]_v = 2000\,\mathrm{dpm/m^3}$, and $\int_V [\mathrm{Rn}]_p \mathrm{d}V = 8 \times 10^{12}\,\mathrm{dpm}$, H_v (Equation 1.27) takes the value 2.3 GW.

Helium profiles taken near the MEF indicate that ~20% of the plume was located beneath 2100 m and therefore unaccounted for in the volume integral (Rosenberg *et al.* 1988). Making this adjustment to H_v ($2.3/0.8 = 2.9$ GW) and rounding up to 3 GW, they declare $H_s = H_v$. Lastly, they state that consideration of plausible extrema for each term in Equation 1.27 leads to an error estimate of ±2 GW, and thus, a final estimate of $H_s = 3 \pm 2$ GW for the MEF.

Thomson et al. 1992

Most recently, Thomson *et al.* (1992) used measurements of H_p in the Endeavour plume (Figure 1.2) to infer H_s for the entire segment, and for the MEF alone. They established 2 control volumes like the one in Figure 1.2, both aligned with the ridge axis and centered on the MEF, but with different dimensions. The larger was 5 km wide (W, across-axis), 15 km long (L), and 300 m thick, extending from 1900 m depth to 2200 m, the approximate depth of the valley floor near the MEF; the smaller was the same thickness, but only ~1 km on a side. Between July 8–26, 1988, 95 hr of CTD and light attenuation data were acquired during 15 VOTs within 15 km of the MEF. Tow speeds of 2±1 m/s and typical oscillations between 1800–2200 m depth resulted in horizontal plume resolution of 500 m to several kilometers. On average, the entire region within the larger control volume was influenced by the plume; ensemble averages from all casts resulted in positive $\Delta_\rho\theta(z)$ for all depths below 1900 m, with limited data deeper than 2200 m (Thomson *et al.* 1992, Figure 3).

Current data used in estimating H_p were from an RCM4 deployed July 10–August 24, 1988, about 4 km southwest of the MEF, atop the west ridge crest, about 25 meters above bottom at a depth of ~2075 m. Throughout the hydrographic survey period, flow was variable and multidirectional, with daily means of 1–2 cm/s, and hourly means of up to 15 cm/s. These observations of v were assumed to characterize a uniform velocity field on all surfaces of both control volumes over their full depth range.

Using the mean of all available July velocities, v =0.35 cm/s at 332°, the across- and along-axis heat flux components ($H_{p\perp}$ and $H_{p\|}$) were calculated. The ensemble average $\Delta_\rho\theta(z)$ was taken to characterize the mean, horizontally-uniform plume condition on each downstream surface of the larger control volume, with the implicit assumption that the upstream surfaces had $\Delta_\rho\theta(z) = 0$ at all z from 1900–2200 m, making $H_a = 0$ on the upstream south and east control surfaces. H_p was then computed for each downstream surface via a variant of Equation 1.2 (Thomson *et al.* 1992, Equations 2 and 3):

$$\begin{aligned} H_{p\perp} &= \rho c_p L v_\perp \int_{h_2}^{h_1} \Delta_\rho\theta(z)\mathrm{d}z = -765 \pm 465\mathrm{MW} \\ H_{p\|} &= \rho c_p W v_\| \int_{h_2}^{h_1} \Delta_\rho\theta(z)\mathrm{d}z = -230 \pm 150\mathrm{MW} \end{aligned}$$

where $(h_1, h_2) = (1900, 2200)$ m, ρc_p was set to 4.3×10^6 J·°C^{-1}·m^{-3}, and the error estimate results from analysis of the standard deviation of v. Applying Equation 1.3, the downstream flux components in Equation 1.28 yield $H_s \simeq$995±605 MW for the entire segment.

Thomson *et al.* (1992) also use plume cross sections from several VOTs that traversed near the MEF to estimate "instantaneous" H_p for the smaller control volume, assumed $H_a = 0$, and took the difference to infer H_s for the MEF. Interpreting the 2 ridge-parallel VOT sections as having intersected a steady state plume extending from the MEF sources, they use the orthogonal component of the hourly current measurement made (by the same RCM4) at the time the plume core was crossed (∼10 cm/s), and an unspecified method of defining the plume edge or core, to compute H_p via a summation like that in Equation 1.6. The area elements involved in the summation are not explicitly defined as areas of particular $\Delta_\rho\theta(z)$ contours or cells in a regular grid on a control surface. A summation over "the entire plume anomaly" yields H_p =12100 MW; summing over data from "the core region alone" of the same plume, H_p =6300 MW. A second serendipitous encounter with a similar MEF plume produced H_p =6800 MW using only the core area. With the assumption of $H_a = 0$, the range of H_p measurements leads to their published value for the instantaneous H_s

associated with the MEF: 12000±6000 MW.

1.3.2 Heat flux measured at MEF sources

Schultz et al. 1992

One of the few direct measurements of H_d was accomplished atop a sulfide structure in the southern MEF in 1988 (Schultz *et al.* 1992). On the the northern lobe of the structure called Peanut, a funnel-shaped electromagnetic flow meter was placed vertically on a level tube worm patch. Over a ∼48 day deployment, the instrument measured 5 s averages of w and T every 5 min. A moderate amount of high-frequency noise in the T and w signals was attributed to an incomplete seal of the funnel base to the underlying structure, and was removed with a moving average filter with a 12.8 hr window. The mean, minimum, and maximum of the low-pass filtered records were about 10, 8, and 14 cm/s for w and 10, 7, and 13°C for T. Taking A as the area covered by the base of the collecting funnel (30.5 cm inner diameter) and using c_p =4.18 kJ·°C^{-1}·kg^{-1} and ρ =10^3 kg/m^3, the mean, minimum, and maximum heat flux densities were 2.91±0.23, 2, and 4 MW/m^2. Schultz *et al.* extrapolate the mean $H_d \sim 3$ MW to the entire top surface of Peanut's northern 4 m×5 m lobe, suggesting that a typical MEF sulfide structure might have $H_d \simeq$60 MW.

For comparison, they also calculate $H_f = 4.1$ MW for a high T vent located ∼150 m north-northeast of Peanut, on Grotto (R. McDuff, pers. comm.), using different techniques. A 5 week deployment of a thermal imaging system on Grotto yielded a maximum T of 352°C at the center of the plume (348°C warmer than the "ambient" sea water adjacent to the vent) and an orifice diameter of 6 cm ($A = 2.8 \times 10^{-3}$m^2). Analysis of video of the vent led to an estimated w of 0.4–0.5 m/s, but uncertainties in the technique led Schultz *et al.* to take w to be ∼1 m/s. Using these values and pure water c_p and ρ, $H_f = (10^3)(4.18 \times 10^3)(348)(1)(2.8 \times 10^{-3}) = 4.1$ MW, or 1455 MW/m^2. Relative to the diffuse site, the focused vent heat flux density is almost 3 orders of magnitude larger. On the other hand, for these 2 particular diffuse and focused MEF sources, the ratio of heat fluxes, not heat flux densities, is $H_d : H_f \simeq 60 : 4 = 15 : 1$, or about an order of magnitude (Schultz *et al.* 1992). The values here differ slightly from the published values because it appears T was taken to be 248°C in SCHULTZ *et al.* (1992), rather than 348°C.

By integrating the total area of active sulfide structures and tube worm patches delineated on a geological map of the MEF (DELANEY *et al.* 1992), SCHULTZ *et al.* further extrapolate their measurement of mean H_d to the field scale. This requires 2 major assumptions: (1) the diffuse measurement is representative of the mean H_d for the range of venting categorized on the map as active sulfide structures and tube worm patches, and (2) the mapping process, based on Alvin heading, long-baseline navigational fixes, and visual interpretation of video footage, generated accurate perimeters for distinct environments throughout the MEF. The first assumption is verified to some degree by unpublished observations of H_d that "reinforce" the results from Peanut (SCHULTZ *et al.* 1992, page 12311); these observations, acquired in 1991, include deployments in diffuse flow atop most of the major structures within the vent field (SCHULTZ *et al.* 1992, page 12311) and 41 spot measurements obtained at Clam Bed (A. Schultz, pers. comm.). Digital analysis of the geologic map gives an integrated top surface area of ~3300 m^2, making H_d for the entire MEF field ~9600±760 MW. A similar extrapolation of H_f from the single vent on Grotto to the ~110 known high B sources within the MEF (*c.f.* 2.1.3) suggests a total $H_f \simeq 451$ MW. Assuming the diffuse and focused measurements are representative of the mapped areas, the partitioning of heat flux over the entire MEF is $H_d : H_f \simeq 9600 : 451 \simeq 21 : 1$.

Ginster et al. 1994

The most direct measurement of H_f in the MEF was accomplished by GINSTER *et al.* (1994) during 5 Alvin submersible dives within the MEF in 1988. At 31 of the 65 distinct MEF focused vents known at the time, a turbine flow meter was placed in the high T "black smoker" fluid, acquiring w (averaged over the 2.65 cm diameter turbine entrance) 2–12 cm above the vent orifice. A platinum resistance thermocouple monitored T alongside the flow meter while the Alvin temperature probe was inserted into the orifice to measure T_o. The radius of the orifice was estimated from video footage analysis and visual observations, with an error of ~5% (GINSTER *et al.* 1994).

Equation 1.2 was evaluated to yield H_f at the source by assuming a top-hat distribution of T_f across the orifice with a value equal to the maximum T_o observed at each vent. The observed maximum value was used, rather than a mean value, primarily because the response time of the thermistor was thought to result in some averaging of small-scale variations. A top-hat distribution was also assumed for w_f, but its magnitude was taken as either the maximum w observed at 2–12 cm above the source, or a model-constrained w that was adjusted according to plume theory to compensate for the deceleration of the fluid in the first 2–12 cm of rise. A was estimated based on video-estimation of orifice radii (1.2–9.5 cm) and an assumption of orifice circularity which introduced a factor of 2 error (Ginster *et al.* 1994). The densities of fluid observed at the orifice and in the plume ~12 cm above were published, but is unclear how they were derived and which value was used in the calculation of H_f. Assuming that the density at the orifice was used, its mean value across the MEF was 664 kg/m^3 (Ginster *et al.* 1994). The value of c_p was not specified, but for some vents back calculation indicates the value was ~5000 J·°C^{-1}·kg^{-1}.

The H_f measured at 31 high B vents was 6.2±8.2 MW/smoker, with extreme values for individual smokers between 0.9 and 42.2 MW, primarily due to variations in orifice radius. Depending on whether the measured or modeled w was used in calculating H_f for individual vents, extrapolation to all 65 known vents yielded H_f for the MEF of 331±68 or 364±73 MW, respectively (Ginster *et al.* 1994). The extrapolation of H_f measured at particular vents to the field scale was executed not through a simple multiplication of the mean and the number of vents, but rather a complicated tabulation of H_f, calculated structure by structure with different combinations of observed and modeled values, and an underlying assumption that the mean H_f measured at a subset of the vents on a particular structure represented the flux through all vents on that structure. Consequently, it is difficult to discern how best to re-evaluate it now that the number of mapped high B vents has increased from 65 to 110. One approach is to assume that all 110 vents existed in 1988, despite some being unknown, and make an upward adjustment by a factor of 1.69 (= 110/65), leading to revised values for the 2 H_f estimates: 559±115 and 615±123 MW. An alternative approach is to assume the mean measured value applies directly to all known vents: 6.2±8.2 MW/smoker × 110 smokers≃682±902 MW. Since the commonly cited published value is 364±73 MW, in the remainder of this dissertation I will consider the associated accurately-extrapolated value 615±123 MW to be the best estimate of H_f (Table 1.2) from GINSTER *et al.* (1994).

Bemis et al. 1993

Simultaneous to the GINSTER *et al.* study, during the same series of Alvin dives in 1988, BEMIS *et al.* (1993) made measurements of T and w in rising plumes 10–50 m above the sources, and inferred H_f through plume theory. Their instruments were arrayed on a 50 m wire that extended upward from the sampling basket on the front of the submersible (Figure 1.9), and remained within 10° of vertical when Alvin was stationary (based on tilt meter records)(BEMIS *et al.* 1993). With the submersible basket positioned near the orifice of a high B source, T was measured every 2 seconds by 5 thermistors spaced ~10 m apart on the wire (at 11.5, 21.4, 30.7, 40.4, and 49.9 m above the basket). A flow meter 22 m up the wire measured w (and the horizontal velocity, u), yielding 14 s mean values over a sampling cross-section of 25 cm^2 that was offset ~0.5 m from the wire in an unknown direction due to wire rotation. A CTD package adjacent to the flow meter gathered conductivity and pressure readings.

Time series were collected continuously during 10 dives within the MEF. At each of the 36 studied vents, the submersible was maneuvered within a few meters of the orifice to sample for GINSTER *et al.* and then remained approximately stationary for 20–30 min. One published example of the raw data is a 4 hr time series from Dive 2113 in the northern MEF near Dante (BEMIS *et al.* 1993, Figure 6). The chronology of GINSTER *et al.* (1994, Table 1) suggests that the 4 hr record includes visits to Crypto and Hulk, as well as Dante 2.6.

While the published raw temperature data are intriguing, they are plotted as temperature anomalies, hereafter ΔT, without a clear explanation of how the anomalies were calculated. The thermistor resolution was reduced from 0.001 to 0.05°C by Alvin electrical noise contaminating the recorded T signals, and there is no discussion of calibrations. Despite these limitations, the ΔT signals are consistent with strong plumes; they have values of a few degrees and high variance relative to the nearly isothermal series recorded during transits between sampling sites. For each of the j thermistors, ΔT_j is probably the raw T_j minus an ambient T_{a_j} "typical" of the low variance transit periods. Thus, I consider the anomalies to be referenced by depth to an unspecified in-field ambient T profile. During each high variance period the peak ΔT decreases with height above the source, typically about $-1°$C/thermistor from 4.5°C at the deepest thermistor.

An expanded plot of a 12 min subset of the same data (Bemis *et al.* 1993, Figure 8) indicates that the averaging period of the T (and w) resulted in smooth series; even at the deepest thermistor, there are few ΔT discontinuities and most positive deviations from near-zero values are roughly Gaussian with typical durations of 0.5–1 min. From deepest to shallowest thermistor, the maximum ΔT measured during this shorter record are 3.10, 1.24, 1.02, 1.28, and 0.71°C; the mean values of all "in plume" ΔT observations (the T_{hot} data of Bemis *et al.*) for each thermistor are 0.86, 0.50, 0.43, 0.40, and 0.27°C.

The 4 hr velocity series also reveals distinct signals in and out of plumes. Between plumes, w has a near-zero mean and variations of ± 5 cm/s; within plumes, w is always positive, with a mean of $\sim$15 cm/s, a typical maximum of $\sim$30 cm/s, and a peak observed value of $\sim$45 cm/s. Although its direction is not specified, u in plumes has a mean of zero and variations of ± 5 cm/s; outside plumes, u is dominated by Alvin motion. Finally, the expanded plot shows that w varies more smoothly than ΔT, as expected from its longer averaging period, but is still correlated with the ΔT signal. The maximum w from the shorter record is 23.5 cm/s, while the mean w associated with the T_{hot} data is 13.4 cm/s (Bemis *et al.* 1993).

Measured at 18 unique MEF vents, these types of data were combined by Bemis *et al.* through methods similar to those of (Little *et al.* 1987) to infer a source heat flux that could be compared with the H_f measured simultaneously by Ginster *et al.*. Motivated by the hypothesis that MEF high B plumes can be considered ideal, axisymmetric, buoyant plumes rising into a uniform, quiescent environment, they use simple plume theory (Fischer *et al.* 1979) to derive 3 equations. The first expresses the relationship between H_f and source buoyancy flux, B_f. The second and third equations describe the average centerline T and w as functions of elevation in the plume and B_f. Then, citing laboratory plume studies (Papanicolaou and List 1987), they assume that the horizontal distributions of T and w

are Gaussian in the rising plume, with maxima equal to the average centerline values. They further assume that their in-plume T data, taken at unknown positions in the Gaussian distribution, characterize a "flow weighted average" equal to half the centerline average. Combining these assumptions and the latter 2 equations, they obtain an expression that allows B_f to be estimated from the T measurements made by pairs of vertically-offset thermistors (Bemis *et al.* 1993, Appendix). Finally, each calculated value of B_f yields an estimate of H_f, since Bemis *et al.* take $H_f = \rho c_p B_f/(\alpha g)$, where α is the coefficient of thermal expansion ($^{\circ}\mathrm{C}^{-1}$).

The published total inferred H_f for the 18 unique MEF vents sampled is 70–239 MW, while the average H_f is 3.9–13.3 MW/vent (Bemis *et al.* 1993, Table 6). Extrapolating the range of average values to the ∼110 vents now known yields a best estimate of H_f for the entire MEF is 429–1463 MW (Table 1.2).

Alternative interpretation of the measurements of Bemis et al.

In this section, I analyze a portion of the Bemis *et al.* (1993) data from a control volume perspective to demonstrate that entrainment is an important plume process that affects the measurement and interpretation of heat flux. The left side of Figure 1.9 depicts the experiment of Bemis *et al.* (1993). On the right side, the plume is overlain with a control volume that is a conic section, in keeping with the hypothesis that the plume can be modeled as axisymmetric. The radius is assumed to increase with height linearly at a rate of $b/z \simeq 1/10$ (Fischer *et al.* 1979; Turner 1986). The control surfaces are annotated with the terms of a heat budget: H_f is the source flux measured by Bemis *et al.* (1993) and Ginster *et al.* (1994), H_e is flux due to entrainment through the conical plume boundary, and H_v is the vertical heat flux in the rising plume, estimated below with data from Bemis *et al.* (1993).

The top surface of the control volume is drawn at the elevation of the flow meter, the only depth at which *both* T and w were measured. I assume that for any plume transect — essentially a random sampling of the Gaussian distribution, the peak values observed constitute best estimate of mean centerline values (Little *et al.* 1987, page 2594). Thus,

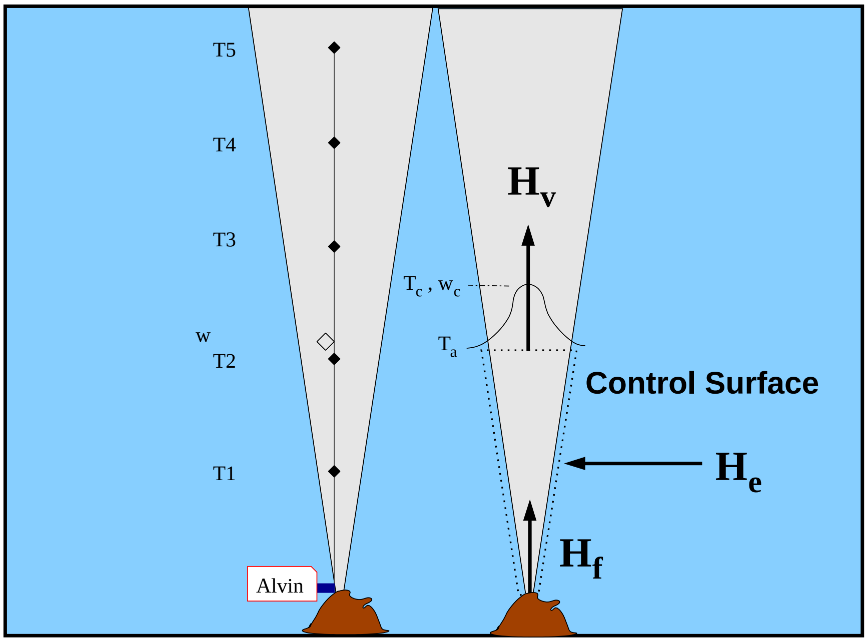

Figure 1.9: Schematic of the Bemis et al. experiment. The plume on the left contains a diagram of the array of thermistor and flow meter instruments. The plume on the right illustrates a control volume and heat fluxes associated with the source (H_f), the rising plume (H_v), and the entrained fluid (H_e). A Gaussian profile of mean T and w across the plume is depicted near the depth of of the T2 thermistor and flow meter. Plume boundaries are drawn approximately to scale if defined by the radial distance from the centerline at which T and w become undetectable by the instruments of Bemis *et al.* (1993) ($\sim$4 m radius at $\sim$20 m elevation).

the mean centerline values are taken to be $\overline{\Delta_z\theta}$ =3.5 °C and $\overline{w}$ =0.3 m/s, the typical maxima observed within rising plumes ∼20 mas by Bemis *et al.* (1993). The smoothness of the raw time series suggests that the 2 s and 14 s averaging periods of each sample were probably sufficient to prevent small-scale variations within the plume from biasing the peak values from the true centerline mean values.

Embracing the assumption of mean horizontal distributions being Gaussian (*e.g.* $\Delta_z\theta(r) = \overline{\Delta_z\theta}_c e^{-r^2/b^2}$), and integrating out to the radius $r = 2.15b$, where the distributions have decayed from the centerline values down to the sensor resolutions stated in Bemis *et al.* (1993), the vertical heat flux H_v through the upper surface is

$$\begin{aligned} H_v &= \rho c_p \overline{\Delta_z\theta}_c \overline{w}_c \int_{\omega=0}^{2\pi} \int_{r=0}^{2.15b} e^{-2r^2/b^2} r \mathrm{d}r \mathrm{d}\omega \\ &\simeq \pi b^2 \rho c_p \overline{\Delta_z\theta}_c \overline{w}_c \\ &\simeq 63.4\,\mathrm{MW} \end{aligned} \tag{1.28}$$

when b =2.14, $\rho c_p = 4.2 \times 10^6\,\mathrm{kJ{\cdot}{}^\circ C^{-1}{\cdot}kg^{-1}}$, $\overline{\Delta_z\theta}_c = 3.5$°C, and $\overline{w}_c = 0.3$ m/s.

This method generates an estimate of H_v that is about 3 times greater than H_f = 24.7 MW measured simultaneously by Ginster *et al.* (1994) at vent 8J, a source on Dante that likely generated H_v (based on Alvin X, Y coordinates for dive-vent 2113-E in Bemis (1990, Table 5a)). The plume model (Figure 1.6) indicates that H_v calculated with $\Delta_z\theta$ is expected to be *less* than H_f, by only a few percent ∼20 m above the source. In contrast, the result in Equation 1.28 is much greater than H_f. This is best explained by the idea that a high B plume will entrain water that has positive $\Delta_z\theta$ due to warming by nearby diffuse vents (*e.g.* Ginster *et al.* 1994, page 4943).

1.3.3 Synopsis

Historical estimates of heat flux at the Endeavour segment are summarized in Table 1.2. The wide range of calculated precisions results from diverse methodologies and assumptions of the studies. The distinct scales and designs of each study also raise questions about the accuracy of attributing a measurement made in the water column with a specific hydrothermal source or area on the sea floor.

Table 1.2: Summary of historical Endeavour heat flux estimates. These "best" estimates may differ from published values because they include adjustments, as discussed in the text. The single lines separate different types of heat flux estimates: first 3 are associated with individual high B vents; next 3 are extrapolations to multiple sources within the MEF; remainder are associated with the MEF and possibly other fields on the Endeavour segment. All fluxes are expressed as absolute values. Where given, the error estimate is either the published value or the standard deviation of samples.

Reference	Heat flux [MW]	Probable source(s)
Ginster *et al.* 1994	6.2±8.2	Mean H_f: 31 vents
Schultz *et al.* 1992	4.1	H_f: 1 vent
Data from Bemis *et al.* 1993	63.4	H_v 20 mas: Dante + entrainment
Ginster *et al.* 1994	615±123	H_f: 110 MEF sources
Bemis *et al.* 1993	359–1224	H_f: 110 MEF sources
Schultz *et al.* 1992	9600±760	H_d: All MEF diffuse flow
Thomson *et al.* 1992	12000±6000	Instant. H_p: MEF (& other fields?)
Thomson *et al.* 1992	995±605	Mean H_p: MEF (& other fields?)
Baker and Massoth 1987	1700±1100	Mean H_p: MEF (& other fields?)
Rosenberg *et al.* 1988	3000±2000	Mean H_p: MEF (& other fields?)

The review in this section sets the stage for the presentation of the Flow Mow field program in the next chapter. Most past heat flux estimates fall within a reasonable range of each other given the differing methodologies, but in many of the studies it is difficult to relate the measurements to specific hydrothermal sources or areas on the sea floor. Chapter 2 presents the setting and methods of the Flow Mow study, as well as the general hydrography and currents over the Endeavour segment. In contrast to past investigations, the Flow Mow study endeavored to measure fluxes on all sides of a control volume so that a net outward flux could be related to a well-defined area of the sea floor, the MEF, and the hydrothermal sources it contains.

Chapter 2

THE FLOW MOW EXPERIMENT

The Flow Mow field program (August 3–21, 2000) was an effort to measure the heat flux of a hydrothermal vent field, specifically the Main Endeavour vent field (MEF) on the Endeavour segment of the Juan de Fuca ridge (Figure 2.1). While previous studies measured heat flux in plumes near their sources or their equilibration depths, the Flow Mow strategy was to intercept plumes at an intermediate, optimal distance above their sources. By establishing a control volume that enclosed the best-mapped hydrothermal field in the world, the stage was set to "mow" the "flow" — to survey the top control surface repetitively, in a back and forth pattern akin to mowing a lawn, as plumes rose through it. The side surfaces were also monitored to assess possible lateral fluxes associated with fluid entrained by the rising plumes or plumes bent over and advected by ambient currents. The methodology was economical because it avoided the expense of acquiring measurements at vents on the sea floor. It was also effective, leading to heat flux measurements that could be accurately associated with specific areas of hydrothermal activity, unlike some past measurements made in advected plumes.

The key to the success of the Flow Mow study was a careful combination of theory for guiding the methodology and technology for acquiring the observations. A numerical model implemented by R. McDuff predicted the elevation at which rising plumes were large enough to be intercepted frequently, but still intense enough to yield a strong velocity and temperature signal relative to noise. An autonomous underwater vehicle called the Autonomous Benthic Explorer (ABE) provided an efficient, economical, and stable platform for repetitively sampling the control surfaces. More traditional instruments — a lowered CTD and moored current meters — served to monitor the ambient hydrography and flow, critically supplementing the ABE surveys of the side control surfaces.

While the primary use of the Flow Mow data is heat flux estimation, the data also

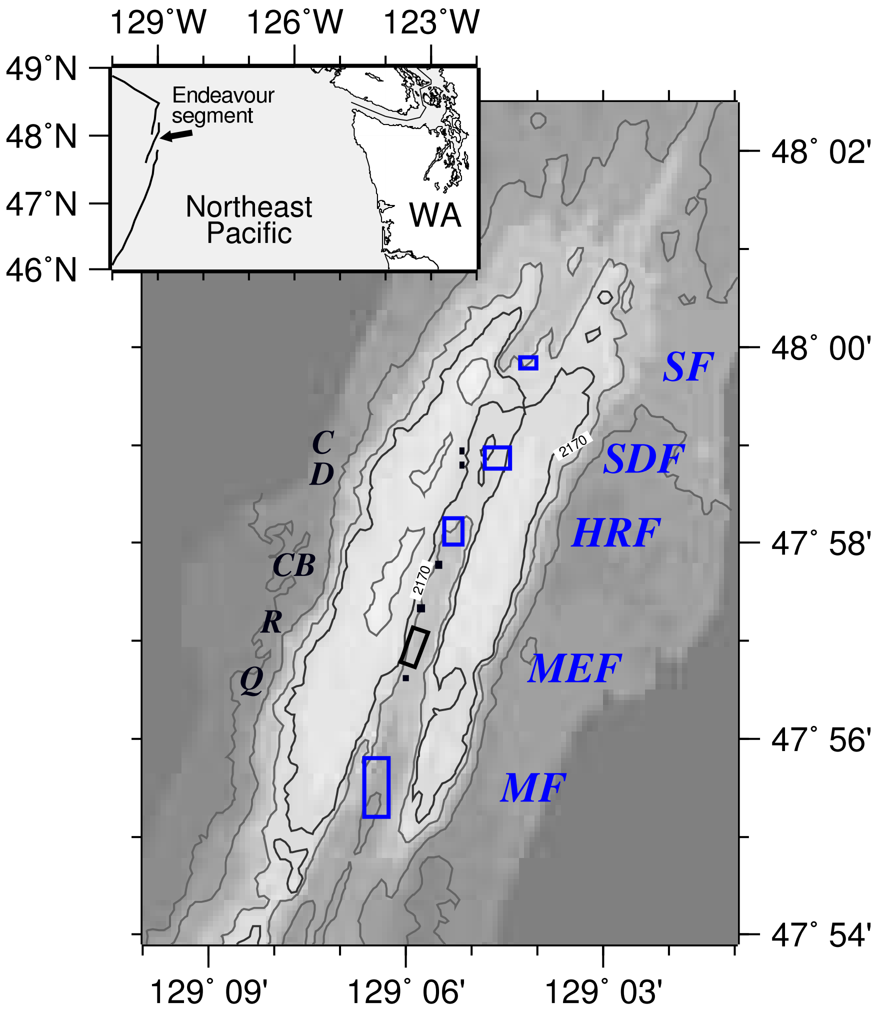

Figure 2.1: Endeavour segment bathymetric map showing known hydrothermal sources: open boxes are major fields (MF=Mothra, MEF=Main, HRF=High Rise, SDF=Salty Dawg, SF=Sasquatch) and small solid squares are diffuse or isolated focused vents (Q=Quebec, R=Raven/ReddFox, CB=Clam Bed, D=Dune, C=Cirque). Contours are every 100 m and at the sill depth, ∼2170 m. Open black box aligned with ridge axis is perimeter of MEF — the boundary of the Flow Mow control volume.

represent an unprecedented characterization of hydrothermal plume hydrography. The majority of plume observations to date are of fluid that is just exiting a vent or is equilibrated; observations in and near buoyant plumes are relatively rare. In contrast, the Flow Mow study focused almost exclusively on intercepting buoyant or equilibrating plumes, and characterizing the environment through which they rose.

This thesis presents the majority of the Flow Mow field data, with an emphasis on synthesizing CTD surveys and current measurements. This chapter presents an overview of the hydrographic and current meter data, while the next 2 chapters present CTD observations made on specific surfaces of the Flow Mow control volume and combine them with data from the current meter moorings to make heat flux estimates. This thesis does not describe in detail the Flow Mow data acquired on the top control surface, as those observations are presented in Stahr *et al.* (2003). It does, however, present the magnitude of the vertical heat flux through that top surface, combines it with magnitudes of other heat flux estimates in a heat flux budget for the MEF, and discusses the implications of the budget.

This chapter provides a synopsis of some of the Flow Mow observations, places them in the context of regional hydrography, and sets the stage for further analysis of plume distributions and heat flux in subsequent chapters. First, I present the details of the study: setting, methodology, and instrumentation. Second, I describe patterns in currents with an emphasis on how the flow differs within and above the axial valley. Third, I scrutinize how the hydrography changes from beyond the ridge flanks, distant from known hydrothermal sources, to the axial environment where both equilibrated and buoyant hydrothermal plumes become increasingly intense and prevalent. Overall, this chapter will introduce some new perspectives on how plumes and currents transport hydrothermal energy and products into the ocean, and will also establish the context for calculating and interpreting heat fluxes in the subsequent chapters.

2.1 Setting

The Endeavour segment presents an unusual opportunity to measure heat fluxes for 2 main reasons. First, the hydrothermal sources and geology within the MEF are well-mapped.

This guarantees that a measurement of net heat flux through control surfaces bounding the field can be related accurately to a specific suite of sea floor hydrothermal phenomena. Second, the topography of the ridge and the hydrography of hydrothermal plumes have similar scales. Unlike at faster- or slower-spreading centers, the vertical relief of the axial valley ($\sim$100 m) is greater than the rise height of diffuse plumes, but less than the rise height of focused plumes (Figure 2.2). The top of the axial valley also marks a change in currents — from strong, multidirectional flow above the ridge crests to relatively slow, rectilinear flow within the axial valley.

The combination of topographic relief, plume rise height, and currents motivate different methodologies for measuring heat flux within the axial valley versus above it. Above the ridge crests, flux measurements depend on interception of advected plumes (*e.g.* Baker and Massoth 1987). This approach is also required at fast spreading centers where the axial valley, or caldera, is typically too shallow to constrain hydrothermal plumes from either focused or diffuse sources. In contrast, a typical slow spreading center has a deep axial valley that can confine all hydrothermal plumes (*e.g.* Rudnicki *et al.* 1994) and motivates a budgetary approach to quantifying fluxes (Murton *et al.* 1999) and diapycnal diffusivities (Thurnherr *et al.* 2002).

The Flow Mow methodology took advantage of the Endeavour setting by intercepting plumes within the axial valley, accounting both for equilibrated plumes advected laterally by the rectilinear flow and for buoyant plumes rising out of the valley, but not yet exposed to the overlying flow (Chapter 3). In order to compare the Flow Mow methods and results with those of previous heat flux measurements made above the ridge in advected, equilibrated plumes, a secondary investigation was conducted near the end of the cruise. At the same time the vertical heat flux in buoyant plumes was being measured, the equilibration depths of the same plumes were surveyed, providing estimates of net horizontal heat flux in the multidirectional flow above the ridge (Chapter 4).

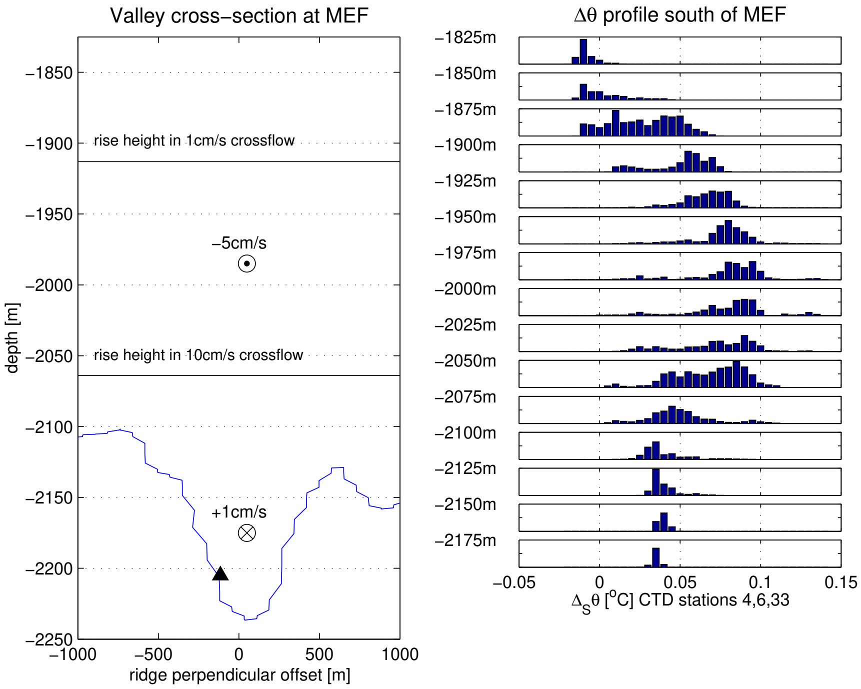

Figure 2.2: Axial valley relief and current shear relative to plume rise heights. The left panel shows an axis-perpendicular cross-section of the Endeavour segment Hydrosweep bathymetry (D. Kelley, 1996), with the location of the MEF indicated by a black triangle. The mean flow within and above the axial valley is indicated, along with the range of rise heights expected in cross flows of 1–10 cm/s. The right panel shows stacked histograms of temperature anomaly data that were acquired during a 14 hr CTD station ∼500 m south the MEF and subsequently grouped into 25 m depth bins.

2.1.1 Bathymetry

From a regional perspective, the Endeavour segment is a series of linear ridges striking $\sim$20° east of north. Along the central ridge, the actively spreading axis, the segment is about 46 km, long when defined by the 2400 m contour (Figure 2.3). While the surrounding basins have depths of 2500–2700 m, the ends of the segment ends descend as deep as 2800 m. Prominent bathymetric features in the vicinity are the Heck and Endeavour sea mounts about 35 km to the north and Split sea mount about the same distance to the south-southeast (Figure 2.3). There are other sea mounts within $\sim$100 km west of the ridge, but none to the east, an asymmetry that has been noted (*e.g.* DELANEY *et al.* 1992), but not related to the regional flow or hydrography near the Endeavour segment.

The Endeavour segment is essentially a short linear ridge with an elongate summit depression, or axial valley, that is open at both the north and south ends, but shoals to a sill near the north end, at 47°59.75'N (Figures 2.1 and 2.4). When defined by the 2170 m isobath (the approximate depth of the sill), the east and west crests of the segment are $\sim$10 and $\sim$12 km long, respectively. At the latitude of the MEF, the segment is $\sim$4 km wide when measured between the points where the outer flanks rise abruptly from adjacent depressions that are 2350–2400 m deep. The rounded outer flanks rise about 250 m to crests near 2100 m depth. The shallowest point on the ridge is $\sim$2050 m atop a rounded summit at the north end of the west crest, adjacent to the axial sill (Figure 2.4).

2.1.2 Geology

Tectonic spreading at a half rate of 29 mm/yr (ELVERS *et al.* 1973) has created an axial valley that has a uniform width of $\sim$1 km between the rims (KAPPEL and RYAN 1986). Near the center of the segment, the valley floor is $\sim$500 m wide and is bounded by basaltic talus slopes and/or fault scarps. Analysis of segment bathymetry (Figures 2.2 and 2.4) shows that these valley walls have an average relief of $\sim$100 m and slopes of 10-30°. Along-axis, the valley floor shoals to the north at an average rate of $\sim$18 m/km.

Within the MEF, it is striking that all known hydrothermal sources rest on a nearly-level, 100×600 m, terrace between 2190–2200 m that narrows dramatically to the north and

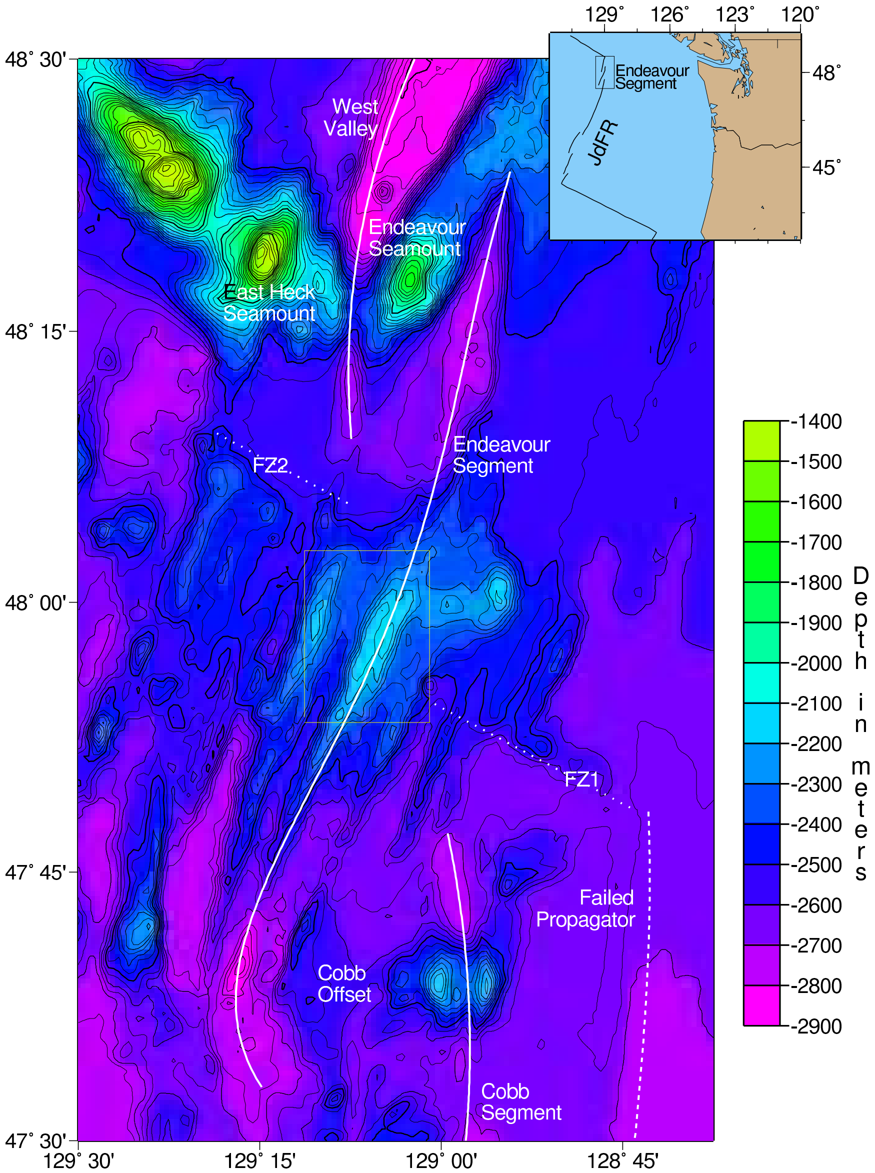

Figure 2.3: Sea Beam bathymetric map of prominent topography in the vicinity of the Endeavour segment. Contour interval is 100 m. Solid lines are inferred tectonic boundaries. Dotted lines are hypothetical boundaries and fracture zones (FZ), suggested by microearthquake distributions. Figure courtesy S. Archer and V. Bhat.

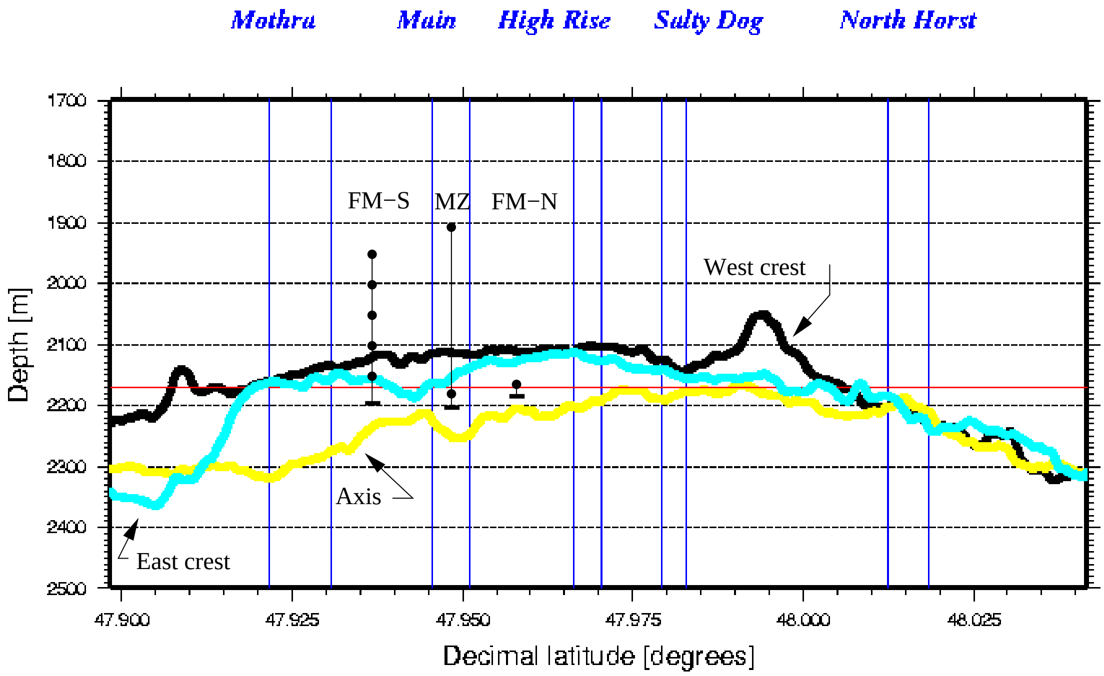

Figure 2.4: Axis-parallel bathymetric sections along the valley floor and ridge crests. Short vertical lines are 3 moorings (FM-S, MZ, and FM-N) with individual current meters (solid circles) at specific depths. Vertical lines with labels at top margin are boundaries of major vent fields. Solid horizontal line at 2170 m marks the depth of the sill near 48°N. Cross-sections are based on Hydrosweep bathymetric data (D. Kelley, 1996). Axis depths are generally deeper than the depths of the mooring bases or hydrothermal fields because the moorings and fields are often located on the shallower sides of the valley, rather than directly on the axis.

south (Figure 2.5). The terrace ends abruptly on its southwest side where the western scarp attains slopes up to 45°. The western wall of the axial valley is less well defined at the north end of the terrace; while the basalt–talus contact at the base of the scarp trends ∼20°N, the western rim of the valley wall diverges to ∼10°N. Like the other known fields to the north and south (Figure 2.1), the MEF rests on the relatively flat valley floor. The surface of the terrace consists of low-relief basaltic pillow and sheet flows that are nearly continuous, except for being broken intermittently by 10–100 cm wide fissures and 1-10 m throw normal faults with strikes parallel or oblique to the 20°N.

The MEF is the most thoroughly mapped hydrothermal area on the Endeavour segment Delaney *et al.* (1992), having been the subject of myriad Alvin dives (more than any other site in the world) and numerous geophysical surveys. It was first located in 1982 when a dredge brought up unexpected sulfide blocks (Tivey and Delaney 1986) and was explored via submersible in 1984 (Hammond *et al.* 1984; Group 1984; Tivey and Delaney 1986). The field consists of 2 clusters of sulfide structures separated by ∼150 m (Figure 2.6). The structures are unusually large, having volumes of 10^5–10^6 m^3 (Wilcock and Delaney 1996) and heights of 3–21 m. Most structures are 10–15 m across (Tivey and Delaney 1986) and are based on basalt near 2195 m depth. While some structures in the north straddle the northeast edge of the terrace and have bases as deep as 2205 m, and a few in the south have bases as shallow as 2190 m, source depths are similar throughout the field because the 7 major northern structures are distinctly larger than the ∼11 southern structures. Based on dimensions noted in the map of Delaney *et al.* (1992), the active sulfide structures in the north have larger diameters (20–40 m versus 10–20 m in the south) and are taller on average (∼12±4 m versus ∼7±2 m). Consequently, the average depth of MEF high B sources is about the same in the north and south clusters (2185±6 m versus 2188±5 m).

2.1.3 Hydrothermal activity

As shown in Figure 2.1, the major vent fields are separated along-strike with spacing of ∼2 km (Delaney *et al.* 1996). A growing number of relatively isolated high and low B

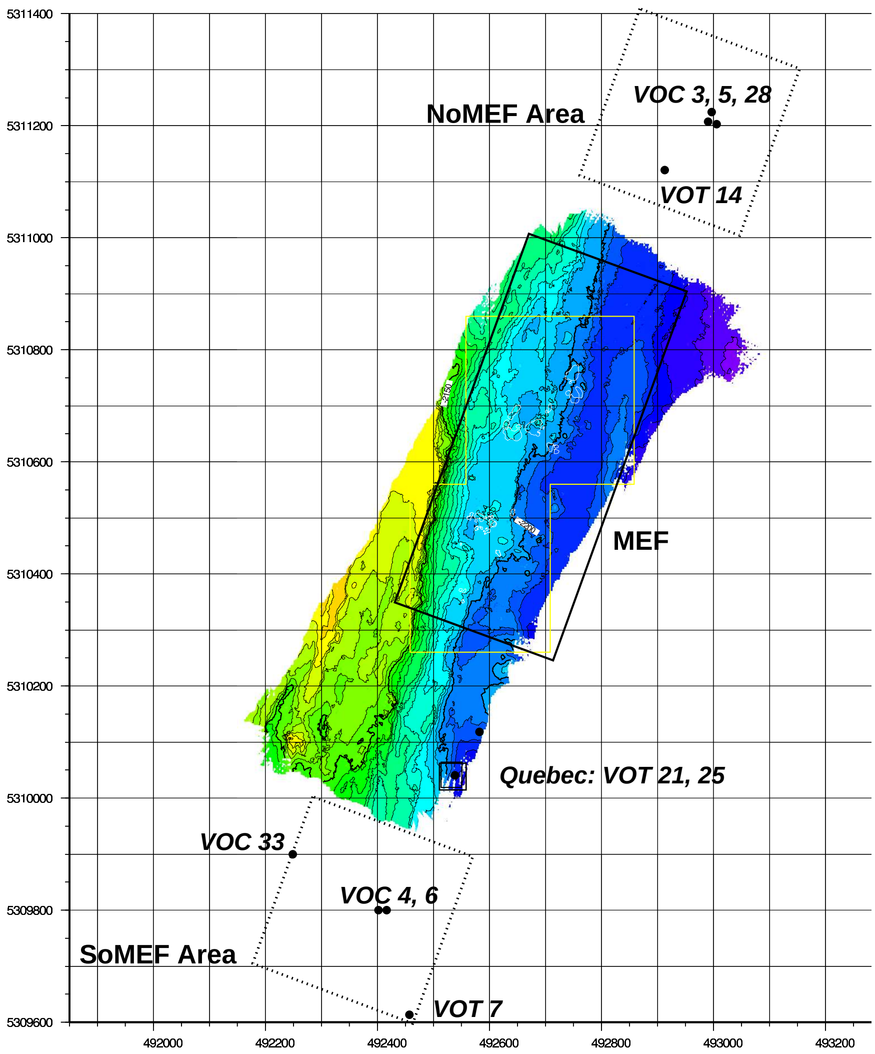

Figure 2.5: Bathymetric map of the MEF vicinity annotated with locations of CTD stations within the NoMEF, SoMEF, and Quebec survey areas. Bathymetric data were acquired with a Mesotech downward-looking sonar mounted on ABE during dive 43, processed by D. Yoerger and C. Parker Sarason. Large rectangle aligned with the ridge axis delineates the boundaries of the Flow Mow control volume. Outlines of actively venting sulfide structures are overlain in red, based on the geologic observations made from the Alvin submersible (within rectilinear polygon) and cataloged by V. Robigou in the map of Delaney *et al.* (1992) (see Figure 2.6). Discrepancies of $\lesssim$30 m between the outlines and local bathymetric highs are likely due to inaccuracies in the absolute location of the Alvin submersible in 1988. Relative locations of structure outlines are accurate to within a few meters. UTM X and Y coordinates are based on zone 9 and the WGS84 ellipse, with the origin of the Alvin coordinate system at X =492638.34, Y =5310510.09.

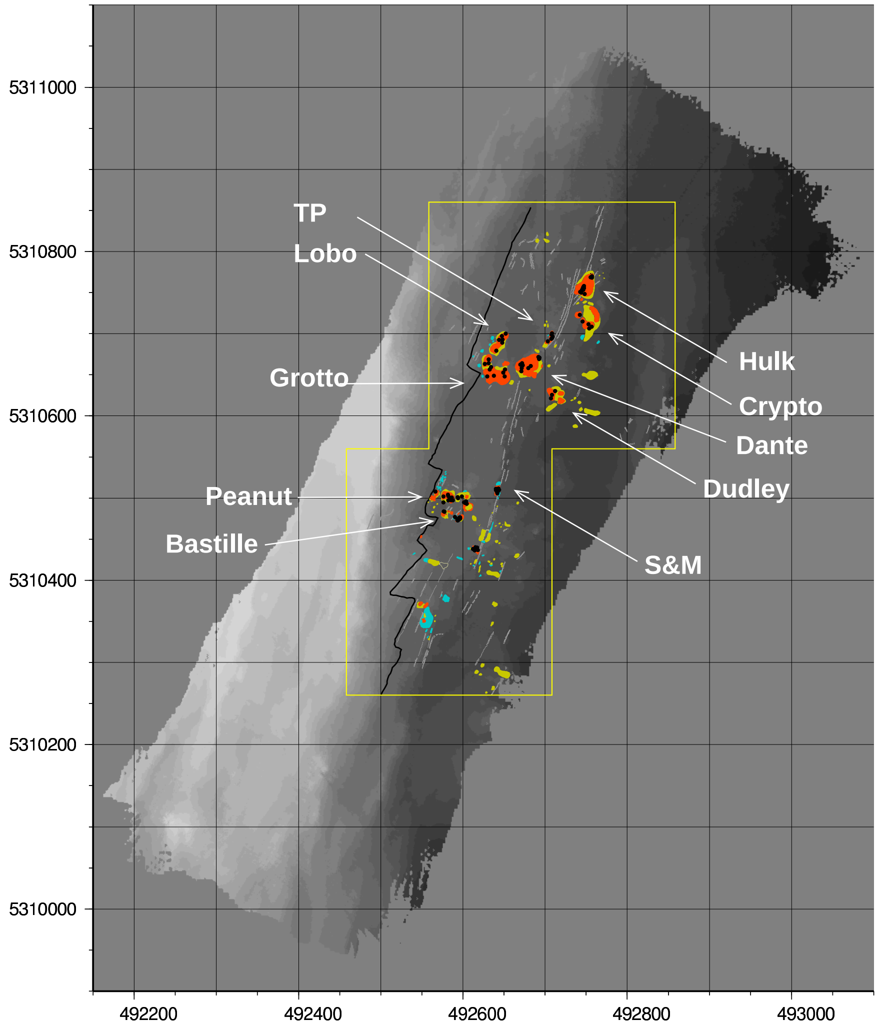

Figure 2.6: Digitized version of the geologic map of the MEF created by V. Robigou (Delaney *et al.* 1992). Arrows connect names to sulfide structures that are actively venting from high B sources (black dots). Inactive sulfide structures are yellow. Areas of diffuse venting are light blue. Major fissures and faults are delineated in grey. Approximate location of contact between talus scarp and valley floor is shown by jagged black line near western edge of field.

sources have been located or are suspected to exist in between (Veirs *et al.* 1999; Johnson *et al.* 2002; Kelley *et al.* 2002)., some of which are mapped Figure 2.1.

The location and intensity of hydrothermal sources close to the MEF, but outside the Flow Mow control volume, are particularly important to this study because of their potential influence on the MEF hydrography. One such source is Quebec, a low B area ~500 m south of the center of the MEF. Quebec is roughly 40 m square, rich in tube worm beds venting ~12°C fluid of unknown salinity (see dive summary at www2.ocean.washington.edu/zephyr/divesum/2998.s and potentially close enough to the MEF to exert an influence on measurements of horizontal heat flux through the south side of the MEF control volume. Another known source near the MEF perimeter is a lone high B source ~500 m north-northeast of the MEF recently dubbed Raven (H. P. Johnson, pers. comm.) and previously noted as Redd Fox (V. Bhat, pers. comm.). A buoyant plume was detected in the Raven/Redd Fox vicinity by M. Landsteiner during VOT t06a of the Mixing Zephyrs hydrographic program (1995).

Within the MEF, ~110 individual focused sources are distributed atop the actively-venting sulfide structures. The hydrothermal fluid typically exits near the tops of sulfide structures through mineralized chimneys that are a few meters high. While there is a gradient of temperature and salinity in the MEF, with temperatures increasing and salinities decreasing to the south (Butterfield *et al.* 1994), the typical vent fluid has θ ~350°C and S between 35 and 15 psu. Analysis of the digitized and updated geologic map of Delaney *et al.* (1992) indicates that there are 96 "active smokers" (Endeavour Segment GIS web site: http://www2.ocean.washington.edu/gis). Cathedral, a cluster of 10–20 high B vents founded on the talus scarp ~50 m SW of Peanut and Bastille (Figure 2.6) was discovered in 2000 (D. Kelley, pers. comm.), and brings the total number of high B sources within the MEF to ~110.

Also within the MEF, the top and side surfaces of the active sulfide structures may act as low B vents with areas up to 20–30 m in diameter. Tube worm patches, typically 2–10 m in extent, constitute low B fluid sources on the sea floor, either abutting sulfide structures or distributed along faults near sulfide structures (Figure 2.6). The maximum vertical separation of MEF sources is 38 m — between a high B source, the 21 m high chimney at 2174 m on Dante, and a low B source, a tube worm bed at 2212 m just southwest of

Crypto. More typical separations are $\lesssim$1 m between sulfide top surfaces and high B vents, and 10–15 m between tube worm beds and nearby black smokers.

2.2 Methodology

Quantification of the heat flux through the MEF requires the specification of a control volume that encloses all sources in the field and intercepts all hydrothermal plumes. Detailed, accurate information about the spatial distribution of distinct hydrothermal sources within the MEF defines the extent of the field with a certainty not possible at less well-mapped fields. With a width of ~300 m and a length of ~700 m, the base of the Flow Mow control volume is a rectangle aligned with the strike of the valley (Figure 2.1) that encompasses all the known MEF hydrothermal sources with a buffer of $\gtrsim$100 m.

The main Flow Mow field program focused on assessing the net heat flux through the top and sides of a lower control volume, while a secondary experiment monitored horizontal fluxes through an upper control volume (Figure 1.3). The top surface of the lower control volume is a horizontal (constant pressure) plane ~80 mas, an altitude near which the signal strength of rising plumes and the likelihood of intercepting them are simultaneously optimized (Stahr *et al.* 2003).

The Flow Mow methodology was to survey the control surfaces as often as possible, measuring temperature and velocity in order to calculate heat flux. A high priority was repetitive surveys of the top surface with which to obtain a mean vertical flux with low variance. A total of 9 ABE dives resulted in 12 complete surveys of the top surface that successfully acquired both T, S, and w data. On a few occasions when the modular acoustic velocity sensor (MAVS) mounted on ABE failed to record useful data, the vertical velocity of the ambient fluid was derived using a hydrodynamic model of ABE (Yoerger *et al.* 2000). In addition, ABE surveyed the north and south surfaces 3 separate times each, and the west and east surfaces once.

During the substantial periods when ABE was on deck, the ship was kept occupied with a second high priority: assessing the side surfaces and nearby hydrography with the lowered CTD. Especially for the hydrographic transects conducted within the axial valley, efforts were made to acquire data at all phases of the tide, from both north and south of the MEF. Since the bottom time of ABE was limited to 6–30 hours, primarily by battery endurance, and because of troubleshooting early in the cruise and frequent rough weather, enough time was available to complete 40 CTD stations during 17 days spent over the Endeavour segment (for details, see Flow Mow electronic cruise report: http://www2.ocean.washington.edu/flowmow/ecr/ctd). The side surfaces of the lower control volume were surveyed from the top surface (~2110 m) to within 5–10 m of the local sea floor (as deep as ~2210 m).

Overall, the Flow Mow study consisted of intermittent monitoring of the control surfaces with ABE and the lowered CTD. When opportunity arose, the lowered CTD was also used to assess the hydrography of the axial region, the MEF vicinity, and areas suspected to be hydrothermally active based on previous reconnaissance (Veirs *et al.* 1999).

2.3 Instrumentation

Hydrographic data were collected with pumped and ducted Sea Bird Electronics 911*plus* with conductivity and temperature (CT) sensors mounted either within a lowered cage or in free flow on the front of ABE (Figure 2.7). On the lowered CTD, the 2 pairs of CT sensors were separated vertically by 142 cm in order to detect vertical gradients. In addition to deriving potential temperature (θ) and S from the CT sensor pairs, the lowered CTD recorded pressure, transmissivity, optical backscatter, fluorescence, oxygen concentration, redox potential, and cage altitude. An acoustic altimeter enabled ABE to monitor its elevation and avoid contact with the sea floor.

For the lowered CTD sensors, pre- and post-cruise calibrations did not differ significantly. The SBE3*plus* temperature sensor resolution was 0.0003°C at 24 samples/second and had an accuracy of ±0.001°C. The SBE4 conductivity sensor has a resolution of 0.00004 Siemens/m at 24 Hz and an accuracy of ±0.0003 Siemens/m. Raw 24 Hz data were bin averaged to 2 Hz. Processing of data from the ABE-mounted CT sensors is detailed in Stahr *et al.* (2003).

The hydrographic observations were located through long-baseline acoustic navigation whenever only one platform (CTD cage or ABE) was submerged. Only at stations >5 km

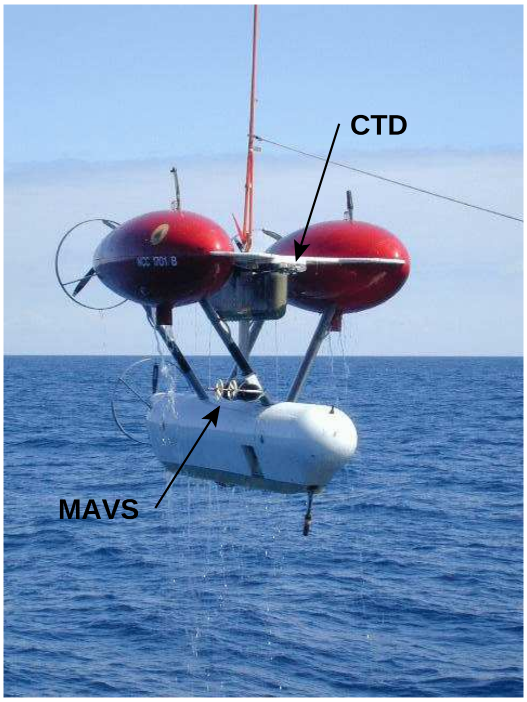

Figure 2.7: The lowered CTD package (left) and the Autonomous Benthic Explorer (right) that were utilized during the Flow Mow cruise. Note the 144 cm vertical separation of the CT sensor pairs (arrows) on the CTD package, and the relative location of CTD and MAVS on ABE.

from the MEF did the long baseline navigation degrade. When both platforms were submerged simultaneously, only ABE was navigated to preclude multiple interrogations of the transponders. In these instances, the CTD cage locations were estimated from the R/V Thompson GPS fixes, the ship heading, and the geometric relation between the block on the CTD boom and the ship GPS antenna. Comparison of CTD long-baseline and ship GPS fixes during similarly slow tows ($\lesssim$10 cm/s) indicates that the CTD rarely deviated laterally more than 10 m from the tip of the boom that supported it. All fixes were edited for outliers and interpolated onto the 0.5 Hz hydrographic time base.

The primary sources of horizontal current measurements during the field program were Aanderaa RCM5 instruments moored ~1.1 km north and south of the MEF (Figure 2.8). Both moorings were deployed and recovered by Rick Thomson of the Institute for Ocean Sciences, Canada, and his associates. He also calibrated and processed the data according to standard IOS procedures. The north mooring (FM-N: 47°57.521'N, 129°5.542'W) consisted of 2 RCM5s, mounted one above the other on the same mooring, 14 and 15 meters above bottom (mab). In calculating heat fluxes in Chapter 3, velocity data are exclusively from the shallower meter (2161 m depth) on the northern mooring because the deeper meter failed prior to the beginning of the Flow Mow field program. The southern mooring (FM-S: 47°56.281'N, 129°5.886'W) supported 5 current meters at 50 m intervals (from 50–250 mab). In Chapter 3, the focus is on the deepest meter from the southern mooring because its depth (2142 m) is comparable to that of the northern meter (2161 m), and both are approximately centered in the Flow Mow control volume depth range (2100–2200 m). The upper meters on the southern mooring are utilized in Chapter 4 to interpret hydrographic variability and compute flux estimates above the ridge crests.

Additional current observations were made with Nobska MAVS. One MAVS was mounted on ABE and sensed relative vertical and horizontal flow components; these were corrected for vehicle motion using the record of ABE depth and navigated location, respectively. Other MAVS were placed near-bottom ($\lesssim$1 mab) within the MEF by collaborating scientific programs and recorded velocity for short periods during the Flow Mow field program. Data from the latter instruments have provided useful comparisons (courtesy of M.K. Tivey, S. Hautala, I. Garcia-Berdeal, and their associates), particularly the MAVS deployed by

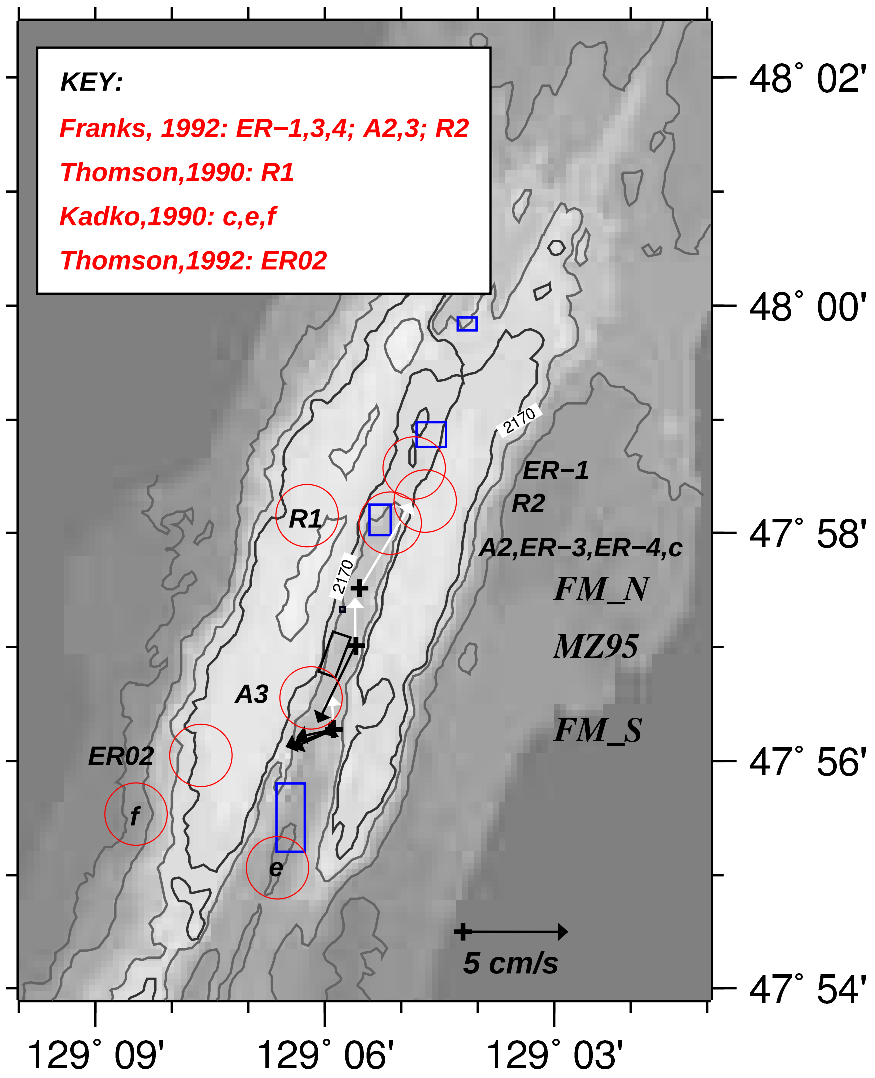

Figure 2.8: Location of current meter moorings, both historic and utilized in the planning or conduction of the Flow Mow field program. The northern and southern Flow Mow moorings are FM-N, and FM-S; the 1995 Mixing Zephyrs mooring is MZ95. Historic moorings are located with large open circles to emphasize the imprecision of Loran-C coordinates; adjacent or central labels are consistent with past studies listed in the key. For each meter on the FM and MZ moorings, the average flow observed over the full record is indicated with a vector. White vectors indicate flow within the axial valley (meter located deeper than 2100 m); black vectors show flow at or above the ridge crests (shallower than 2100 m). A 5 cm/s reference vector is provided in the lower right hand corner. To minimize clutter only major hydrothermal fields are delineated.

M.K. Tivey ~0.5 mab near the center of the MEF, about 40 m north of the S&M sulfide structure (Table 2.1).

A final source of information about Endeavour currents that is utilized in this dissertation is the hourly mean record from the MZ95 mooring deployed over the summer of 1995, ~200 m east of the northeast corner of the MEF perimeter (Figure 2.8). The mooring was approximately centered in the axial valley and supported 2 Aanderaa RCM5 meters, one within 25 m of the axial valley floor, the other 300 mab at a depth of 1900 m (see Table 2.1). The 1995 data were used by H. Mofjeld to predict the phase of the tidal currents within the axial valley in order to guide hydrographic deployments during the Flow Mow field program. They are also utilized in Chapter 3 to characterize the typical near-bottom oscillations in a model of plume dispersion.

During the summer of 2000, pressure sensors were deployed atop the southern mooring, on the sea floor within the MEF (by M. Lilley and associates), within ABE, and on the lowered CTD. The sea floor and moored P records provide information about the ambient pressure field, as well the effect of currents on the tall southern mooring, but neither are analyzed in this thesis.

2.4 Flow

A broad spectrum of plume-related research projects have involved deployment of current meters at the Endeavour segment during the last 20 years (Dymond and Roth 1988; Kadko *et al.* 1990; Franks 1992; Thomson *et al.* 1990; Thomson *et al.* 1992; Allen and Thomson 1993; Veirs *et al.* 1999). The data from moored meters have been supplemented with ADCP observations (*e.g.* Thomson *et al.* 1989). These measurements have been acquired near and above equilibration depths over the ridge crests and axis, within the axial valley, and occasionally on the southwest flank of the segment (Figure 2.8). The patterns of flow observed during these projects and the Flow Mow study are discussed in this section.

In distilling basic features of the Endeavour flow, it must be noted that past mooring arrays have been primarily axial, and that the moorings deployed during the summer of 2000 were exclusively axial (Figure 2.8). Mooring deployments on the ridge crests or flanks

Table 2.1: Current meter and pressure sensor deployments that collected data used in this thesis. Elevation in meters above bottom (mab) is based on mooring engineering specifications and the assumption that each mooring was deployed on level terrain. MZ = 1995 Mixing Zephyrs cruise; FM=2000 Flow Mow cruise. MJD=modified Julian day. T_e=Expanded temperature sensor (small range, high resolution). Y=sensor present, N=no sensor, M=sensor malfunctioned, and P=partial record. MEF MAVS data provided courtesy of M. Tivey. For reference, the Flow Mow cruise period is 8/04/00–8/21/00, or MJD 51760–51777. All T values recorded on the moorings are in °C on the International Temperature Scale 1968 (ITS-68).

Name	Depth	Elevation	Deploy date	Recover date	Data start	Duration	Sample	Sensors			
	m	mab			MJD	days	period	T	T_e	S	P
MZ25	2175	25	05/24/95	07/23/95	49866.076	52.56	10 min	Y	Y	Y	N
MZ300	1900	300	05/24/95	07/23/95	49866.076	52.56	10 min	Y	Y	Y	N
FM-N15	2161	15	05/21/00	10/09/00	51685.000	141.75	1 hr	Y	Y	Y	N
FM-N14	2162	14	05/21/00	10/09/00	51685.042	58.75	1 hr	Y	Y	Y	N
FM-S50	2142	50	07/27/00	10/09/00	51752.833	73.96	1 hr	Y	Y	N	N
FM-S100	2092	100	07/27/00	10/09/00	51752.833	73.96	1 hr	Y	Y	N	N
FM-S150	2042	150	07/27/00	10/09/00	51752.833	73.96	1 hr	Y	Y	M	M
FM-S200	1992	200	07/27/00	10/09/00	51752.833	73.96	1 hr	Y	Y	N	N
FM-S250	1942	250	07/27/00	10/09/00	51752.833	73.96	1 hr	Y	N	M	P
MEF MAVS	~2200	0.5	07/25/00	09/25/00	51710.000	87.74	2 min	Y	N	N	N

are comparatively rare, especially on the historically neglected east side.

This section presents the current observations made during the Flow Mow field program and compares them with past observations of Endeavour currents. After an initial discussion of regional flow patterns — from the surface currents of the northeast Pacific down through the flows observed over the entire Juan de Fuca ridge — the focus narrows to the Endeavour segment. Current observations made at the Endeavour during the Flow Mow and past studies are juxtaposed in 3 subsections that describe mean flows, characteristic oscillations, and spatial coherence. In each of these subsections, the differences between flow within versus above the axial valley are highlighted.

2.4.1 Regional overview

The Endeavour segment of the Juan de Fuca ridge is centered latitudinally beneath the divergence of the Subarctic current which shifts seasonally between ∼45°N (winter) and ∼50°N (summer) (Thomson 1981). The bifurcation of the Subarctic current occurs between 150–130°W longitude and generates a complicated field of meanders and 10–100 km diameter eddies. By the time the flow has reached the Endeavour segment (∼ 129°W), it typically has split into 2 distinct currents: the California current going southeast and the Alaska current headed north-northeast to feed the Alaska gyre. Consequently, the area over the Endeavour, between the diverging currents, tends to experience confused and variable near-surface currents. While the mean eastward velocity is typically <10 cm/s, absolute velocities in eddies commonly attain speeds of 25 cm/s, at least for short periods (Thomson 1981). In the region over the ridge and as far east as Station Papa (50°N, 145°W), oscillations within the wind-mixed layer (15 m drogue) and at the base of the pycnocline (120 m) are dominated by inertial currents with RMS speeds of ∼50 cm/s, but also involve diurnal currents of similar magnitude (∼10 cm/s) (Thomson *et al.* 1998). Thomson (1981) notes that ship drift has identified a Subarctic counter-current that flows westward in mid-winter at $\lesssim$ 10 cm/s between 48–51°N and most frequently east of 160°W (Figure 2.9).

Regional patterns of flow from below the surface currents to within a few hundred meters of the segment topography (∼1800-2400 m) are relatively less well understood, but

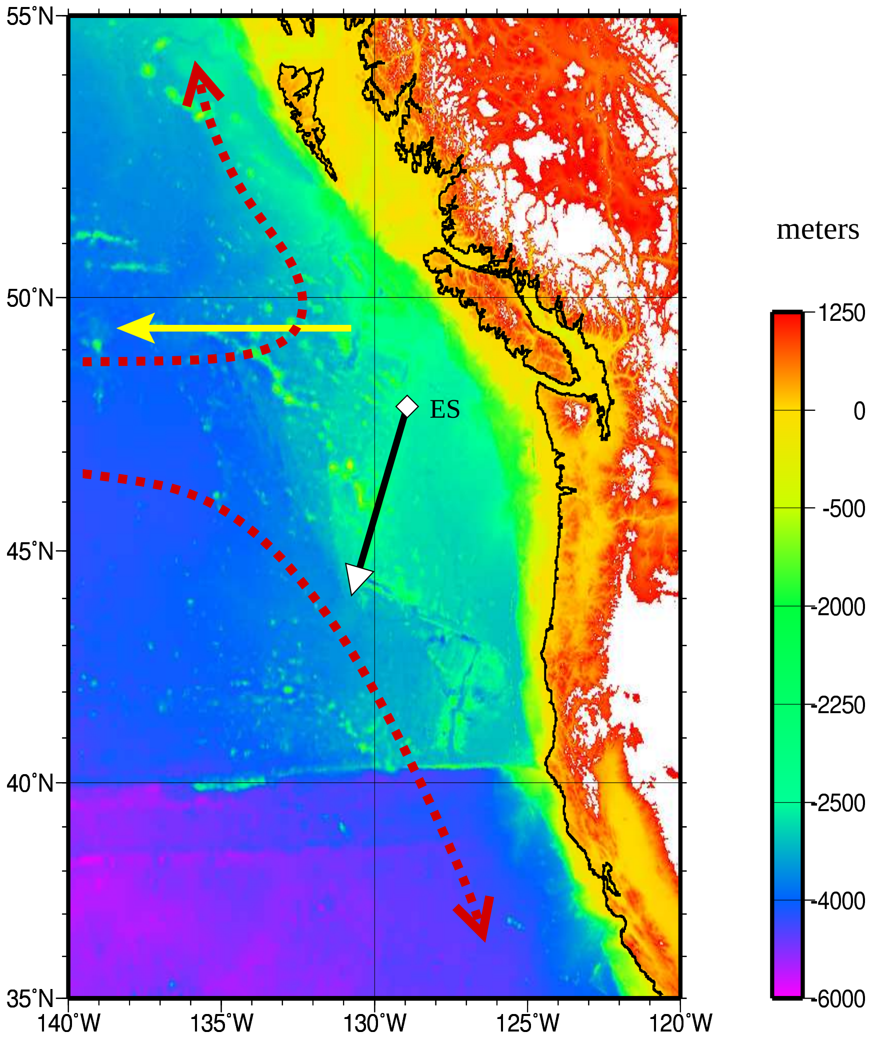

Figure 2.9: Bathymetric map of the northeast Pacific ocean off the coast of Washington (Smith and Sandwell 1997) with regional mean currents overlain. Dashed arrows indicate bifurcating surface currents. Solid arrow shows westward Subarctic counter-current on surface. Solid arrow indicates long-term mean flow over the Endeavour segment near 2000 m, a typical plume equilibration depth (denoted by white diamond).

some basic characteristics have been discerned. Mean values from the uppermost meters presented in Thomson *et al.* (1990) indicate that flow decreases from ~1.19 cm/s to the east-southeast at 60 m depth to only 0.15 cm/s to the northwest at 486 m depth. At mid-depth (near 1500 m,) the mean flow is generally faster, ~1 cm/s, but in directions that are inconsistent; mid-depth flow recorded by Franks (1992) varied between east, south, and southwest directions, while Thomson *et al.* (1990) observed flow to the southwest to south-east. Franks (1992) discerned a vertical shear between mid-water depths (~1600 m) and plume equilibration depths (near 1900 m). Examination of her progressive vector diagrams (PVDs), based on moorings with 3–4 meters distributed between 1600–1900 m, suggests that with every 100 m descent, the mean current direction shifted counter-clockwise (-5 to $-20°$) while the magnitude increased by about a factor of 2.

Models provide one perspective on the flow expected over the Juan de Fuca ridge and the Endeavour segment, with the assumption of an ideal forcing function and simplified topography (Allen and Thomson 1993; Lavelle and Cannon 2001). For diurnal and weather band forcing, motions are amplified over the ridge and the flow is rectified on the ridge flanks, generating a mean northward flow on the western flank and a mean southward flow on the eastern flank (Lavelle and Cannon 2001) (animation by J.W. Lavelle: pmel.noaa.gov/~lavelle/Review/Workstation/Anim/ridge.fli). While the models indicate that oscillatory flows can displace isotherms and isopycnals and perturb the velocity field in a broad region over the ridge flanks and crests, the resolution of the Lavelle and Cannon (2001) model is too coarse to elucidate the details of the shear immediately above the axis or within the axial valley. This is problematic when attempting to interpret the current meter records from the Endeavour segment because, for the most part, they derive from moorings placed close to the bottom and almost exactly on axis, rather than atop the ridge crests or on the outer ridge flanks.

Some model predictions have been confirmed by observations of the flow over the Juan de Fuca ridge. Most studies have focused on segments south of the Endeavour and depths of the ridge crest and equilibrated hydrothermal plumes (~1700–2300 m). Early studies (Cannon *et al.* 1991) detected opposite mean flows along the flanks in the directions later predicted by models. Denser arrays of meters stretched across the northern Cleft segment on the southern Juan de Fuca ridge discerned similar flank flows (HELFRICH *et al.* 1998) and elucidated details of the anticyclonic shear near an axial hydrothermal source (CANNON and PASHINSKI 1997; JOYCE *et al.* 1998). Near 2100 m, the mean flows parallel to the Cleft segment had magnitudes that peaked at 2–3 cm/s about 8 km off-axis, and decreased to 0.8–1.0 cm/s at the axis (CANNON and PASHINSKI 1997). The broadest geographic perspectives on flow near 2100 m depth suggest that the circulation in the interior of the northeast Pacific may be relatively simple, mimicking the gyre above, but the flow over and around the Juan de Fuca ridge and associated sea mount chains is strongly steered by topography (CANNON *et al.* 1991; CANNON *et al.* 1993; CANNON and PASHINSKI 1997).

2.4.2 Mean currents

Mean flow above the ridge crests

The general consensus among Endeavour researchers is that the mean flow *above* the ridge is usually to the southwest. While it is true that the mean flow typically has a southward component, the extant observations contain many exceptions to the rule of mean flow to the southwest. A review of past studies in this section suggests that the upper level mean flow can be consistent for many days but can also change direction dramatically for periods of days to weeks. There is evidence of horizontal coherence during some periods, while at other times there is also some evidence of horizontal shear along and across axis on spatial scales of a few km (FRANKS 1992). Some of the confusion that often occurs at sea when tracking and mapping hydrothermal plumes may stem from assuming that the long-term mean flow is characteristic when the flow at any given moment is likely to be much more variable. This section also highlights how the flow patterns over the ridge differ from those *within* the axial valley.

The idea that mean flow over the Endeavour segment is generally to the southwest, in rough alignment with the ridge axis, is an oversimplification that appears to have originated in measurements made by S. Roth Franks (THOMSON *et al.* 1990; FRANKS 1992) in support of the plume study of BAKER and MASSOTH (1987) (*c.f.* Section 1.3.1). During the field program of BAKER and MASSOTH (1987) the mean flow above the ridge was at 205° true, almost directly along-axis. Just prior to the hydrographic survey, however, the mean flow was to the southeast. Examination of the PVDs from all meters above the ridge crests over the non-synoptic and primarily axial array deployed by FRANKS (1992) indicates that the mean flow almost always has a southward component. In some PVDs, the flow is aligned with the axis consistently for periods of up to 259 days; in others, the mean flow ranges through the southeast and southwest quadrants.

In a subsequent study by KADKO *et al.* (1990) that did not overlap temporally with the deployments of FRANKS (1992), periods of mean flow to the southwest were recorded, but only at 1 of the 3 meters located near plume equilibration depths above the ridge crests. The 3 moorings were deployed by KADKO *et al.* (1990) for 17–19 days in September, 1988. Their mooring F was located on or near the outer southwest flank, mooring E was at the same latitude but on axis south of Mothra, and mooring C was on axis near the High Rise field (Figure 2.8). Comparing simultaneous periods for the meters near 1950 m depth, mooring E showed consistent flow to the southwest at ~2.25 cm/s, mooring F experienced flow to the west at ~0.6–1.2 cm/s interrupted by a few days of northward flow, and mooring C was exposed to a brief southward flow and subsequent, consistent flow to the east-northeast at ~1.4 cm/s. This suggests that the currents above the ridge can exhibit substantial horizontal shear over spatial scales as small as 2 km across axis and 5 km along axis.

Southwest flow was only observed during a few days of a 45 day deployment (ER02) by THOMSON *et al.* (1992) on the western crest near 2075 m (Figure 2.8) that also did not overlap temporally with previous records. The low-pass filtered data (40 hr cutoff) reveal currents of ~2–3 cm/s in almost all directions, but primarily to the northwest to northeast. Such extended periods of northward mean flow are unusual enough above the ridge to raise questions about whether this variable record represents clear flow above the crest or is substantially influenced by local topography, being only 25 mab. While the text of THOMSON *et al.* (1992) indicates the mooring was based near the 2100 m bathymetric contour about 4 km southwest of the MEF, the accompanying map suggests it was closer to the 2200 m contour, which would put the meter near 2175 m depth. Near the latitude of the deployment, the closest 2100 m bathymetric contour is about 2000 m to the north atop a prominence at the south end of the western crest. The uncertainty of the mooring depth

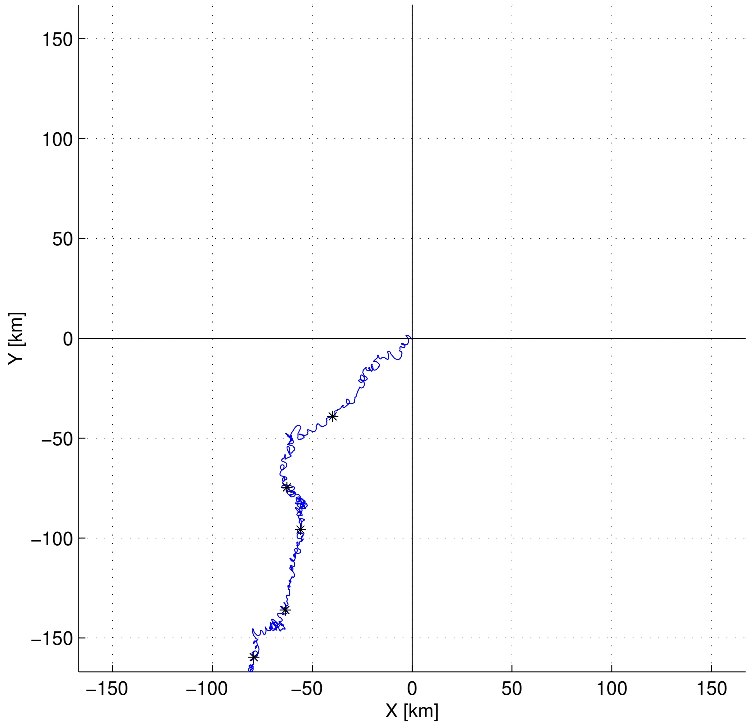

Figure 2.10: Progressive vector diagram for the 1995 current meter (300 mab, 1900 m) near the northeast corner of the MEF field. The mean flow for this 52.5 day record is 4.10 cm/s at 206°. Black asterisks symbolize 10 day intervals.

and location, given a Loran-C location error of ∼1 km, make it difficult to know whether this record should be associated with flow over the western ridge crest or on the western flank.

The 1995 deployment of a meter 300 mab on the MZ95 mooring was definitively on axis, just a few 100 m northeast of the MEF (Veirs *et al.* 1999), and recorded mean flow to the southwest at a depth of 1900 m over ∼2 months (Figure 2.8). During periods of a few days, however, the average flow ranged from southeast to west-southwest (Figure 2.10). This variability may explain why efforts to intercept the MEF hydrothermal plume during the same Mixing Zephyr field program were successful on some days, but found no plume in the expected downstream direction on other days.

Overall, past measurements of the mean flow above the ridge suggest that a southward component is typical. At depths shallower than 2100 m, northward mean flow is rarely observed over periods longer than a few days. In the 3 exceptional current meter records (Kadko *et al.* 1990; Thomson *et al.* 1992) it is most likely that topographic effects are the cause of the northward mean flows. Both mooring ER02 (Thomson *et al.* 1992) and f (Kadko *et al.* 1990) were unique in being located on the outer edge of the western flank of the Endeavour segment (Figure 2.8) where they may have been subject to northward ridge-parallel mean circulation. Such flows have been observed on the western flank of the southern Juan de Fuca ridge (Cannon and Pashinski 1997) and are generated by nonlinear rectification of oscillatory flow over model ridges (Lavelle and Cannon 2001). The third exceptional record, from mooring c of Kadko *et al.* (1990) was located on-axis and is therefore less likely to have been affected by an episode of northward flow along the western flank.

An alternative explanation for the distinct sequences of mean flows observed by nearby meters deployed simultaneously above the ridge is that rotational dynamics of hydrothermal plumes affect the flow field above the ridge, at least intermittently overpowering the ambient mean flows (*e.g.* Speer 1989). According to this theory, a meter placed west of a strong hydrothermal source and within the equilibration depths where an anticyclonic flow is expected could record a northward mean flow. This may have been the case for mooring c which was located very near the High Rise vent field (Figure 2.8), but the uncertainty in the location of that mooring means it is unclear whether the mooring was west or east of the field. Rotation associated with hydrothermal plumes is also a tenable explanation for the northward flow observed at moorings ER02 and f, both of which were located ~ 1 km west of the Mothra vent field.

Analysis of the Flow Mow current meter data, presented next, cannot resolve questions about what processes govern the patterns of mean flow over the Endeavour segment, primarily because the moorings were all axial. Discerning the relative influence of topography and plume dynamics on the flow field will probably be contingent on a *synoptic* observational program that encompasses not only the Endeavour axis, but also the crests and flanks.

Vertical shear in the mean flow

Data from the meters at 5 different depths on the southern mooring FM-S (Figure 2.4) show with greater vertical resolution than ever before how the mean flow above the ridge differs from that within the axial valley. The progressive vector diagrams from FM-S (Figure 2.11) provide a rare perspective on the vertical structure of the horizontal flow.

The 3 uppermost meters generate remarkably similar progressions: southwest for the first 30 days, northwest for the next 30 days, and west-southwest for the remainding 13 days of the record. The sequence of flow resulted in average flow to the west-southwest over the full record of each meter (Figure 2.8). These meters, at depths of 1942, 1992, and 2042 m, are each well above the east and west ridge crests, which at the latitude of FM-S are at ~2110 and 2150 m, respectively (Figure 2.4). Of the 3 upper meters, the central one at 1992 m exhibits the greatest PVD displacements, which implies relative enhancement of the mean flow at that depth. This enhancement may be related to the equilibration depth of MEF plumes being 2000 m (*c.f.* Figure 2.23). Is it possible that the mean flow is accelerated, perhaps by divergence of the equilibrating plumes, in the same 200 m thick zone centered at 2000 m in which near-inertial motions are amplified by a factor of 1.2–1.7 (Thomson *et al.* 1990)? ADCP profiles taken in the same vicinity also show a maximum relative velocity near 2000 m (Thomson *et al.* 1989).

The next deepest meter, FMS100 (Figure 2.8) at a depth of 2092 m — just above the adjacent valley walls — shows a similar sequence of direction changes. However, the direction is shifted $\sim 30^\circ$ relative to the overlying flow: counterclockwise during the first 30 days and clockwise during the next 30. During the last 13 days the flow direction is identical to the overlying meter. Additionally, the individual displacements are smaller, resulting in a reduced net displacement. The deepest meter, relatively protected within the axial valley at a depth of 2142 m, shows shifts in direction that are comparatively slight and not clearly correlated with the overlying changes.

Figure 2.11 also shows that *during the Flow Mow study*, the mean flow at each depth was in a consistent direction. Above the ridge (150–250 mab), the flow was to the southwest at ~4 cm/s, resulting in a moderate cross-axis component to the west. Near the depth of

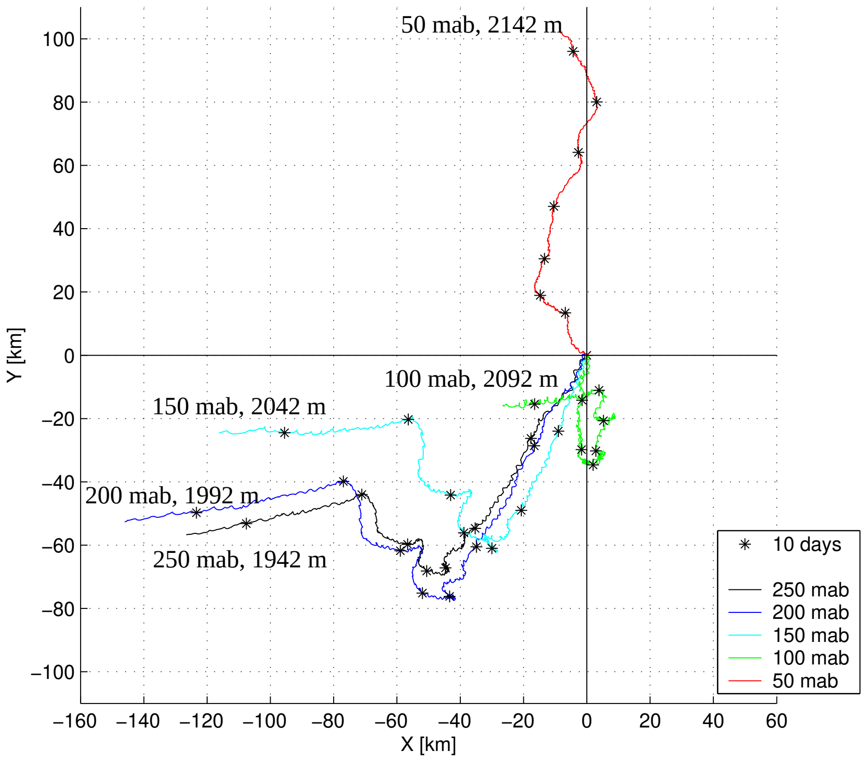

Figure 2.11: Progressive vector diagrams for 5 current meters on mooring FM-S (Table 2.1). Entire 74 day record is used with asterisks indicating 10 day intervals. Relative to these intervals, the 17 day Flow Mow cruise period (Julian day 217–234) was from day 7 to day 24.

the ridge crests (100 mab) flow due south (180° true) at ∼3 cm/s resulted in a cross-axis component to the east. Just within the axial valley, the flow was to the northwest at 1–2 cm/s — almost directly opposed to flow of the same magnitude only 50 m above. Thus, the greatest shear observed between the deepest pair of meters in the 74 day record happened to occur during most of the 17 day Flow Mow cruise period. During other periods the flow measured at the 2 deepest meters was either aligned or orthogonal.

While most of the vertical current meter arrays deployed by Franks (1992) did not extend deep enough to characterize the flow within the axial valley, one mooring did (ER3 in Figure 2.8) and generated PVDs that show a similar pattern of shear. For the 4 meters at depths of 1686, 1936, 2036, and 2136 m, the respective mean current speeds and directions were 1.1 cm/s at 210°, 2.0 cm/s at 190°, 1.4 cm/s at 200°, and 0.5 cm/s at 30°. The 3 records from above adjacent ridge crests (∼2100 m) indicate southward mean flow, while the meter located below the crests shows northward flow.

Similar patterns of vertical shear persists at shorter averaging periods. Figure 2.12 displays a daily resampled time series of the low-pass filtered (35 hr) currents from all of the FM-S meters. The upper 3 records are remarkably similar with little speed or direction shear, despite the variable, multidirectional currents. The flow at 100 mab is directionally similar to the overlying flow, but is consistently diminished in speed. Near Julian day 235 and 260, the low frequency flow is essentially zero, despite substantial flow at the other depths. Finally, the flow at 50 mab seems independent of the overlying flow; it is directly opposite to the flow 50 m above near Julian day 217, but perfectly aligned near Julian day 254.

Mean flow within the axial valley

Prior to ∼1995, the mean flow *within* the axial valley received little attention, because most current meters were deployed to facilitate interpretation of the hydrography of plumes equilibrated *above* the ridge crests. While mean flows to the north had been observed previously in near-bottom axial records (R. Thomson, pers. comm.; Franks 1992), deployment of the MZ mooring in 1995 (Table 2.1) also revealed a consistent northward mean flow at 25 mab,

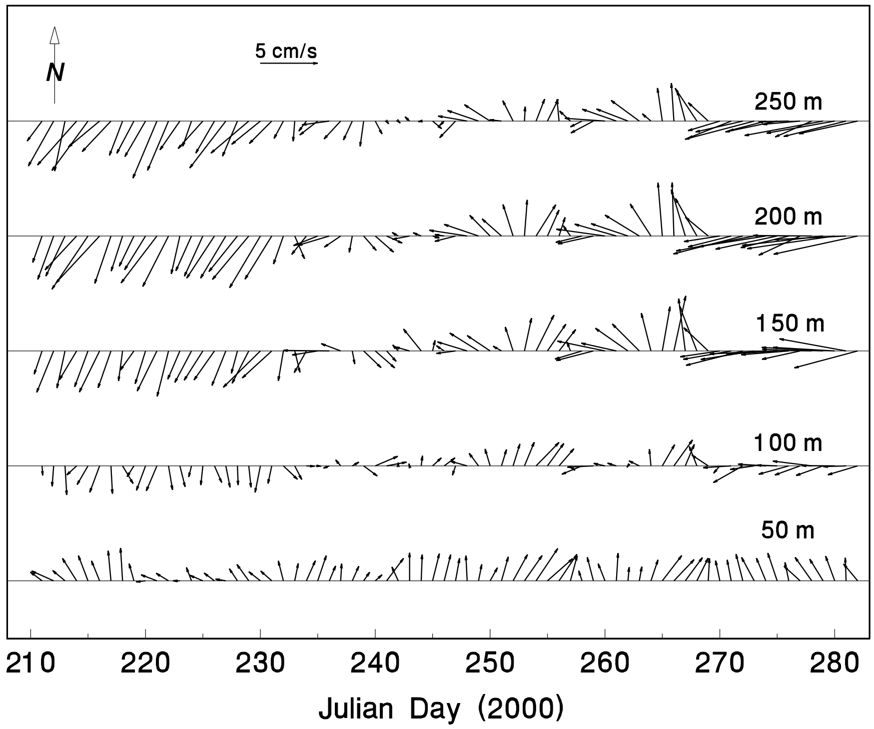

Figure 2.12: Daily mean currents from 5 meters on southern mooring based on the 35 hr low-pass filtered record. Flow Mow cruise was from Julian day 217–234. Used with permission, courtesy R. Thomson, from (Thomson *et al.* 2003).

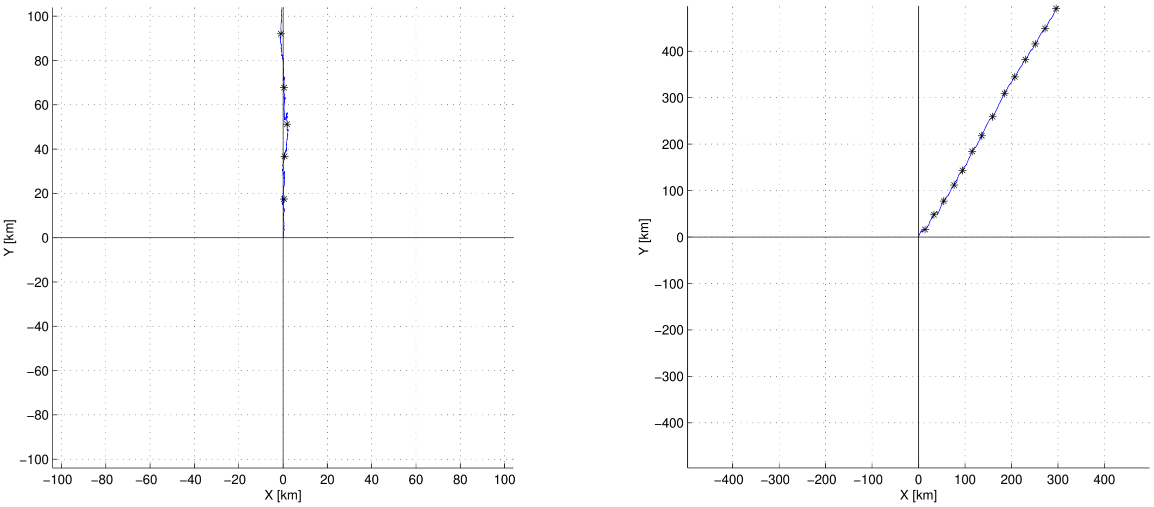

Figure 2.13: Progressive vector diagrams for axial valley currents measured at the central mooring in 1995 (MZ95, 25 mab, 2175 m) and the northern mooring in 2000 (FM-N, 15 mab, 2162 m). Mean flow is 4.74 cm/s at 31° for MZ95, and 2.29,cm/s at 0° for FM-N15. Relative to the multidirectional flow above the ridge, the mean flow in the valley at these meters is rectilinear and consistently northward. Black asterisks are 10 day intervals. Note that domain and range are different between plots.

or 2175 m (Figure 2.13). This observation helped guide the design of the Flow Mow study because rectilinear flow within the Flow Mow control volume simplifies the task of measuring heat flux by reducing the number of side surfaces that need to be monitored. Whether the flow within the axial valley is uniform as the valley is crossed, or if lateral shear is common is a topic of ongoing investigation; initial analysis of Jason-mounted ADCP transects of the axial valley collected in 2000 and 2001 suggests that substantial cross-valley shear may occur, albeit intermittently (S. Hautala, pers. comm.).

Northward mean flow within the axial valley is also evident in the records from both Flow Mow moorings (Table 2.1). The mean flow at FM-N is as consistently northeastward (∼35°) as the flow at MZ95 is due northward (Figure 2.13). In contrast, the northward mean flow at FM-S varies from northeast to northwest (Figures 2.11 and 2.12). While the flow within the axial valley is primarily rectilinear, it is not necessarily aligned with the overall strike of the ridge axis (20°). This may be due to a combination of the along-axis variations in the strike of the valley walls and the proximity of each mooring to the topographic variations along each wall and ridge crest. Using the 2200 m isobath in Figure 2.8 as an indicator of the local valley width and axial strike, FM-S is close to the eastern wall and a gap in the east ridge crest, while FM-N is closer to the western wall; MZ95 is close to the eastern wall, but is not far from the ~20 m sulfide structures and complex topography within the MEF (Figure 2.5). In all three cases, the mean flow vector is roughly aligned with the strike of the nearest 2200 m isobath (Figure 2.8). Intermittent flow through the gap in the east crest may account for the westward component that is occasionally evident in the FM-S record (Figure 2.11).

The magnitude of the northward mean flow increases from FM-S to FM-N (1.6, 4.7 cm/s), while the meter elevation decreases (50, 15 mab). This suggests that the flow within the axial valley is intensified near the bottom. This possibility is discounted, however, by a similar set of observations made in 2001. With moorings deployed during the same 4 summer months, approximately from July through October, and in the same locations as FM-S and FM-N, Thomson *et al.* (2003) measured a similar increase in mean flow within the axial valley, but the meters were both ~15 mab. An alternative explanation for the north-to-south increase in the mean flow is the decrease in cross-sectional area of the axial valley. Based on cross-sections taken orthogonal to the ridge axis and through the mooring locations, the area beneath the 2170 m isobath decreases from ~56,000 m^2 at FM-S to ~23,000 m^2 at FM-N. This could account for a factor of 2 increase in the along-axis flow within the valley.

An additional, important aspect of the Thomson *et al.* (2003) deployment in 2001 was the placement of a meter ~15 mab on a mooring located further north in the axial valley, just south of the 2170 m saddle. The mean flow recorded there was southward at 1–2 cm/s (Thomson *et al.* 2003). Thus, the 3 meters at ~15 mab in 2001 a most striking pattern: convergence of the near-bottom mean flow within the axial valley.

One possible exception to the pattern of near-bottom convergence within the axial valley comes from the southernmost axial current meter mooring described in Franks (1992). The mooring A3, was deployed ~1 km south of the MEF near the 2250 m bathymetric contour in 1985–1986 (Figure 2.8) and supported near-bottom meters at 2155 and 2156 m depth, or ~100 mab, and upper level meters at 2055 and 1955 m. Since the adjacent axial valley walls are well-defined up to ~2110–50 m at this latitude (Figure 2.4), the deepest 2 meters are just within the axial valley. While the uppermost meter recorded mean flow to the southwest, the three deeper meters have PVDs that indicate extremely consistent mean flow (~2.7 cm/s) directly along-axis to the south. The persistent southward flow at the pair of deepest meters, roughly 50–100 m above the bottom, does not match the northward flow observed in 2000 by a meter at roughly the same location, elevation, and depth (2142 m on the FM-S mooring). While a latter portion of the v record at 2155 m is erroneous and the mean value of the T record at 2156 m is suspect, the good v data that overlap temporally generate completely consistent PVDs that suggest the southward flow persisted from October, 1985 to June, 1986.

The differences between the winter 1985 and summer 2000 data are puzzling. One explanation is that the prevailing flow within the axial valley shifts seasonally from north in summer to south in winter. This is consistent with the observations made *south* of the MEF at depths near the top of the axial valley, but is not satisfactory for similar depths north of the MEF because in the winter of 1986–1987, during a deployment of similar duration but ~2 km *north* of the MEF (mooring ER-3 in Figure 2.8), FRANKS recorded northeastward mean flow at ~0.5 cm/s within the axial valley near 2136 m depth. Another explanation is that during winter 1985, unusual conditions – either hydrothermal or in the ambient flow – led to southward mean flow within the axial valley. While it is true that all of the meters deployed by FRANKS that winter *above* the ridge crests did exhibit southward components of flow, the PVD for the 1 month record from the deepest meter on mooring A2 at 2106 m (north of the MEF and *below* the ridge crests) shows mean flow to the north-northwest at ~1 cm/s. An alternative explanation is that flow within the axial valley is northward near the eastern valley wall and southward near the western valley wall (Figure 2.8). More observations close to the western valley wall would help test this explanation. Another explanation is that the mean flows within the valley are generally convergent, but also influenced by proximity to topography. The uncertainty in the Loran-C coordinates of the moorings deployed by FRANKS precludes assessment of this possibility, but it remains plausible that the ER-3 mooring fell close to the western valley wall adjacent to topographic features that generated a southward flow at the meters near 2155/6 m depth. The possible importance of valley topography on 10–100 m scales, including the ~20 m sulfide structures, is reinforced by observations made by an array of MAVS distributed within the MEF ~1 mab during summer 2000; despite tidal coherence across the array, the mean flows were random with each MAVS apparently affected differently by the local topography (I. Berdeal, pers. comm.).

Anticipating consideration of current oscillations in the next section, it is helpful to recall that the magnitudes of instantaneous flows within axial valleys may be much higher than the mean flows. This is illustrated by 2 interesting accounts from submersibles operating in axial valleys. Within the Mid-Atlantic ridge FAMOUS axial valley, near a meter that recorded a mean flow of 8.2 cm/s and a maximum speed of 24.2 cm/s over a 50-s averaging period, French submersible divers claimed to have struggled against a 39 cm/s current (Keller *et al.* 1975). Similarly, the Alvin submersible was overpowered by a strong current during a dive within the MEF in 2000, causing it to be rammed into a sulfide structure (M. Lilley, pers. comm.). The differences between these first-hand observations of near-bottom velocities and associated, simultaneous current meter measurements made nearby that topographic constrictions may significantly accelerate mean flows within the axial valley. It is also possible that entrainment by hydrothermal plumes may accelerate ambient flows, but significant effects are likely to occur only close to the vent where the entrainment velocities are highest (~10 m laterally and ~25 m vertically from a high B source).

2.4.3 Oscillatory currents

Current oscillations are ubiquitous in the open northeast Pacific, and are prominent both above the Endeavour topography and within the confines of the axial valley. Both observations and models show that oscillatory currents are nearly rectilinear away from the ridge, but are amplified and predominantly clock-wise rotary immediately over the ridge (Franks 1992; Allen and Thomson 1993; Lavelle and Cannon 2001). Relative to mid-water conditions, the semi-diurnal, inertial (16.1 hr), diurnal, and low-frequency oscillations are amplified just above the ridge crests, especially in a depth range of 1800–2100 m, and attenuated within the axial valley (Franks 1992; Allen and Thomson 1993).

Analysis of data from FM-S by THOMSON *et al.* (2003) characterizes this depth progression with unusually fine vertical resolution for component inertial and tidal oscillations (Figure 2.14). Relative to the highest meter, the diurnal, inertial, and M_2 semi-diurnal bands are amplified with proximity to the ridge crest (near 2100 m). The diurnal and inertial bands are also become more circular at ridge crest depth, and are attenuated within the axial valley. Relative to their orientation above the ridge, both the M_2 and the S_2 ellipses are more aligned with the topography within the axial valley.

The most prominent oscillation within the axial valley is at the M_2 semidiurnal frequency. At all depths on all moorings deployed by THOMSON *et al.* (2003) in 2000 and 2001 the semidiurnal frequency band, dominated by M_2 but also including S_2 energy, accounts for a greater proportion of the variance than any other constituent (low- or high-, inertial, or diurnal frequencies). Within 100 m of the bottom the M_2 consistently accounts for more than 50% of the total variance (THOMSON *et al.* 2003). Most of the rotary spectra from the Juan de Fuca ridge showcased in FRANKS (1992) and CANNON *et al.* (1991) have spectral energy density maxima in the semi-diurnal band. The M_2 tidal ellipses in Figure 2.14 show amplitudes that diminish from ∼3.5 cm/s at and above the ridge crest to 3 cm/s within the valley (THOMSON *et al.* 2003). The ±3 cm/s flow within the valley, aligned with local topography, competes with the mean flow to produce occasional reversals at the FM-S50; in contrast, the oscillatory amplitude rarely exceeds the mean flow at FM-N15, so such reversals are rare (Figure 2.15). At the 1995 meter MZ25, the semi-diurnal and mean flow also combine to generate reversals, less frequently than at FM-S50, but more frequently than at FM-N15.

The influence of the topography on distinct oscillations is also illustrated by power spectra of available near-bottom v time series from different parts of the axial valley (Figure 2.16). Relative to FM-S50, FM-N15 has greatly reduced inertial energy, equivalent semi-diurnal energy, and enhanced diurnal energy (see also upper panel in Figure 2.17). The reduction in inertial energy is consistent with the inhibition of near-inertial motions by the topography of the axial valley (*e.g.* THOMSON *et al.* 1990), as FMS-50 is less constrained by the valley walls than FM-N15. The relative increase in diurnal energy is probably also a consequence of the greater topographic constriction of flow at FM-N15.

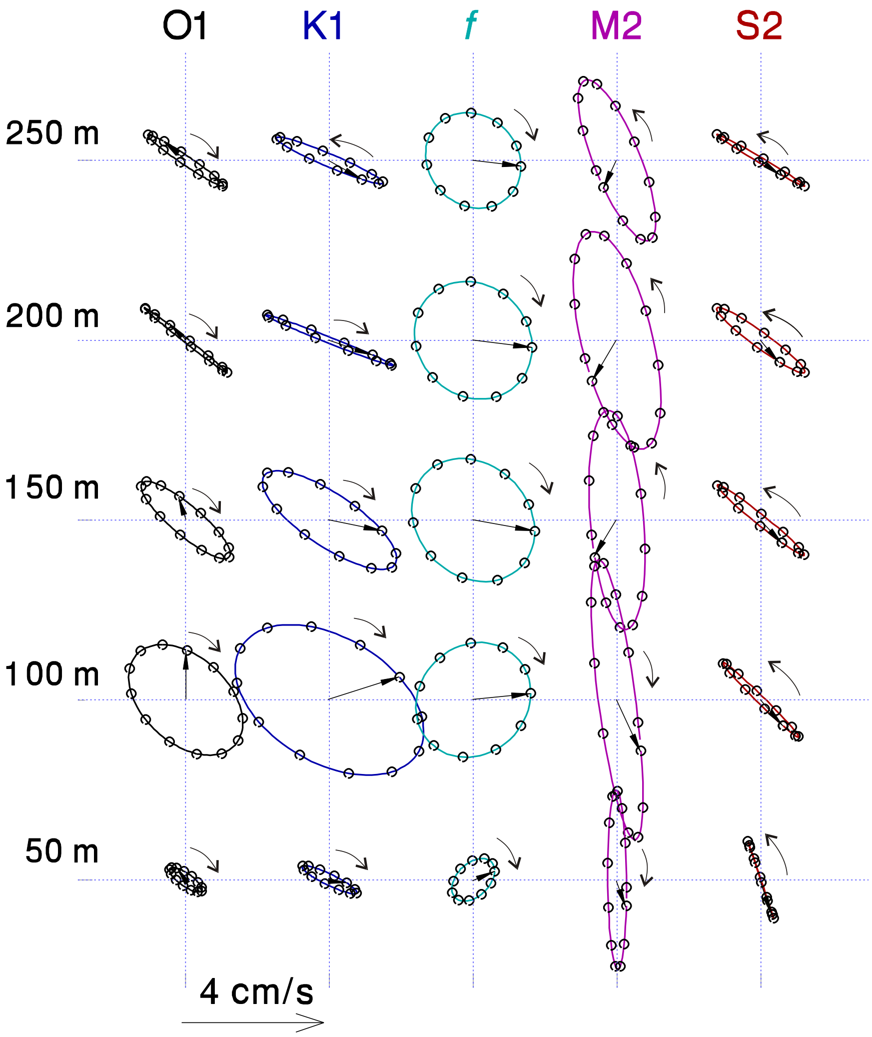

Figure 2.14: Current ellipses and vectors at 5 depths on the southern mooring for the main tidal frequency bands (O_1, K_1, M_2, S_2) and the inertial frequency band (f). Meter elevation is noted on the left in meters above bottom. Current vectors indicate a reference time to illustrate relative phase. Small circles denote hourly mean values for current vectors. Outer arrows show direction of vector rotation. Along-axis (20° True) direction is upward. Figure used with permission from THOMSON *et al.* (2003), courtesy R. Thomson.

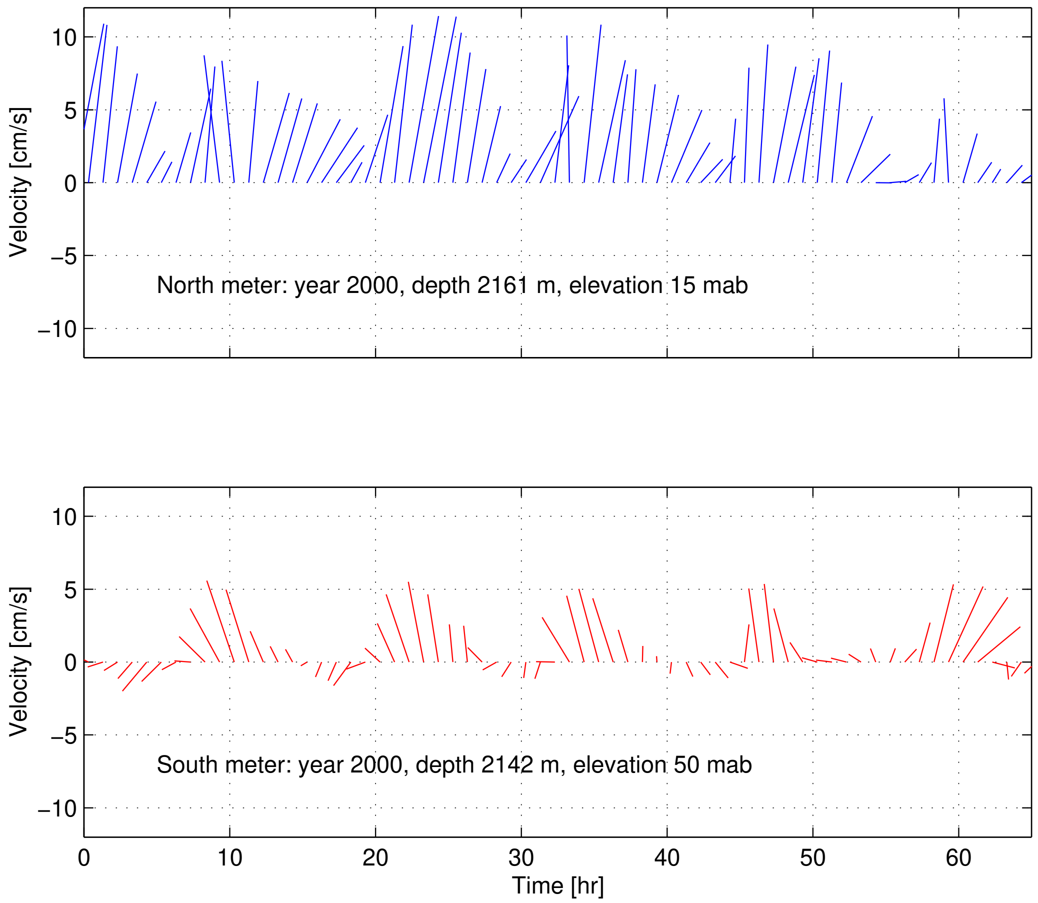

Figure 2.15: A characteristic 65 hr time series of hourly-mean currents within the axial valley north (top) and south (bottom) of the MEF. True north is up.

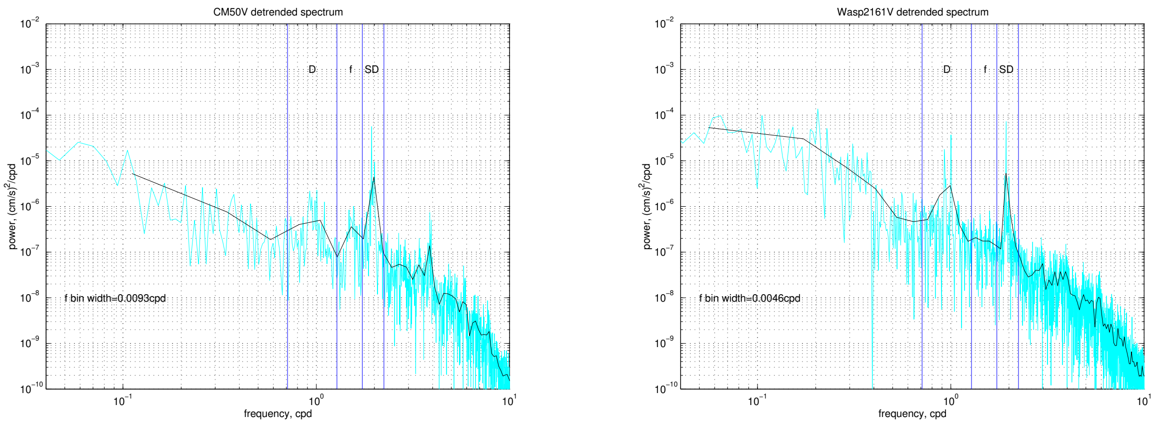

Figure 2.16: Power spectra of near-bottom v at FM-S50 (left) and FM-N15 (right). The diurnal, inertial, and semi-diurnal frequency bands are labeled D, f, and SD.

At the Endeavour, the combined oscillatory components of flow are capable of transporting fluid about the same distance as the mean component during any given half-period. This is true both above the ridge and in the valley. The displacement by a pure oscillation with amplitude v_o and period τ that occurs during $0 <= t <= \tau/2$ is

$$\Delta x = \int_0^{\tau/2} v_o \sin\left(\frac{2\pi}{\tau} t\right) dt = v_o \tau / \pi. \tag{2.1}$$

Values of v_o typical of the flow above the ridge and within the axial valley can be taken from the maximum amplitude of the current ellipses in Figure 2.14. Using these values and the associated period, Equation 2.1 yields the maximum displacement that can be affected by each oscillatory component of the characteristic flow. Table 2.2 presents these displacements and compares them to the distance traveled in typical mean flow (1–5 cm/s) during the corresponding half-periods.

Above the ridge, oscillatory flow can displace fluid 0.48–1.37 km, depending on the relative duration and amplitude of a particular component. These component displacements are comparable to the ~1 km semi-diurnal and diurnal "excursions" noted by Baker and Massoth (1987) as being much smaller than the horizontal scale of the Endeavour hydrothermal plumes. They are also similar to the "maximum daily movements" of ~0.7 km

Table 2.2: Typical displacements (Δx) by oscillatory and mean components of Endeavour currents over 1/2 tidal or inertial periods (τ). Values for main tidal frequency bands (O_1, K_1, M_2, S_2) and the inertial frequency band (f) are calculated with Equation 2.1, using amplitudes (v_o) taken from major axes of ellipses in Figure 2.14. This is done first for typical flow above the valley, then for characteristic flow within the valley. Last 2 columns show displacements due to mean flows of 1 or 5 cm/s acting over 1/2 of each period. Last row gives maximum displacement by composite oscillations (calculation described in text).

		Above valley		*In valley*		*Mean flow*	
Constituent frequency	τ hr	v_o cm/s	Δx km	v_o cm/s	Δx km	Δx km @1 cm/s	Δx km @5 cm/s
O_1	25.82	3.0	0.89	1.5	0.44	0.46	2.30
K_1	23.93	5.0	1.37	2.0	0.55	0.43	2.15
f	16.10	3.5	0.65	2.0	0.37	0.29	1.45
M_2	12.42	7.0	1.00	6.0	0.85	0.22	1.10
S_2	12.00	3.5	0.48	3.0	0.41	0.22	1.10
Composite		Max Δx: 2.2 km		Max Δx: 1.3 km			

east-west and ~1.0 km north-south estimated from currents measured at Endeavour (Roth and Dymond 1986; Dymond and Roth 1988).

Larger displacements are possible, however, if the component oscillations act together and have the same direction. A function that describes a *composite displacement* Δx_c caused by combined oscillatory components (in phase) is the sum of 5 terms, one for each of the 5 main component frequencies and amplitudes:

$$\Delta x_c = \sum_{i=1}^{5} \frac{\tau_i}{2\pi} v_{oi} \cos \frac{2\pi}{\tau_i} t. \tag{2.2}$$

The maximum of this function, obtained graphically in this case, is an estimate of the maximum composite displacement. The maximum for the characteristic oscillations above the ridge is 2.2 km; for oscillations within the axial valley it is 1.3 km (Table 2.2).

Displacements by typical mean flow above the ridge (~5 cm/s) range from 1.1–2.3 km, depending on the duration of 1/2 period. This means typical component oscillations are unlikely to overcome the mean flow above the ridge. Only maximum composite oscillations are likely to reverse the mean flow and displace fluid upstream. Transport of fluid over distances greater than 2.2 km, however, are rarely accomplished through composite oscillatory flow alone; such large displacements require an extended period of mean flow in a steady direction. This insight will also be realized through an advection/diffusion model in Chapters 3 and 4.

The range of displacements caused by mean flows (~1–5 cm/s) within the axial valley are also rarely overcome by the oscillatory components. Relative to the 1.1–2.3 km displacements caused by the ~5 cm/s mean flow at FM-N15, the displacements caused by individual oscillations in the valley are small: 0.37–0.85 km. But the 1.6 cm/s mean flow at FM-S50 is close to 1 cm/s, generating displacements of only ~0.22–0.46 over the respective 1/2 periods. This suggests that a typical diurnal, inertial, or semi-diurnal oscillation can displace fluid upstream in the slower mean flows in the axial valley, but is unlikely to do so where the mean flow is faster.

The maximum composite displacement in the axial valley, 1.3 km, indicates that combined oscillatory flow will commonly overpower a slower mean flow and may even counter the faster flow on occasion. The maximum displacement is also similar to the 2 km spacing of known hydrothermal vent fields along-axis. This has interesting ramications for larval dispersal and other exchange processes within the axial valley. In the absense of a mean flow, fluid parcels may be moved ±1.3 km by the composite oscillatory flow; the M_2 component alone could transfer parcels back and forth over ±0.85 km. With the addition of only a slight mean flow (~5 cm/s), larvae might move between major vent fields in a single semi-diurnal period, and will gain multiple exposures to an individual point on the sea floor.

2.4.4 Coherence and phase

When comparing current records from similar depths above the Endeavour ridge crest, both along and across-axis flow are in phase and have high horizontal coherence at semi-diurnal, inertial, and diurnal frequencies within several kilometers of the MEF (Thomson *et al.* 1990;

FRANKS 1992). This is also true over larger scales, albeit to a lesser extent; for tidal and inertial oscillations recorded near 2000 m at both the A2 mooring (Figure 2.8) and a mooring 15 km to the SE, coherence is near 1 and phase is $\sim 0°$ for the along-axis component and $\lesssim 45°$ for the across-axis component (FRANKS 1992). At near-inertial frequencies, horizontal coherence scales exceed 50 km in this depth range (THOMSON *et al.* 1990). Taken together, these observations imply that the *oscillatory components* of horizontal flow are uniform near 2000 m, the depth at which many MEF hydrothermal plumes equilibrate and are dispersed, over horizontal scales of at least a few km.

The majority of historical current meter arrays positioned above the Endeavour axis, crests, or flanks, suggest that the *low-frequency component* of the horizontal flow is relatively uniform near the plume equilibration depths and within ~ 1 km of the axis. For example, PVDs from an array of meters deployed by FRANKS (1992) simultaneously near 2000 m indicate that the low-frequency motions induce net southward transport in all cases; at the same time, the presence of horizontal (or possibly vertical) shear caused meters separated by only ~ 1 km (A2 at 2005 m and R2 at 1985/86 m) to differ in mean flow direction by up to 45°. Similarly, the mean flow recorded at 1942–2042 m by the 3 highest meters on the FM-S mooring (Table 2.1) is vertically uniform, showing only slight differences in patterns of flow (Figures 2.12 and 2.11). FRANKS (1992) describes a counterclockwise or "helical" rotation in mean flow recorded by vertical pairs of meters near plume equilibration depths, specifying that on average the mean flow backs $-25°$ for every 100 m of descent, while the flow magnitude decreases. Studies at other ridges indicate that this degree of uniformity may be typical of the flow over spreading center topography. Within the MAR/FAMOUS axial valley, for example, KELLER *et al.* (1975) report high coherence between 2 meters (A and C) offset 150 m vertically and ~ 3 km horizontally.

Within the axial valley, there are limited opportunities to assess horizontal flow coherence. During the Flow Mow study, the only meters occupying similar depths simultaneously were within the axial valley, near 2150 m, the central depth of the Flow Mow control volume. The meters, FM-N15 at 2161 m and FM-S50 at 2142 m, were separated along-axis by 2.2 km. Before calculating and modeling horizontal heat fluxes through the MEF control surfaces using particular measured current velocities, it is important to examine similarities and differences the FM-N15 and FM-S50 records by means of horizontal coherence calculations (Figure 2.17). Auto- and cross-spectral analysis of these near-bottom meters reveals statistically significant coherence and a 0–20° phase difference at the dominant (semidiurnal) frequency; the south meter (50 mab) leads the north meter (15 mab) by $\lesssim$45 min. This phase lag is unexpected and may be insignificant, given its similarity to the sampling period of the current meters (30 min). Unfortunately, the horizontal coherence of near-bottom currents cannot be assessed using the data of Franks (1992) because only 1 meter was deployed within the axial valley at any given time.

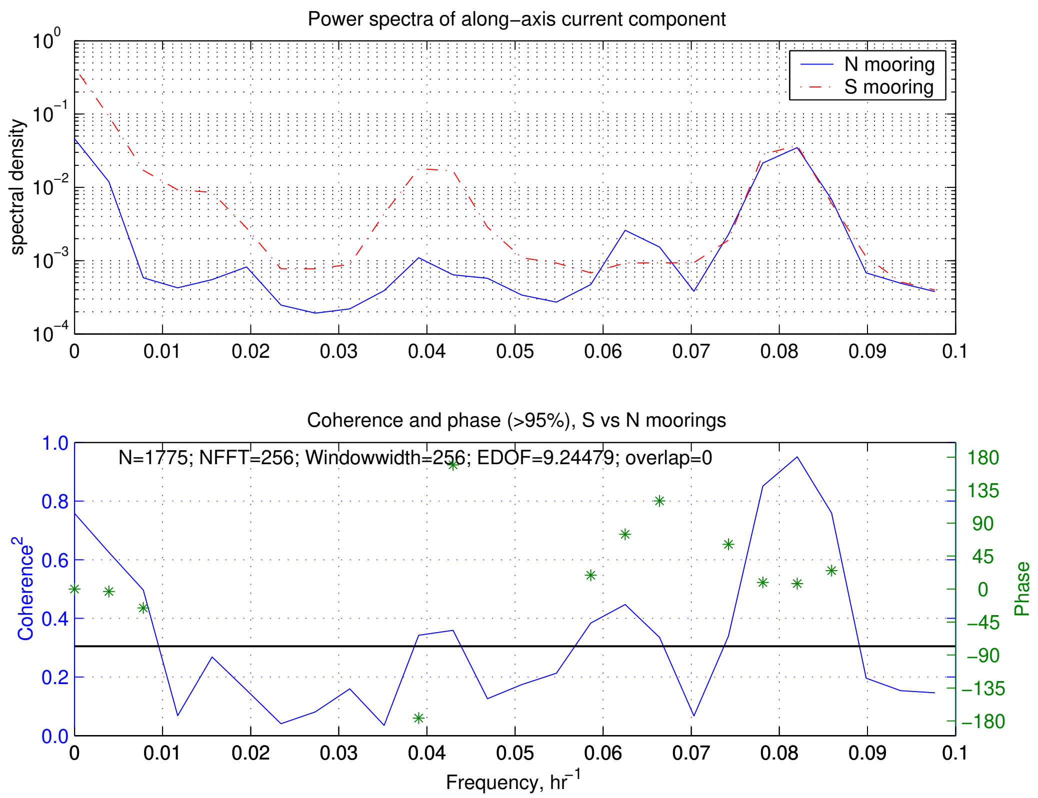

Figure 2.17: Power spectral density of the along-axis component of flow measured at the N and S moorings (top), and coherence (solid line) and phase (asterisks) between the 2 moorings (bottom). The level of 95% confidence is indicated by the horizontal line. The three significant peaks (excluding the low frequency shoulder) correspond with the diurnal, inertial, and semidiurnal periods. Positive phase means that S leads N.

Figure 2.15 provides an additional demonstration of the similarity of the oscillations at FM-N15 and FM-S50. In these 65 hr records, the magnitude of the mean flow relative to the amplitude of the tidal oscillations determines whether flow reversals occur. These short time series also characterize how rarely fluid is advected southward in the axial valley.

Further evidence that currents within the axial valley were strongly tidal and approximately in phase is given by a few short records acquired *within* the MEF during the Flow Mow field program. Figure 2.18 juxtaposes the zero-mean, along-axis component of near-bottom flow from FM-N15 and FM-S50 with 3 additional time series: the flow predicted through harmonic analysis of MZ25 (Table 2.1, H. Mofjeld, pers. comm.); the record from a MAVS deployed by M. Tivey 1 mab in the center of MEF; and ambient current inferred from a MAVS mounted on ABE during 2 of the longest dives. The latter series was calculated by subtracting ABE velocity, derived from navigational fixes of ~1 m accuracy, from the ABE-mounted MAVS readings. That this method resolved the ambient current at all is a tribute to both the MAVS, the stability of the ABE platform, and the long baseline navigation system. During this characteristic 65 hr period (the same as in Figure 2.15), the flow is dominated by semidiurnal oscillations and all records are approximately in phase. Most zero-crossings of the de-meaned records fall within ±1 hr of the predicted flow reversals.

2.4.5 Synopsis

As the resolution of the flow field above the Endeavour segment and within its axial valley has increased, some consistent characteristics have become evident. First, the mean horizontal flow is dramatically sheared near 2100 m depth over the axis. Above the ridge axis (shallower than ~2100 m), mean currents are typically directed southwestward in rough alignment with the ridge axis. Within the valley, the mean flow is often in an opposite direction and can also be reduced in magnitude. South of the sill (near 48°N), it is typically directed up-valley at 1–5 cm/s to the north or northeast. A recent synoptic deployment indicates convergent flow within the axial valley, with near-bottom (~15 mab) mean flow to the south at the sill and to the north adjacent to the MEF (Thomson *et al.* 2003). A second characteristic is that the mean flows in both depth ranges are remarkably consistent.

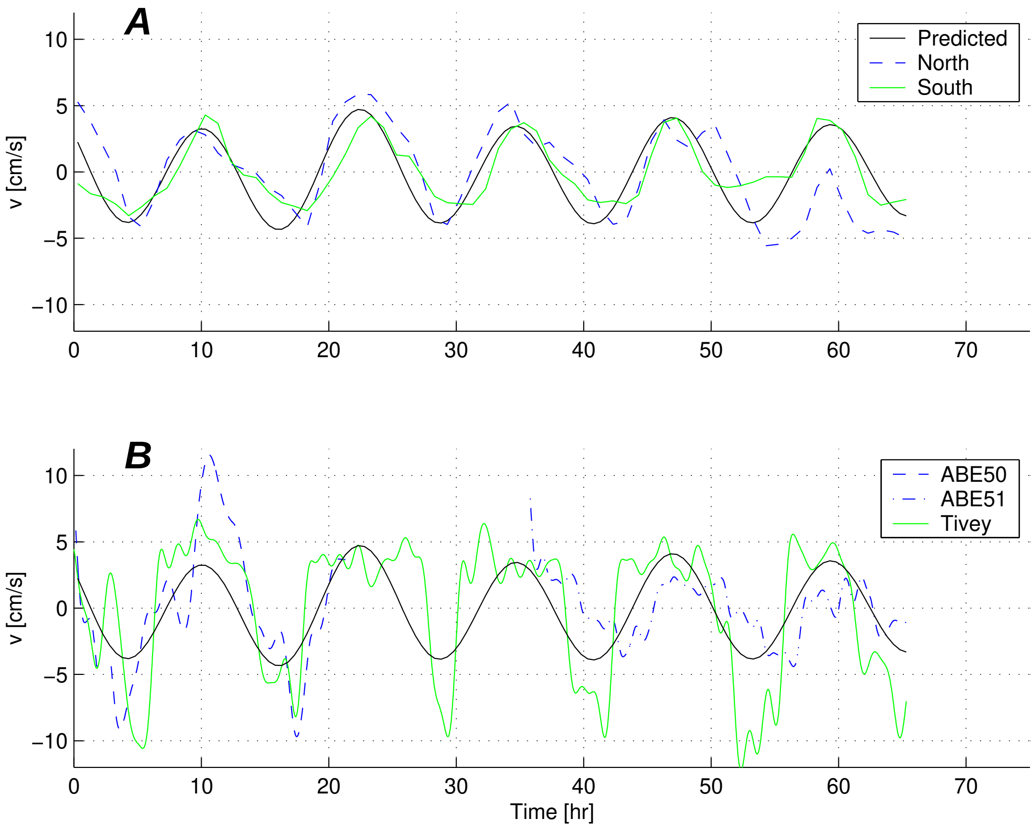

Figure 2.18: The zero-mean, along-axis component of flow measured at A) FM-N15 north of MEF (dashed blue) and FM-S50 south of MEF (solid green), and B) by ABE on the Flow Mow control surfaces (dashed blue) and by a near-bottom MAVs in the middle of the MEF (solid green). Each series covers the same period as in Figure 2.15 and is overplotted with a solid black curve: flow extrapolated to the year 2000 through harmonic analysis (H. Mofjeld, pers. comm.) using 60 days of 10 min mean data from MZ25 (Table 2.1). Time series in B) derive from: a MAVS deployed by M. Tivey ∼0.5 mab and 40 m north of the S&M sulfide structure (Figure 2.6); a MAVS mounted on ABE during the 2 longest dives (ABE50 and ABE51). All MAVS data were smoothed with Butterworth low pass filters (*e.g.* Emery and Thomson 2001).

Only intermittently do the axial valley currents appear to be overpowered by the overlying mean flow (Thomson *et al.* 2003). Finally, oscillations are prominent at all depths, but rectilinear and dominated by the M_2 semi-diurnal frequency only within the confines of the axial valley.

The methodologies for quantifying heat flux in the Endeavour flow field will be applicable in other parts of the oceans only to the extent that the current characteristics are similar there. Combinations of oscillatory and mean flows have been observed near hydrothermal sites within the axial valleys of other oceanic ridges (Keller *et al.* 1975; Thurnherr 2000). In the vicinity of the Rainbow vent field on the Mid-Atlantic ridge, for example, mechanical mixing at sills driven by tidal oscillations appears to maintain a northward mean flow along an axial valley that is open only at its south end (Thurnherr *et al.* 2002). Because the problem of measuring horizontal heat flux is significantly simpler in slower, rectilinear, nearly unidirectional flow than in faster, multidirectional, oscillatory flow, Chapter 3 presents the problem within the axial valley, while Chapter 4 examines the more complicated setting above the ridge crests.

2.5 Hydrography

2.5.1 Regional overview

The hydrography in the northeast Pacific near the Juan de Fuca ridge is generally consistent with long-term mean flow to the southwest at the depths hydrothermal plumes equilibrate (2000 m) and ∼500–1500 m below (*e.g.* Cannon *et al.* 1993). Anomalies of θ, S, Si, and He on the $\sigma_\theta = 27.675$ isopycnal surface tend to have maxima atop the Juan de Fuca ridge and decrease to the west along or near 45°N. In a study of biochemical transformations in plumes advected from the MEF, Lilley *et al.* (1995) detected concentrations of Mn and ATP 25 km southwest of the MEF that were elevated relative to undetectable levels at background stations 10 km east of MEF, but decreased by a factor of ∼4 from concentrations directly over the MEF. There is some evidence that hydrothermal signatures remain detectable in θ–S plots as far as 1000 km to the west-southwest of the ridge. The lateral distributions are relatively heterogeneous at large scale for the mid-depth open ocean, but often show local maxima that have lateral scales from 10 to a few 100 km, and are separated by similar to slightly larger distances (Cannon *et al.* 1993). An outstanding question is whether these "patches" of anomalous fluid are coherent mesoscale hydrothermal eddies, rotating in geostrophic equilibrium after separating from their vent field sources (Speer 1989; Helfrich and Battisti 1991) or simply a manifestation of the way that equilibrated hydrothermal plumes are dispersed by a combination of rotary oscillations and mean flow. Given the depths of nearby volcanically active ridge segments and the 1000 m rise height of event plumes observed above the Juan de Fuca ridge (Baker *et al.* 1989), these patches appear to be too deep to be remnant megaplumes from local sources.

Current records from *above* the ridge crests near 1900–2100 m during the Flow Mow field program and previous Endeavour segment studies also indicate that regional mean flow is to the southwest, at ~5 cm/s. Although tidal and inertial oscillations are amplified in this depth range (Thomson *et al.* 2003), none are capable of displacing hydrothermal plumes more than a few km from their axial sources, even when acting together to affect a maximum composite displacement (Table 2.2). Consequently, we assume that vertical CTD casts acquired 10 and 15 km due east of the MEF prior to the axial investigations define the regional hydrographic context, or "background" for the Flow Mow field program. The more distant station was at 47°57.01'N, 128°54.02'W, while the closer station was at 47°56.99'N, 128°58.02'W.

I assume that these eastern, upstream stations define the condition of the northeast Pacific deep water prior to topographic and hydrothermal influences. Like other casts taken at similar distances east of the axis, these stations display a near-linear θ–S trend and constant (clear water) transmissivity or backscatter signals over the depths where Endeavour hydrothermal plumes typically equilibrate (1700–2300 m). I calculate an *isohaline* potential temperature anomaly (hereafter simply $\Delta\theta$), using as a reference a 2nd-order polynomial fit to the near-linear θ–S background data (10-m depth-binned average of both stations).

2.5.2 Transition to geothermal hydrography

When averaged in 10 m depth bins, the data from the 20 Flow Mow CTD stations located over the Endeavour axis (722 separate up or down casts) show positive θ and S anomalies relative to background trends that are linear with respect to potential density, σ_θ (Figure 2.19). Deviation from the background trends typically begins near 1900 m, the same depth at which light attenuation decreases to a local minimum from a maximum near 2000 m (THOMSON *et al.* 1992). From an isopycnal perspective, the overall influence of the hydrothermal system on the ocean below ~1900 m is a shift from background fluid to "plume fluid" which is saltier and warmer, on average, at all densities greater than $\sigma_\theta \simeq 27.64$.

The axial average θ, S, and σ_θ data in Figure 2.19 show the deviation from the background trends begins at σ_θ =27.64 kg/m^3, or ~1860 m on the background σ_θ profile (see also Figure 2.21). The axial mean values diverge from the background trend until σ_θ =27.656. At higher densities, the data parallel the background slope with remarkable consistency, generating average isopycnal temperature and salinity anomalies of $\Delta_\rho\theta \simeq +0.04$°C and $\Delta_\rho S \simeq +0.004$ psu, respectively. Then, at densities higher than σ_θ =27.666 there is a subtle convergence back toward the background data. The observed mean isopycnal anomalies in Figure 2.19 are comparable to the means reported by THOMSON *et al.* (1992) for the neutral plume: 0.05 °C, 0.005 psu, and 0.03 m^{-1} light attenuation. They noted maximum isopycnal anomalies in the plume core (2000–2050 m) of +0.17 °C, +0.016 psu, and +0.20 m^{-1}.

While the average profiles have positive isopycnal anomalies at all depths, *individual* axial casts commonly exhibit layers of plume fluid ($\Delta_\rho\theta > 0$) interspersed with background fluid ($\Delta_\rho\theta = 0$). Above the ridge crests, individual casts show that background and plume layers are both common and occur at variable depths, evidencing a hydrography that is heterogenous; when averaged together spatially or temporally, however, the individual casts generate a mean profile with $\Delta_\rho\theta > 0$ at all depths (Figure 2.19). Within the axial valley, however, background fluid is rarely seen — even in individual casts, and the hydrography is less variable. Valley fluid almost always has positive $\Delta_\rho\theta$ and $\Delta_\rho S$, even within 5 m of the sea floor. Further from the axis and downstream of the volcano (with respect to the mean flow above the ridge), casts that extend deeper than the valley floor depths show that the

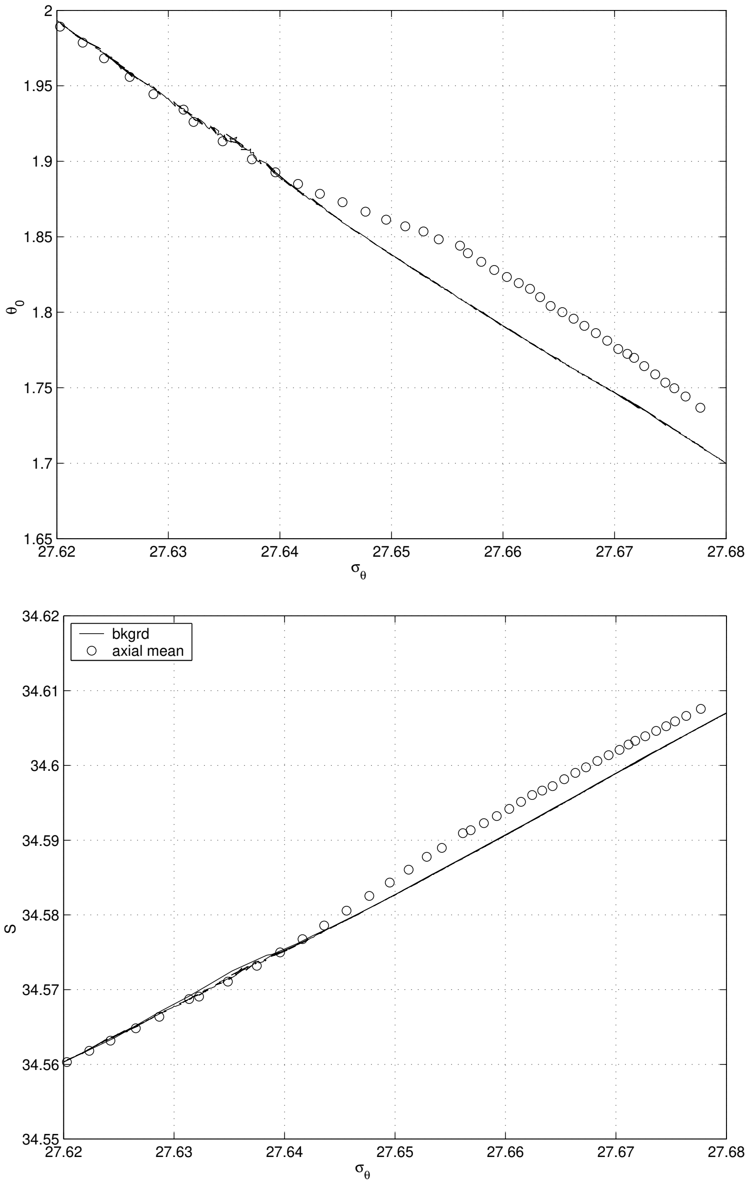

Figure 2.19: σ_θ versus mean θ and S for Flow Mow background and axial CTD stations. The solid line represents the background data (from both stations and both pairs of sensors), while the open circles represent 10 m depth-binned averages of data (from the second pair of C/T sensors only, Figure 2.7) at stations located along the ridge axis. Specific station numbers included in these averages are: 3–8, 10, 12–14, 16, 17, 19, 20, 21, 23, 24, 27, 28, 33, and 34 (see Flow Mow CTD web site, www2.ocean.washington.edu/flowmow/ecr/ctd for details and data).

positive anomalies typical of axial valley depths on axis decrease to zero below ~2250 m. This downstream return to background conditions below plume equilibration depths has has often been used to justify the definition of an anomaly by extrapolating a slope from above the plume through intermediate depths, rather than by fitting a line to data from background data above *and* below the equilibration depths.

Plotting these same θ and S data against each other (rather than density) also reveals positive temperature anomalies (Figure 2.20), though in this case they are isohaline (referenced to salinity). On average, the observed isohaline temperature anomaly is ~0.05°C roughly 2 times the isopycnal anomaly (*c.f.* Section 1.2.7). As with the isopycnal anomalies, individual axial casts show highly variable isohaline anomalies above the ridge crests — from intense plumes to background conditions at different depths at different times — and relatively uniform conditions within the confines of the axial valley. Stations as close as 1 km from the axis often reveal positive isohaline anomalies near the plume equilibration depths that are bounded above and below by background fluid.

A number of mixing processes could be responsible for the departure in θ–S conditions at the axis from the background trend (Figure 2.20). The relatively rough topography of the ridge may cause enhanced vertical mixing by increasing turbulence and boundary layer thickness, but in the absence of a warm, salty water mass, this process can only redistribute the $\theta - S$ data along the background trend. The elevated (warmer/saltier) values observed over the Endeavour axis could be due to mixing of background fluid with a variety of other fluid sources: a water mass on the west side of the ridge that is warmer and/or saltier than the fluid sampled on the east side at the Flow Mow background stations; deeper, saltier background water that has been warmed geothermally; shallower, warmer background water to which salt has been added; or an end member that is both warmer and saltier than the background.

Interleaving of distinct water masses across the Mid-Atlantic ridge has been observed near ridge crest depths (Thurnherr 2000). The northeast Pacific, however, has a much more uniform hydrography. Stations from multiple years and both sides of the Endeavour segment suggest that the regional hydrography is temporally stable and does not show across-axis gradients.

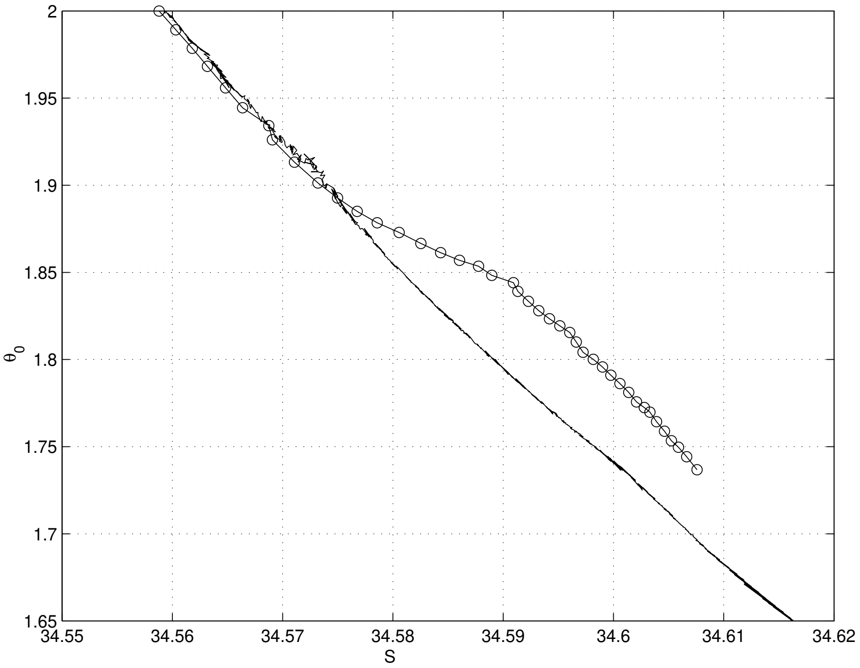

Figure 2.20: The depth-binned average θ and S from background (solid line) and axial (open circle) stations, over the depth range common to all stations.

A final and illuminating way to visualize the density, temperature, and salinity fields over the Endeavour segment is in space. A depth profile of the mean density observed at background and axial stations (Figure 2.21) immediately highlights the dynamic interaction of the hydrothermal plumes and the deep ocean. On average, the fluid above 2000 m is denser than the surrounding ocean, while the deeper axial water is less dense than the background. This is the mean manifestation of the equilibration process at the segment scale, and represents a dynamic equilibrium in which the plume layer, supplied by hydrothermal venting, is actively intruding into the deep ocean.

Geographic grouping of the vertical profiles provides evidence that hydrothermal activity causes the transition from background to axial conditions. Figure 2.21 emphasizes how the level anomalies increase as one progresses from the background stations, through the axial stations at the north and south ends of the segment, and into the axial valley. Both near the bottom and at upper levels, the absolute values of the level anomalies (*c.f.* Section 1.2.6) $\Delta_z \sigma_\theta$, $\Delta_z \theta$, and $\Delta_z S$ increase to maxima at the SoMEF and NoMEF stations, in the vicinity of the MEF.

Given the positive $\Delta_\rho \theta$ and $\Delta_\rho S$ in Figure 2.19 at all densities, a critical question is how the fluid below ~1975 m in Figure 2.21 has negative $\Delta_z \sigma_\theta$. At first glance, this density structure in Figure 2.21 indicates vertical mixing, but the θ profile is not consistent with vertical mixing because it is not displaced to values cooler than the background above 1975 m. The fluid deeper than ~2075 m has positive $\Delta_z \theta$ and negative $\Delta_z S$.

A similar geographic grouping of θ–S profiles (Figure 2.22) cannot be explained by mechanical vertical mixing, for that process could only redistribute depth-bin averaged points along the background trend. Instead, the average profiles are displaced furthest from the near-linear background trend near the center of the Endeavour segment, where the hydrothermal activity is most intense. This suggests that hydrothermal water is being mixed into the deep ocean over a broad region, affecting the spatially- and temporally-averaged θ–S profiles over the length of the segment and within $\sim$ 1 km of the Endeavour axis. Below ~2075 m, the positive $\Delta_z \theta$ and negative $\Delta_z S$ must be due to a hydrothermal input of relatively warm, fresh water, not simply a vertical circulation of relatively warm, fresh water from overlying depths.

The observations in Figure 2.21 indicate, overall, that below the equilibration depth, average isopycnal, isohaline, and isotherm surfaces all dip downward over the axis. The density profiles imply that isopycnal surfaces are level near 1975 m and bowed upward between 1975 m and $\sim$1800 m. Such downward and upward "bowing" of isopycnals has been observed in many hydrothermal environments (*e.g.* HELFRICH *et al.* 1998) and inspired ideas about plume-induced motions: radial motion in response to horizontal pressure gradients and pursuant rotation (*e.g.* SPEER 1989). Isohaline surfaces mimic the isopycnal ones, although they are level at a greater depth, near 2075 m, and must slope more steeply than the isopycnals to generate positive $\Delta_\rho S$ at all depths. Isotherms dip downward at all depths (also more steeply than do isopycnals) below 1900 m, causing positive $\Delta_z\theta$; they may bow slightly upward at shallower depths, accounting for the slight negative $\Delta_z\theta$ above 1900 m. At the north end of the segment the isotherms begin to dip only below $\sim$1975 m.

Positive $\Delta_z\theta$ in near-bottom fluid has been attributed to hydrothermal venting within the topographically-constrained depths of the Broken Spur segment of the MAR (MURTON *et al.* 1999). There, the depth profile of *in situ* temperature T is nearly vertical within the confines of the segment, but about $6.7\times10^{-4}\,^\circ$C/m both at similar depths in the adjacent Atlantis fracture zone and at depths above the Broken Spur ridge crests.

East of the Endeavour segment in the Cascadia basin, THOMSON *et al.* (1995) identify positive $\Delta_z\theta$ relative to a background profile acquired at the southern end of the basin, near the deep Blanco fracture zone where the north Pacific deep water (NPDW) is thought to intrude the basin. They use the positive $\Delta_z\theta$ to define a "geothermal boundary layer" (GBL) that extends from the basin sea floor at $\sim$2700 m up to $\sim$2250 m. They posit that the warming is caused by a combination of conductive heat flux through the sea floor sediments, convective heat flux from diffuse vents on basement outcrops near 2600 m, and long-term turbulent mixing of the geothermal signal as high as 250 m above the outcrops (THOMSON *et al.* 1995, Figure 14). A composite of the θ–S data obtained near the Baby Bare diffuse flow site shows a departure within the GBL from the near-linear trend in the overlying water. Inversions in the θ profiles were interpreted as plumes from the diffuse vents, while vertical near-bottom gradients evidenced benthic boundary layers 10–30 m thick. THOMSON *et al.* also suggest that a change in the slope of the θ profile near 2250 m marks the upper

Figure 2.21: Depth profiles of mean σ_θ, θ, and S from Flow Mow stations grouped geographically. Emphasis is on the transitions between background and axial stations. Axial stations are: "Deep S," the southernmost stations (23, 24, 27, and 34), from the southeast flank to the Mothra vicinity; "SoMEF," stations 4, 6, and 33, $\sim$500 m south of MEF; "NoMEF," stations 3, 5, 14, and 28, $\sim$500 m north of MEF; "Deep N," stations 17 and 19, just north and south of the saddle.

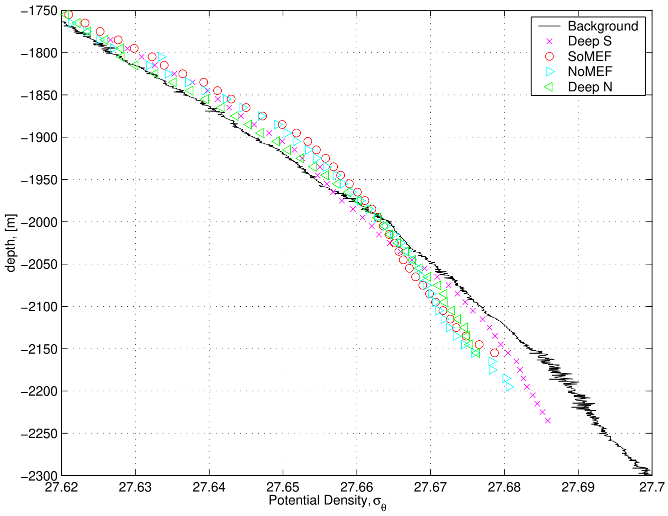
Background
Deep S
SoMEF
NoMEF
Deep N
depth, [m]
Potential Density, σ_θ

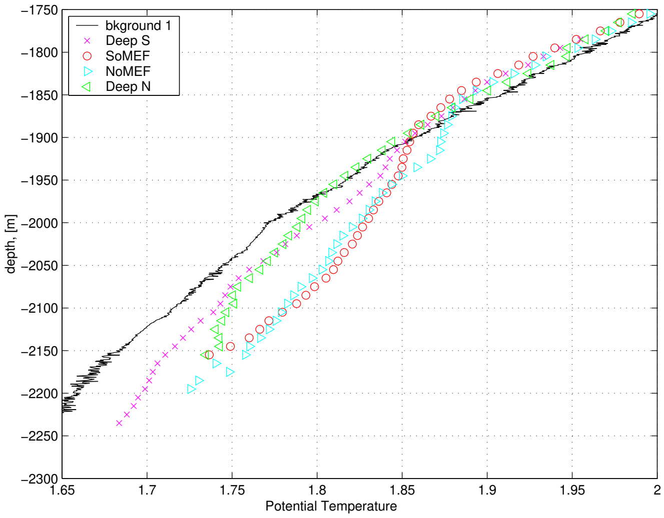
bkground 1
Deep S
SoMEF
NoMEF
Deep N
depth, [m]
Potential Temperature

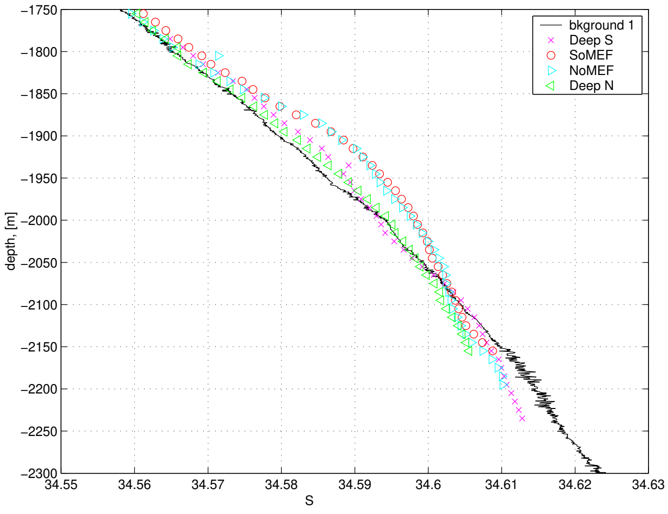
bkground 1
Deep S
SoMEF
NoMEF
Deep N
depth, [m]
S

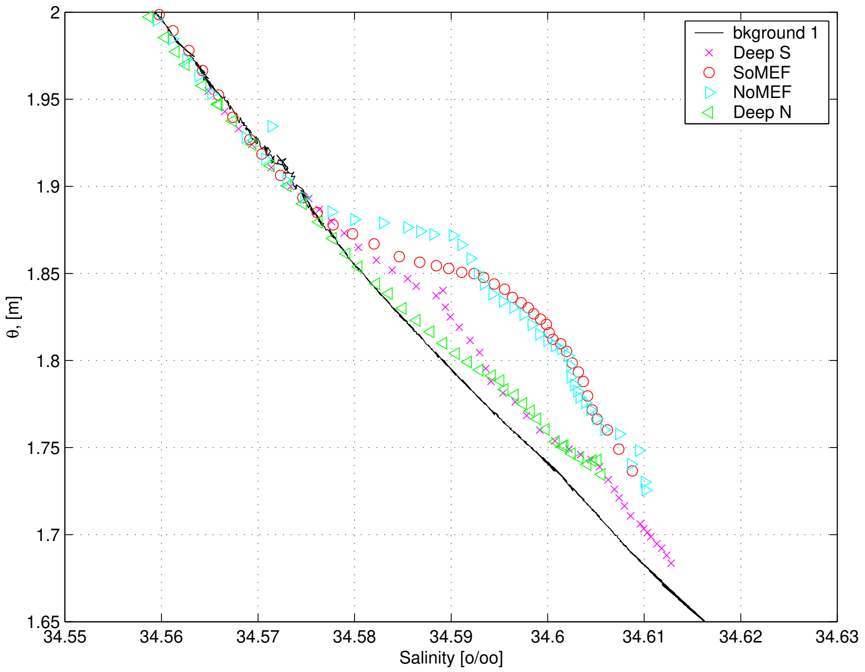

Figure 2.22: θ–S profiles based on data, averaged in 10 m depth bins, from Flow Mow stations grouped geographically and labeled as in Figure 2.21.

boundary of the NPDW; $\mathrm{d}\theta/\mathrm{d}z$ decreases from $5.19\times10^{-4}\,°\mathrm{C/m}$ between 2000–2200 m to $1.91\times10^{-4}\,°\mathrm{C/m}$ between 2250–2525 m. In comparison, the Flow Mow background slope is $5.7\times10^{-4}\,°\mathrm{C/m}$ between 2000-2200 m, but is decreased to $4.4\times10^{-4}\,°\mathrm{C/m}$ within the axial valley, close to the MEF. Taken together, these observations imply that the GBL is established over the Cascadia basin below 2250 m, but is thickened by additional geothermal sources near 2250–2150 m on the Endeavour segment, ultimately extending up to near ~1900 m (Figure 2.21).

The same pattern of level anomalies is evident in an average of data from NoMEF and SoMEF stations, including 2 long (10–14 hr) VOCs (Figure 2.23). The profile of backscatter evidences that the particle rich plume layer is centered on average near 1980 m, the depth where the background and axial mean σ_θ trends intersect. Note that the mean values below 2200 m are derived only from the SoMEF area because the sea floor depth is ~2200 m in the NoMEF area. The mean $\Delta_z\sigma_\theta$ is positive up to a depth of ~1800 m. The main plume has positive $\Delta_z\theta$ below 1900 m, and $\Delta_z S$ that is positive from 1900–2060 m, but negative at greater depths. The negative $\Delta_z\theta$ above 1900 m may be the result of small changes in the water properties relative to the background, but may also be evidence that vertical circulation induced nearby buoyant plumes causes isotherms to bulge upward on average. The negative $\Delta_z\theta$ begins in the 50 m below the top of the particle plume, a depth range where $\Delta_z S$ and $\Delta_z\sigma_\theta$ are positive as expected.

Many aspects of the vertical profiles observed at this distance from high B sources are explained by a numerical model of a hydrothermal plume rising from a 1 MW/m line source in a steady cross flow of ~1.5 cm/s (Lavelle 1994). The model includes ambient stratification (with T and S profiles typical of the Juan de Fuca ridge), a cross flow velocity that is steady >100 mab and decreases to zero at the sea floor, constant source heat flux, and variable source salinity. Although the linear nature of the source exaggerates the vertical recirculation between the plume cap and stem, and may therefore perturb nearby isopleths more than a plume from a point source (J.W. Lavelle, pers. comm.), vertical S and T profiles taken through the model domain upstream and downstream of the source are remarkably similar to the mean MEF profiles (Figure 2.24). Source salinities of *both* 34.7 and 15 psu result in positive $\Delta_z\theta$ below the equilibration depth (~2100 m) and a $\Delta_z S$ "dipole." The

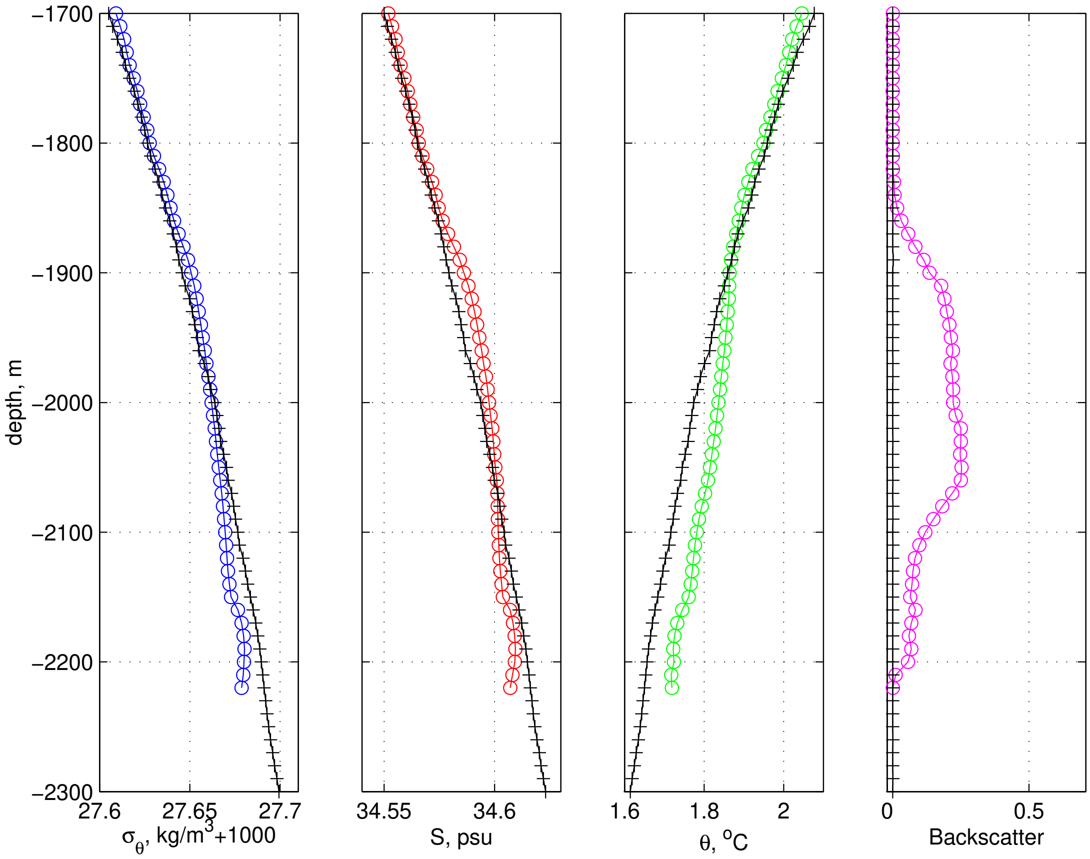

Figure 2.23: Observed profiles of mean σ_θ, S, θ, and backscatter data combined from the NoMEF and SoMEF areas, ~500 m north and south of the MEF. Each circle is the mean of all data within a 25 m depth bin centered at that depth. Note that the deepest 2 bins include data from the SoMEF area only.

upstream S plume profile intersects the background profile at a depth 25–50 m below the equilibration depth, while the downstream $\Delta_z S$ is zero even deeper, 75–125 m below 2100 m.

Figure 2.23 also displays typical near-bottom conditions within the axial valley, close to the MEF. Mean and individual profiles of σ_2 are often vertical near the valley floor, evidencing a well-mixed boundary layer that is $\lesssim$50 m thick. On rare occasions the near-bottom fluid is unstable. The fluid below ~2150 m typically has $\sim$ 1/5 the backscatter intensity found in overlying equilibrated plumes. Taken together with the near-bottom mean flow, these observations suggest that the increase in $\Delta_z\theta$ and $\Delta_S\theta$ toward the center

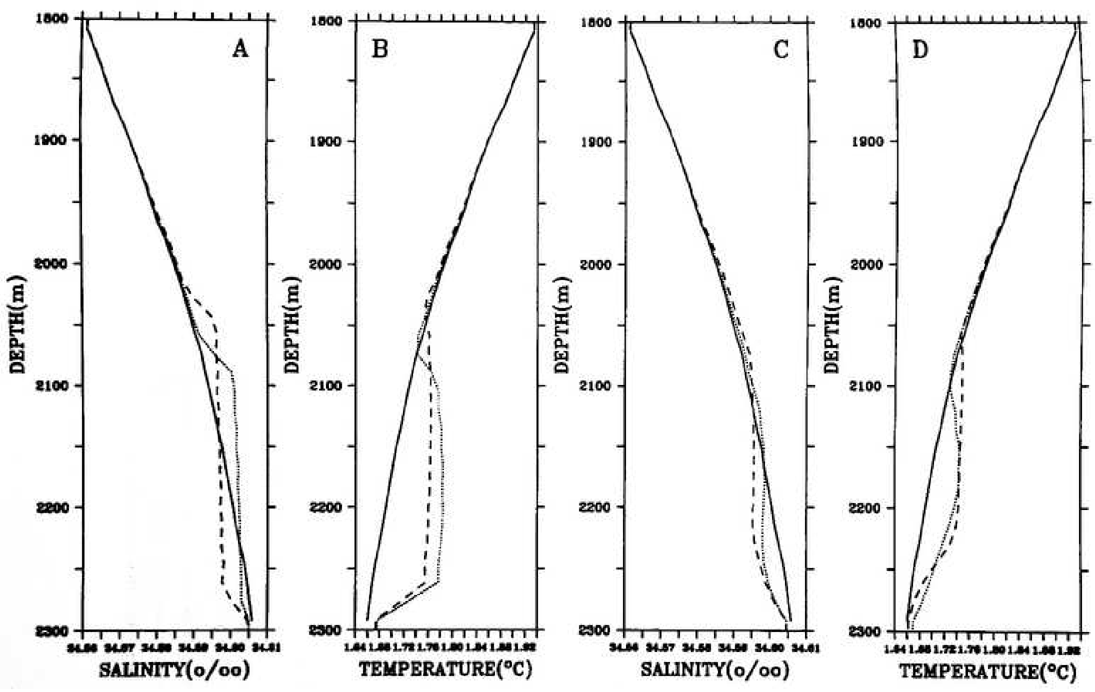

Figure 2.24: Modeled profiles of S and T 300 m downstream (A & B) and 200 m upstream (C & D) of a line plume source. The solid lines represent background profiles from the Juan de Fuca ridge, the dotted lines correspond to a source $S = 34.7$ psu, and the dotted lines are for a fresher source, with $S = 15$ psu. Reproduced with permission from Lavelle (1994).

of the segment is caused by a heat flux to the fluid as it progresses along the axial valley. This could occur through multiple processes: sea floor geothermal heating of relatively fresh, clear background water; injection of warm, fresh, clear vent fluid; or downward recirculation of overlying plume fluid in which the backscatter signal is decreased. Subsequent mechanical mixing may help to homogenize the added heat, resulting in a reduction of $\Delta\theta$ variance with increasing time and/or distance from a sea floor source.

Approaching Endeavour ridge from the east, hydrothermal influence on the θ–S trend first becomes evident on the outer ridge flank (Veirs *et al.* 1999). Above 2100 m on the southeast flank (only about 1 km southeast of the MEF) water properties are nearly indistinguishable from the background stations. Below 2100 m, the water is slightly above background in θ–S space, but less so than at any more central axial station. Similarly, a station taken on axis, but at the extreme north end of the segment, ~15 km north of MEF, reveals no departure from the background trend over a wide range of depths (1700–2250 m).

In contrast, axial stations located over or between the vent fields always sample fluid that has positive $\Delta\theta$ (Figure 2.25) and high backscatter, indicating hydrothermal plume influence. Above and near ridge crest depth, background water is interspersed with layers of this plume water that vary in depth and thickness between sequential casts that are typically 0.3 hr apart or offset by ~100 m. In this upper layer (1850–2100 m), stations taken $\lesssim$1 km southwest (downstream with respect to the regional mean current) of known fields tend to be the most anomalous. The intermittent returns to the background in this depth range (as well as below plume depths in distal downstream casts) assure that the near-linear background relationship can be extended, rather than extrapolated, through equilibrated plumes, as well as the axial valley depths.

Within the axial valley ($\gtrsim$2100 m) near MEF, water with background θ–S character is extremely rare. The $\Delta\theta$ of near-bottom fluid is almost always positive and generally increases along-axis toward the center of hydrothermal activity. In θ–S space, the average profile within the valley typically plots nearly parallel to, but above the background trend (Figure 2.25).

Other investigators have also noted that the fluid below ~2100 m within the axial valley has distinctive characteristics. Based on samples taken near the MEF, Rosenberg *et al.*

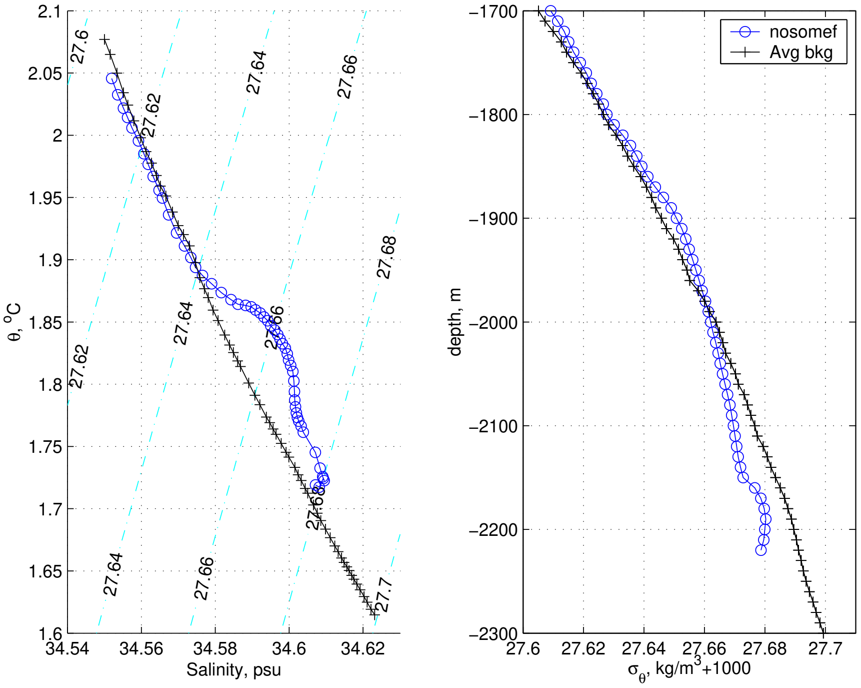

Figure 2.25: Mean θ–S and σ_θ profile based on data combined from NoMEF and SoMEF areas and averaged in 10 m depth bins. The equilibration depth, 1980 m, is associated with the σ_θ =27.66 kg/m^3 isopycnal. Note that isopycnals in the θ–S plot are only parallel to isobaths (lines connecting bins of the same depth) at the equilibration density, 27.66 kg/m^3; that is, at all depths greater than ∼1800 m the mean isopycnal surfaces are sloped above and below 1980 m.

(1988) note that the concentration of radon relative to ^{3}He increases with depth, and does so dramatically below 2100 m. The most enriched sample was taken from a depth of ∼2180, likely ∼20 mab, and was almost 3 times greater than the next sample above at 2110 m. They explain the trend by suggesting that the near-bottom water is enriched in radon through low T venting and is subsequently entrained and transported vertically by high B plumes. This supposition is strengthened by the observation that the ratio Rn/T is higher at low T vents than at high T vents (Kadko and Moore 1988).

2.5.3 Observations in and near buoyant hydrothermal plumes

This subsection advances what is known about the physical characteristics of rising hydrothermal plumes and how they evolve as the plumes equilibrate within the ocean. The focus is on new insights derived from the Flow Mow hydrographic data set. Some of the data analyzed here have also been utilized to estimate the net vertical heat flux from the MEF (Stahr *et al.* 2003).

During the Flow Mow hydrographic survey numerous rising plumes were intercepted by the lowered CTD when it was towed horizontally through the MEF at heights of ∼5–60 mas. ABE traversed hundreds of plumes as they rose through the top of the control volume, ∼85 mas. The final Flow Mow CTD VOT characterized the plume tops above the MEF. And the many CTD casts within ∼100–1000 m of the MEF inform the equilibration process, helping to explain how differences between axial and background hydrography arise.

This section is organized as a tour through rising plumes at increasing elevations above the source. Examples are taken from the CTD stations during which buoyant plumes were observed (Table 2.3).

Station 10 began as a VOT along the north MEF control surface between 1800–2200 m. Toward the end of the station, after encountering multiple intense plumes at similar positions but on different passes along the surface, an excursion was made southward in an attempt to intercept buoyant plumes from the supposed source, the sulfide structure called Hulk. A map of the excursion and the associated time series are shown in Figure 2.26.

The data from Station 10, acquired in and around plumes 5–400 m above known sources,

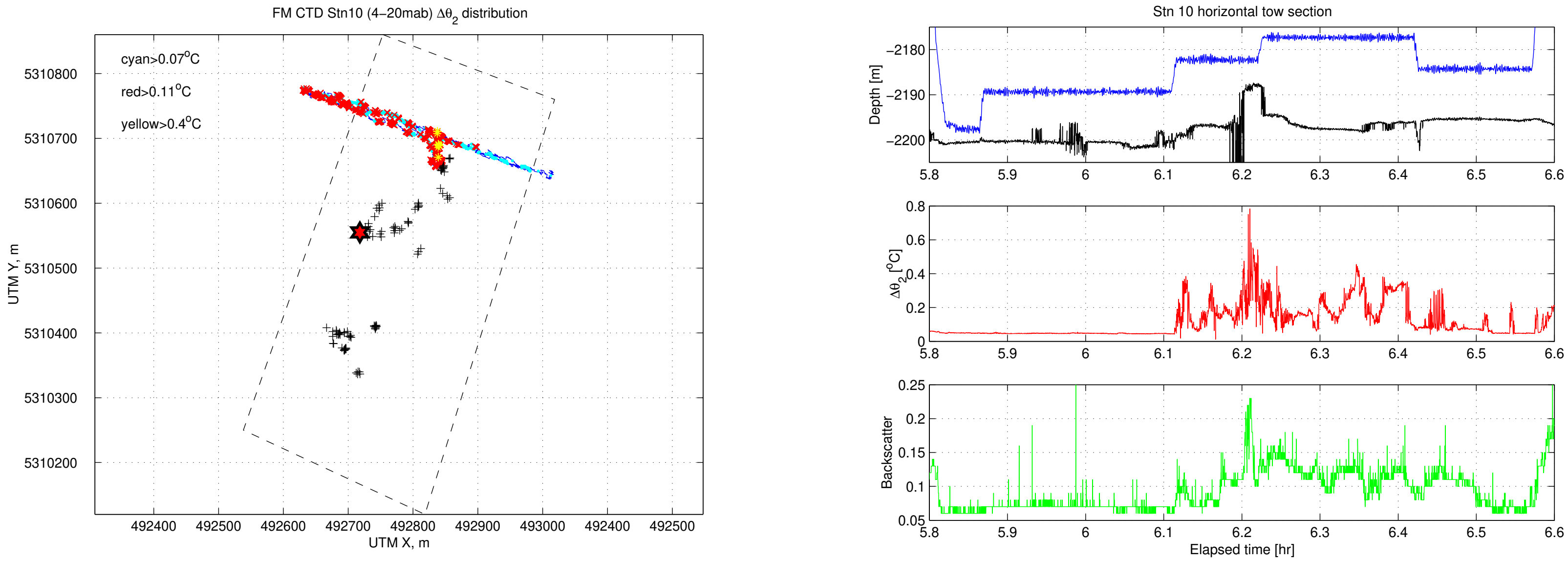

Figure 2.26: Location map and time series from horizontal tow through buoyant plumes during CTD 10 which proceeded from north to south. Left panel symbols: dashed line is MEF control volume perimeter; each + is a known individual high B source; colored x and * symbols indicate thresholds of $\Delta\theta$ annotated in upper left corner. Right panels shows time series of depth and bottom traces (upper), $\Delta\theta$ (middle), and backscatter (lower). Bottom depth values are sum of CTD pressure depth and altimeter reading.

Table 2.3: $\Delta\theta$ observed at various depths and elevations in rising plumes during Flow Mow CTD stations. The depth ranges result from minor changes in the CTD or ABE depth during a single station (CTD 10 depths refer to horizontal tow section only). Elevation ranges are due to both changes in CTD depth and the topography of the underlying sea floor and sulfide structures. Last 2 columns show the elevation at which the buoyant plume was intercepted and the associated peak $\Delta\theta$ value.

Station	Depth range (m)	Elevation range (mas)	Buoyant plume (mas)	Peak $\Delta_S\theta$ (°C)
CTD 10	2177–2198	05–20	07	0.79
CTD 11	2145–2155	25–35	22	2.71
CTD 15	2150–2160	25–45	~40	0.75
CTD 30	2140	30–60	33	1.25
CTD 31	2110–2125	65–90	80	0.35
CTD 32	2105–2125	50–70	70	0.72

provide an unusual opportunity to compare the physical hydrography of buoyant plumes with the fluid through which they rise – from the sea floor to above the equilibration depth. Figure 2.27 shows the raw θ–S distribution and σ_θ profile for the entire station, including 3 traverses of the north surface (*c.f.* Figure 4.3) and the horizontal tow. The left panel reveals the degree of scatter that underlies the average θ–S distribution near the MEF(*c.f.* 2.25) — equilibrating plumes interspersed with background fluid above ridge and points more uniformly above the background trend within the valley — but superimposed are data points from within the buoyant plume. The right panel also shows the majority of points scattered around the mean density profile typical of the MEF vicinity, but the buoyant plumes are clearly evident in the bottom 100 m. Indeed, the magnitude of the near-bottom $\Delta_z\sigma_\theta$ appears to decrease rapidly with elevation above the sea floor. Above ~2030 m where $\Delta_z\sigma_\theta$ goes to zero, there is a population of points with moderate positive $\Delta_z\sigma_\theta$ comparable to the average anomaly, but there are also individual layers with greater $\Delta_z\sigma_\theta$ and sharp upper boundaries. I interpret these signals to be evidence of negatively buoyant fluid near the MEF plume tops, high above its ultimate equilibration depth.

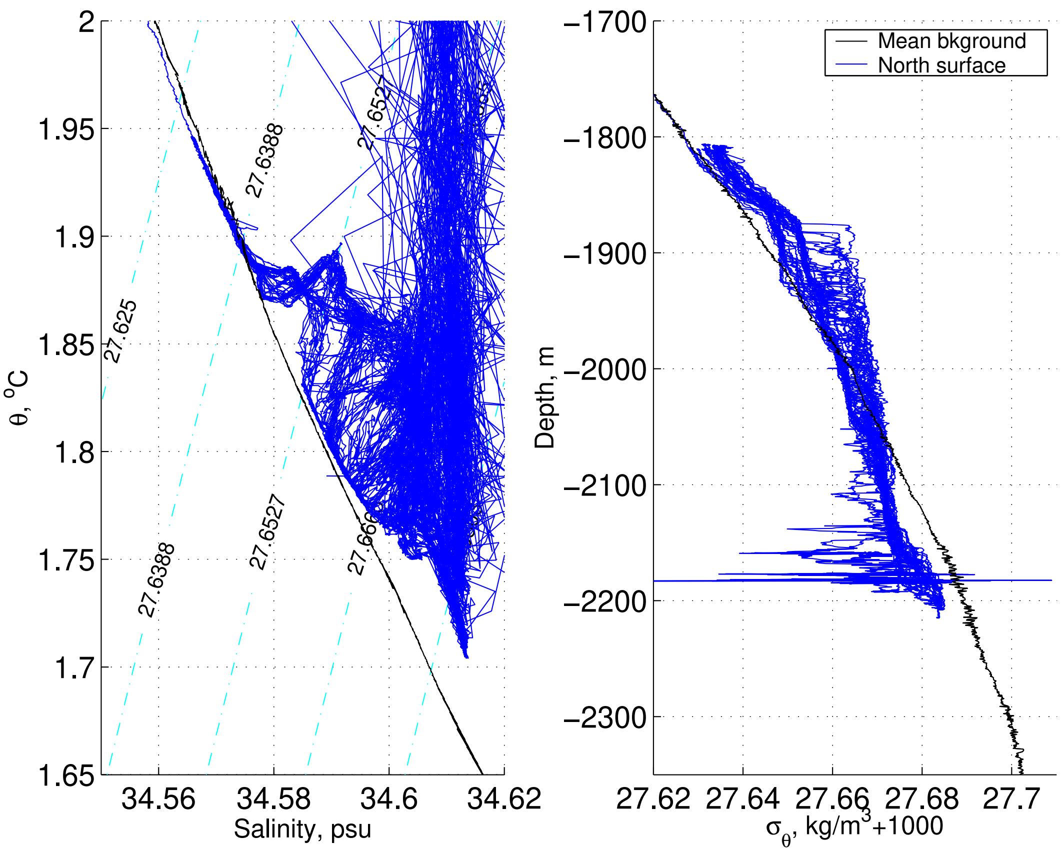

Figure 2.27: Raw 0.5 Hz data from CTD station 10, both the VOT portion along a cross-axis plane just north of the MEF, and the horizontal tow portion that passed through a buoyant plume near Hulk. Left panel shows the θ–S trends over σ_θ isopycnals. Right panel shows the σ_θ depth profile. Black trace is the mean of both background stations; blue trace represents station 10 data.

Though the scatter of the θ–S data is relatively high in Figure 2.27, it is intriguing to note that a straight line fit to the points with $\Delta_S\theta > 0.2$°C constitutes a mixing line that should point toward the θ and S of the source fluid. For the station 10 data, the line has a slope of about -0.01 psu/°C. Extending this line from a point in the buoyant plume data ($S = 34.61$, $\theta = 2.0$) to $\theta_f = 334$°C observed at Hulk in the year 2000 (D. Butterfield, pers. comm.) suggests that the source $S \simeq 31.29$ psu. For comparison, the value of S measured in source fluid sampled directly from Hulk in 2000 is ~30.56 ([Cl]=477 mM/kg, D. Butterfield, pers. comm.). The similarity of the extrapolated and directly measured values indicates that with enough data from a buoyant plume, source properties may be accurately inferred.

Station 11 was a horizontal tow that traversed north–south across the MEF, passed directly over a number of known structures, and intercepted at least 3 distinct, rising hydrothermal plumes (Figure 2.28). It is particularly noteworthy because it recorded the largest temperature anomaly within a buoyant MEF plume, 2.71°C (Table 2.3), and because the altimeter trace suggests that steep-sided topography (sulfide structures) underly *each* major plume. Station 15 was an almost identical tow and stations 30–32 were horizontal tows that traversed the northern MEF in a roughly regular grid pattern; both generated results similar to those shown for station 11, and are therefore not presented graphically.

A final feature of the horizontal tows through the interior of the MEF control volume is the relative uniformity of $\Delta\theta$ *between* the rising plumes. While it is clear that the source θ values rapidly with elevation in the rising plumes (Table 2.3), the ambient fluid within the bottom ~75 m has relatively uniform $\Delta\theta$. For ~30 short sections taken from the horizontal tow stations (~2110–2200 m depth), the mean $\Delta\theta$ observed between adjacent rising plumes is ~0.05±0.02°C during. The $\Delta\theta$ conditions between many plumes are completely homogeneous, with very low variance relative to the time series acquired within the buoyant plumes. In a few cases there are gradual departures or minor steps from the otherwise constant $\Delta\theta$ values between plumes; these are interpreted as evidence of diffuse plumes adjacent to focused plumes. The transition into rising plumes from the steady ambient $\Delta\theta$ values is generally abrupt, indicating sharp gradients at the plume edge (*c.f.* Figure 2.26), despite the expectation of Gaussian time-averaged temperature profiles from laboratory plume analysis (Papanicolaou and List 1987).

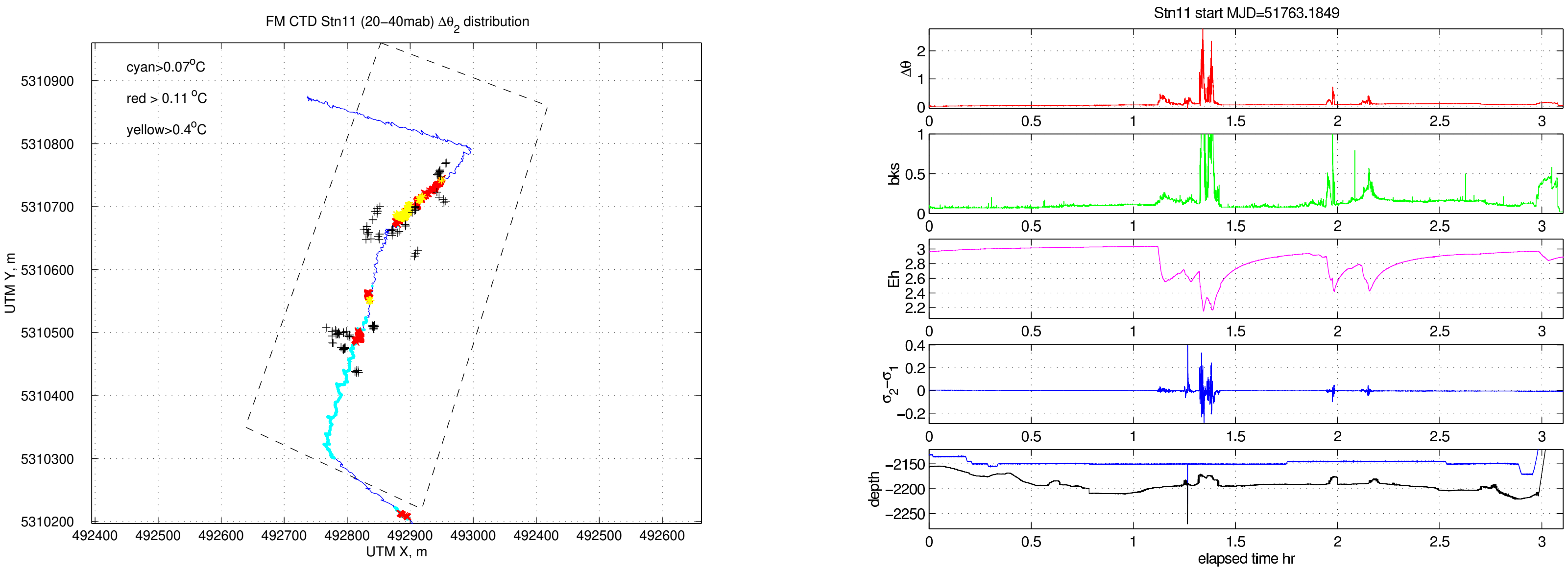

Figure 2.28: Location map and time series from horizontal tow through buoyant plumes during CTD station 11, which proceeded from north to south. Left panel symbols: dashed line is MEF control volume perimeter; each + is a known individual high B source; colored x and * symbols indicate thresholds of $\Delta\theta$ annotated in upper left corner. Right panels (top to bottom) show time series of: (1) $\Delta\theta$, (2) backscatter, "bks," (3) Redox potential, "Eh" (values decrease in reducing solutions, K. Nakamura, pers. comm.), (4) difference in potential density observed at upper and lower CT pairs (*c.f.* Figure 2.7), indicating fluid instability (Veirs *et al.* 1999), and (5) depth and bottom traces (based on CTD depth and altimeter readings).

This tour through the Flow Mow control volume completes the setting of the stage for calculating and interpreting heat fluxes. The next 2 chapters present hydrographic observations on the surfaces of the control volume. The $\Delta\theta$ fields on the surfaces greater than $\sim$50–100 mab are surprisingly heterogeneous relative to the ambient fluid observed near the center of the MEF on the horizontal tows. In contrast to the variability observed on the MEF perimeter, the uniformity of the $\Delta\theta$ within the MEF control volume makes it easier to characterize the fluid that is likely to be entrained by MEF plumes. This characterization will help to justify the method of calculating net heat flux from the lower control volume in the next Chapter.

Chapter 3

PLUMES AND HEAT FLUX IN THE VALLEY – RECTILINEAR FLOW

During the Flow Mow study, currents within the axial valley near the Main Endeavour field consisted of a northward ~1-5 cm/s mean flow superimposed on along-axis tidal oscillations of comparable amplitude. When this type of flow distributes energy from a hydrothermal source within a control volume, the net outward heat flux through the bounding control surfaces can vary significantly over time. Even if the source heat flux is constant, temperature anomalies in the water column can change quickly as thermal energy pools above a vent during slack flow periods and streams away from it during peak cross flow. Attempts to measure the total flux through control volume surfaces can result in a time series that has surprisingly high variance and, depending on how temperature and velocity signals are averaged, a mean magnitude dramatically different from the source magnitude (Wetzler *et al.* 1998).

In this chapter I begin with a description of the method used to calculate total lateral heat flux from the MEF within ~100 mab. After presenting the temperature anomaly measurements made on or near the vertical control surfaces, I combine the temperature and current data to estimate the net horizontal heat flux through the side surfaces of the lower control volume (Figure 1.3). Subsequently, I use a simple advection-diffusion model to interpret the observed flux magnitudes and gain insight into the flux variance caused by variable currents near the MEF. Finally, I combine the horizontal and vertical heat flux estimates in the lower control volume to infer the partitioning of heat flux between diffuse and focused hydrothermal venting within the MEF.

3.1 Calculated horizontal heat flux

Heat flux is calculated by integrating over a control volume surface the product of $\Delta\theta$ and current velocity. The net horizontal heat flux H_h out of the control volume is the sum, minding flux direction, through all 4 vertical control surfaces (*c.f.* Equation 1.9). In this section, however, I make 2 assumptions that simplify the heat flux calculation, both based on the nature of the flow within the axial valley and the observational limitations of the Flow Mow data set.

First, I assume the consistent northward mean flow and rectilinear tidal oscillations within the axial valley (*c.f.* Section 2.4) mean that only the north and south control surfaces are important in the computation of net horizontal flux from the MEF. That is, I assume the heat flux through east and west surfaces is negligible. This is reasonable because the east and west surfaces are oriented parallel to the ridge axis and are therefore approximately aligned with the local, rectilinear flow. This assumption is also necessary because the Flow Mow hydrographic program, motivated by previous observation of rectified, along-axis flow at the MEF, focused on monitoring the north and south surfaces repetitively and at multiple tidal phases, while the east and west surfaces were surveyed only 1–2 times.

Second, I assume that measurements from current meters moored ~1.1 km north or south of the MEF can be used to calculate accurately the horizontal heat flux at the MEF control surface locations. This is justified by the northward mean flow within the axial valley consistently observed at meters north and south of the MEF (FM-N15 and FM-S50, Table 2.1), and by the spatial coherence of the oscillatory flow between this pair of meters. The assumption is also necessary because velocity measurements were not made alongside the CTD observations on the lowered instrument package.

In this section, with these simplifications, I calculate a range of observed net horizontal heat fluxes from the MEF using temperature anomaly data from the north and south control surfaces and northward mean velocities of 1–5 cm/s measured at the moorings. The first consideration, tackled in the next subsection, is making an accurate assessment of $\Delta\theta$ on the control surfaces. The subsequent subsection addresses integration of the $\Delta\theta$ and current meter observations to calculate net horizontal heat flux. Estimates of vertical heat flux through the upper surface are presented in Stahr *et al.* (2003).

3.1.1 Observed $\Delta\theta$

During the Flow Mow field program, spatial hydrographic variability was monitored on the side surfaces of the lower control volume (Figure 1.3) through repetitive surveys with ABE or a navigated CTD. Transects of individual surfaces took ~1.5–3 hrs, came within ~5 m of the sea floor, and reached maximum heights of ~100 mab. ABE surveys, primarily in the form of descending sequences of lateral transects, acquired hydrographic data with horizontal resolution as high as ~2 samles/m and vertical resolution of ~1 sample/10 m (Figure 3.1). Vertically oscillating CTD tows (VOTs) along side surfaces generated data with vertical resolution as high as ~4 samples/m and horizontal resolution of ~1 sample/25 m (Figure 3.2). Temporal hydrographic variability was also monitored during the field program, most intensely during 10–14 hr-long vertically oscillating casts (VOCs) between 2100 and 2200 m (Figure 3.4) at fixed locations ~500 m north and south of the MEF.

Samples of θ and S were converted into $\Delta\theta$ (isohaline anomaly) using an expression like Equation 1.16, but with a polynomial fit to the average background θ–S relationship observed at CTD station 1 and 2 between 1700–2375 m: $\Delta\theta = \theta - (-24480.315 + 1409.267S - 20.283S^2)$. In preparing the figures in this section, the location of navigated $\Delta\theta$ values from ABE or CTD were projected orthogonally onto the appropriate side surfaces of the lower control volume. This was necessary because most ABE and CTD surveys extended above or beyond the edges of the control surfaces; only those measurements located on the control surfaces after orthogonal projection were included in heat flux estimations. Typical lateral separation between a point projected on a control surface and the corresponding ABE or CTD measurement location was < 20 m. The projected $\Delta\theta$ values on each surface were then aggregated into bins of height and width, averaged, and color-coded according to the resultant mean $\Delta\theta$ value. Bin size was specified with the goal of containing data from adjacent tracks. For ABE surveys, bins with dimensions of $\Delta x = 10$ m and $\Delta z = 25$ m typically contained $\gtrsim 100$ samples/bin; for VOTs, $\Delta x = 100$ m, $\Delta z = 5$ m, and typical bins held $\gtrsim 40$ samples/bin. Bins with no data were left blank (white). Using this bin-averaging technique, no contouring was performed.

In this subsection, I present 3 perspectives on $\Delta\theta$ variability and patterns near the MEF within the axial valley ($< 2100\,\mathrm{m}$). First, I examine spatial variability with the ABE surveys of the north and south surfaces of the lower Flow Mow control volume. A second, similar description of spatial variability comes from CTD surveys of the same surfaces. Finally, I illustrate temporal variability with 2 time series acquired at CTD stations ~500 m north and south of the MEF boundaries.

ABE surveys of north and south surfaces

The $\Delta\theta$ fields on the north and south surfaces of the MEF control volume were observed during 3 separate ABE dives (45, 46, and 50) and are presented in Figure 3.1. Each of the 6 panels in the figure represents a separate transect of a surface with $\Delta\theta$ values overlain by the ABE track line. Dives 45 and 50 have mean anomalies on their north surfaces that are 0.013–0.020°C larger than on their south surfaces. Dive 46 has a mean anomaly on its south surface that is 0.008°C larger than on its north surface; even when only the upper 50 m of the unequally-covered surfaces are compared for Dive 46, the mean anomaly at the south surface (0.077°C) is slightly larger than at the north surface (0.074°C). Successive north surfaces were separated by 13.8 and 199.9 hr, and south surveys were separated by 23.0 and 122.1 hr. The results thus show the strong variations in time of excess heat at the north and south surfaces.

Figure 3.1 also shows the degree of spatial variability in plumes in this depth range and at this distance from the MEF sources. On any given pass across the 300 m wide surface, plumes or thermal patches as narrow as 20 m are observed. Sequential passes, sometimes separated only 10 m vertically and ~10-20 min temporally, commonly encounter $\Delta\theta$ that varies by as much as a factor of 2.

CTD surveys of north and south surfaces

An additional perspective on the $\Delta\theta$ spatial variability comes from data taken on 3 VOTs (Figure 3.2). During station 10, the CTD was towed back and forth across the north

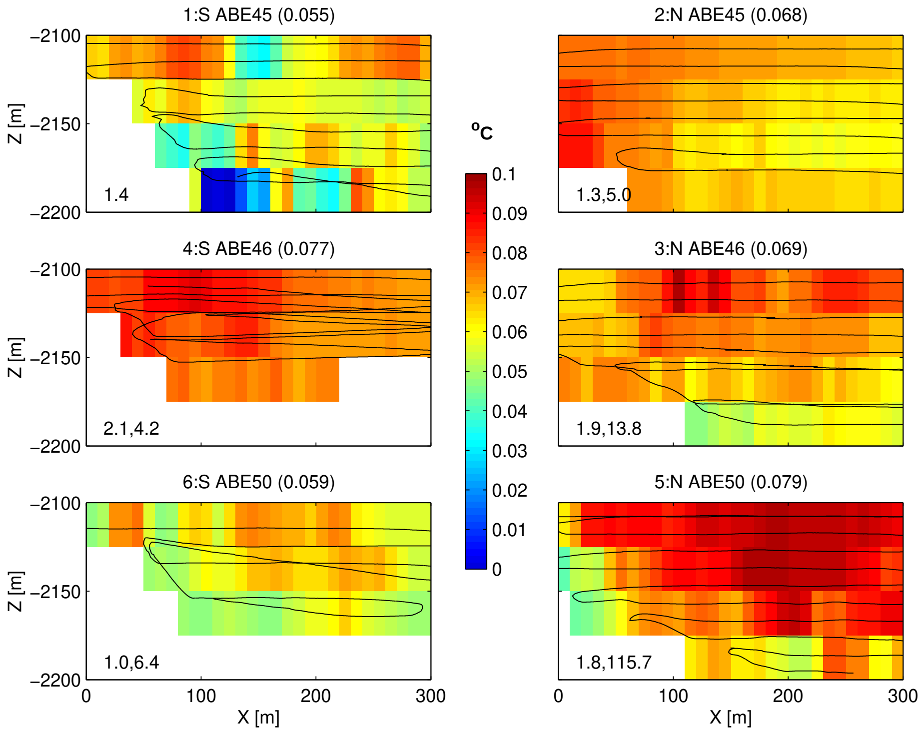

Figure 3.1: $\Delta\theta$ on south and north control surfaces during ABE dives 45, 46, and 50. Successive north surfaces (right 3 panels) were separated by 13.8 and 199.9 hr, and successive south surveys (left 3 panels) were separated by 23.0 and 122.1 hr. The title over each panel contains: a number indicating the order in which the surfaces were surveyed; the dive number; and the mean $\Delta\theta$ of all bins (noted parenthetically). Averaging bins are 10 m wide and 25 m high. White areas have no data. Annotations in lower left corner of each panel are times in hours: first the survey duration for that surface, then the time since the end of the previous surface (*e.g.* survey 5:N began 115.7 hr after the end of survey 4:S). Black line represents the ABE track. Varying maximum survey depths are due to changes in ABE's bottom-avoidance algorithm.

surface 3 times, generating 3 surveys of the north surface. The south surface was similarly surveyed ~5.5 times during stations 12 and 13. Since the VOTs were continuous, there is no temporal separation between sequential surveys of a given surface; when the end of a surface was reached during a particular station, the ship immediately reversed direction and began another survey of the same surface. Each surface survey took ~80–100 min and extended to within 5–10 m of the sea floor.

When all samples from 2100–2200 m are averaged together on each surface in Figure 3.2, north surfaces have mean $\Delta\theta$ from 0.053–0.091°C, while south surfaces have mean $\Delta\theta$ from 0.053–0.076°C. In the *sequential* panels of Figure 3.2 (Stn 10: N#1–3, Stn 12: S#5, Stn 13: S#1), the first north surface has the highest mean $\Delta\theta$, but many of the south surfaces have greater mean $\Delta\theta$ than the second and third north surfaces. Compared to north surfaces, the south surfaces are more uniformly warm in their upper 25 m. The lowest 25-50 m of the south surfaces are variable and generally cooler than in the same depth range on the north surface.

When the surfaces in Figure 3.2 are sorted into north and south groups and averaged, the mean $\Delta\theta$ on the south surface (0.0677°C) is slightly less than on the north surface (0.0690°C). This result is consistent with the overall average $\Delta\theta$ differences detected in the ABE survey of the north and south surfaces. Though the difference is smaller in this case, it is well within the the sensor resolutions (*c.f.* Section 2.3).

Interestingly, in almost every survey of the south surface that approached within 50 mab (Figures 3.1 and 3.2), a 20–50 m wide and $\lesssim$25 m tall patch of fluid with $\Delta\theta$ ~0.06–0.09°C was encountered within 25 mab, usually near $X = 200$ m. It is possible that the patch was a plume from Quebec (*c.f.* Section 2.1.3), a diffuse flow site located ~250 m south of the MEF (Figure 3.3), that was advected along-axis in northward mean flow. The rise height of the Quebec plume cannot be constrained because the salinity and volume flux of the fluid venting at Quebec are unknown. During the Flow Mow study, however, the Quebec plume was detected at depths of 2125–2200 m (Figure 3.3) in 2 VOTs that criss-crossed and circumnavigated the 1995 Alvin coordinates where Quebec was discovered. The peak $\Delta\theta$ sensed in the Quebec vicinity was 0.12°C and 10 m thick layers had $\Delta\theta$ of 0.05–0.09°C. These values are only slightly higher than the mean $\Delta\theta$ values of the warm patch on the

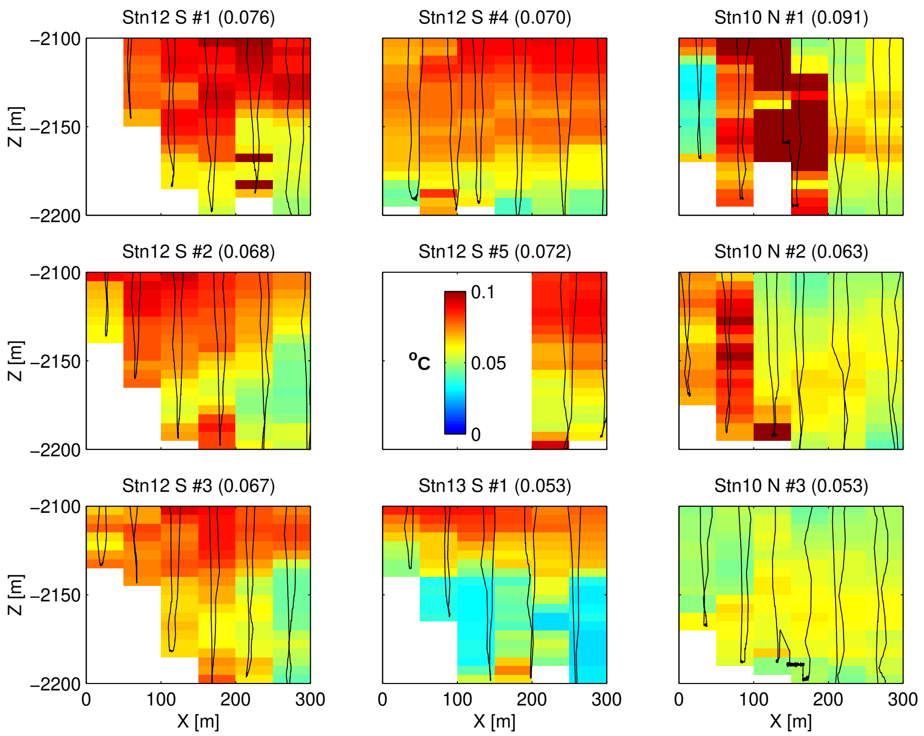

Figure 3.2: Isohaline potential temperature anomaly $\Delta\theta$ on south (left 2 columns) and north (right column) control surfaces during CTD stations 10, 12, and 13. Title above each panel indicates: CTD station number; south (S) or north (N) surface; order (#) in sequence of surface surveys during each station; mean of all bins (noted parenthetically). Station 12 began ∼3.8 hr after station 10 ended, and station 13 began ∼14.2 hr after the end of station 12; sequential surveys during each station are temporally contiguous. Bottoms of successive vertical oscillations are spaced ∼20 min apart; surfaces were surveyed in ∼80–100 min. Black line represents CTD track. Averaging bins are 100 m wide and 5 m high. White areas have no data.

south control surface. Assuming a small source size ($\lesssim$ 10 m) and reasonable value for near-bottom diffusivity (0.4 m^2/s, OKUBO 1971), diffusion of a plume from Quebec during advection at 1–5 cm/s over the 250 m distance to the south surface would result in a plume width of roughly 60–140 m (CSANADY 1973). This width is also consistent with that of the patches observed on the south surface.

A probable explanation for the temporal variability of average $\Delta\theta$ on individual surveys of the north and south control surfaces is advection of MEF plumes by oscillatory currents and mean flows within and above the axial valley. This possibility is further explored through analysis of time series from stationary CTD profiles.

CTD time series north and south of the MEF

The mean northward flow that had been indicated by the 1995 current meter motivated special emphasis during the Flow Mow field program on monitoring and comparing 2 CTD survey areas (dubbed "NoMEF" and "SoMEF") located ~500 m along-axis north and south of the MEF boundary (Figure 2.5). Both areas were monitored at various tidal phases for periods of 0.5–14 hr during the CTD stations spaced 1–5 days apart. NoMEF was assessed during stations 3, 5, 14, and 28, while SoMEF was studied during stations 4, 6, 7, and 33 (Figure 3.4). During stations 28 and 33, NoMEF and SoMEF were reoccupied for 10 and 14 hrs, respectively, approximately a full semidurnal tidal period. NoMEF was monitored during station 28 for about 10 hr during a VOC between 1800 and 2200 m. 3 days later during station 33, SoMEF was assessed (~200 m west of previous SoMEF CTD stations 4 and 6) for 14 hr during a VOC between 1800 and 2150 m. To examine the temporal variability of $\Delta\theta$, samples from each CTD station are averaged in depth-time bins with dimensions chosen to contain at least 2 sequential CTD casts and ~20 samples (Δz =5 m, Δt =30 min). Then, the intermittent surveys are concatenated, creating a series of observations characterizing the NoMEF and SoMEF areas (Figure 3.4).

The $\Delta\theta$ profile at NoMEF and SoMEF changes with time (Figure 3.4). At NoMEF $\Delta\theta$ is elevated in an upper layer (2100–2150 m) relative to the layer within 50 mab. In both depth ranges $\Delta\theta$ is consistent from hour to hour, but changes by $\sim 0.05°$C over time scales longer

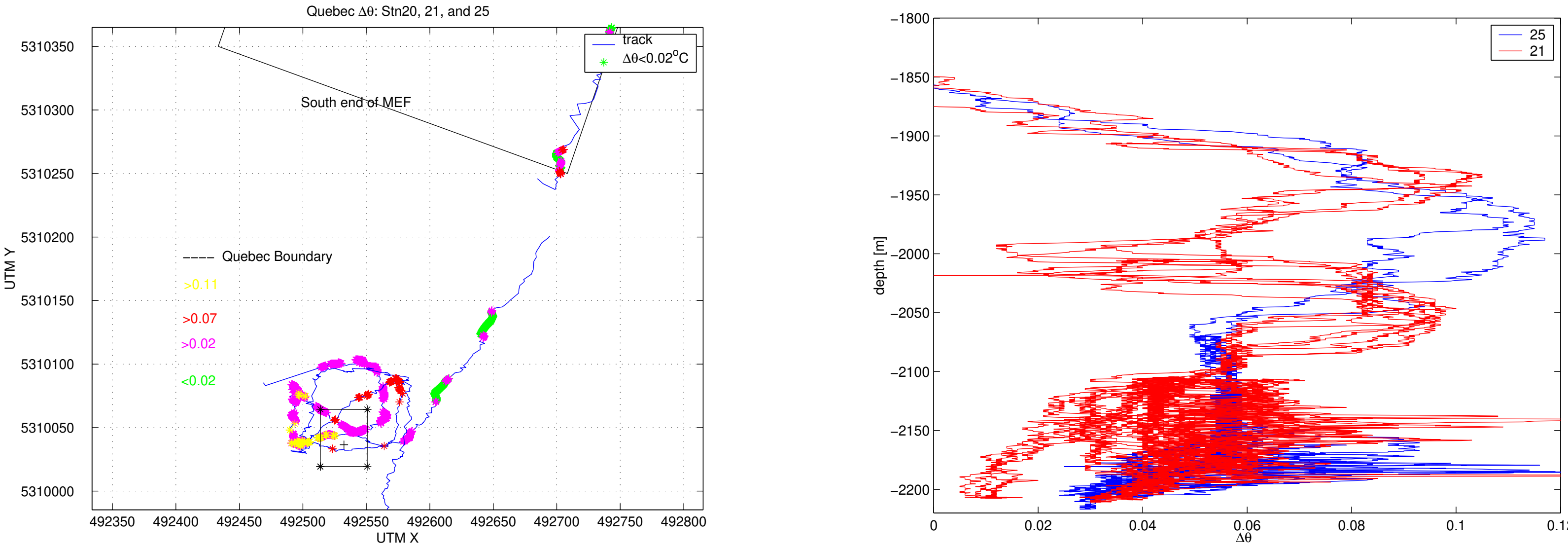

Figure 3.3: Map on left shows the CTD track during 2 VOTs around and over the Quebec diffuse flow site (47°56.62'N, 129°6.0'W). Overlain in color are ranges of $\Delta\theta$ encountered along the tracks; see legend for temperature ranges. Quebec coordinates, based on a 1995 Alvin dive, are delineated by the small box containing the + symbol. The southern end of the MEF is near the top of the map, along with the beginning of the track for CTD station 20, which traversed the east side of the MEF. The $\Delta\theta$ profiles at right are derived from the 2 stations that surveyed Quebec (21 and 25).

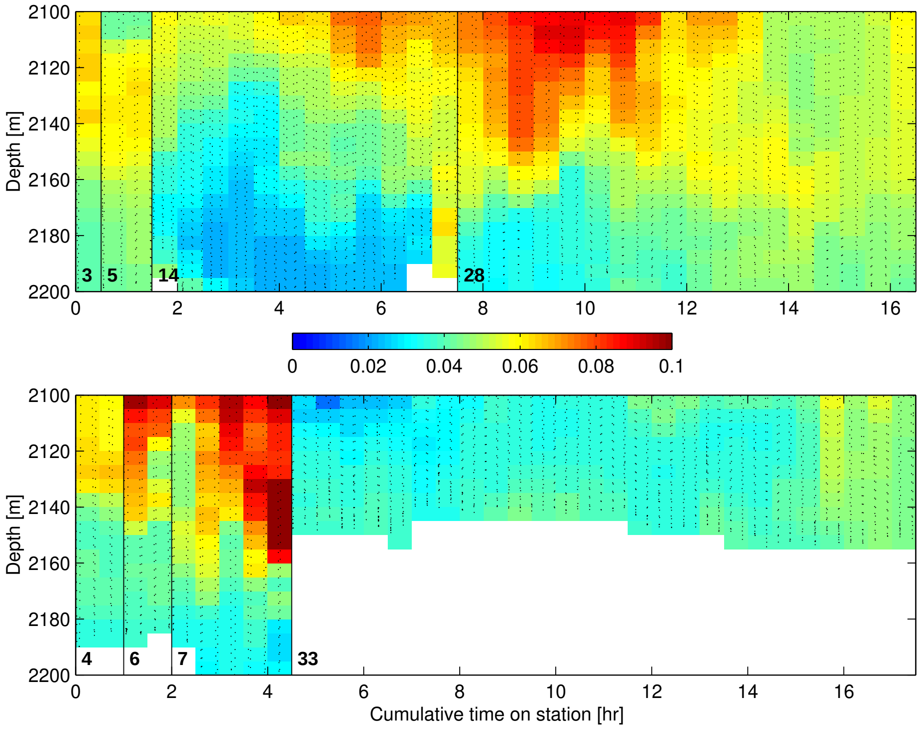

Figure 3.4: Time series $\Delta\theta$ from vertical CTD casts in the NoMEF area (top panel) and SoMEF area (bottom panel). Before plotting, data were averaged in vertical bins 5 m high and 1/2 hr wide. White areas contain no data. Dotted black line represents CTD depth history. Vertical black lines mark temporal breaks of ~1-5 days between stations, each of which is numbered in lower left corner. Station 33 does not extend below 2155 m because it was located west of stations 4, 6, and 7, where the western scarp shoals to ~2160 m (see dual SoMEF locations, Figure 2.1). For additional context, see Figure 4.1.

than a semi-diurnal half-period. An upper layer with relatively high $\Delta\theta$ is also present at SoMEF during stations 4, 6, and 7; during the same period $\Delta\theta$ in the SoMEF lower layer varies only $\sim$0.02°C, less than the variations in the lower layer at NoMEF. While large near-bottom $\Delta\theta$ attributed to a plume from Quebec was observed on south control surfaces (Figures 3.1 and 3.2), no similar anomalies are observed at SoMEF, which is located south of Quebec (Figure 2.5) and therefore upstream with respect to the northward mean flow in the axial valley. The warmer upper layer evident in most of Figure 3.4 was not present during station 33 (which was located further east and up on the western scarp of the axial valley, Figure 2.5), but $\Delta\theta$ still varied during station 33 up to $\sim$0.04°C at some depths over time scales of about a semi-diurnal half-period. These observations suggest the $\Delta\theta$ field at this distance from the MEF changes over semi-diurnal time scales, while closer to the MEF sources the $\Delta\theta$ distribution on particular control surfaces in Figure 3.2 changes between CTD surveys, on time scales of 1–2 hrs. Thus, temporal variability appears to increase with proximity to the MEF.

Despite the exhibited temporal variability, the average $\Delta\theta$ taken over all depths and times (Figure 3.4) is 0.050°C at NoMEF and 0.043°C at SoMEF. As was the case with the control surface surveys, the *spatial and temporal average* $\Delta\theta$ is greater north of the MEF than south of it.

Synopsis of spatial and temporal variability

A final perspective on axial valley hydrography comes from a nearly synoptic observation of $\Delta\theta$ on *all 4* MEF control surfaces, accomplished during ABE dive 50 in 15.4 hr (Figure 3.5). ABE surveyed the north surface first, taking 1.8 hr. After completing a survey of the top surface in 6.3 hr (Stahr *et al.* 2003), ABE surveyed the south, east, and west surfaces sequentially, taking 1.0, 4.2, and 1.1 hr on each surface, respectively. The transition between south and east surfaces took 18 min, while the last transition, from east to west surfaces took 40 min.

Figure 3.5 shows that fluid with the smallest $\Delta\theta$ is predominantly near the bottom, and on the east and southeast sides of the MEF. This is consistent with other casts that contain

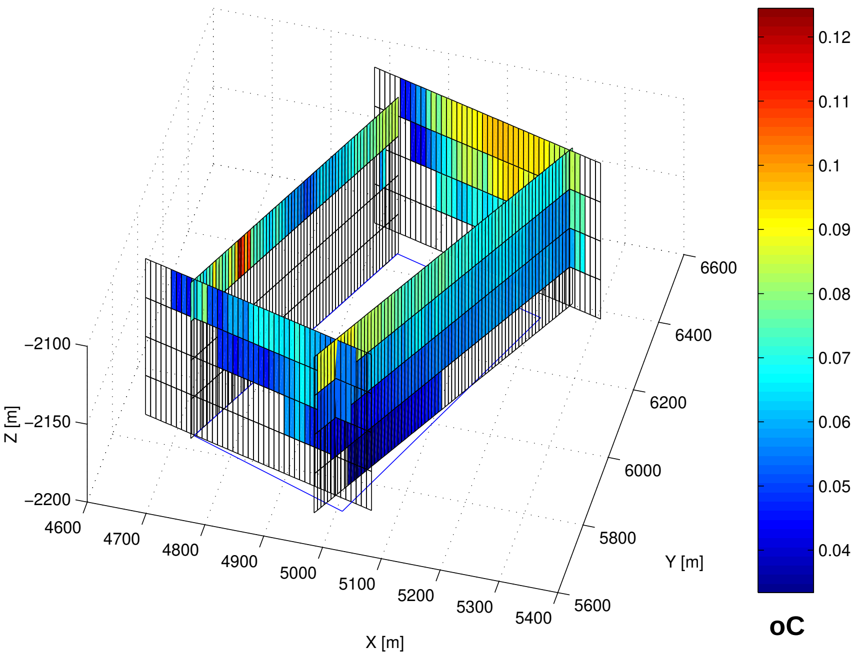

Figure 3.5: $\Delta\theta$ distribution on all 4 side surfaces of the MEF control volume, acquired within a 15.4 hr period during ABE dive 50. Observations are projected on to vertical planes aligned with the mean track of ABE on each side, rather than on to the control surfaces. Coordinates are relative to the Alvin origin.

relatively rare encounters with near-zero $\Delta\theta$ axial valley fluid (*c.f.* stations 20, 21, and 25 in Figure 3.3); the deep areas to the south and east of the MEF tend to have the smallest $\Delta\theta$. This pattern supports the idea that *on average* the mean northward flows bring relatively cool fluid into the MEF through the south control surfaces and transport relatively warm hydrothermal plumes through the north surfaces.

Considered along with the other Flow Mow observations presented in this section, Figure 3.5 also describes a high level of $\Delta\theta$ variability on the MEF control surfaces. While it is not possible to distinguish between spatial and temporal variability with a moving sensor, the successive ABE or CTD transects of the control surfaces imply scales of $\lesssim$10 m or $\lesssim$20 min. On the whole, the Flow Mow observations evidence a level of hydrographic heterogeneity, or "patchiness," within the Endeavour axial valley that was poorly characterized before the Flow Mow study. Past hydrographic surveys of the MEF vicinity suggested that

$\Delta\theta$ within the valley was generally homogeneous, despite the rare serendipitous encounters with unusually high $\Delta\theta$ fluid that sometimes led to successful inference of diffuse vent locations (Veirs *et al.* 1999). Previous investigations generally viewed the bottom 50–100 m as a relatively well-mixed boundary layer, vertically and horizontally homogeneous, and less anomalously warm than the overlying plume layers (*e.g.* Thomson *et al.* 1989).

Calculation of the horizontal heat flux through the lower control volume requires the mean isohaline potential temperature anomaly (hereafter $\overline{\Delta\theta}$) observed on the north ($\overline{\Delta\theta}_N$) and south ($\overline{\Delta\theta}_S$) control surfaces. Later in this chapter, an advection/diffusion model forced by tidal oscillations is used to understand the variability of $\overline{\Delta\theta}$ observed near the MEF. Here, however, I obtain an estimate of $\overline{\Delta\theta}_N$ and $\overline{\Delta\theta}_S$ by generating depth-binned histograms of $\Delta\theta$ samples acquired north or south of the MEF — either during ABE or CTD surveys of the control surfaces, or CTD surveys of the NoMEF and SoMEF areas.

Observations of $\Delta\theta$ at MEF both above and below the ridge include those data in Figures 3.1, 3.2, and 3.4, and all data acquired *above* the ridge crests during the same set of stations (to be further analyzed in Chapter 4). Aggregating all these data into north and south groups and sorting into 25 m depth bins, histograms of $\Delta\theta$ are generated for each bin. The resulting distributions of $\Delta\theta$ (Figure 3.6) characterize the full range of depths (1800–2200 m) influenced by plumes in the vicinities north and south of MEF, and therefore provide some context for Figures 3.1, 3.2, and 3.4 which portray data from only the deepest 4 bins (2100–2200 m). While the spatial and temporal variability of near-bottom $\Delta\theta$ around the MEF was higher than expected, the $\Delta\theta$ variance is low in the bottom 100 m relative to the depths above 2100 m, where cross-axis flow increases the variability of plume distributions (c.f. Section 4.1.2).

Figure 3.6 can also be used to quantify north–south differences in $\overline{\Delta\theta}$. In the bottom 100 m, each 25 m bin has a $\overline{\Delta\theta}$ that is greater in the north. The average $\overline{\Delta\theta}$ taken over these 4 deepest bins is 0.063°C in the north, versus 0.056°C in the south. These are the values I use to estimate horizontal heat flux in the next section.

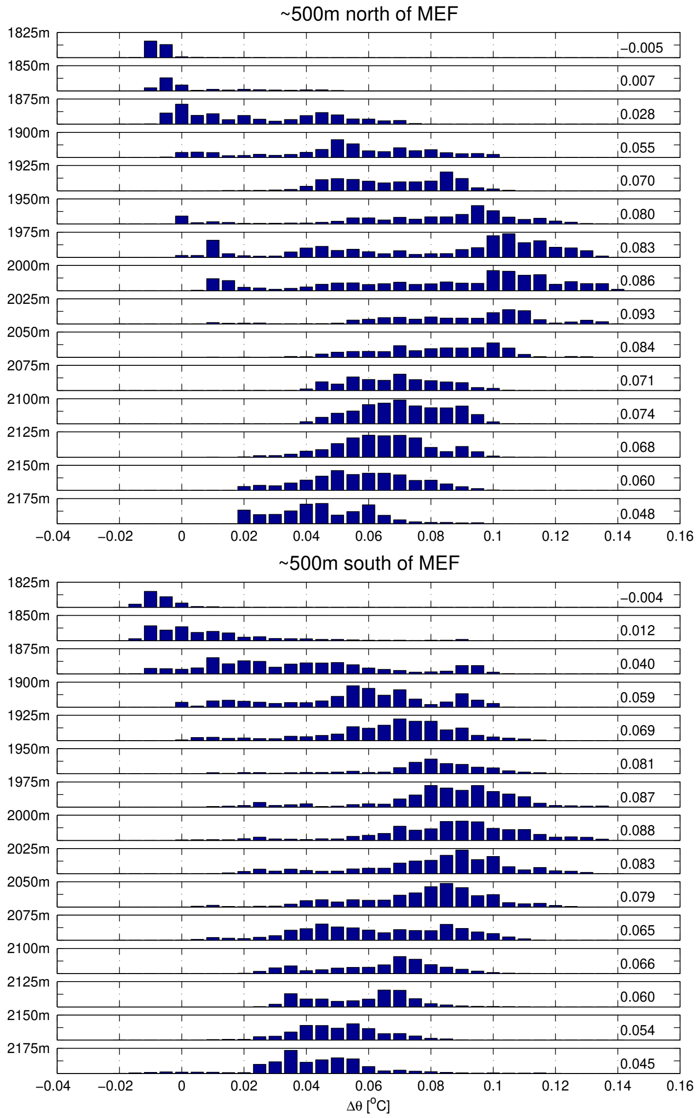

Figure 3.6: Stacked histograms of depth-binned $\Delta\theta$ observed north (upper) and south (lower) of the MEF. Depth range of each bin is 25 m and upper extent of each bin is noted on the left axis. For reference, the nearby ridge crests have a mean depth of ∼2100–2125 m. $\Delta\theta$ for each distribution is tabulated at right. North data is from CTD stations 3, 5, 10, 14, and 28, and ABE dives 45, 46, and 50; south data is from CTD stations 4, 6, 7, 12, 13, and 33, and ABE dives 45, 46, 50.

3.1.2 Horizontal heat flux estimation

The patchiness of hydrothermal plumes in the axial valley indicates thermal heterogeneity and suggests that unequal lateral fluxes through the different control surfaces are probably commonplace. In light of this variability, I use $\overline{\Delta\theta}$ from the bottom 100 m of Figure 3.6 to characterize the temperature field on the north and south surfaces of the lower Flow Mow control volume (Figure 1.3). The mean net horizontal heat flux H_h is then computed as the sum of the *mean* horizontal heat flux through the north surface ($\overline{H}_N$) and south surface ($\overline{H}_S$) via an adaptation of Equation 1.11:

$$H_h = \overline{H}_N + \overline{H}_S = \rho c_p \overline{v} A(\overline{\Delta\theta}_N - \overline{\Delta\theta}_S). \tag{3.1}$$

In this expression, the area A ($3 \times 10^4\,\mathrm{m}^2$) is assumed to be the same for both north and south surfaces. Additionally, the along-axis component of mean flow $\overline{v}$ is assumed to be identical at both surfaces. The product of the reference density ρ and heat capacity c_p is taken to be $4.2\,\mathrm{MJ{\cdot}m^{-3}{\cdot}{}^{\circ}C^{-1}}$.

An important difference between Equation 3.1 and Equation 1.11 is that here $\overline{\Delta\theta}$ is used in place of $\overline{\theta}$. This means that $\overline{H}_N$ and $\overline{H}_S$ are isohaline heat fluxes, the horizontal components of the H_{isoS} term in Equation 1.22. Since progressive vector diagrams show that v consistently dominates the across-axis component near the MEF (Figure 2.13), heat fluxes through the east and west control surfaces are assumed negligible. Consequently, the *net* horizontal isohaline heat flux H_h is the sum of $\overline{H}_N$ and $\overline{H}_S$. H_h represents the heat flux from MEF sources that leaves the control volume by horizontal advection within 100 m of the sea floor. The remaining MEF source heat flux passes vertically through the top control surface.

Using the north–south difference in $\overline{\Delta\theta}$ values from the bottom 100 m of Figure 3.6 ($0.063 - 0.056 = 0.007$°C) and the values of $\overline{v}$ observed north and south of the MEF (~1 cm/s at FM-S50 and ~5 cm/s at FM-N15), I obtain an estimate of H_h: 10–50 MW. Changing the difference $\overline{\Delta\theta}_N - \overline{\Delta\theta}_S$ by 0.001°C changes the value of H_h by 1.25 MW, while increasing the magnitude of $\overline{v}$ by 1 cm/s increases H_h by 10 MW.

The Flow Mow hydrographic survey resolved the MEF temperature field at unusually high temporal and spatial scales. Despite the thermal variability, the north and south control surfaces were sampled frequently enough, and at a wide enough range of tidal phases, to enable estimation of the *mean* net flux, H_h. However, the observations are too sparse to capture the variations of *instantaneous* net flux out of the control volume. Indeed, given the limitations of the acoustic navigation network and our instruments, it was a challenge to assess a single side and a top simultaneously. It was impossible to monitor all 4 sides and the top at once, though that ability is critical if instantaneous fluxes are sought in such variable hydrography. Consequently, I use synthetic data to understand the high variability and interpret our sparse, non-synoptic observations.

3.2 Modeled horizontal heat flux

To understand the observed hydrographic variability near the MEF and the effect of variable currents on heat flux, I model the 2-dimensional distribution of tracer from a point source subjected to a combination of advection and diffusion. The model is similar to advection/diffusion models that have been used extensively to investigate dispersion in the atmosphere (*e.g.* Pasquill 1974) and ocean (*e.g.* Csanady 1973). In particular, I use a form of advection/diffusion model common in studies of pollutant transport and known as a “puff” model (Schnell and Dey 2000).

This section begins with a description of the puff model. The model is then used to simulate the dispersion of a plume from the MEF in combinations of oscillatory and mean flow characteristic of the axial valley. The main product of the simulations is a statistical analysis of the horizontal heat flux through the MEF perimeter, and its relationship to the steady source heat flux. Finally, the observed horizontal heat flux is discussed with respect to the model results.

3.2.1 The puff model

At each time step of a puff model a “puff” of tracer is added at the source, constituting a constant flux into the model domain. The distribution of tracer in each puff is governed by the sum of 2 error functions; initially a top hat profile with half width r, the distribution quickly becomes Gaussian. As each puff ages and is advected according to the current record,

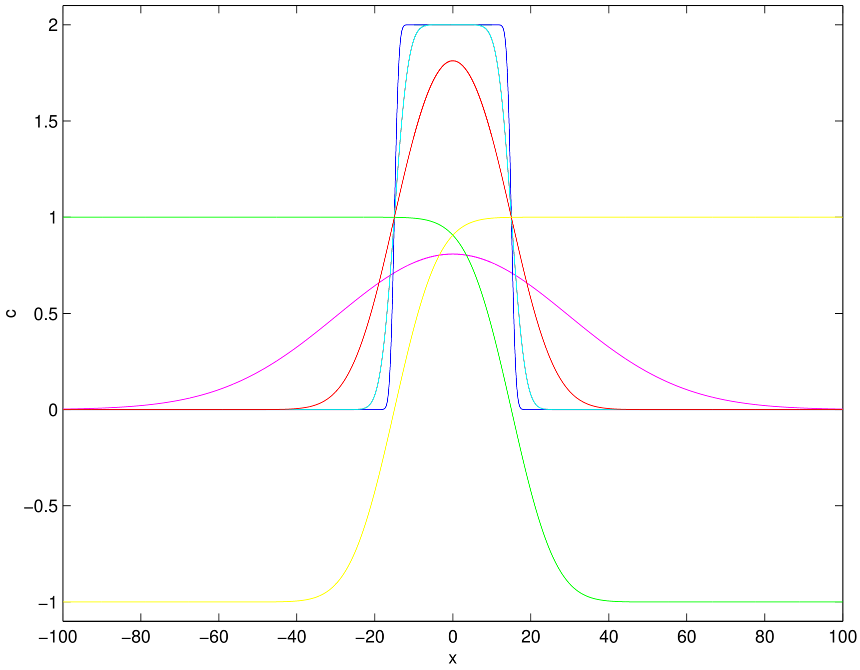

Figure 3.7: Examples of concentration c profiles for an individual puff as a function of distance x. The distribution in each dimension is governed by the sum of 2 error functions; the sum of the 2 error functions that intercept $c = \pm 1$ describes the initial top hat profile, but as the error functions evolve with time, their sum yields increasingly broad Gaussian curves. In this example, the initial half-width $r = 15$ m.

its Gaussian distribution broadens (Figure 3.7). Thus, each puff diffuses as it is advected, and the sum of all puff concentrations simulates the plume distribution. Similar "puff" models have been used to understand atmospheric plume distributions (e.g. Rao *et al.* 1989) and more recently to interpret temperature and current records from moorings near a hydrothermal field (Wetzler *et al.* 1998; Lavelle *et al.* 2001). (See related animations of plume dispersion from a diffuse hydrothermal vent, courtesy of J.W. Lavelle from NOAA's Pacific Marine Environmental Laboratory.)

The puff model domain is 4×4 km square with a horizontal grid resolution of 50 m, resulting in an 80×80 cell grid. The origin of an X–Y coordinate system is located at the center of the domain. A single source is placed at the origin and is assigned a steady heat flux. The heat flux, time step, and initial puff dimensions determine the initial temperature anomaly ($\Delta\theta_o$) of the puff. For example, a constant source flux of 300 MW delivered during a 1/2 hr time step to an initial (cubical) puff 100 m on a side (r =50 m) results in an initial uniform temperature anomaly $\Delta\theta \sim 0.1°$C. Vertical diffusivity is set to zero, so the puff thickness remains constant throughout its lifetime. Horizontal diffusivity is uniform and given a value typical of the interior ocean, $k = k_x = k_y = 0.4$ m^2/s (OKUBO 1971). For computational efficiency, puffs are eliminated if they move beyond the 4×4 km domain. To minimize rendering time and file size, only a 2×2 km sub-domain is displayed in the model animations (Figure 3.8).

In the first time step, the first puff is emitted at the source. During the next time step, it diffuses and is advected according to the spatially uniform velocity series $\mathbf{v}(t)$, reaching a new position (x_p,y_p) just as a new puff is emitted at the origin. At the end of each time step, any puff that moves beyond the 4×4 km domain are eliminated. Finally, with n puffs in their new positions, the $\Delta\theta$ contribution from each puff in the domain (at x_p,y_p) to each cell in the grid (at x,y) is computed to yield the $\Delta\theta$ distribution over the whole domain, an evolving function of time t:

$$\Delta\theta_{x,y}(t) = \sum_{i=1}^{n} \frac{\Delta\theta_o}{4} \left(\mathrm{erf}(\frac{r + \mathrm{d}x_i}{\sqrt{4k_x t_i}}) + \mathrm{erf}(\frac{r - \mathrm{d}x_i}{\sqrt{4k_x t_i}}) \right) \left(\mathrm{erf}(\frac{r + \mathrm{d}y_i}{\sqrt{4k_y t_i}}) + \mathrm{erf}(\frac{r - \mathrm{d}y_i}{\sqrt{4k_y t_i}}) \right) \quad (3.2)$$

in which t_i is the age of the ith puff, r is the initial puff half-width, $\Delta\theta_o$ is the initial puff temperature anomly, k is diffusivity, and dx_i,dy_i are distances from the center of each grid cell (x,y) to the center of each puff (x_p,y_p). After the summation is conducted for every grid cell in the domain, the $\Delta\theta$ field is visualized by coloring each cell (according to a palette that does not change between animation frames). In each subsequent time step, the value of $\Delta\theta_{x,y}$ changes when advection alters the spatial distribution of puffs and diffusion shifts the concentration contributions of individual puffs.

The instantaneous horizontal heat flux through a particular surface of the MEF control volume is found at each time step by multiplying ρ, c_p, $\Delta\theta$, the orthogonal component of flow, the grid cell width, and the initial puff height for each cell, and summing the products over all cells that make up the surface. Alternatively, the time series of $\Delta\theta$ at a particular point can be recorded and later used to compute mean $\Delta\theta$ and/or heat fluxes. Note that the summation in Equation 3.2 can be undertaken for any x,y position in the domain, not just the centers of the grid cells.

3.2.2 Modeled variance and mean magnitudes

The horizontal heat flux through the MEF control volume is studied by running the puff model with observed currents, specifically characteristic oscillations derived through harmonic analysis of the along-axis component of flow measured at the 1995 near-bottom current record (MZ25, Table 2.1). Mean flow of 0–7 cm/s is added in steps of 0.5 cm/s to the oscillatory flow in a series of simulations. Each simulation generates a unique $\Delta\theta$ field that is monitored on 4 control surfaces bounding the MEF, yielding a time series of net heat flux for each mean flow. Since the current is aligned with the east and west control surfaces in this case, only the fluxes through the north and south surfaces contribute to the net flux. These simulations reveal how flux magnitude and variance evolve as the mean flow balances and then exceeds the amplitude of the oscillations.

The time series of $\mathbf{v}$ and $\Delta\theta$ can be used to calculate 4 different types of net horizontal heat flux. (1) The $\Delta\theta$ time series can be multiplied by the corresponding current velocities to obtain a series of *instantaneous* net flux across the control surfaces. The instantaneous flux series can have extraordinarily high variance and include magnitudes surprisingly different from the steady source flux (Figure 3.8, top panel). (2) The temperature series can be averaged before multiplying by the velocity series, or (3) visa versa; this results in *temperature-averaged* or *velocity-averaged* flux series, respectively, both of which have variances and means that are different from the instantaneous flux series. Finally, the average of the instantaneous, temperature-averaged, or velocity-averaged series can be taken, yielding in all 3 cases the same (4) mean net heat flux, which must equal the magnitude of the source flux.

Analysis of these modeled flux series reveals a dependence of the net flux on the mean velocity. Figure 3.9 shows how the mean and standard deviation (σ) of the different net heat flux series (based on a ~360 hr simulation) evolve as the mean flow added to the oscillations is increased in magnitude in the puff model. The mean of the instantaneous flux series (<T v>) is 100% of the source flux (H_s) at mean flows >1 cm/s. At 0 cm/s mean flow,

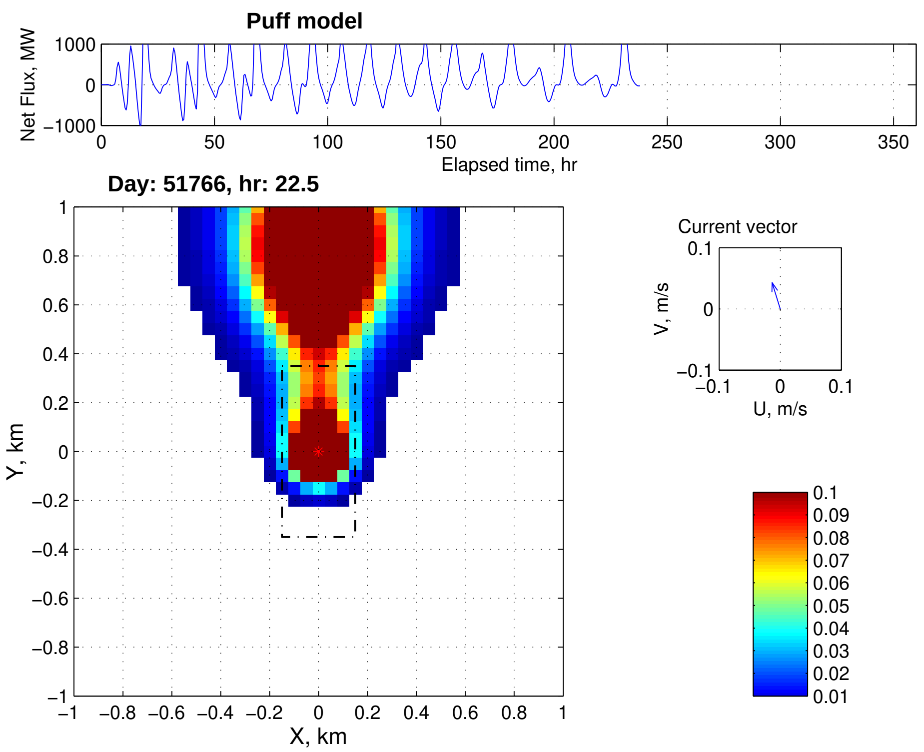

Figure 3.8: A single frame from a puff model animation showing a plan view of a thermal plume extending northward from the MEF (dashed black rectangle). In this snapshot, 240 hr into a 360 hr simulation, the puffs are advected by idealized flow (a 1 cm/s mean added to an oscillation derived by H. Mofjeld through harmonic analysis of the record from the MZ25 current meter; *c.f.* Figure 2.18.) and the source flux is constant (300 MW). Smaller panels show: time series of instantaneous net flux through the MEF perimeter (top); half-hourly current vector (middle right) with reference arrow indicating true north; and color bar with temperature anomaly units in °C (lower right). At this moment in the simulation, despite the substantial anomalies on the north surface, the net flux has dropped to zero because the flow is near zero. Animations of the puff model and Bill Lavelle's diffuse plume model are provided as supplementary material: website: econscience.org/scott/pubs/thesis/animations.html

<T v> must also be zero because the series is a product of a the (zero-mean) velocity series. At $\leqq$1 cm/s the $\Delta\theta$ gradients are so steep that $\sim$5% of the heat diffuses through the control surfaces and is not accounted for. The averaged flux series (<T>v and T<v>) have mean magnitudes (<T><v>) of $\sim$75% of the source flux at mean flows of 1–5 cm/s. This underestimation is due to averaging one of the time series prior to multiplication, and motivates the adjustment in the next section of observed H_h by a factor of $\sim 1.3 (= 1/0.75)$. The σ of the instantaneous flux series is greater than the σ of either averaged flux at all flows. In the 1–5 cm/s range of mean flow, the instantaneous σ is $\sim$100–200% of H_s. The σ of the velocity- and temperature-averaged series converge from low-flow values of 150% and 30% of H_s, respectively, to $\sim$60% of H_s above 2 cm/s. Over a range of flow typical of the MEF environment (1–5 cm/s plus characteristic oscillation), the model leads to the general expectation that flux observations near the MEF will yield averaged flux series with σ equal to 50–150% of H_s.

3.2.3 Model implications for observed horizontal flux

Since our estimates of observed H_h are essentially velocity- and temperature-averaged fluxes made in an environment where mean flow is 1–5 cm/s, the model indicates that the estimates should be adjusted upward by a factor of $\sim$1.3 (= 1/0.75). This adjustment for the uncertainty in a particular averaging procedure increases the estimate of observed H_h from 10–50 MW to $\sim$15–65 MW. Within the same mean flow range, the standard deviation of the modeled averaged flux is $\lesssim$100% of the source flux. Taking the high end of our H_h magnitudes (65 MW) as the source flux that warms the north control surface, the model results suggest that if the Flow Mow methodology were redesigned to monitor both north and south control surfaces simultaneously, then the time series of observed averaged horizontal heat flux would have a maximum standard deviation of $\sim$150% of 65 MW, or $\sim$100 MW.

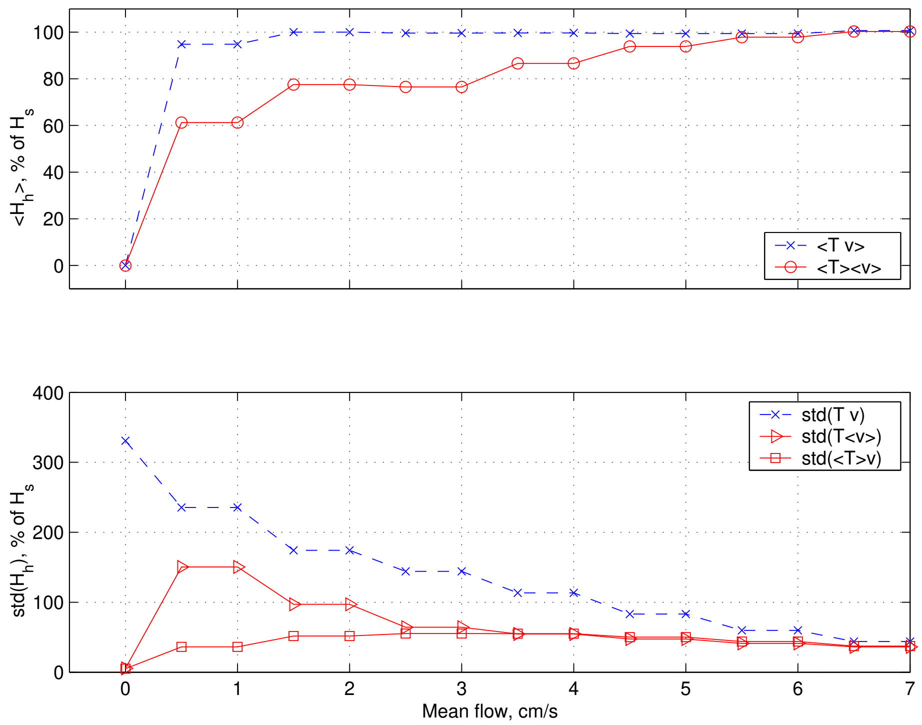

Figure 3.9: Means and standard deviations (std) of net horizontal flux (H_h) series from puff model simulations in which mean flow of 0–7 cm/s were added to characteristic oscillations. Statistics are expressed as percentage of source heat flux (H_s). Lower panel shows standard deviations of the 3 types of net heat flux *series*: instantaneous (T v), velocity-averaged (T<v>), and temperature-averaged (<T>v). Upper panel shows the mean of the instantaneous series (<Tv>) and either averaged series (<T><v>) for each mean flow.

3.3 Discussion

3.3.1 Sources of variability in MEF hydrography

We used both ABE and CTD to monitor the hydrography near the MEF, and endeavored to survey all sides of the lower control volume at multiple phases of the tide. The observed spatial heterogeneity of the plume distribution was higher than expected and increases with proximity to the MEF. Temporal variability on the north and south control surfaces was also surprisingly high. Although the north surface had greater $\overline{\Delta\theta}$ than the south surface on average, as expected in the northward mean flow, there were multiple occasions when the south $\overline{\Delta\theta}$ was greater than at the north surface.

While the puff model produces highly variable $\Delta\theta$ distributions through advection and diffusion, it does not include other possible sources of plume variability that are likely at work within the MEF. Source flux may vary, as temperature variability has been observed at some MEF vents on time scales as short as tidal periods (R. McDuff, pers. comm.), but such variations are unlikely to alter source fluxes by more than ~10%. There are multiple constant-flux sources with distinct effluent characteristics (as opposed to the single model source). Plume rise heights are not uniform (as in the model), but vary because of distinct source B and changing cross flow magnitude. Although I have documented significant coherence in the axial currents, small amounts of vertical or horizontal shear in the velocity field will affect the plume distribution and its variability, and would also influence the calculation of net heat flux. A final source of variability is the proximity of other heat sources, beyond the perimeter of the MEF. Not only is the diffusely venting Quebec area located nearby, but a major vent field, Mothra, lies upstream of the MEF. The puff model indicates that plumes from either source are likely to be advected intermittently through the MEF.

The puff model does, however, explain major aspects of the observed hydrographic patterns and variability. Model results show that tidal pooling and streaming cause dramatic plume non-uniformity and net heat flux variability (Figure 3.8), even when the plumes are advected in idealized, exclusively along-axis oscillating and mean flow. Modeled plume heterogeneity and variability are even higher in 2-axis currents. Diffusion, likely enhanced in bottom boundary layers within the axial valley (Thomson *et al.* 1989), reduces plume heterogeneities over time. Acting in concert, advection and diffusion distribute thermal anomalies that are reduced in intensity and more uniform away from hydrothermal sources. On the periphery of hydrothermal fields observed and modeled $\Delta\theta$ magnitude increases.

Overall, advection and diffusion generate a $\Delta\theta$ distribution that complicates the task of measuring the net flux from a vent field. If mixing rates were greater or there were no mean flow, then the valley would eventually acquire a uniform hydrothermal anomaly that could be more easily inventoried. The observed complexity of the hydrography in the valley suggests that the most successful efforts to measure field-scale fluxes will be those that correctly establish and simultaneously monitor up- and downstream positions over many tidal cycles, or otherwise integrate the variability induced by the tides, and then use a sophisticated model to help interpret the results.

The high spatial and temporal heterogeneity in the observations are not resolved by the puff model with a single source, but are both likely caused by *multiple and distinct* MEF sources venting into variable cross flow. The distribution of hydrothermal sources within the MEF is certainly more complicated than a single central source (Figure 2.6). Studies of fluid properties at focused vents evidence higher T and lower S at southern vents compared to northern vents (Butterfield *et al.* 1994). During the summer of 2000 all MEF sources had negative salinity anomalies (ΔS): -9 to -14 psu for high B sources in the south part of MEF; -4 to -8 psu in northern high B vents; and about -0.5 psu for low B vents in general (D. Butterfield, pers. comm.).

Numerical models of diffuse plume rise (J.W. Lavelle, pers. comm., see caption of Figure 3.8) indicate that in typical stratifications, vents with negative ΔS, no matter the magnitude of their positive source $\Delta\theta$, will produce plumes that separate from the sea floor downstream of the source. When the source properties (measured S and T, and estimated w and A) are used to quantify a range of B for MEF low T vents, and the results are used to initialize the plume rise models (along with a reasonable range of environmental conditions, namely the buoyancy frequency, N, and cross flow velocity, U), the range of expected rise heights and plume thicknesses creates significant temperature anomalies at elevations of 15–35 m for $\Delta S = +0.5$ psu and 20–90 m for $\Delta S = -0.5$ psu. In cross flow of 5 cm/s the modeled plumes equilibrate $\lesssim$250 m downstream of their source. While plumes from some low B vents have been observed to hug the sea floor (tri ; RONA *et al.* 1997), the plumes from slightly fresh MEF diffuse sources are expected to separate from the sea floor and be nearing equilibration >15 mas by the time they cross the Flow Mow control surfaces. These plumes may even rise through the top surface of the control volume (at 100 mas) during periods of low cross flow, if they are not first entrained by high B plumes.

The behavior of focused hydrothermal plumes in uniform cross flow has been modeled both analytically (MIDDLETON and THOMSON 1986) and numerically (LAVELLE 1997). With some approximation of the typical in-valley stratification, plumes from MEF focused sources (with the observed range of source S and T) are expected to rise anywhere from 200 m in nearly quiescent conditions (1 cm/s cross flow) to 100 m in typical peak MEF cross flows of 10 cm/s (~5 cm/s mean flow combined with ~5 cm/s oscillatory flow). Although measurements of 20 cm/s peak cross flows are rare in the 1995 and 2000 records (~1 event in 20 days), focused plume rise during such flow could be reduced to ~50 m.

These predictions suggest that plumes from both diffuse and focused MEF sources may be bent over and dispersed in complex patterns at multiple depths by cross flow, but are unlikely to equilibrate outside of the depths monitored during Flow Mow. Taken together, the lower and upper Flow Mow control volumes (Figure 1.3) span from ~10–400 mab, or ~2190–1800 m depth. The only unmonitored area of the lower control surfaces was within 5–10 mab, a gap that was avoided to prevent equipment collision with the sea floor. With respect to measuring heat flux, if plumes and currents were uniform from 0–100 mab, the error introduced from not monitoring the gap would be 5–10%. Given MEF source fluids properties (*c.f.* Table 1.1), however, modeled plume rise heights suggest that the heat flux through this gap is negligible compared with the flux through the control surfaces in the 5–100 mab depth range.

The small-scale heterogeneities observed at different depths on the control surfaces probably originate when diffuse sources with different B and depth (10–15 m vertical separation) vent into a mean cross flow, generating plumes with distinct rise heights. When tidal oscillations also influence the dynamics and distribution of plumes, high temporal variability becomes the norm, especially when observations are made close to the hydrothermal sources.

During peak cross flows, even plumes from high B sources may bend over far enough to transit the upper 1/2 of the side surfaces of the lower control volume.

3.3.2 Corrections to horizontal and vertical heat flux estimates

The heterogeneous hydrography observed within the axial valley implies that the fluid entrained by rising MEF plumes may have variable temperature. This complicates the interpretation of heat flux measurements made on the top surface of the Flow Mow control volume because relating measured anomalies to source heat flux through 1-dimensional plume theory requires an assumption of a unchanging background θ–S relationship in the entrained fluid.

However, the consistent northward flow within the axial valley means that fluid entrained by MEF plumes enters the field predominantly through the south side of the control volume. The mean $\Delta\theta$ of the fluid as it enters the lower Flow Mow control volume within 100 mab is $\overline{\Delta\theta}_S \simeq 0.05°$C. As with the horizontal isohaline heat flux H_h in Equation 3.1, the vertical isohaline heat flux H_v can be calculated by subtracting $\overline{\Delta\theta}_S$ from the mean $\Delta\theta$ measured on the top surface ($\overline{\Delta\theta}_v$) by ABE:

$$H_v = \rho c_p A_v w(\overline{\Delta\theta}_v - \overline{\Delta\theta}_S) \tag{3.3}$$

where w is vertical velocity and A_v is the area of the top surface. Equation 3.3 yields $H_v = 550 \pm 100$ MW for observed w and $\overline{\Delta\theta}_v$ (Stahr *et al.* 2003) and involves the assumption that fluid entrained at any depth within ~100 mas has the same average T and S. This assumption is justified partially by the observation of intermittent well-mixed layers < 50 mab. and partially by the observation during horizontal CTD tows through the MEF at depths of 30–60 mas that the $\Delta\theta$ between buoyant plumes is consistently $0.05 \pm 0.02°$C (*c.f.* Section 2.5.3). Altering the value of $\overline{\Delta\theta}_S$ by $0.01°C$ changes the vertical flux estimate by ~10 MW.

Prior to comparing Flow Mow heat flux estimates with historic estimates (in the next section, and in Chapter 5), the isohaline heat fluxes H_h and H_v (calculated with $\Delta_S\theta$) must be converted to level heat fluxes H_h^* and H_v^* (calculated with $\Delta_z\theta$) in accordance with

Equation 1.24. Multiplication of H_h =65 MW and H_v=550 MW by the correction factor $C = 1.17$ yields $H_h^* = 76{\pm}114$ MW and $H_v^* = 643{\pm}116$ MW, respectively.

3.3.3 Partitioning of power

Best estimates of H_h^*, H_v^*, and H_f can be used to infer how MEF heat flux is partitioned between focused and diffuse vents. This is accomplished by assuming that the net heat flux through the sea floor ($H_f + H_d$) into the lower control volume (*c.f.* Figure 1.3) is equal in magnitude to the net heat flux out ($H_v^* + H_h^*$). The assumption leads to an expression for the steady state heat budget in the lower Flow Mow control volume (Figure 1.3) in which all heat fluxes are based on level-to-level potential temperature anomalies ($\Delta_z\theta$):

$$H_d + H_f = H_v^* + H_h^*. \tag{3.4}$$

To calculate H_d, the heat flux from diffuse sources, I take $H_f = 615{\pm}123$ MW, the best estimate of GINSTER *et al.* (1994) (*c.f.* Section 1.3). This value of H_f has the advantage of a relatively low, well-determined uncertainty (20%) and is near the middle of the range of H_f (359–1224 MW) estimated by BEMIS *et al.* (1993). A limitation of this approach is that H_v^* and H_h^* are based on measurements made in 2000, while H_f is based on measurements made in 1988. Since more recent independent estimates of H_f are not available for the MEF, I proceed with these values. Solving Equation 3.4 for H_d and substituting $H_f = 615{\pm}123$ MW along with the Flow Mow estimates of $H_v^* = 643 \pm 116$ MW and $H_h^* = 76 \pm 114$ MW yields $H_d = 104{\pm}253$ MW. This magnitude of H_d is close to the preliminary results of JOHNSON *et al.* (2002), in which point measurements of vertical heat flux in diffuse vents were extrapolated to the total area of diffuse flow within the MEF, mapped by acoustic scintillation tomography, generating an estimate of $H_d \sim 150$ MW.

Thus, MEF heat flux is inferred to be partitioned between diffuse and focused sources in a ratio of 104:615, or about H_d:H_f =1:6=0.17. This partitioning of power contrasts with the idea that diffuse flux generally dominates focused flux in a ratio of about 10:1 in the MEF (SCHULTZ *et al.* 1992), 10:1 in the ASHES vent field at Axial volcano (RONA and TRIVETT 1992), or 2:1 in the north Cleft vent field on the Juan de Fuca ridge (BAKER *et al.* 1993). Given the combined standard uncertainty of the inferred value of H_d (50%) and the uncertainty in the best estimate of H_f (20%), the ratio H_d/H_f could be as high as 0.72 $(= (104 + 253)/(615 - 123))$. Such a value would be comparable the ratios of about 1:1 inferred by Lavelle *et al.* (2001) at Axial sea mount further south on the Juan de Fuca ridge.

Assuming that only diffuse sources are responsible for the observed horizontal flux $H_h^* = 76\,\mathrm{MW}$, then an additional implication of H_d having a magnitude 104 MW is that roughly 1/4 of H_d is entrained into rising plumes within the MEF perimeter. The other $\sim 3/4$ must escape the field laterally.

Chapter 4

PLUMES AND HEAT FLUX ABOVE THE RIDGE – MULTIDIRECTIONAL FLOW

Above the Endeavour ridge, multidirectional mean flow and amplified oscillations constitute the currents near the equilibration depths of hydrothermal plumes from high B sources. Accurate quantification of heat flux in this type of flow is operationally more difficult than in the axial valley where the flow is rectified and dominated by the semi-diurnal tide (Chapter 3). Fundamentally, 4 side surfaces must be accounted for instead of 2, meaning that there is approximately twice the observational demand during any given oscillation. Faster speeds, shifting directions, and amplified oscillations at multiple frequencies conspire to generate more variable plume distributions and heat fluxes.

During investigations of equilibrated plumes above ridge crests, plume distributions are often described as more variable or unpredictable than expected. The assumption of a unidirectional long-term mean flow and an anticipated downstream direction complicated the experiment of Rosenberg *et al.* 1988; the Endeavour plume distribution was judged steady enough to assess the standing stock of radon only during ~5 of the 23 days devoted to the assessment. During the 1995 Mixing Zephyrs field program (bromide.ocean.washington.edu/zephyr) a regional hydrographic survey of 48 VOTs above the Endeavour segment revealed a plume distribution that was generally centered over the MEF, but extended in different directions on different days (Veirs *et al.* 1999). While the plume was often elongated to the southwest, it was intermittently absent in the southwest quadrant and present in the southeast or northeast quadrants. Equilibrated hydrothermal plumes with laterally continuous distributions on scales of ~10 km have been observed ~5 km from known sources in rotary flow on the southern Juan de Fuca ridge (Baker and Massoth 1986), but over the Endeavour segment the plume distribution commonly changes on weekly (Kadko *et al.* 1990) to hourly time scales. As will become evident in this chapter, plume variability and inhomogeneity appears to be the norm above the ridge crests within a few km of the MEF. The "patchiness" of the Endeavour plume (Franks 1992, page 203) has complicated the analysis and interpretation of results from studies of the downstream evolution of plume properties (*e.g.* McLaughlin 1998).

Efforts to measure the heat flux from hydrothermal fields or ridge segments by intercepting equilibrated plumes have historically generated results with large formal uncertainties (*e.g.* Baker and Massoth 1987, Thomson *et al.* 1992). While some sources of uncertainty are peculiar to the methods of each study, I posit in this chapter that the pooling and streaming of plumes in multidirectional flow generates a level of hydrographic variability that is commonly observed over Endeavour ridge and is probably responsible for the wide-ranging estimates of MEF heat flux.

This chapter begins with a presentation of hydrographic observations made above the ridge crests during the Flow Mow study, focusing on spatial and temporal variability of plumes. With a subset of the observations, I estimate the net horizontal heat flux through the upper control volume (Figure 1.3). I then use a puff model to study how plumes disperse in multidirectional flow above the ridge. The model results guide the interpretation of the hydrographic observations and also indicate how measured heat flux precision increases with longer observation periods. Finally, I compare the observed net horizontal heat flux through the control surfaces of the upper Flow Mow control volume with the vertical flux into the volume measured by Stahr *et al.* (2003). This leads to a discussion of sources of uncertainty in horizontal fluxes estimated above the ridge in this chapter, as well as in previous Endeavour endeavors.

4.1 Observations above the ridge crests

While ABE operated exclusively below ∼2100 m depth throughout the Flow Mow study, the majority of the CTD casts extended from within a few meters of the sea floor up to ∼1800 m, well above the maximum rise height for typical MEF plumes. The upper 300 m of these casts provide insights into the distribution and dynamics of Endeavour plumes that have risen out of the axial valley. As mentioned in the previous chapter, these upper-level plumes either originate directly from high B sources, or represent plumes from low B sources that have been entrained into higher-rising plumes.

In this section, I characterize the spatial and temporal variability of plumes near the upper Flow Mow control volume using 3 basic types of CTD stations. First, I present time series from the NoMEF and SoMEF areas (Figure 2.5), including VOTs and VOCs from 1800–2200 m. Then I describe VOTs along the north and south side surfaces of the control volume, also from 1800–2200 m. The last suite of observations is a series of 5 circumnavigations of the control volume perimeter accomplished with a slow ($\sim$0.1 m/s ship speed) VOT from 1850–2070 m. This $\sim$24 hr "ribbon" of data around the MEF, acquired despite being particularly mind-numbing for the winch operators and mates, resolves changes in plume distribution on hourly time scales and 50 m lateral scales.

4.1.1 Time series north and south of the MEF: 1800–2200 m

It was particularly exciting to collect the long time series from the NoMEF and SoMEF areas $\sim$500 m north and south of the MEF (Figure 2.5, *c.f.* Section 3.1.1) because even at sea it was apparent that the hydrographic variability was surprisingly high and had some tidal periodicity. Figure 4.1 shows the $\Delta\theta$ and backscatter data from all CTD stations in the 2 areas, over the full depth range of 1800–2200 m. The most prominent features of the hydrographic evolution are the sharp upper boundary, the relatively warm, particle-rich waters centered near 2000±100 m, and the underlying cooler, clearer fluid within $\sim$100 m of the valley floor.

The upper boundary of the plume, defined by steep vertical gradients in $\Delta\theta$ and backscatter, occupies a mean depth of $\sim$1890 m, both north and south of the MEF. The mean depth varies temporally, however, with an amplitude of $\sim$25 m. During the long stations (28 and 33) the boundary undulates vertically with an approximate period of 12 hr, implying that the depth of the upper boundary is related to the semi-diurnal tide. The currents recorded at the uppermost meter on the southern mooring (FM-S250, 1942 m, Table 2.1) are indeed dominated by semi-diurnal oscillations during both station 28 and 33, but there is no obvious correlation of boundary height and hourly mean velocity. At station 28, for

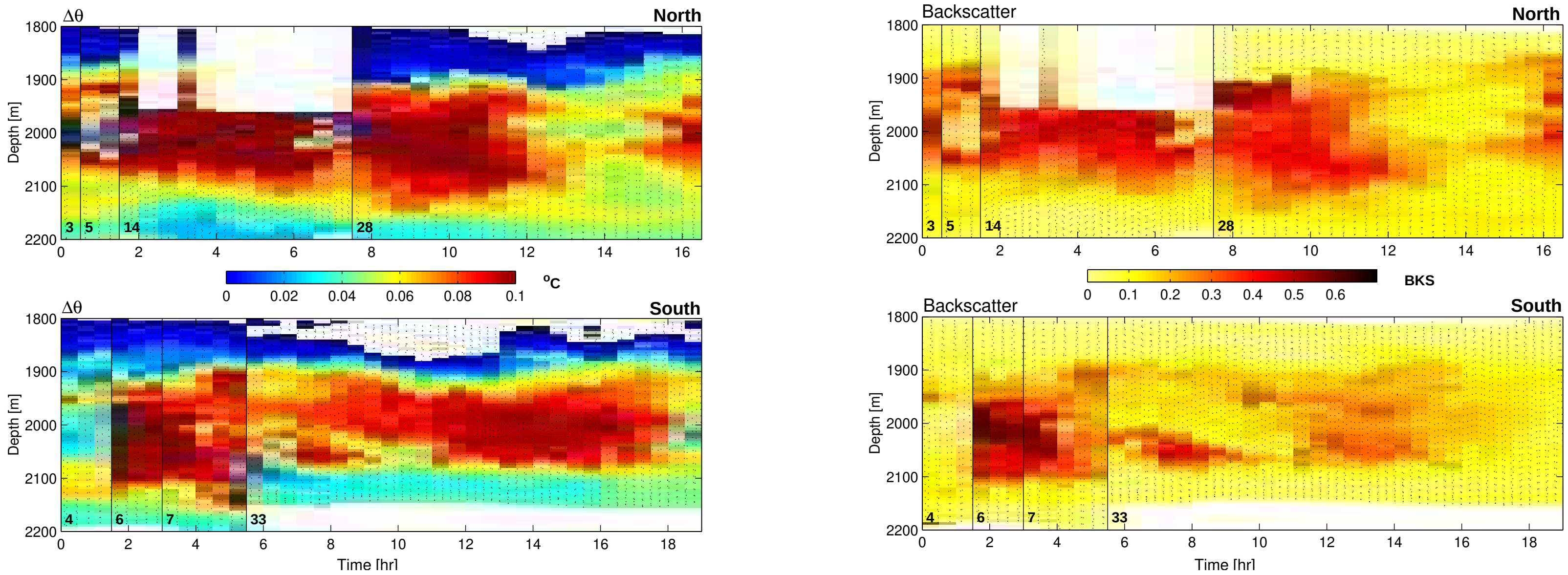

Figure 4.1: Time series of spatially and temporally averaged $\Delta\theta$ (left) and backscatter (right) from CTD surveys of the NoMEF (upper) and SoMEF (lower) areas. Dotted black line is CTD track. Averaging bins are 1/2 hr wide and 5 m high. Vertical black lines mark temporal breaks (~1-5 days) between stations, each of which is numbered in lower left corner. White areas have no data (or $\Delta\theta < 0°$C). See Figure 3.4 for additional notes and $\Delta\theta$ detail in bottom 100 m.

example, the upper boundary reaches high points at 2.5 and 8 hr elapsed time, when the flow at the FM-S250 was 5 cm/s southeast and 10 cm/s southwest, respectively; at the intermediate low near 4.5 hr, the flow was 7 cm/s southwest. While plume theory suggests that rise height will be reduced in faster cross flows (Middleton and Thomson 1986), the maximum and minimum elevations of the upper boundary occurred at similar mean flow speeds. Of course, a straightforward correlation should not be expected because the 500 m lateral distance between known sources and the monitoring stations could result in lags of order $\sim$(500 m)/(0.05 m/s)$\sim 10^4$ s, or about 3 hr. An additional reason to not expect direct correlations is that the flow history can juxtapose plumes that experienced different conditions while reaching equilibrium.

The temporal evolution of the warm, particle-rich plume centered near 2000 m is a manifestation at NoMEF of vent fluid advected from either the MEF or High Rise fields and background water brought in from off-axis. The puff model with flow determined by the record from FM-S250 simulates the combined effects of flow history and lateral separation of hydrothermal source and hydrographic station. For example, the simulation shows that prior to station 28 the upper level flow was exclusively to the south and brought a plume from High Rise (Figure 2.1) to the NoMEF vicinity. (Station 28 occurs from MJD 51771, 20.4 hr and MJD 51772, 6.5 hr in the animation.) As station 28 began (Figure 4.1), the High Rise plume was advected westward by 10 cm/s flow. As the plume intensity decreased at NoMEF in response, the flow decreased to near-zero. The flow then increased to 7 cm/s south-southeast, ultimately delivering another pool of warm, particle-rich fluid from High Rise to the NoMEF area near the end of the station. Interpreted with respect to this flow history, it is plausible that the maximum observed elevation of the upper plume boundary was attained (above a high B High Rise source) when the cross flow was near zero.

A similar progression of flow from south to west and back to south occurred just before and during station 33 (MJD 51774, 2.5 hr and MJD 51774, 17 hr in the animation). Results from the puff model, with flow determined by the record from FM-S250 and a single source at MEF, indicate that the SoMEF area (Figure 2.5) should have been swept free of MEF plume about midway through the station during the period of westward flow, but the observed plume intensity increases during this period. With the flow determined by the observed current record from FM-S200 or FM-S150 (1992 or 2042 m, respectively), however, the area is swept free for a briefer period. The intensification of the observed plume during the period of flow to the west-northwest could be explained if a source existed to the east-southeast of station 33. Hydrographic evidence of such a source was gathered in 1995 (Veirs *et al.* 1999) and confirmed during Flow Mow CTD surveillance between MEF and Mothra. This example illustrates the limitations of using the puff model with a single source to predict or interpret plume distributions. The modeled distribution can be altered substantially by subtle changes in the input velocity field, the addition of a source, model resolution, and level of diffusivity. For these reasons, I use the puff model primarily to study the statistics of plume variability (*c.f.* Section 4.3).

One of the major features of the plume centered near 2000 m is that it is usually present and about 200 m thick, but is intermittently replaced with near-background cold, clear fluid. Specifically, plume intensity decreases during stations 4 and 5, at the end of 14, the middle of 33, and the beginning and end of station 33. A simple explanation for this variability comes from the puff model. Though it may not simulate the plume distributions exactly, it does demonstrate that a point source venting steadily into the typical flow above the ridge generally gives rise to a heterogeneous distribution of plume and ambient fluid.

Another feature of the central plume is its vertical heterogeneity. Particularly during station 5 and the beginning of stations 33 and 28, there are distinct layers in the central plume. Throughout station 5, similar upper and lower plume layers are separated by background fluid. During the first 2 hours of station 28, the upper portion of the plume has a backscatter–$\Delta\theta$ ratio that is distinctly higher than the lower portion of the plume. A similar layering is evident in the first 5 hours of station 33, but the lower plume is both warmer and richer in particles than the upper plume. These sorts of spatial variations are likely responsible for the multiple trends observed in scatter plots of $\Delta_\rho\theta$ versus light attenuation data from Endeavour plumes (Baker and Massoth 1987, Figure 5) and from plumes within 1 km of the MEF (Thomson *et al.* 1992, Figure 4). While the distinct trends have been attributed to vents with distinct source temperatures and chemistries, in the case of station 28, the puff model indicates that the responsible sources were probably all located within the High Rise field.

A final important feature of both time series in Figure 4.1 is that the anomalies of both θ and backscatter in the lower depths ($\sim$2100–2000 m) are not clearly correlated with the θ and backscatter anomalies in the overlying plumes. Station 14 exhibits an intense, uniform upper plume, but some of the smallest anomalies observed in the lower layer. Station 28 shows a similar anti-correlation, to some extent, with the least intense upper plume near hour 14 accompanied by some of the largest anomalies in the lower layer. These anti-correlations might be expected given the sheared flows between the 2 depth ranges and the likelihood that plumes in the 2 layers originate from different points on the sea floor. In contrast, stations 3–7, the end of 28, and the first half of station 33 exhibit trends in anomalies that are similar in both the upper and lower layers. These positive correlations support the idea that anomalies in axial valley water are enhanced, at least intermittently, by downward fluxes of heat, salt, and/or particles from plumes passing overhead.

The differences in particle concentration profiles from the NoMEF and SoMEF areas can be further illustrated with depth-binned histograms of the backscatter data (Figure 4.2). In the bottom 100 m the fluid is more uniformly clear south of the MEF. At both NoMEF and SoMEF, backscatter values in the overlying plume are higher than near the bottom. The peak values tend to occur higher in the water column north of the MEF, a pattern that is evident in Figure 4.3, as well. The mean values between 1900–2100 m, however, are similar between NoMEF and SoMEF, suggesting that the difference in backscatter values near the bottom is not due to a greater downward flux of settling hydrothermal particles at NoMEF than at SoMEF. An alternative possibility is that hydrothermal particles (mineral or biological) in diffuse or focussed plumes from MEF sources are predominantly transported northward by the mean flow in the bottom 50–100 m. This interpretation is consistent with the average pattern of near-bottom $\Delta\theta$ being higher at NoMEF than at SoMEF.

4.1.2 North and south control surfaces: 1800–2200 m

Figure 4.3 showcases the south and north control surfaces during 3 separate navigated CTD stations (10–13), each a VOT that traversed the surface 1–5 times from 1800–2200 m (*c.f.* Section 3.1.1). Note that these surfaces extend from above the ridge, higher than

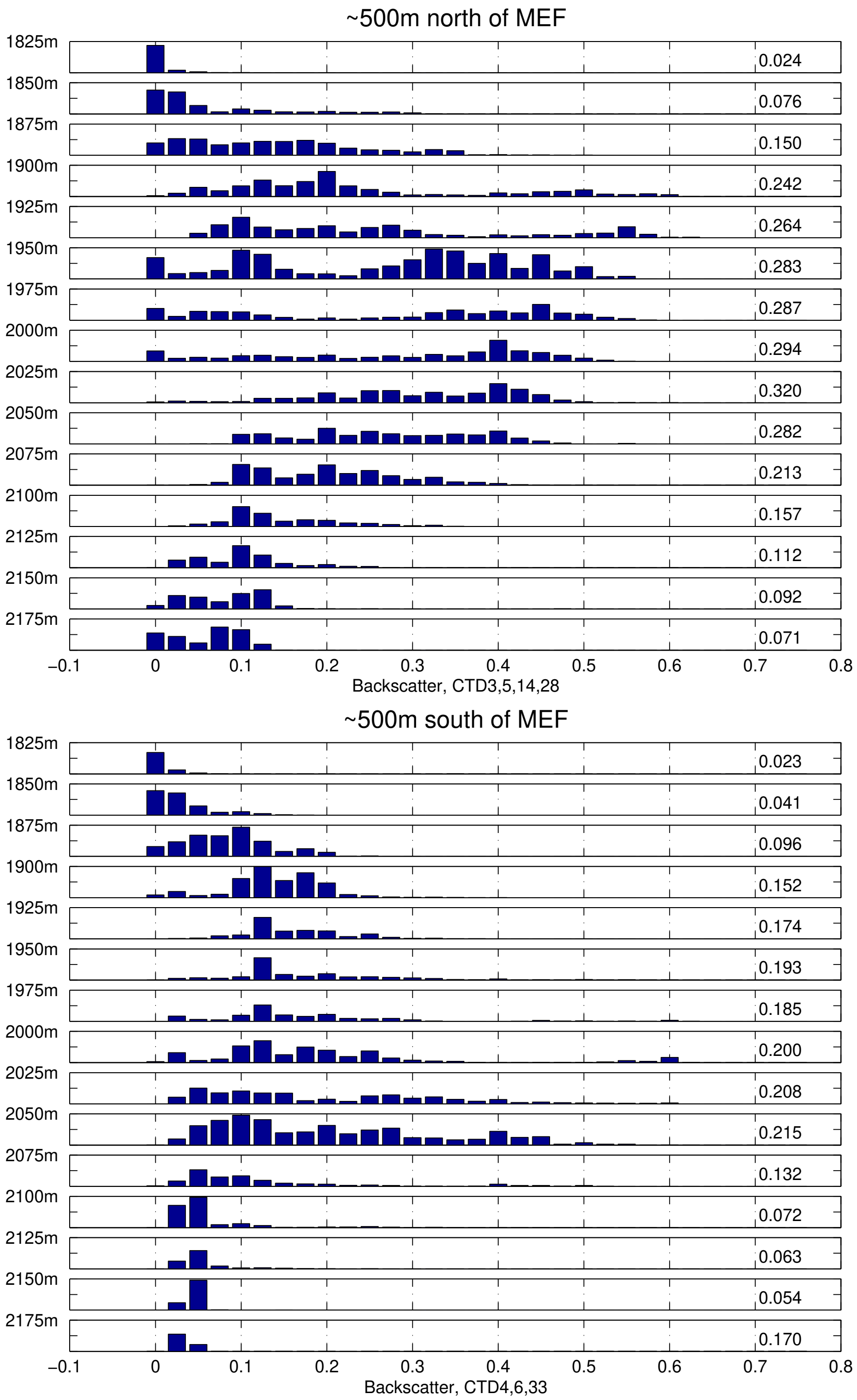

Figure 4.2: Histograms of all backscatter data from the NoMEF (upper) and SoMEF (lower) areas (Figure 2.5), except station 7, binned in depth intervals of 25 m. Mean values of distribution in each bin are listed at right.

typical rise heights of MEF high B sources, to within the axial valley, $\lesssim$5 m above the sea floor. This depth range spans the observed vertical shear between the axial valley flow and the currents above the ridge crests.

Closer to the MEF, the observed $\Delta\theta$ and backscatter fields on the north and south control surfaces in Figure 4.3 reveal a similar pattern of a sharp upper plume boundary, a 100-200 m thick plume, and an underlying layer of cooler, clearer fluid (Figure 4.3). But the spatial horizontal and vertical heterogeneity is noticeably increased compared to levels observed on VOTs through the more distant SoMEF and NoMEF areas. On these surfaces, laterally offset just 100–200 m from the MEF high B sources, background fluid is often interspersed with intense plumes near the equilibration depths. In such cases, observed across-valley gradients ($\mathrm{d}\Delta\theta/\mathrm{d}x \simeq 0.1/50 \sim 2\times10^{-3}\,^{\circ}\mathrm{C/m}$) begin to rival vertical gradients ($\mathrm{d}\Delta\theta/\mathrm{d}z \simeq 0.1/10 \sim 1\times10^{-2}\,^{\circ}\mathrm{C/m}$). The upper plume boundary is again quite consistent, $\sim$1870$\pm$20 m, but is slightly shallower on average than observed during the NoMEF and SoMEF time series. It is poorly defined on some surfaces (stations 10#1, 12#2, and 12#3) and exceptionally sharp during station 13.

The main plume between $\sim$1850–2150 m is remarkably less homogeneous than in the time series from the more distant NoMEF and SoMEF stations. On all surfaces except station 13, not only does the main plume contain finer scale heterogeneities (order 10 m thick and 50 m wide), but also it is more layered and laterally patchy at scales of 50–100 m. During station 12, background fluid is more prevalent on the west edge of the southern surface, while on the northern surface (station 10), background fluid is more common on the eastern edge. In general, the plume distribution on the northern surfaces is less continuous, both laterally and vertically. Consequently, the mean $\Delta\theta$ on each of the northern surfaces is lower than the mean on any of the southern surfaces. This is consistent with the pattern predicted by the puff model. Station 10 occurred during a transition from southward to westward flow in which the model suggests plumes from High Rise were advected through the western side of the northern MEF control surface. A few hours later, the upper level flow was unidirectional and to the south-southeast during station 12, bringing the MEF plumes through the south surface and resulting in elevated mean values. The next day, south-southwest flow before and during station 13 caused the maximum observed mean

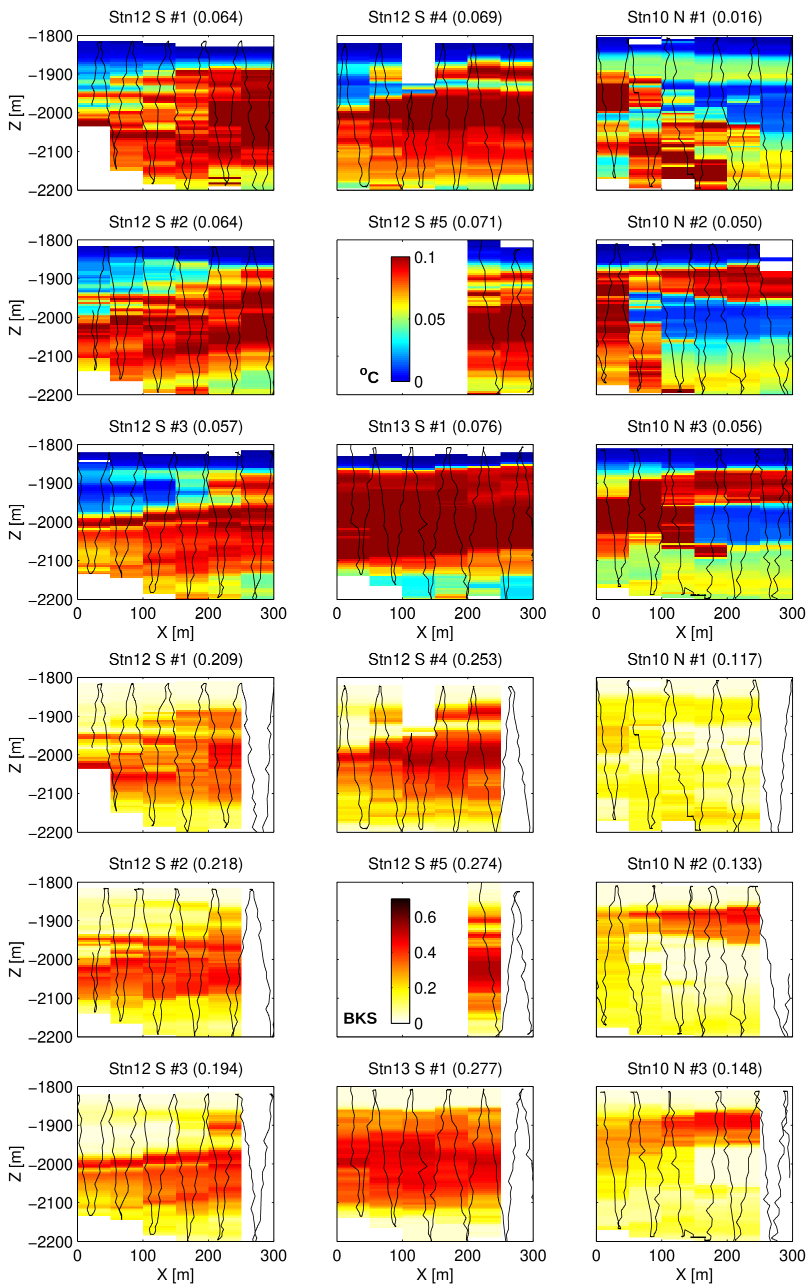

Figure 4.3: $\Delta\theta$ (upper panels) and backscatter (lower panels) distribution on north and south MEF control surfaces: 1800–2200 m. Left 2 columns depict surveys of south surface; right column depicts surveys of north surface. Each survey is labeled with: its station number; its order in the sequence of surfaces surveyed during that station (*e.g.* 12#3 is the 3rd surface observed during station 12); and the mean value of $\Delta\theta$ or backscatter (noted parenthetically). White areas have no data (or $\Delta\theta < 0$); black lines are CTD track. Central color scales give values.

values in Figure 4.3.

With increasing proximity to the MEF, the lower layer is thinner and warmer than at the more distant stations. While the backscatter data generally suggest the overlying plume is still separated vertically from the sea floor by 50–100 m, the $\Delta\theta$ data from station 12 indicate the separation on the south surfaces is only 10–40 m. In some places, near-bottom anomalies make the lower layer ill-defined (*c.f.* section 3.1.1). During station 13 a cooler, clearer layer is evident and separation is closer to 50–100 m. On the north surfaces a lower layer (2050–2200 m) is warm and particle rich relative to the overlying background fluid on the east edge, but essentially continuous with the overlying plume on the west edge. Additionally, the north surfaces are distinct from most of the south surfaces in that the $\Delta\theta$ increases into the bottom along a greater portion of their bottom edge.

4.1.3 Consecutive surveys of the MEF perimeter: 1800–2070 m

At the end of the Flow Mow field program, the perimeter of the upper control volume was slowly circumnavigated counterclockwise ~5 times during a ~24 hr VOT. The VOT focused on the depths from 1850–2070 m in an effort to intercept equilibrated or equilibrating MEF plumes. During the same period, ABE surveyed the top surface of the lower control volume near 2110 m, acquiring 2 estimates of the vertical heat flux (Stahr *et al.* 2003).

In this section I present the data from the circumnavigations. In the following section the observations are used to assess the net horizontal heat flux through the upper control volume, which is then compared to the vertical heat flux input from below.

Figure 4.4 displays the 5 circumnavigations, illustrating the spatial and temporal variability in $\Delta\theta$ on the 220 m tall side surfaces (1850–2070 m) of the upper control volume (Figure 1.3). Overall, the temporal variability is high and suggestive of semi-diurnal oscillations, with sequential surveys of particular side surfaces often showing dramatic changes in plume distributions despite being separated by only 4–4.5 hr. The north surfaces, for example, alternate between near background fluid at all depths and laterally-continuous plumes with peak $\Delta\theta$ values that are comparable to the highest values on the west, south, or east surfaces. A single south surface is also nearly completely plume-free, while the previous and

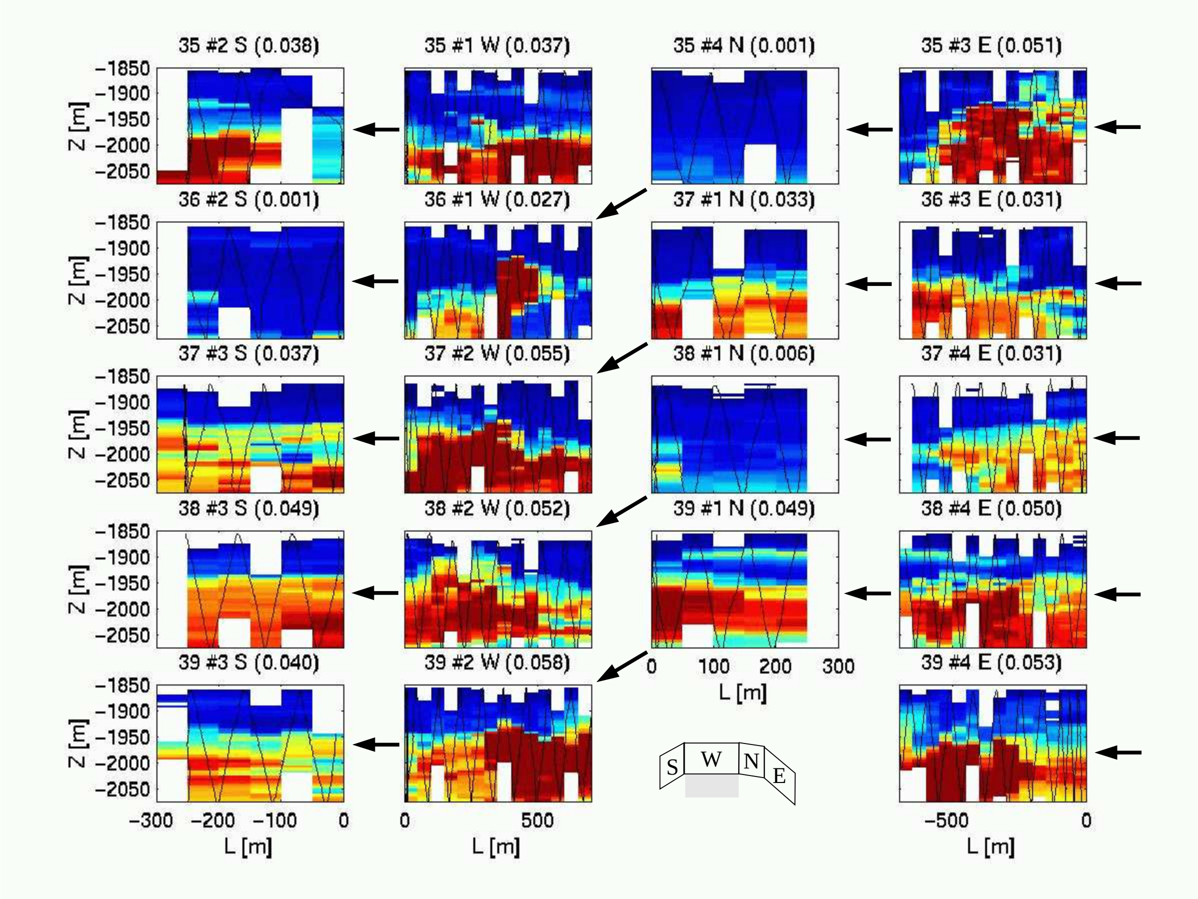

Figure 4.4: $\Delta\theta$ observed during 5 counterclockwise circuits of MEF perimeter starting on the west surface during station 35 and oscillating through 1850–2070 m. Data are projected orthogonally onto control surfaces (width L is 300 or 700 m, height Z is 225 m) and averaged in grid cells that are 50 m wide and 5 m tall. The south, west, north, and east side surfaces are displayed as if a continuous ribbon were broken at the southeast corner of the MEF and folded open (see schematic at bottom). The title above each surface labels: the CTD station number (35–39); the number of the surface surveyed sequentially during each station; the cardinal direction of the surface (S, W, N, or E); and the mean $\Delta\theta$ (noted parenthetically). Each column constitutes a time series of the same surface, with temporal separation of ∼4–4.5 hr. Color scale is the same as in Figure 4.1. Black line is the CTD track.

following surveys of the same surface (~4.5 hr before and after) are dominated by plumes. The east and west surfaces are comparatively consistent between surveys. Both tend to have higher mean $\Delta\theta$ than the north and south surfaces, and the west surfaces have the highest mean $\Delta\theta$, overall.

The upper boundary of the plume is deeper and more variable than in Figures 4.1 and 4.3, with a mean depth of $\sim$ 1950±40 m. On some surfaces the plume is homogeneous (surfaces 38#3 and 39#1), while on many it is horizontally and vertically patchy (*e.g.* surfaces 37#3–4). On surface 36#1, the main plume is almost as narrow as it is thick, ~100 m, and surfaces 38#4 and 39#1 captured an unusually thin plume near 1900 m that is clearly separated from the underlying plume.

On each surface that is free of major plumes the bottom edge is relatively warm. At a depth of 2070 m the bottom edge is near the depth of the west ridge crest adjacent to the MEF (Figure 2.4), but is not within the axial valley. Thus, higher $\Delta\theta$ values along the bottom edges of the upper control volume surfaces suggest that fluid near the top of the axial valley is heated in part by a source other than overlying plumes. Currents measured at 2092 m by FM-S100 indicate that fluid near the bottom edge of the upper control volume is also shielded to some degree from advection off-axis by the overlying currents (Figure 2.11), and may therefore retain plumes even when higher plumes are swept away.

The upper edge of the control volume at 1850 m was consistently well above the loftiest plume. This supports the assumption that there was no vertical heat flux through the top of the upper control volume. In contrast, only occasionally is a lower plume boundary evident on the surfaces above the lower edge (2070 m). It is therefore possible that some of the horizontal heat flux was not assessed because plume fluid escaped through the ~30–40 m gap between the bottom of the upper control surfaces and the top of the lower control volume where ABE measured H_v. This possibility is discussed further below.

4.2 Calculated horizontal heat flux

Calculation of horizontal heat flux through the upper control volume requires the $\Delta\theta$ observed during the circumnavigation stations and a source of current measurements. The southern current meters at 1942, 1992, and 2042 m depth (FM-S150, FM-S200, and FM-S250, Table 2.1) provide the best available measurements of the flow through the upper control volume during the Flow Mow field program. A PVD for any of the 3 upper meters indicates that during the Flow Mow cruise prior to the circumnavigation stations (MJD 51760–51774), the mean flow was primarily to the southwest (Figure 2.11). Examination of the puff model based on the record from any of the 3 meters shows that during the same period before the circumnavigation stations, the mean flow moved plumes to the southwest overall, but oscillatory flow caused the plume to undulate between the west and southwest directions.

During the period of the 5 CTD circuits around the MEF (MJD 51775.60–51776.52), the flow exhibited relatively unusual variations compared to the majority of the current record. Near the end of the Flow Mow cruise when the circumnavigating CTD stations were undertaken, and for a few days after the cruise ended, the mean flow weakened substantially and the oscillatory component strengthened and became more rotary. Figure 4.5 shows the hourly current sequence that occurred at each of the 3 upper meters during the circumnavigation stations (35–39). Flow at the 2 deeper meters (1992 and 2042 m) was very similar; it was initially $\sim$8 cm/s to the southeast, then weakened to $\sim$1 cm/s, shifted clockwise to the southwest, and increased to $\sim$4 cm/s. Finally, it decreased through zero, rose to $\sim$3 cm/s northeastward, and ended by decreasing in magnitude as it rotated clockwise. At FM-S250 (1942 m) the sequence of flow direction mimicked the deeper 2 meters, but the magnitudes remained above 5 cm/s.

Faced with this unusual period of current direction changes and potential pooling events, and indications from the puff model that plumes from High Rise may have been entering the MEF during the circumnavigations, I endeavor in this section to characterize the net horizontal heat flux through the upper control surface through 2 distinct methods. First, I estimate the heat flux through each individual surface by averaging the $\Delta\theta$ and u data. These fluxes are then averaged and summed to estimate the mean net flux. Second, I compute 16 estimates of "quasi-synoptic" net flux by summing the heat flux through all available sets of 4 sequential surfaces.

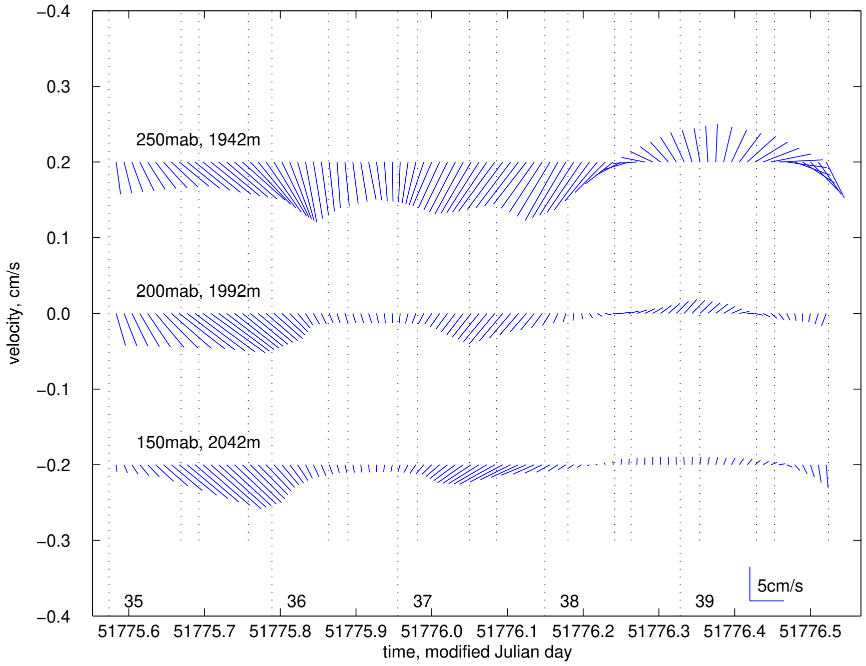

Figure 4.5: Time series of quarter-hourly mean currents observed during 5 circuits of the upper control volume at depths of 1942 m (top), 1992 m (middle), 2042 m (bottom) on the southern mooring (FM-S, Table 2.1). Vertical dashed lines show the time at which the survey of each surface began during stations 35–39 (see Figure 4.4). Each station label is just to right of time at which first surface survey began for each station.

4.2.1 Mean net horizontal flux

I begin the process of calculating the mean net horizontal flux $\overline{H_h}$ by estimating the mean heat flux H_h for each of the 19 surfaces in Figure 4.4. This is accomplished by first computing the mean $\Delta\theta$ on each surface, $\overline{\Delta\theta}$. After spatial averaging of the raw data in $5{\times}50$ m cells, 65–87% of the cells contain data. These data gaps are distributed about equally along the warm lower edge and cool upper edge of each surface (Figure 4.4) and are most likely to have $\Delta\theta$ similar to adjacent cells. Consequently, the data gaps are assumed to have $\Delta\theta = \overline{\Delta\theta}$ and $\overline{\Delta\theta}$ for each surface is therefore left unadjusted. Next, the normal component (outward positive) of the mean $\mathbf{u}$ observed during the traverse of each surface is assessed using the current record from FM-S200 (1992 m). While FM-S250 at a depth of 1942 m is more central to the upper control surface depth range (1850–2070 m), I elect to use FM-S200 because it recorded intermediate speeds — slower than the flow 50 m above at FM-S250, but faster than flow 50 m below at FM-S150 – and therefore will generate more reasonable estimates of the horizontal heat flux through the entire surface. Since some surfaces were traversed in $\lesssim$1 hr, the FM-S150 was interpolated from 1 hr samples to 0.25 hr samples in order to obtain an accurate estimate of mean $\mathbf{u}$ for each surface. Finally, the orthogonal component of mean flow $\overline{u}$ was computed and multiplied by $\overline{\Delta\theta}$, $\rho c_p = 4.2\,\mathrm{MJ{\cdot}m^{-3}{\cdot}^{\circ}C^{-1}}$, and surface area A of each respective surface, yielding an estimate of H_h for each surface.

In a steady cross flow typical of the equilibration depths (u ~5 cm/s), the heat flux through a single MEF control surface with $\overline{\Delta\theta} \simeq 0.04$°C (Figure 4.4) should be approximately

$$H_h = \rho c_p \overline{u}\,\overline{\Delta\theta} A \simeq 1.85L, \tag{4.1}$$

where A is the product of Z, the vertical extent of the surface (220 m) and L, the length of the surface (either 300 or 700 m). Using L of 300 and 700 m, H_h is 550 and 1300 MW, respectively. An increase of 0.01 units in $\overline{u}$ or $\overline{\Delta\theta}$ increases H_h by ~20%.

The observed values of H_h have absolute magnitudes of 0–1850 MW and are presented in Figure 4.6 for each of the 19 surfaces, along with the associated sequences of $\overline{u}$, $\overline{\Delta\theta}$, and data coverage as a percent of total surface area, A. Positive fluxes are oriented outward for any given surface. The peak magnitudes of H_h, about -1000 and $+2100$ MW, were observed

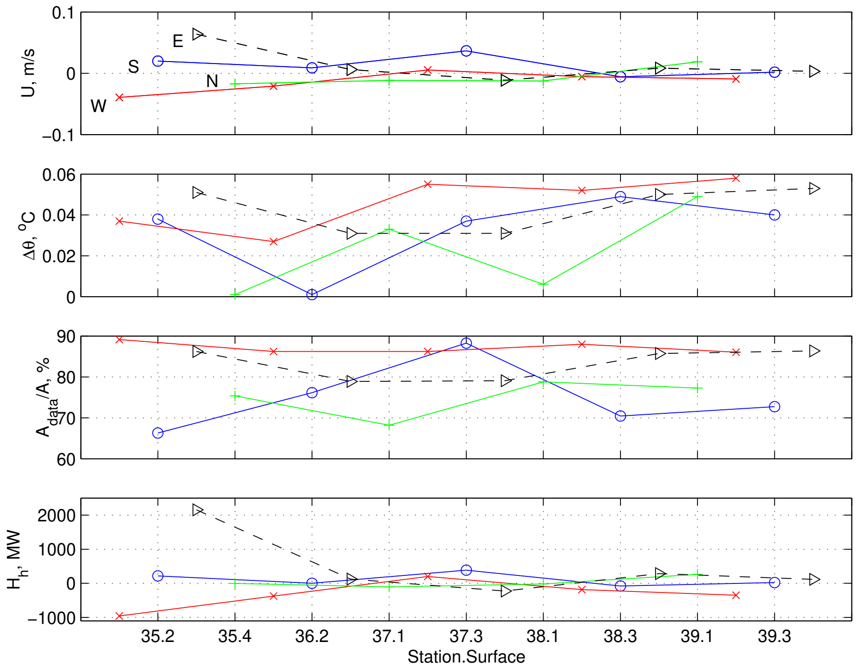

Figure 4.6: Time series of observations made on individual side surfaces during circumnavigation of the upper control volume (Stations 35–39). Panels (top to bottom) portray: mean orthogonal u; mean $\Delta\theta$; data coverage as percent of total surface area; and heat flux (positive outward). Lines connect sequential observations made on the same side surface and are labeled only in upper panel: circles=south; x=west; +=north; triangles=east. Horizontal axis labels indicate the station number and surface number during that station, separated by a decimal point (station.surface).

on the west and east surfaces, respectively (sides 1 and 3 of station 35 in Figure 4.4), indicating eastward advection of the $\Delta\theta$ distribution. The $\overline{\Delta\theta}$ on these 2 surfaces was not exceptional, but the mean flow to the south–southeast was consistent and relatively strong (~5–7 cm/s). The magnitude of the peak H_h, ~2100 MW, is ~1/3 the estimates by Thomson *et al.* (1992) of “instantaneous” flux through a single cross section of the MEF plume core: 6300 and 6800 MW.

The observed ranges of $\overline{u}$, $\overline{\Delta\theta}$, and percent data coverage in Figure 4.6 are -3.5–7.5 cm/s, 0.001–0.058°C, and 67–89%, respectively. It may seem surprising that the maximum $\overline{\Delta\theta}$ observed during circumnavigations of the upper control volume is 0.058°C when $\overline{\Delta\theta}$ is higher

Table 4.1: The average and standard deviation of the sequence of horizontal heat flux observed on each surface of the MEF control volume. The group mean fluxes $\overline{H_g}$ and $\overline{H_{hj}}$ are calculated slightly differently, as explained in the text (see Equation 4.2). The sequences are portrayed in the bottom panel of Figure 4.6. The right hand column lists the total, or net heat flux and the sum of the standard deviations.

Side surface	South	West	North	East	Total, $\overline{H_h}$
$\overline{H_g}$	109	−334	32	489	+296 MW
Standard deviation	187	417	159	950	
$\overline{H_{hj}}$	90	−358	−24	339	+47 MW

on many north and south surfaces of the lower control volume (*c.f.* Section 3.1.1). This occurs because the $\Delta\theta$ sample population on the surfaces of the upper control volume contains many near-zero values that reduce $\overline{\Delta\theta}$, despite the presence of many samples with $\Delta\theta$ much higher observed on the lower control surfaces. As with other data collected near the equilibration depths of MEF plumes, the variance of $\Delta\theta$ sampled during the circumnavigation stations is elevated compared to data from the surfaces of the lower control volume (Figure 3.6), reflecting the multidirectinal versus rectilinear nature of currents above versus within the axial valley.

To estimate the net mean horizontal flux $\overline{H_h}$, the values of H_h for the individual surfaces are grouped by cardinal direction (the 4 groups of connected points in the bottom panel of Figure 4.6). Each group of values is then averaged to yield the group mean flux $\overline{H_g}$ through each side of the control volume. The 4 resultant magnitudes are tabulated in Table 4.1 and summed to yield $\overline{H_h}$ =296 MW.

An alternative mean net horizontal flux in the upper control volume can be derived by finding the mean values of $\overline{u}$ and $\overline{\Delta\theta}$ for each group first, and then multiplying according to

$$\overline{H_{hj}} = \rho c_p \overline{u}_j \overline{\Delta\theta}_j A, \tag{4.2}$$

to estimate the mean flux through each of the j side surfaces. The resulting values are listed in the last row of Table 4.1 and sum to give a different estimate of $\overline{H_h}$ =47 MW.

The discrepancy between these alternative estimates of $\overline{H_h}$ implies that the instantaneous net heat flux through the upper control volume varies on short time scales and yields different mean values depending on the averaging period. This suggests that an accurate value of H_h depends on longer averaging periods and/or sampling more synoptically and frequently. Since the overall duration of the hydrographic observations (circumnavigation stations 35–39) is limited to only a single day, my approach is to treat the available observations as nearly synoptic and use them to approximate an instantaneous heat flux series.

4.2.2 Quasi-synoptic horizontal flux

Full resolution of the variations in net heat flux through the MEF perimeter over the equilibrium depths would require synoptic monitoring of $\Delta\theta$ and $\mathbf{u}$ at all points on all side surfaces. During the circumnavigations of the upper control volume, the current field was resolved much more coarsely (at a single point ~1 km to the south) and the $\Delta\theta$ distribution was assessed on each surface only once every 4–4.5 hr. Given the variability of the $\Delta\theta$ field and the dominant current oscillation period of 12 hr, the time required to circumnavigate the upper control volume is still undesirably slow. Nevertheless, it is possible to assume each set of 4 sequential surfaces is an instantaneous and synoptic observation and to calculate a "quasi-synoptic" flux, H_{qs}, by summing the fluxes through each side. Using all 19 surfaces, a series of 16 (=19+1-4) estimates of H_{qs} is obtained that describes approximately the temporal evolution of the net horizontal heat flux through the upper control volume.

The 16 estimates of H_{qs} are generated by first calculating H_h for each of the 19 surfaces, as described in the previous section, and then summing over each unique set of 4 sequential side surfaces, according to

$$H_{qs_j} = \sum_{i=j}^{j+4} H_{hi} \tag{4.3}$$

in which j proceeds from 1, when the first 4 surfaces are summed, to 16, when the final 4 surfaces are summed. The resulting series of estimates is displayed in Figure 4.7, along with the mean $\overline{H_{qs}}$.

The first few estimates have the largest magnitudes (1400–2000 MW) because of the relatively high $\overline{u}$ and $\overline{\Delta\theta}$ observed on the first 3 surfaces during the first circumnavigation (Figure 4.6). Subsequent estimates are between ±600 MW. Averaging the 16 estimates

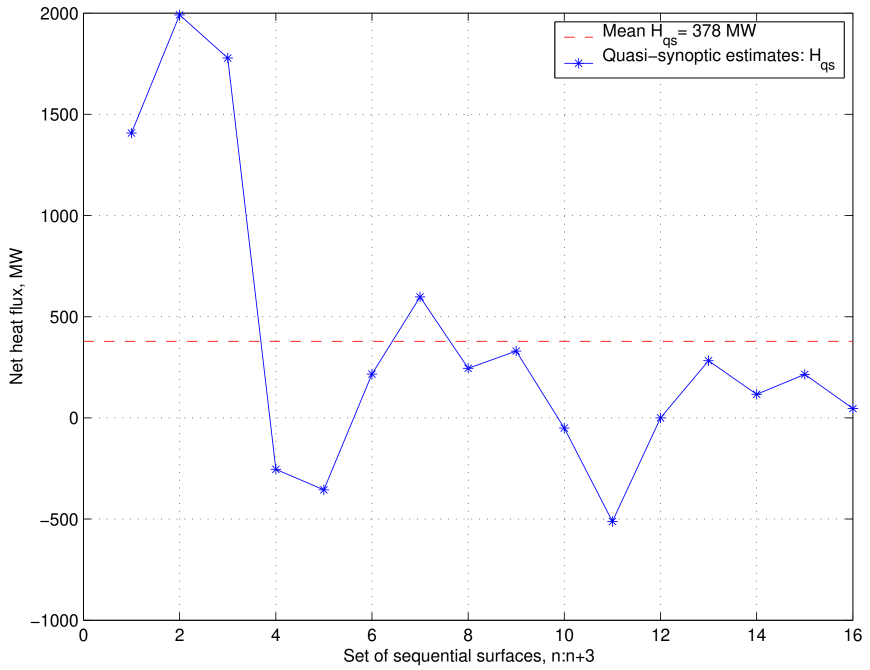

Figure 4.7: Series of 16 estimates of the "quasi-synoptic" net horizontal heat flux H_{qs} through the upper MEF control volume. The mean magnitude $\overline{H_{qs}}$, is overlain for reference. Each estimate was derived by summing a set of 4 sequential surfaces from the 19 total observed surfaces (see Equation 4.3). The mean, standard error of the mean, and standard deviation of the quasi-synoptic estimates are 378, 182, and ± 730 MW, respectively.

yields the mean quasi-synoptic net flux, $\overline{H_{qs}}$ =378±730 MW. The standard error of the mean is $730/\sqrt{16} \simeq 182$ MW, indicating an uncertainty of $182/378 \simeq 48\%$. The puff model analysis in the next section illustrates that even if the side surfaces were instrumented to continuously monitor $\Delta\theta$ and u at all points, the standard deviation of the instantaneous net H_h would be surprisingly high, requiring longer observational periods to achieve more precise estimates of the mean horizontal flux.

4.3 Modeled horizontal heat flux

The puff model simulations for the equilibration depths were conducted with the same puff model used for the lower control volume (*c.f.* Section 3.2.1), but the input flux was set to 600 MW and the flow was determined by *observed* current records from above the ridge crest. The MEF perimeter, horizontal diffusivity, and initial puff dimensions were held constant. In some cases, grid resolution and time step interval were altered to optimize computational efficiency.

In this section I present puff model runs based on the longest available current meter records, with attention to the statistics of the net heat flux time series that is generated by the observed flow. I also use the puff model to consider whether plumes from non-MEF sources may have influenced the upper control volume during the circumnavigation stations.

4.3.1 Modeled variance in flow above ridge crests

The puff model with upper level flow is interesting to watch because of the complexity of distinct plume distributions that are generated during different combinations of oscillatory and mean flow. The simulation based on FM-S200 at 1992 m, for example, has long periods where the plume streams fairly steadily and unidirectionally, and occasional stretches where the plume stalls and oscillates directly over the MEF (Figure 4.8).

While the typical situation during long current meter records is a plume that is advected on average to the southwest as it whips between south and west directions, the plume distribution exhibits a wide range of alternative evolutions. (Links to animations: FM-S200 at 1992 m; FM-S250 at 1942 m; MZ300 at 1900 m.) Advection of these diverse and hetero-

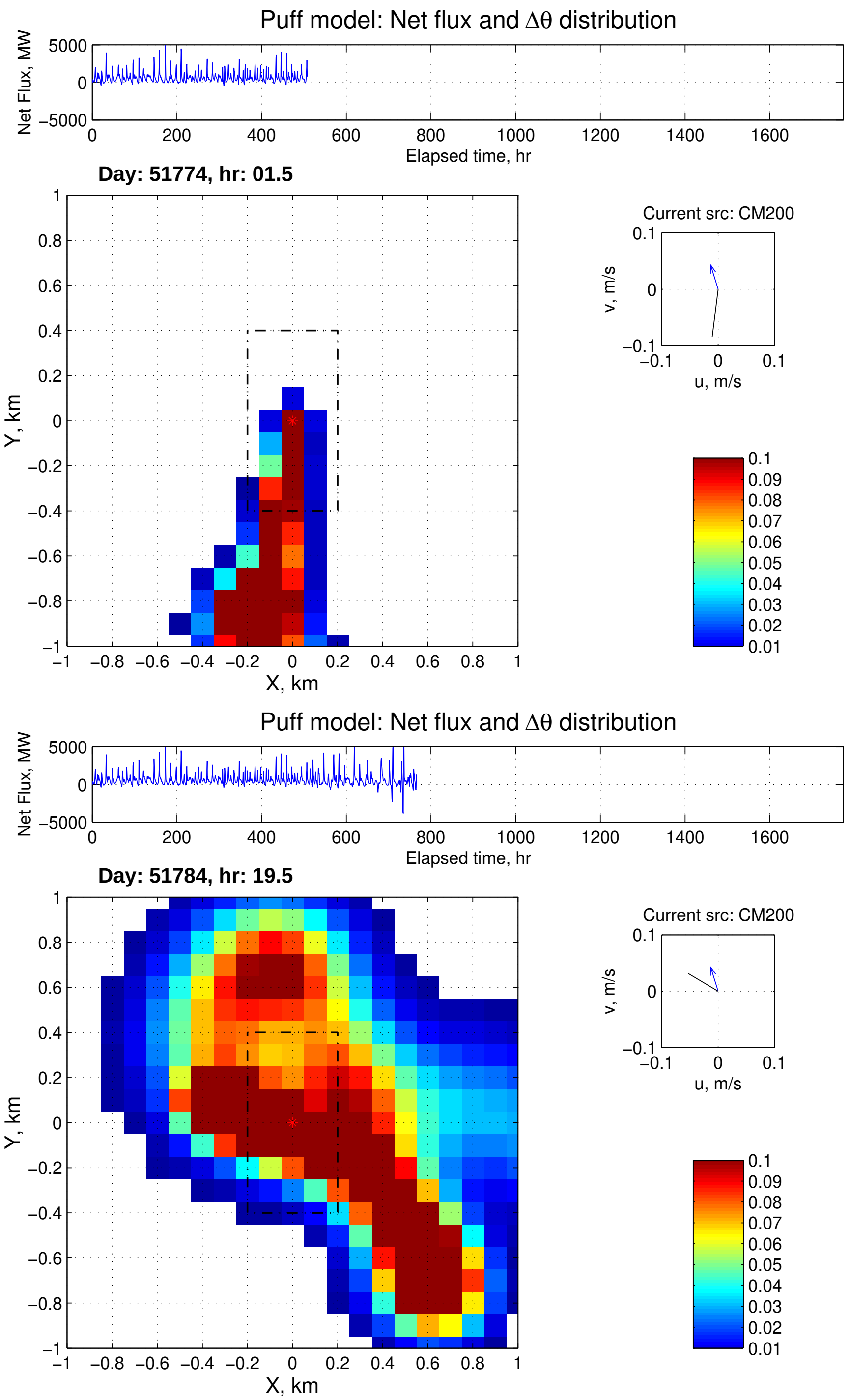

Figure 4.8: Individual "snapshots" or frames from the puff model animations illustrating streaming (upper) and pooling (lower) plumes. Flow is determined by the full record from FM-S200, the current meter at 1992 m on the southern mooring. See Figure 3.8 for additional details.

geneous $\Delta\theta$ distributions through the control surfaces leads to a high standard deviation of the instantaneous net heat flux (displayed in uppermost panel of animation frames). For the full record of FM-S200, the standard deviation is ± 800 MW, or $\sim$130% of the 600 MW input flux. The peak magnitude of the modeled instantaneous heat flux is much greater, ranging from -3800 to $+8700$ MW.

The standard deviation of the time series of modeled net heat flux is lowest during consistent streaming periods, moderate during pooling events, and highest during intermediate combinations of oscillation and mean flow. In the intermediate type of flow, the peak instantaneous flux occurs when warm pooled water is advected through only a *single* surface, leading to a large net flux because the outward downstream flux is not offset by an inward upstream flux. Additionally, the velocity associated with flushing of the pool out one side of the volume is generally higher than the typical flow speed during the pooling event. In contrast, the standard deviation is lower when oscillations dominate mean flow and generate a plume larger than the control volume. Within such a plume $\Delta\theta$ distributions are similar on both upstream and downstream surfaces, so inward and outward fluxes tend to balance, resulting in lower variance in the net flux. The variance in net flux is also relatively low in streaming flow because $\Delta\theta$ varies less on the downstream surface than when oscillations are strong enough to cause pooling.

During the Flow Mow hydrographic survey period (MJD 51761.0–51776.6; see Appendix B) the animation of the model with flow determined by FM-S250 shows a plume advected along-axis to the south-southwest on average, but intermittently transported up to $\sim$1 km in directions between west-northwest and south-southeast. A reasonable initial estimate of the standard deviation of the observed net flux through the upper control volume is the standard deviation of the modeled net flux based on the entire FM-S200 record: ± 800 MW.

One way to refine the expected standard deviation of the observed $\overline{H_h}$ is to analyze the mean and standard deviation of the modeled instantaneous net flux. From the standpoint of designing methods to measure $\overline{H_h}$, a useful approach is to examine how the statistics of the time series changes with the length of the observational period (often the key constraint on a field program). I do this by breaking the full simulation period ($\sim$1800 hr) into a

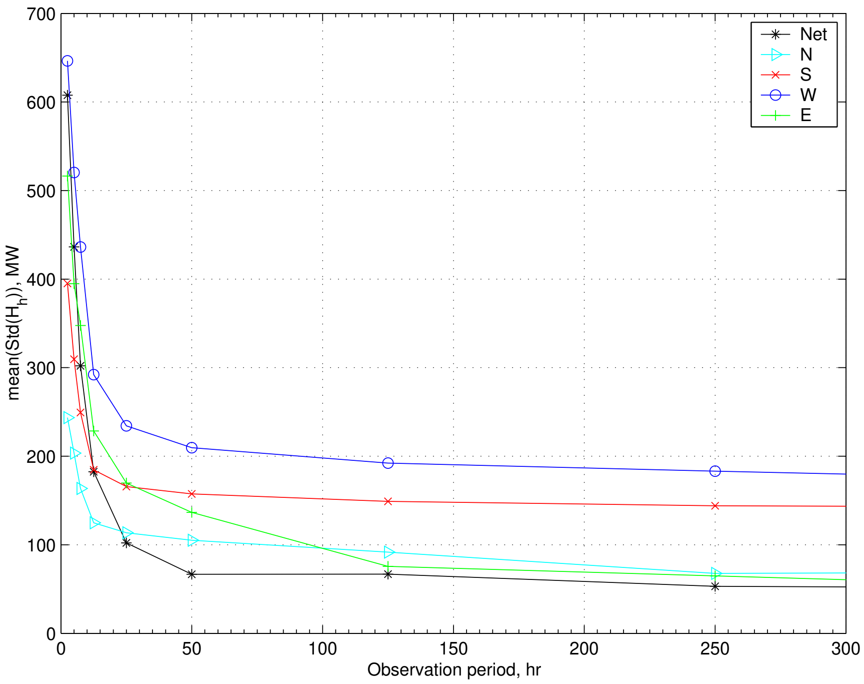

Figure 4.9: Standard deviation of modeled flux as a function of duration of observation period. Curves are shown for the net instantaneous flux, as well as the instantaneous flux through individual surfaces (south, west, north, and east). Data are from puff model with currents from FM-S200 and input flux set to 600 MW.

range of shorter periods (1, 5, 10, 15, 25, 50, 100, 250, 500, and 1000 hr) and computing the standard deviation and mean of each sub-series. The average value of the standard deviation, taken over all available sub-series of a given period, is presented as a function of the observation period in Figure 4.9, using data from the model forced with the record from FM-S200 (1942 m).

This main insight from this analysis is that the standard deviation of instantaneous net heat flux is expected to decrease rapidly with the duration of synoptic observations. While the average standard deviation is ∼100% of the input flux for a 5 hr observational period, for a slightly longer observational period like the ∼25 hr circumnavigation survey, the average standard deviation of the modeled net instantaneous flux drops to ∼100 MW, or about 17% of the 600 MW input flux. Assuming that the input flux is the observed $H_v \simeq 550$ MW

(Stahr *et al.* 2003), and that the estimates from the quasi-synoptic circumnavigation survey represent instantaneous flux estimates, the average standard deviation of the observed $\overline{H_h}$ is expected to be $\sim \pm 92$ MW. Note also that the curves for individual surfaces differ dramatically, implying that observations of H_h on a single surface will yield a mean value *and* standard deviation that depend on which surface is surveyed.

4.3.2 Plumes from other vent fields

Another result from the puff model is a synoptic simulation of the changing $\Delta\theta$ distribution on each surface of the upper control volume. Based on the FM-S250 current record, Figure 4.10 shows a time series of the modeled $\Delta\theta$ distribution on each control surface, spread flat as in the presentation of the observed $\Delta\theta$ distributions (Figure 4.4).

The full simulation record (Figure 4.10, upper panel) shows that during the Flow Mow cruise period (MJD 51761.0–51776.6) the horizontal heat flux associated with the MEF sources was most commonly through the west surface, as it was for $\sim$10 days prior to the cruise. Using current data collected after the cruise, however, the model indicates the maximum flux was through the east or south surfaces. Significant fluxes through the north surface occurred only during 3 short periods (near MJD 51772, 51783, and 51794). In contrast, the available observations of the north surface show non-zero heat fluxes at other times, too. The model simulates neither the 2 north surfaces with non-zero fluxes observed during the circumnavigation period (Compare Figures 4.4 and lower panel of Figure 4.10) nor the non-zero fluxes through the upper portion of the 3 north surfaces observed during station 10 (Figure 4.3; MJD 51762.85–51763.16). The simulation does show heat flux through the north surface during NoMEF station 28 (MJD 51771.85–51772.27), when positive $\Delta\theta$ was recorded near the equilibration depths (Figure 4.1).

During the circumnavigations of the upper control volume, puff model simulations based on flow at FM-S200 and FM-S250 both suggest that plumes from High Rise, and possibly other upstream hydrothermal sources, were likely advected through the Flow Mow control volume along with MEF plumes. Such juxtaposition of plumes is probably common at all but the northernmost vent field on the Endeavour segment, given that the southwestward

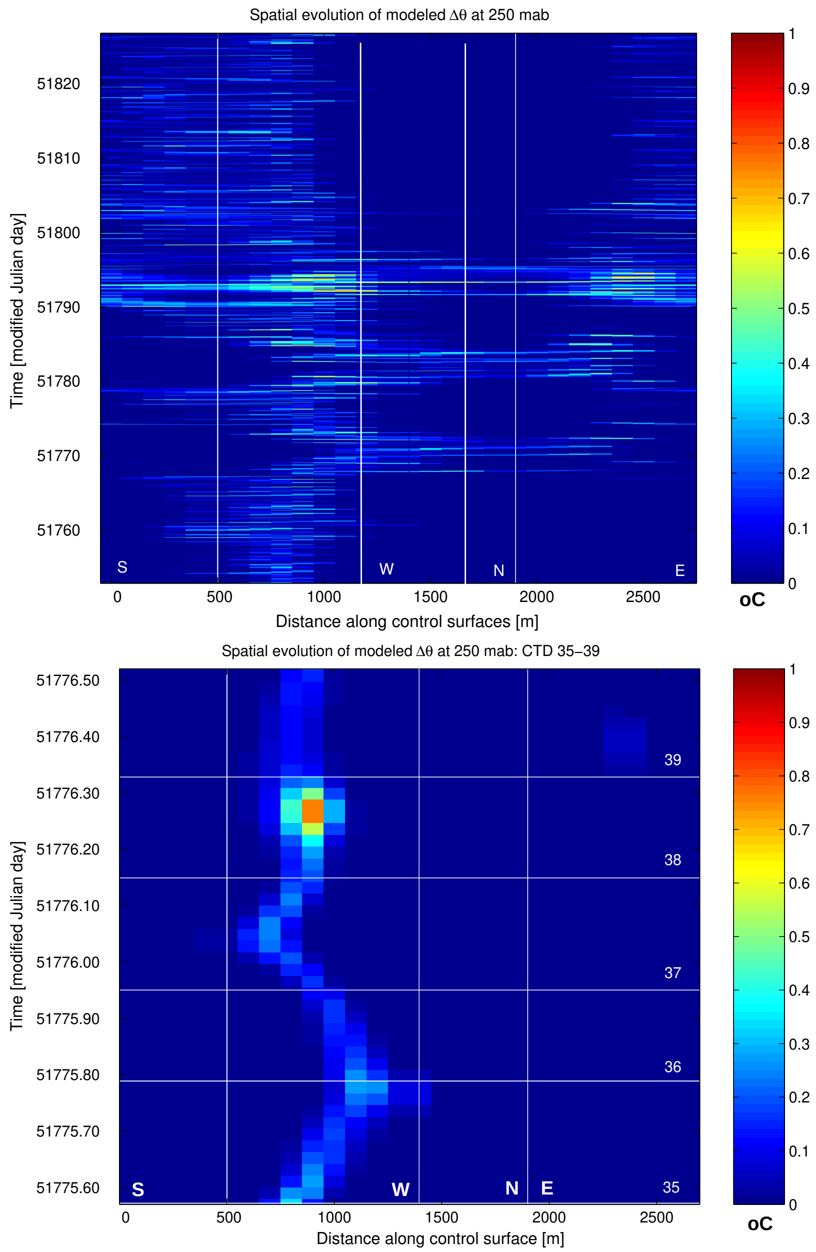

Figure 4.10: Time series of $\Delta\theta$ on the 4 MEF control surfaces, based on the current record from FM-S200. Vertical axis is time in days with model time steps of $1/2\,\mathrm{hr}$; horizontal axis is distance along successive control surfaces. Upper panel shows the full current meter record (Flow Mow cruise period is MJD 51760–51777); lower panel shows only the period of the circumnavigation stations (MJD 51775.60–51776.52). Horizontal white lines mark the beginnings of CTD stations 35–39, while vertical white lines represent boundaries between the 4 control surfaces (folded flat as in Figure 4.4 and labeled with a letter denoting cardinal direction).

mean flow above the crests is approximately aligned with the strike of the ridge and fields are distributed along the axis.

The likelihood of plume juxtapositioning underscores the importance of monitoring all 4 sides of the control volume when attempting to measure the net horizontal flux accurately over the Endeavour segment. An upstream source will generate hydrographic variability that will increase the variance in $\overline{H_h}$ when the plumes from the upstream source traverse the control surfaces. Thus, the estimated standard deviations presented in the previous section are most likely minima because the puff model does not include upstream sources.

4.4 Discussion

4.4.1 Sources of hydrographic variability

Considered together, the Flow Mow observations of hydrothermal hydrography above the ridge and near the MEF describe heterogeneity at scales as short as 10–50 m and 1 hr and high variability at the scale of the MEF (100–1000 m). These non-uniform distributions of the equilibrating plumes imply that mesoscale vortices (*e.g.* Speer 1989) were not forming above the MEF during the Flow Mow cruise period. The similarity of the flow above the ridge during the cruise to the flow recorded during much longer periods (*e.g.* Franks 1992) suggests that the observed variability is probably typical. This indicates the dispersion of MEF plumes is governed predominantly by multidirectional advection, rather than plume-induced rotational dynamics (*c.f.* Section 5.2.1).

Each animation of the puff model forced with upper level flow illustrates that plume distributions are non-uniform and hydrographic variance is high when a even a single source is venting into multidirectional flow. Only over long observation periods should the Endeavour plume be considered a steady state feature, extending in a downstream direction on average, with concentrations simply related to plume age or distance from the source. To properly account for the complexity of plume distributions, all investigations — of plume dynamics, the evolution of conditions with plume age, or the advected heat flux — should include observation of the currents. Successful analysis and interpretation of the observed plume distributions and variance will hinge upon the use of advection/diffusion models which provide insights that are otherwise unavailable. More sophisticated puff models, for example, could simulate the dispersion of plumes from multiple sources in non-uniform flow fields, and thereby help to locate new sources (*e.g.* LAVELLE *et al.* 2001) and calculate accurate net heat fluxes through a control volume.

Multiple sources distributed along the axial valley contribute to the hydrographic variability above the Endeavour segment. Because the mean flow over the ridge is approximately aligned with the axis, it is reasonable to expect that plume measurements made above a known source will commonly be conflated with plumes from nearby sources, especially those that are upstream with respect to the mean flow. This possibility is confirmed by the difference between observations made during the circumnavigation survey and modeled distributions for the same period. It is evident that plumes from the High Rise field were mixing with MEF plumes, a situation which underscores the importance of assessing $\Delta\theta$ on both up- and downstream surfaces when measuring net horizontal heat flux through a specified volume.

The multidirectional, oscillatory cross flow also affects the vertical distribution and variability of plumes. The rise height z_r of a buoyant plume in a steady cross flow U is

$$z_r = 2.6(\frac{B_o}{UN})^{1/3} \tag{4.4}$$

where B_o is the source buoyancy flux, N is the buoyancy frequency in the ambient fluid (a measure of the density stratification), and 2.6 is a empirically derived constant (BRIGGS 1969; MIDDLETON and THOMSON 1986). In the ridge crest environment where cross flows are amplified and of the same or greater magnitude than vertical velocities in rising plumes, this rise height equation is more appropriate than the expression derived for quiescent conditions by TURNER (1973): $z_r = 5.0B^{1/4}N^{-3/4}$. Dividing the derivative of Equation 4.4 by Equation 4.4 itself yields an expression of how a change in rise height Δz_r relates to a change in cross flow velocity ΔU (J. W. Lavelle, pers. comm.):

$$\frac{\Delta z_r}{z_r} = -\frac{1}{3}\frac{\Delta U}{U}. \tag{4.5}$$

The observed variations in plume rise height indicate $\Delta z_r \simeq 25\,\mathrm{m}$. With a typical value of z_r above the MEF (300 m) and u taken to be either 0.01 m/s or 0.05 m/s, Equation 4.5

Table 4.2: Comparison of vertical and horizontal heat fluxes in the upper control volume measured during the Flow Mow study, and the horizontal flux associated with the MEF plume measured by THOMSON *et al.* (1992). The error estimate for $\overline{H_v}$ and $\overline{H_{qs}}$ is the standard error of the mean, while for the instantaneous flux of THOMSON *et al.* (1992) it is based on the approximate range of magnitudes observed in the entire plume versus its core.

Heat flux	Mean (MW)	Error (±MW)	Uncertainty (%)
$\overline{H_v}$	550	100	18
$\overline{H_{qs}}$	378	182	47
THOMSON *et al.* (1992)	12000	6000	50

suggests that ΔU of only 0.25 cm/s to 1.25 cm/s will cause the observed Δz_r of ~25 m. If ΔU is ~0.05 m/s, a flow variation that is common in the hourly mean flow $u \simeq 0.05$ m/s over the Endeavour, Equation 4.5 with $z_r \simeq 300$ m yields $\Delta z_r \simeq 90$ m. This implies that MEF plumes will be distributed by typical cross flow over Endeavour in a layer that extends ±90 m around the average equilibration depth for any particular source. The observed thickness of the plume layer over the MEF is ~200 m (Figure 4.1).

4.4.2 Comparison of vertical and horizontal heat flux

The magnitude of the isohaline heat fluxes H_v and $\overline{H_{qs}}$ should be comparable, assuming that H_v during the ~24 hr survey of the side surfaces of the upper control volume was steady and equal to the mean observed vertical flux $\overline{H_v}$ (STAHR *et al.* 2003). Table 4.2 juxtaposes the means, standard errors, and uncertainties of horizontal and vertical flux for the upper control volume. The mean quasi-synoptic heat flux, $\overline{H_{qs}}$ is ~$2/3\overline{H_v}$; the magnitudes are equivalent, given the standard errors of the 2 means. The uncertainty of $\overline{H_{qs}}$ is 2–3× the uncertainty of $\overline{H_v}$.

A partial explanation for the underestimation of H_v by H_{qs} is the 30–40 m gap between upper and lower control volumes. Assuming that any fluid that escaped assessment had a mean $\Delta\theta$ equal to that in the upper portion of the plume and was advected with the same velocity that was acting on the surface above, then the heat flux estimates can be adjusted by the ratio of the gap height to the surface height, (Z_{gap}/Z_{surf} = (30 to 40)/220 =14–18%. Making an intermediate upward adjustment of 15% results in H_{qs} =434.

The discrepancy between H_v and H_{qs} may also be attributed to: (1) the non-synoptic observations which underlie H_{qs}; (2) variations in currents assumed to be uniform; (3) heat flux contributions from non-MEF sources not accounted for perfectly in the non-synoptic observations; and (4) the strong dependence of the mean value of the instantaneous net horizontal flux on the observation duration (Figure 4.9), which in the case of the circumnavigation survey was only ~25 hr. The flow during the circumnavigations, unusual in that oscillations dominated the mean flow, may also have elevated variance above typical values. Nevertheless, $\overline{H_{qs}}$ is equivalent to $\overline{H_v}$, within the standard error of the means.

The "instantaneous" horizontal heat fluxes estimated by THOMSON *et al.* (1992) are juxtaposed with H_{qs} in Table 4.2 to emphasize that the 2 estimates may be consistent. There are 2 explanations for the factor of 10–20 difference between the 2 estimates. First, the puff model indicates that peak instantaneous heat flux through a single surface can be much higher than the input flux. This is confirmed by observations: H_h through individual surfaces during the circumnavigation survey were as high as 2000 MW (Figure 4.7), almost 4× the probable input flux, H_v =550 MW. It is possible that the "instantaneous" estimate of THOMSON *et al.* (1992) would be greatly reduced to a magnitude closer to H_{qs} if an upstream surface had been assessed and used to compute a *net* horizontal flux through a control volume enclosing the MEF. Second, the modeled time series of instantaneous net flux has peaks of ~5000 MW, roughly 10× the 600 MW input flux. The modeled peaks are infrequent enough that the standard deviation during an average 25 hr period is roughly an order of magnitude lower than peak values. This implies that even if an upstream surface had been assessed and found to have background conditions ($\Delta\theta$ =0), the "instantaneous" estimate of THOMSON *et al.* (1992), 10–20× H_{qs} or H_v, would not constitute an unreasonable peak value of the MEF instantaneous net heat flux.

Chapter 5

CONCLUSIONS AND IMPLICATIONS

The Flow Mow study generated a rich set of observations of hydrothermal plumes, currents, and hydrography. Analysis of observed and modeled plumes in this dissertation has led to some conclusions about how plumes disperse over the Endeavour ridge and within its axial valley, and how the heat flux of their sources might optimally be measured. The primary result of the Flow Mow study is a new set of heat flux estimates for the MEF derived through synthesis of the current and hydrographic data.

This chapter begins with a synopsis of the main observations made during the Flow Mow study. The observations are then interpreted to formulate conclusions about the 2 central issues that motivated this work:

- What form do plumes take in different types of cross flow?
- How can the heat flux from their sources best be determined?

For each issue, I also offer ideas about further research. In a final section, I discuss the implications of the main observations and major findings with respect to some of the interdisciplinary questions posed in the introduction (*c.f.* Section 1.1).

5.1 Main observations

5.1.1 General flow and hydrography

Regional patterns

1. A hydrographic transition from background to axial mean profiles of θ, S, density, and back scatter intensity begins within ~1 km of the ridge axis. Level-to-level anomalies of each variable increase with proximity to the ridge axis and reach peak along-axis values near the center of hydrothermal activity.

2. Comparison of Flow Mow and past current meter data suggests that the mean flow direction above the ridge crests is usually to the southwest. However, mean flow in other directions also has been observed for periods of ~10-100 days. While northward mean flow is generally rare above the ridge, it has been recorded most frequently over the western flank. This may be an effect of geographical sampling biased to the axis, or it may be a manifestation of vorticity conservation when oscillatory flow crosses a topographic high in the northern hemisphere (Lavelle and Cannon 2001): northward mean flow on the western flank of the ridge; southward mean flow on the eastern flank.

Axial patterns

1. Flow energy above the ridge crest is dominated by tidal and inertial frequencies; oscillatory flow is generally amplified near ridge crest depth and attenuated within the axial valley (Thomson *et al.* 2003).

2. Rectilinear mean flow within the axial valley appears to be independent of multidirectional mean flow above the ridge crests. Currents are generally sheared in speed and direction near 2100 m, the approximate depth of both the ridge crest and the base of the most intense plume layer.

3. Mean flow within the axial valley is persistently unidirectional and appears to converge along axis on the center of hydrothermal activity (somewhere between FM-N15 and the 48°N sill). In 2000 and 2001, the mean flow $\lesssim$ 50 mab within the valley was northward at 1–5 cm/s at all moorings south of the sill. In 2001, a record from the same depth range on a mooring at the sill showed southward mean flow simultaneous to the northward flow observed further south (Thomson *et al.* 2003).

4. Flow variability within the axial valley is dominated by rectilinear semi-diurnal oscillations that are aligned with local topography. All oscillations within the valley are coherent and approximately in phase between points ~1 km north and south of the MEF.

5. The mean isohaline potential temperature anomaly ($\overline{\Delta_S\theta}$) of fluid within the valley increases in mean value from the ends of the segment, reaching peak values north of the MEF.

Hydrography at the MEF and in rising plumes

1. The variance and mean values of $\Delta\theta$ and back scatter intensity are generally higher above the ridge crests (1800–2100 m) than within the axial valley (>2100 m).

2. Both individual vertical casts and average density profiles indicated negative $\Delta_z\sigma_\theta$ below a depth of ~2000 m and positive $\Delta_z\sigma_\theta$ above.

3. Horizontal CTD tows through buoyant plumes intercepted 7–80 m above various MEF sources, $\Delta\theta$ is 2.71–0.35°C. Between the buoyant plumes within the MEF, in the same elevation range, $\Delta\theta$ is typically 0.05±0.02°C.

4. The mean vertical heat flux through the top surface of the lower control volume is $\overline{H_v^*} = 643 \pm 116$ MW.

5. A mixing line fit to θ and S data from within buoyant plumes yields accurate prediction of source salinity when extrapolated to source temperature.

5.1.2 Plumes and heat flux within the axial valley

1. Spatial and temporal hydrographic variability in the near-field have scales as short as 10 m and 1 hr. The puff model simulates this level of temporal variability; spatial heterogeneity at the 10 m scale is expected from multiple sources, based on numerical models of diffuse plumes rising in a cross flow from sources like those in the MEF.

2. Despite varying from 0.053–0.092°C on individual vertical surfaces of the Flow Mow control volume, spatially and temporally averaged $\overline{\Delta_S\theta}$ is 0.007°C greater north of the MEF than to the south.

3. The mean net horizontal heat flux through the lower Flow Mow control volume is $\overline{H_h^*} = 76 \pm 114$.

4. A heat budget for the lower control volume, constrained by $\overline{H_h^*}$, $\overline{H_v^*}$, and the best estimate of focused MEF heat flux H_f from GINSTER *et al.* (1994), implies that diffuse MEF heat flux $H_d = 104 \pm 253$ and that $\sim 1/4$ of H_d is entrained and transported by high B plumes through the top surface.

5. The puff model indicates that in rectilinear flow with a mean speed that does not exceed the oscillatory half-amplitude, the variance of instantaneous horizontal heat flux will typically be 100–300% of a steady input heat flux.

5.1.3 Plumes and heat flux above the ridge

1. In the depths above the ridge crest where plumes from high B MEF sources equilibrate, spatial and temporal hydrographic variability have scales as short as 10–50 m and 1 hr. Typical lateral extent of plumes above the MEF is 100–1000 m and longer time series hint that plume intensity varies with semi-diurnal periodicity.

2. Top boundary of plumes above MEF is sharp at mean depth of 1890 and undulates ± 50 m with approximately semi-diurnal periodicity. Lower boundary is also well-defined at 2100$\pm$50 m.

3. Horizontal fluxes through the upper Flow Mow control volume have peak observed values of ~1000-2000 MW. The best estimate of the mean net quasi-synoptic horizontal flux is $\overline{H}^*_{qs} = 442 \pm 213$ MW (Table 5.1).

4. Puff model simulations with observed currents suggest that southward flow brought plumes from High Rise through the upper MEF control volume when the net horizontal heat flux was being assessed.

5. Puff model analysis indicates that averaging synoptic measurements of net horizontal heat flux over periods of only 25 hr will reduce standard deviation from 100% to ~15%

of the input heat flux.

5.2 Central issues and conclusions

In this section I revisit the 2 central issues of this thesis and present concluding thoughts about each issue and the extent to which it has been addressed by the main observations of the Flow Mow study. I also offer ideas about how to address the central issues further through ongoing or future research.

5.2.1 What form do plumes take in different types of cross flow?

Understanding the form, dynamics, and dispersal of plumes is a major issue in the study of hydrothermal systems. Information about hydrothermal plumes from field observations, numerical models, and lab experiments has led to competing ideas about the form plumes take in different types of cross flow. The spectrum of ideas is encompassed by 2 alternate, but not mutually-exclusive hypotheses: (1) rotational dynamics determine the form and dispersal of hydrothermal plumes, generating uniform, oblate spheroid forms that spin (*e.g.* Speer and Marshall 1995); (2) ambient cross flow controls the form and dispersal of hydrothermal plumes, generating bent over plumes with relatively elongated and heterogeneous forms (*e.g.* Lavelle 1997). Past studies have primarily attempted to test hypothesis 1 by looking for patterns of vorticity indicative of rotational dynamics (*e.g.* Lupton *et al.* 1998). Both hypotheses are tested in this section for consistency with Flow Mow field observations and results from an advection/diffusion model of plume dispersal that does not include rotational physics.

MEF plume form and dispersal are controlled by advection

Helfrich and Speer (1995) argue that 2 types of observations are suggestive of mesoscale circulation forced by steadily venting hydrothermal plumes. First, they note that the lateral scale of observed plume distributions (*e.g.* Baker and Massoth 1987) can suggest vortices if it is about 1 Rossby radius of deformation:

$$l = NZ_m/f, \tag{5.1}$$

where N and f are the local buoyancy and Coriolis frequencies, and Z_m is the equilibration height. In the vicinity of the MEF, where $N = 1$ to $2 \times 10^{-3}\,\mathrm{s}^{-1}$, $f = 1 \times 10^{-4}\,\mathrm{s}^{-1}$, and $Z_m \simeq 200\,\mathrm{m}$, Equation 5.1 indicates $l \simeq 2$–$4\,\mathrm{km}$.

Plumes with similar or smaller lateral scale, however, are also predicted by the puff model. and the theoretical displacement of fluid during a half-period of observed oscillations. When a plume from a point source is dispersed through diffusion and the typical multidirectional, oscillatory flow above the ridge crests, a plume is distributed over and downstream from the source. Particular combinations of mean and oscillatory flow result in streaming and pooling behavior which generates non-uniformities in the plume distribution; the characteristic horizontal scale of the non-uniformities is ∼100–1000 m. Even without a mean flow, the typical displacement of fluid during a half-period of a tidal, inertial, or composite oscillation is 0.5–2.2 km.

Flow Mow observations characterize the plumes over the Endeavour as having lateral scales of ∼100–1000 m. Broader surveys of the hydrography over the Endeavour segment confirm that this is a typical width of a plume cross-section (*e.g.* Thomson *et al.* 1992). The largest observed scale supports both hypotheses, but the smaller observed scales helps to discriminate between the 2 possible plume formation mechanisms. Only dispersal by advection generates the smaller observed plumes.

Second, Helfrich and Speer (1995) suggest that shear on the vertical scale of plumes constitutes evidence of vortices, because the pattern of flow in theoretical and laboratory vortices is cyclonic around the rising plume stem and anticyclonic near the equilibration depths. Strong vertical shear was observed by the Flow Mow current meter array, as well as at past MEF moorings (*e.g.* Franks 1992). Lateral shear observed over the Juan de Fuca ridge was interpreted by Joyce *et al.* (1998) as consistent with stacked hydrothermal vortices rotating in opposite directions, but by Helfrich *et al.* (1998) as also suggestive of topographic rectification of tidal and 4-day oscillations flow over the ridge. At the Endeavour segment, the flow within the axial valley is often sheared with respect to the overlying flow, but the directional sense of vertical shear changes with both location and time. While the vertical scale of the shear (∼100 m) is comparable to the equilibrium rise height of the hydrothermal plumes (∼200 m), it is also about the same as the valley relief.

At the Endeavour, the presence of vertical shear near 2100 m does not constitute strong evidence of hydrothermal voritices; it is equally possible the shear is generated by flow interacting with the local topography. It is certain that topography affects oscillatory flows differently above and within the valley: oscillations are amplified in the depths just above the ridge crests, and attenuated and aligned with topography within the axial valley (Thomson *et al.* 2003). It is also evident that topography interacts with entrainment to drive mean flows along the axial valley, often in a direction different from the overlying mean flow. A comprehensive assessment of vorticity, not just shear, above the ridge and/or within the axial valley would be necessary to discriminate between the 2 plume formation hypotheses.

A third characteristic of hydrothermal vortices is vertical spreading or "bulging" of isopycnals, isohalines, and isotherms. Isopycnals are expected to bow upward above the equilibration depth and downward below it. Numerical models of mesoscale circulation forced by hydrothermal plumes predict detectable spreading of isopycnals at distances less than 1–2 Rossby radii from a high B source (Speer 1989), or 2–8 km from the MEF.

The *average* depth profiles of θ, S, and σ_θ observed at axial stations (Figure 2.23) are consistent with the expected pattern of spreading isopleths. Additionally, geographically-averaged level anomalies of θ, S, and σ_θ decrease from maxima near MEF to zero near the segment ends (Figure 2.21), over a ~ 5 km distance — roughly comparable to the expected extent of isopycnal spreading.

Yet the *individual* casts which generate the average depth profiles in Figures 2.21 and 2.23 often reveal multiple plume layers that vary from hour to hour, not a uniform lens of plume fluid with a radius of 100–1000 m (Helfrich and Speer 1995; Speer and Marshall 1995). Indeed, the vertical and horizontal heterogeneity observed in individual casts directly over the MEF, with horizontal and spatial scales as short as 10–50 m, is too high to be consistent with a vortex maintained over a source in a cross flow.

What processes, then, are responsible for both the small-scale heterogeneities and variability, as well as the segment-scale deflection of isopleths? A likely possibility is that individual plumes from sources of variable B distributed along the axial valley generally create small-scale heterogeneities, but such plumes are integrated over time and space by oscillatory and mean cross-flows, thereby affecting the *average* near-field and regional hydrography. This integrating effect should extend from each axial source at least as far as the expected displacements from oscillatory flow compoents, $\sim$0.5–2.2 km (Table 2.2).

Small-scale heterogeneity and perturbation of isopleths are both features of a 3 dimensional numerical model of a hydrothermal plume from a single high B source in a steady cross flow (Lavelle 1997). The model accounts for rotational forces and turbulent mixing, and uses parameter values consistent with MEF source properties and ambient conditions. At a cross flow speed of 1.5 cm/s, the modeled plume is $\sim$30–50 m wide and $\sim$100 m thick (based on extent of 0.005°C isotherms) and exhibits thermal heterogeneity and associated temporal variability within the equilibrating plume. The modeled plume also perturbs the ambient velocity and stratified property fields downstream, and up to $\sim$100 m upstream of the source. A similar spatial extent of isopleth perturbation is evident in a 2-dimensional model of a line plume in a cross flow (*c.f.* Section 2.5.2, Lavelle 1994) In the stronger flows observed above the ridge crests (1–5 cm/s means) such upstream effects will be lessened.

At the Endeavour, it is likely that plumes like the one modeled by Lavelle (1997) rise from 100s of high B vents distributed along the axis. With the added possibility of distinct source properties and multidirectional flow, the spatial and temporal heterogeneity of each individual plume will generate a complex plume distribution with many of the observed features. Different source B and cross-flow histories will lead to distinct layers at different depths. Multidirectional mean flow will cause temporal variability at any particular depth. Streaming periods will create narrow plumes. Pooling periods will generate more uniform plumes with lateral scales characteristic of the displacements by tidal and inertial oscillations ($\sim$0.5–2.2 km, Table 2.2).

The integrated effect of multiple plumes in multidirectional cross flow may also explain the remarkably consistent depth of the top of the plume layer frequently present over the MEF. While the observed depth variability is $\pm$25 m, the variation in rise height expected from increasing the cross flow from 0 to $\sim$15 cm/s is $\gtrsim$100 m (Middleton and Thomson 1986; Lavelle 1997). The unexpectedly small observed variability is likely due to the effect of cross flow on plume rise height being averaged over current oscillations and changes in mean flows. In quiescent conditions, the source with highest B would generate the highest rising plume. Strong cross flow would reduce the rise height. In oscillatory flow within the Mid-Atlantic ridge, for example, the elevation of a plume from the TAG hydrothermal field shifted smoothly over ~100 m, and was correlated with the magnitude of tidal flow (Rudnicki *et al.* 1994). However, it may also be possible in oscillatory flow for the top of a plume layer to occupy an unexpectedly constant depth above a vent field because it may be common for plumes that rose through different amounts of cross flow to merge or be juxtaposed by horizontal advection.

The perturbation of isopleths due to a single plume (Figure 2.24) must be integrated over many plumes at the MEF and at other hydrothermal sites along the Endeavour axis. Despite the spatial heterogeneity and temporal variability of the plume distribution observed in any individual CTD cast, when averaged geographically and in depth bins, the same casts evidence a density profile that crosses the background profile near ~2000 m (Figure 2.23). While individual modeled plumes deflect isopleths on lateral scales much smaller than a Rossby radius, an interpretation of the observed mean profiles is that the integrated effect of multiple plumes may be more far-reaching.

The extent of isopleth perturbation may be enhanced from 100 m to 1000 m scales by topographic constraint of plume-induced circulation. For most Endeavour plumes, fluid entrained within the first 100 m of rise can only enter the valley *laterally* through the open south end or over the northern sill. Vertical recirculation may transport some plume fluid down into the valley, but the observed northward mean flows and the consistent downstream increase in near-bottom thermal anomalies along the axis both imply that lateral entrainment is important. Stratification and topography may constrain the entrainment of fluid by axial high B plumes in such a way that isopleths are perturbed on a regional scale. This would help explain the geographic patterns in the depth profiles of $\Delta_z\sigma_\theta$, $\Delta_z\theta$, and $\Delta_z S$, especially the negative $\Delta_z S$ below ~2100 m (Figure 2.21).

This combination of dispersal in multidirectional ambient flow, plume-forced circulation, topographic restriction, and low and high B vents distributed along the axis could explain the otherwise confusing main hydrographic observations of the Flow Mow study: high spatial heterogeneity and temporal variability near the equilibration depth (2000 m), regional isopleths spread on average near the same depth, and near-bottom thermal anomalies that increase toward the center of the segment. It also explains the observed convergence of currents toward the center of the segment within the axial valley (Thomson *et al.* 2003).

The Flow Mow study was not designed to resolve what form plumes take in different types of cross flow, but the observations nevertheless include evidence that bears on both hypotheses. On the whole, I conclude that the Flow Mow results support the idea that advection dominates rotation in controlling the dispersion of hydrothermal plumes, at least for plumes venting steadily from ~500 MW sources in the currents and topography of a typical intermediate-rate spreading center.

Future work on plume formation and dispersal

Further investigation of Endeavour plumes and the processes that govern their distribution and dispersal may be warranted by the potential biological ramifications alone (*e.g.* Mullineaux and France 1995). A new study at Endeavour could also help to resolve which body of physical oceanographic theory, laboratory results, and field observations best describes the behavior of plumes from steadily venting hydrothermal sources in typical cross-flows. The issue of how plumes form and disperse at the Endeavour segment could be further addressed through the following on-going and future research:

- Trace fluid (and larval) trajectories with Lagrangian methods. What paths do RAFOS floats take when deployed near 2000 m above the MEF and over the flanks? What is the fate of artificial, trackable particles (dye release, drogues) when released within the axial valley? Is entrainment inevitable?

- Study oscillatory flow over ridges that are not hydrothermally active. What differences in flow and hydrography would be expected? Are isopleths perturbed by oscillatory flow over the ridge as predicted by the model of (Lavelle and Cannon 2001), an affect that will vary with latitude? This could be accomplished on a dormant portion of the Juan de Fuca ridge, or the outer ridges adjacent and parallel to the Endeavour axial ridge, particularly those that are upstream in a mean sense from hydrothermal areas.

- Emplace upward-looking ADCP arrays near an isolated high B source to measure radial entrainment and/or cyclonic vorticity within the axial valley (S. Hautala and I. Berdeal, pers. comm). Groups of sources should be avoided as the vorticity signatures of adjacent sources may combine and complicate interpretation of results (*e.g.* JOYCE *et al.* 1998).

- Conduct a synoptic survey of flow over the Endeavour segment, including the flanks, with an across-ridge array of ADCPs and/or moored meters. This might require 10s of instruments and is unlikely to detect plume-induced vorticity, but would help to resolve whether mean flow over the flanks is similar to mean flow over the axis, a question with important implications for larval transport along the ridge. Are mean flows along isobaths in opposite directions on the ridge flanks as observed on the southern Juan de Fuca ridge by CANNON and PASHINSKI (1997) and predicted in general by LAVELLE and CANNON (2001)? Is shear present across the Endeavour segment, as HELFRICH *et al.* (1998) discerned it to be on the southern Juan de Fuca ridge?

5.2.2 How can hydrothermal heat flux best be determined?

The challenge of estimating the hydrothermal heat flux of MEF sources has been approached through a spectrum of methods, each with different benefits and costs. In this section I compare and contrast 4 general strategies often used for estimating the heat flux of a hydrothermal source:

1. Quantify flux at the source directly (*e.g.* GINSTER *et al.* 1994). This strategy is generally the most financially expensive.

2. Quantify flux through surface(s) of a bounding control volume to infer source flux. This is the most common strategy for quantifying heat flux in advected plumes, though many studies only survey a single surface.

3. Assess the standing stock θ (or a related variable, like [Rn]) within a bounding control volume, and then establish the rate of change of the stock to infer source heat flux

(*e.g.* ROSENBERG *et al.* 1988). The biggest disadvantage of this strategy is the amount of time it takes to survey the entire control volume, as opposed control surface(s).

4. Infer source flux through plume theory based on a measurement like rise height (*e.g.* CHERKAOUI *et al.* 1997). This strategy may be inaccurate in situations where there are multiple sources and/or variable cross flows, or where source salinity varies and is unknown.

Accurate estimation of net heat flux through a control volume

The Flow Mow study, measuring both vertical and horizontal flux components, has produced the first estimate of *net* heat flux through a set of control surfaces bounding the MEF. Earlier studies (Section 1.3) measured the vertical heat flux through specific parts of the MEF sea floor, or estimated the horizontal flux in advected plumes that may have originated, at least in part, within the MEF. With greater confidence than past estimates made in hydrothermal plumes, the Flow Mow estimate of net outward flux through the lower control volume can be taken to represent accurately the *net* heat flux into the volume through the MEF sea floor. Overall, the Flow Mow estimates improve on past results, primarily by quantifying *net* heat flux, but also by having relatively low observed uncertainties (Table 5.1): $\lesssim$20% in the mean $\overline{H}_v$; ~50% in the mean horizontal flux through the upper control volume ($\overline{H}_{qs}$); and a model-constrained uncertainty of ~150% in the mean horizontal flux through the lower control volume ($\overline{H}_h$).

Each of the isohaline heat fluxes has been calculated using a potential temperature anomaly referenced to salinity, and must therefore be corrected to compensate for the possibility of variable source salinities (*c.f* Section 1.2.7). While almost no correction is necessary for source salinities near the salinity of the ambient sea water ($\sim$ 35 psu), the freshest sources in the MEF have $\Delta_z S_o \simeq -20$ psu and require correction of $H(\Delta_S\theta)$ by a multiplicative factor C as high as 1.39. Given the observed range of source salinity in the MEF (~15–35 psu), a "best" estimate of level heat flux (based on $\Delta_z\theta$) is derived by adjusting the isohaline heat fluxes by an intermediate multiplicative factor, $C = 1.17$. The Flow Mow results are presented as both uncorrected isohaline heat flux estimates and best estimates in Table 5.1 along with previous estimates of comparable MEF heat fluxes.

Heat flux results from past Endeavour studies are summarized in Table 5.1 as published "uncorrected" estimates, and in some cases as best estimates that involve an adjustment, either to correct for the calculation of heat flux using a particular temperature anomaly (usually $\Delta_\rho\theta$), or to compensate for a source of inaccuracy identified after publication (*c.f.* Section 1.3).

Heat fluxes quantified at or just above sources have uncertainties that are low compared with heat fluxes associated with advected plumes. Retrospective adjustment of the published magnitudes is warranted in some cases, however. The estimates of MEF H_f (GINSTER *et al.* 1994; BEMIS *et al.* 1993) are both adjusted upward by extrapolating the average H_f per source to 110 high B sources known now, rather than 65 known then. The uncertainty of the BEMIS *et al.* estimate is approximated by assuming the mean H_f is the midpoint of the published range (~155 MW), and the standard error is the difference between midpoint and range extremes (±85 MW). The estimate of MEF H_d by SCHULTZ *et al.* (1992) is left unadjusted. The largest potential source of inaccuracy in the SCHULTZ *et al.* estimate of H_d is the possibility that the point measurement is not characteristic of average conditions in the area of MEF diffuse flow over which it was extrapolated.

Heat fluxes associated with advected plumes have historically been calculated using $\Delta_\rho\theta$, and should therefore be adjusted by a factor of $1/0.4 = 2.5$ (MCDUFF 1995; LAVELLE *et al.* 1998), under the assumption that the sources of the surveyed plumes had a mean $\Delta_z S_o$ in between -20 and 0 psu (*c.f.* Section 1.2.7). The THOMSON *et al.* estimates of instantaneous H_p are left unadjusted, because a multiplicative factor of 2.5 does not change their order of magnitude. However, the larger-scale mean H_p of both THOMSON *et al.* (1992) and BAKER and MASSOTH 1987 are adjusted to compensate for being calculated with $\Delta_\rho\theta$. The estimate of H_p assigned to the MEF by ROSENBERG *et al.* (1988) is left unadjusted; it involved the use of $\Delta_\rho\theta$, but only as a proxy for radon concentration.

Do the differences in the estimates in Table 5.1 suggest that a particular method is "better" than another? One metric for the accuracy of a method is the consistency of its results with other independent measures. What accounts for the consistencies and differences between the Flow Mow estimates and historical estimates of heat flux near the MEF?

Table 5.1: Summary of uncorrected and best estimates of heat flux from the Flow Mow and other Endeavour studies, including magnitudes expressed as absolute values. Rows above the single line hold estimates of fluxes through distinct surfaces of the Flow Mow control volume: mean vertical flux between upper and lower control volumes, $\overline{H}_v$; mean quasi-synoptic net horizontal flux through upper volume, $\overline{H_{qs}}$; mean net horizontal flux through lower volume; vertical flux through diffuse MEF vents, H_d, inferred from a heat flux balance in the lower control volume between $\overline{H}_v^*$, $\overline{H}_h^*$, and the best estimate of $H_f \sim 615\,\mathrm{MW}$ from GINSTER *et al.* 1994 (*c.f.* Section 3.3.3). Lower rows contain published (uncorrected) estimates and in some cases best estimates from past studies, as discussed in the text. Uncertainty is estimated as the standard deviation (of samples or mean) over the mean value; standard deviation of summed quantities is computed as combined standard uncertainty.

Heat flux	Uncorrected Estimate [MW]	Best Estimate [MW]	Uncertainty [%]	Probable source(s)
$\overline{H}_v$, $\overline{H}_v^*$	550±100	643±116	18	MEF H_f & H_d
$\overline{H}_{qs}$, $\overline{H}_{qs}^*$	378±182	442±213	48	MEF H_f & H_d
$\overline{H}_h$, $\overline{H}_h^*$	65±100	76±114	154	MEF H_d
$\overline{H}_v^* + \overline{H}_h^*$		719±220	23	MEF total: $H_f + H_d$
Inferred H_d		104±253	50	MEF H_d
GINSTER *et al.* 1994	364±73	615±123	20	MEF H_f
BEMIS *et al.* 1993	70–239	359–1224	∼55	MEF H_f
SCHULTZ *et al.* 1992	9600±760		8	MEF H_d
THOMSON *et al.* 1992 (instantaneous)	12,000±6000			H_p: MEF (& other fields?)
THOMSON *et al.* 1992 (mean)	995±605	2500±1525	61	H_p: MEF (& other fields?)
BAKER and MASSOTH 1987	1700±1100	4250±2750	65	H_p: MEF (& other fields?)
ROSENBERG *et al.* 1988	3000±2000		67	H_p: MEF (& other fields?)

The observations and models considered in this dissertation help to evaluate 3 possible responses:

- Estimates of H_p are expected to be higher than MEF source fluxes because (1) the associated plumes may integrate contributions from other fields that will not be accounted for without assessing an upstream control surface, and (2) in oscillatory flow, plume fluid can alternately pool over and stream from a source, resulting in high variance of the net heat flux through the surfaces of a bounding control volume.

- H_f and H_d may be changing over time.

- Distinct assumptions, especially concerning spatial extrapolation, underlie the methods of quantifying each flux and assessing uncertainty.

Despite their relatively high magnitude, the best estimates of mean H_p from past studies (Table 5.1) fall within the range of heat flux magnitudes generated by the puff model. With a 600 MW source and observed flow over the Endeavour ridge, the modeled heat fluxes — both net instantaneous values and means through individual surfaces — commonly exhibit peak magnitudes of 1000–5000 MW. In contrast, the modeled range does not encompass the values of instantaneous H_p estimated by Thomson *et al.* (1992). The large instantaneous H_p magnitudes probably result from a fast observed mean current (10 cm/s) being applied to a plume that had previously pooled over the MEF (and possibly adjacent, upstream fields), rather than a plume steadily streaming from the MEF (as was assumed). Had an upstream surface been assessed, the magnitude of the flux might be reduced to the magnitude of the MEF source flux estimates. The estimates of mean H_p by both Thomson *et al.* (1992) and Baker and Massoth 1987, based on segment-scale hydrographic surveys, most likely are associated with hydrothermal plumes from multiple fields along the Endeavour and should be associated with the entire segment, not only the MEF. For similar reasons, the estimate of H_p assigned to the MEF by Rosenberg *et al.* (1988) is probably an overestimate. If the upper level flow was typical during their experiment, then extra radon (from the MEF and/or adjacent sources) likely accumulated in a plume that was intermittently pooling and streaming, rather than extending downstream in a steady state, as was assumed. This would increase the volume integral of radon concentration in Equation 1.27, resulting in overestimation of the source heat source flux.

Because of the oscillatory nature of deep sea currents, the net mean horizontal heat flux will rarely equal the input flux, even when evaluated for a control volume that contains a steady source heat flux. This has serious ramifications for past estimates of H_p that assume a steady-state hydrothermal plume distribution in a constant mean cross flow (*c.f.* 1.3.1). Re-interpretation of past hydrographic observations, and possibly renewed analysis with puff models forced by historic current meter records, could refine or clarify the significance of the previous heat flux estimates.

With the exception of the H_d estimated by SCHULTZ *et al.* (1992), the historic estimates of heat flux based on measurements made at or immediately above MEF sources are consistent with each other and with the Flow Mow estimate of net outward heat flux through the lower control volume (Table 5.1). The magnitudes of H_f estimated by (GINSTER *et al.* 1994) and (BEMIS *et al.* 1993) are consistent within their respective uncertainty and range, and are comparable to the net outward flux $\overline{H}_v^* + \overline{H}_h^*$. One explanation for the 2 orders of magnitude difference between the inferred and observed estimates of H_d is that the nature of diffuse and/or focused venting in the MEF changed over the ~10 years that elapsed between the the past investigations and the Flow Mow study in 2000. This possibility is called into question by the relative stability of source fluid temperatures observed within the MEF since the mid-1980s (*e.g.* BUTTERFIELD *et al.* 1994). Though it is possible that flow through vents has decreased while temperatures remained constant, and thereby lowered heat fluxes over time, it is unlikely. I assume that H_d did not decrease 2 orders of magnitude over ~10 years, and that the infered value of H_d is not in error by more than ~250 MW. Based on a review of past methods, particularly those of SCHULTZ *et al.* (1992) and (GINSTER *et al.* 1994), I apply Occam's razor and suggest that a simpler explanation for the difference is that the H_d of SCHULTZ *et al.* (1992) is an overestimate caused by inaccurate extrapolation of a point measurement to the top surfaces of all known sulfide structures in the MEF. While the estimate of the total surface area used in the extrapolation is unlikely to be off by more than an order of magnitude, reasonable variations in diffuse θ and w across the

MEF could account for the 2 order of magnitude discrepancy.

A final ramification of a velocity field that oscillates with periods as short as $\sim$12 hr is that the inference of H_f from observed rise height using the equation for quiescent, stratified environments (MORTON *et al.* 1956) can result in high variance on short time scales (*e.g.* CHERKAOUI *et al.* 1997). Since the maximum rise height of a plume (z^*) from a focused high B source is a function of ${H_f}^{1/4}$ (MORTON *et al.* 1956; TURNER 1986), the observed change in the upper MEF plume boundary ($\pm$50 m from a mean of $\sim$400 m) would require an unreasonably large change in H_f. This suggests that factors other than H_f exert dominant control on the maximum rise height. Given the observed variability in u and N, both of which affect z^*, using a rise height equation to infer H_f from the MEF would be fruitless.

The Endeavour environment makes the control surface methodology advantageous for a key reason: the distance between known hydrothermal sources along the Endeavour segment is similar to the displacement achieved by local current oscillations. This means plumes from one venting area will commonly be located above an adjacent venting area. The Flow Mow methodology successfully accounted for such juxtaposition of plumes, leading to heat flux estimates that are more likely than past estimates to be related to a specific area of sea floor: the MEF. Future attempts to infer source heat flux from measurements made in advected hydrothermal plumes should utilize a control volume methodology to estimate *net* H_p and associate it definitively with the enclosed area of sea floor.

Future work on heat flux

A recent proposal, funded by the National Science Foundation in December, 2002 (R. McDuff and R. Thomson), will build on the Flow Mow methodology, but will involve a bigger control volume. At its largest, the volume will be bounded by the axial valley walls, 2 instrumented cross-sections of the axial valley (oriented orthogonal to the axis), and a top surface that intercepts rising plumes at an optimal elevation ($\sim$75 m) over all known hydrothermal sources. ABE will measure H_v on key portions of the top surface while flow and hydrography are monitored continuously on the cross-sections by ADCP arrays, moored instruments, and CTD VOTs. Heat flux estimates for individual fields, like those presented for the MEF in this thesis, will be summed over all known fields to obtain a segment-scale flux. An overarching goal of the new study will be to assess the "Sea Breeze" hypothesis: mean flows within the axial valley are driven by entrainment and are therefore directly related to the integrated hydrothermal heat flux of all sources in the topographically-bounded control volume.

This hypothesis is motivated by observed convergence of mean flow within the axial valley (THOMSON *et al.* 2003) and an intriguing consistency between the horizontal transport inferred from the observed mean flow and the total expected vertical transport in plumes rising from known hydrothermal fields (R. McDuff, pers. comm. and THOMSON *et al.* 2003). Assuming that the majority of fluid entrained by plumes rising from sources within the axial valley is drawn in horizontally below a surface ∼75 mab (rather than vertically down through that surface), then the along-axis transport (Q_h) can be estimated as the product of the valley cross-section (A_h) and the along-axis mean flow ($\overline{u}$):

$$Q_h = A_h \overline{u}. \tag{5.2}$$

Using an average value of $A_h = 4.5 \times 10^4\,\mathrm{m}^2$ measured with bathymetric data and $\overline{u}$ of 0.016 to 0.044 m/s observed at FM-S50 and FM-N15, respectively (Table 2.1), Equation 5.2 yields Q_h =720–1980 m^3/s.

The total vertical transport in plumes rising through the surface 75 mab from all known hydrothermal fields within the axial valley (Q_{75}) can be estimated by first computing Q_v for the MEF and then extrapolating to other venting areas based on the relative number of vents, each with source transport Q_f. Taking the dilution factor to be ∼1500 at 75 mas,

$$Q_v = 1500 Q_f = 1500 \frac{H_f}{\rho c_p \Delta_z \theta}. \tag{5.3}$$

With $H_f = 615$ MW (Table 5.1), $\Delta_z\theta$ =350 °C, and $\rho c_p = 4.2\,\mathrm{MJ \cdot m^{-3} \cdot {}^\circ C^{-1}}$, Equation 5.3 yields Q_v =627 m^3/s.

To estimate Q_{75}, I assume that the MEF heat flux (from ∼110 known high B sources) is about equal to the combined heat flux from all other axial sources: High Rise (∼25 sources), Salty Dawg (∼10 sources), Mothra (∼20 sources), known diffuse flow sites, and other suspected sites (an unknown number of sources between High Rise and Salty Dawg and between MEF and Mothra). This leads to $Q_{75} \simeq 2Q_v \simeq 1250\,\mathrm{m}^3/\mathrm{s}$.

Thus, Q_{75} is approximately equal to Q_h. Significant inflow over the northern sill could increase Q_h, but it will still be of the same order of magnitude as Q_{75}. Since the valley cross-sectional area A varies along axis, if integrated entrainment is driving the flow, then spatial accelerations will be expected near topographic constrictions. This is a possible explanation for the distinct magnitudes of the mean flows observed at the near-bottom current meters south and north of the MEF(*c.f.* Subsection 2.4.2).

Instrumenting the segment will help to discern whether warm near-bottom fluid is exported laterally below the equilibrium depths, vertically through entrainment in higher-rising plumes, or both. An outstanding question is whether heat flux associated with conduction (H_c) or diffuse flow (H_d) through the sea floor of the entire axial valley is ultimately entrained by high B plumes, and thereby integrated in H_v. If this is the case, it may be possible to establish a simple relationship between that segment-scale heat flux H_s and transport into the axial valley Q_h. Such a relationship would enable continuous measurement of $\overline{u}_h$ to be used to detect changes in hydrothermal output, particularly those that may occur in response to a seismic or volcanic event within the valley.

When topographic relief and plume rise height are of similar scale, such a proxy measurement of segment scale heat flux H_s might be realized economically with a minimal density of current meters, possibly only a single central meter 10–50 mab at each end of the axial valley. This may not be possible in the much broader axial valleys of the MAR and other slow-spreading centers, but moorings spaced ∼3 km apart over a ∼14 km wide valley in the "bath tub" experiment of Murton *et al.* (1999) suggest that the mean flows may be well-correlated across the valley, at least near the bottom.

5.3 Implications

5.3.1 A heat budget for newly formed oceanic crust

Estimates of the hydrothermal heat flux from the MEF and Endeavour segment (Table 5.1) are significantly higher than expected from basic models of crustal formation and cooling

(Wilcock and Delaney 1996; R. McDuff, Marine Geological Processes course notes, www2.ocean.washington.edu/oc540). Assuming a crustal thickness of $h \simeq 6$ km, an average density of $\rho_r = 2950$ kg/m^3, and a full spreading rate of $u_r \simeq 6$ cm/yr for the Juan de Fuca ridge, the rate of production of crust per km of ridge is $Q_R = \rho_r h u_r \simeq 3\times10^{-2}\,\mathrm{kg{\cdot}s^{-1}{\cdot}km^{-1}}$. If we further assume that magma forming the crust solidifies completely and is convectively cooled from $T_o = 1200$°C to $T_f = 200$°C by high T hydrothermal circulation within the axial zone, then the power loss per km of ridge (H_R) can be estimated as

$$H_R \;=\; Q_R(L_r + \int_{T_o}^{T_f} c_r(T)dT) = 42\,\mathrm{MW/km} \tag{5.4}$$

in which L_r is the latent heat of crystallization for basalt or gabbro (400 kJ/kg) and c_r is the specific heat capacity of the rock (1 kJ·kg^{-1}·°C^{-1}) (Turcotte and Schubert 1982).

The value in Equation 5.4, 42 MW/km, is consistent with the estimates of Wilcock and Delaney (1996) for heat fluxes per km of ridge required to maintain a steady-state magma lens at 1.5 km depth in 6 km thick crust spreading at a full rate of 10 cm/s. In their more detailed assessment, the heat flux from the cooling of dikes and extrusives is 21 MW/km, the flux through the top of the magma lens is 16 MW/km, and the flux from cooling the lower crust is up to 48 MW/km (Wilcock and Delaney 1996, Figure 1). Thus, the heat flux associated with hydrothermal circulation that potentially reaches axial sea floor vents has an expected range of 21–85 MW/km, which includes the estimate in Equation 5.4.

Applying $H_R = 42$ MW/km to the Juan de Fuca ridge, which extends ~500 km between the Sovanco and Blanco transform faults, the mean convective heat flux over geologic time scales is ~21 GW. Over the ~10 km length of the Endeavour segment where high T venting has been observed, the expected heat flux from the segment is ~420 MW.

In contrast, the total heat flux from just 1 of 5 known major high-temperature vent fields, the MEF, is 719±220 MW (Table 5.1). Under the assumption that the MEF is cooling a 2 km length of the ridge, the long-term hydrothermal heat flux for the whole field is not expected to be more than ~82 MW. What could account for the difference between the theoretical long-term mean flux and the observed convective heat flux?

One possibility, implied by the morphology of the segment, is that the magma supply is intermittent. Kappel and Ryan (1986) argue that parallel sets of ridges, like those that flank the central Endeavour ridge, begin on axis as whole ridges formed during periods dominated by magmatic activity. During subsequent periods when tectonism dominates, the central ridge is split and the 2 halves become separated over time, first by an axial valley, and then by deep basins. If the rate of production of crust increases by a factor of 2, then the mean heat flux could approach ~840 MW during the magmatic period. The heat flux from a rapidly emplaced volcanic ridge and the fresh underlying crust will be initially high and decay over time (Wilcock and Delaney 1996), generating a time series of instantaneous heat flux that yields the long-term mean in Equation 5.4.

An alternative explanation is that the temporal evolution of the flux of heat through the MEF is related to the nature of the *underlying* heat source and the mechanisms which transfer energy from magma to hydrothermal fluid. In the process of solidifying an axial magma chamber, a cracking front descending through the crust is expected to generate a relatively continuous heat flux function that decreases slowly over time (Lister 1974). In contrast, intrusions of magma from a chamber into the upper crust occur intermittently, with each diking events cooled successively (Wilcock and Delaney 1996). Convective cooling of an individual dike, like the one that induced hydrothermal convection and fed a surface sheet flow on the CoAxial segment in 1993, lead to convective heat fluxes per km of dike that are initially ~10,000 MW/km and decrease to ~1000 MW/m in about 1 yr (Cherkaoui *et al.* 1997).

Motivated by a desire to determine whether the MEF is powered by intermittent intrusions of magma or the heat flux from an axial magma chamber, the Flow Mow study was proposed to acquire a time series: precise estimates of heat flux through the MEF once a year, over a 3 year period. The investigation was funded only for a single field season, however; this is unfortunate from a geophysical perspective, because it is the temporal change in the heat flux magnitude that enables discrimination between 2 of the volcanic processes that form oceanic crust. Thankfully, the Sea Breeze proposal has been funded and will lead to repeat measurements of the MEF heat flux over the next few years.

BIBLIOGRAPHY

ALLEN, S. E. and R. E. THOMSON, 1993 Bottom-Trapped Subinertial Motions Over Midocean Ridges in a Stratified Rotating Fluid. J. Phys. Oceanogr. **23:** 566–581.

BAKER, E. T., J. W. LAVELLE, R. A. FEELY, G. L. MASSOTH, and S. L. WALKER, 1989 Episodic venting of hydrothermal fluids from the Juan de Fuca Ridge. J. Geophys. Res. **94:** 9237–9250.

BAKER, E. T. and G. J. MASSOTH, 1986 Hydrothermal Plume Measurements: A Regional Perspective. Science **234:** 980–982.

BAKER, E. T. and G. J. MASSOTH, 1987 Characteristics of hydrothermal plumes from two vent fields on the Juan de Fuca Ridge, northeast Pacific Ocean. Earth Planet. Sci. Lett. **85:** 59–73.

BAKER, E. T., G. J. MASSOTH, and R. A. FEELY, 1987 Cataclysmic hydrothermal venting on the Juan de Fuca Ridge. Nature **329:** 149–151.

BAKER, E. T., G. J. MASSOTH, S. L. WALKER, and R. W. EMBLEY, 1993 A method for quantitatively estimating diffuse and discrete hydrothermal discharge. Earth Planet. Sci. Lett. **118:** 235–249.

BEMIS, K. G., 1990 Geothermal heat flux from hydrothermal plumes on the Juan de Fuca ridge. Master's thesis, Massachusetts Institute of Technology, pp. 131, MIT Library, Boston, USA.

BEMIS, K. G., R. P. VON HERZEN, and M. J. MOTTL, 1993 Geothermal heat flux from hydrothermal plumes on the Juan de Fuca Ridge. J. Geophys. Res. **98:** 6351–6369.

BISCHOFF, J. L. and R. J. ROSENBAUER, 1985 An empirical equation of state for hydrothermal seawater (3.2% NaCl). Am. J. Sci. **285:** 725–763.

Briggs, G. A., 1969 Plume Rise. U.S. Atomic Energy Commission Critical Review Series. 81pp.

Butterfield, D. A., R. E. McDuff, M. Mottl, M. D. Lilley, G. J. Massoth, and J. E. Lupton, 1994 Gradients in the composition of hydrothermal fluids from the Endeavor Ridge vent field: Supercritical phase separation and brine loss. J. Geophys. Res. **99:** 9561–9583.

Cannon, G. and D. Pashinski, 1997 Variations in mean currents affecting hydrothermal plumes on the Juan de Fuca Ridge. J. Geophys. Res. **102:** 24965–24976.

Cannon, G. A., D. J. Pashinski, and M. R. Lemon, 1991 Mid-depth flow near hydrothermal venting sites on the southern Juan de Fuca Ridge. J. Geophys. Res. **96:** 12815–12831.

Cannon, G. A., D. J. Pashinski, and M. R. Lemon, 1993 Hydrothermal effects west of the Juan de Fuca Ridge. Deep Sea Res. **40:** 1447–1457.

Cherkaoui, A. S. M., W. S. D. Wilcock, and E. T. Baker, 1997 Thermal fluxes associat4ed with the 1993 diking event on the CoAxial segment, Juan de Fuca ridge: A model for the convective cooling of a dike. J. Geophys. Res. *102*(B11)**:** 24887–24902.

Csanady, G. T., 1973 *Turbulent diffusion in the environment*. Holland: D. Reidel Publishing Company, pp. 248.

Delaney, J. R., M. Lilley, R. E. McDuff, D. Kelley, W. Wilcock, and V. Robigou, 1996 Cellular hydrothermal circulation in a submarine system. Eos. Trans. AGU **77:** 756.

Delaney, J. R., V. Robigou, R. E. McDuff, and M. K. Tivey, 1992 Geology of a Vigorous Hydrothermal System on the Endeavour Segment, Juan de Fuca Ridge. J. Geophys. Res. *97*(19)**:** 19663–19682.

Dymond, J. and S. Roth, 1988 Plume dispersed hydrothermal particles: A time series record of settling flux from Endeavour Ridge using moored sensors. Geochim. Cosmochim. Acta **52:** 2525–2536.

Edmond, J. M., K. L. Von Damm, C. I. Measures, and R. E. McDuff, 1982 Chemistry of hot springs on the East Pacific Rise and their effluent dispersal. Nature **297:** 187–191.

Elvers, D., S. Srivastava, K. Potter, J. Morley, and D. Solidel, 1973 Asymmetric spreading across the Juan de Fuca and Gorda rises as obtained from a detailed magnetic survey. Earth Planet. Sci. Lett. **20:** 211–219.

Emery, W. J. and R. E. Thomson, 2001 *Data analysis methods in physical oceanography.* Netherlands: Elsevier, pp. 638.

Fischer, H. B., E. J. List, R. C. Y. Koh, J. Imberger, and N. H. Brooks, 1979 *Mixing in inland and coastal waters.* San Diego, CA, USA: Academic.

Fofonoff, 1985 Physical properties of seawater. J. Geophys. Res. **90:** 3332–3342.

Franks, S., 1992 Temporal and spatial variability in the Endeavour ridge neutrally buoyant hydrothermal plume: Patterns, forcing mechanisms and biogeochemical implications. Ph. D. thesis, Corvallis, OR, USA.

Ginster, U., M. J. Mottl, and R. P. Von Herzen, 1994 Heat flux from black smokers on the Endeavor and Cleft segments, Juan de Fuca Ridge. J. Geophys. Res. **99:** 4937–4950.

Gold, T., 1992 The deep, hot biosphere. Proc. Natl. Acad. Sci. **89:** 6045–6049.

Group, M., 1984 Regional setting and local character of a hydrothermal field/sulfide deposit on the Endeavour Segment of the Juan de Fuca Ridge. EOS **65:** 1111.

Halliday, D. and R. Resnick, 1988 *Fundamentals of physics.* USA: John Wiley & Sons, pp. 977.

Hammond, S. R., J. S. Lee, A. Malahoff, R. Feely, E. R. W., and J. Franklin, 1984 Discovery of high-temperature hydrothermal venting on the Endeavour Segment of the Juan de Fuca Ridge. EOS **65:** 1111.

Helfrich, K. R. and T. Battisti, 1991 Experiments on baroclinic vortex shedding from hydrothermal plumes. J. Geophys. Res. **96:** 12,511–12,518.

Helfrich, K. R., T. M. Joyce, G. A. Cannon, S. A. Harrington, and D. J. Pashinski, 1998 Mean hydrographic and velocity sections near Pipe Organ vent at Juan de Fuca Ridge. Geophys. Res. Lett. **25:** 1737–1740.

Helfrich, K. R. and K. G. Speer, 1995 Oceanic Hydrothermal Circulation: Mesoscale and Basin-Scale Flow. In S. E. Humphris, R. A. Zierenberg, L. S. Mullineaux, and R. E. Thomson (Eds.), *Seafloor Hydrothermal Systems: Physical, Chemical, Biological, and Geological Interactions*, pp. 347–356. American Geophysical Union.

Hoult, D. P., J. A. Fay, and L. J. Forney, 1969 A theory of plume rise compared with field observations. Journal of the Air Pollution Control Association **19:** 585–590.

Johnson, H., S. Hautala, M. Tivey, C. Jones, J. Voight, M. Pruis, I. Garcia-Berdeal, L. Gilbert, T. Bjorklund, W. Fredericks, J. Holand, M. Tsurumi, T. Kurakawa, K. Nakamura, K. O'Connell, L. Thomas, S. Bolton, and J. Turner, 2002 Survey studies hydrothermal circulation on the northern Juan de Fuca Ridge. Eos Trans. AGU *83*(8)**:** 73–79.

Joyce, T. M., G. A. Cannon, K. R. Helfrich, S. A. Harrington, and D. Pashinski, 1998 Vertical and temporal vorticity observation at Juan de Fuca Ridge: hydrothermal signatures. Geophys. Res. Lett. **25:** 1741–1744.

Kadko, D. C. and W. S. Moore, 1988 Radiochemical constraints on the crustal residence time of submarine hydrothermal fluids: Endeavour ridge. Geochim. Cosmochim. Acta **52:** 659–668.

Kadko, D. C., N. D. Rosenberg, J. E. Lupton, R. W. Collier, and M. D. Lilley, 1990 Chemical reaction rates and entrainment within the Endeavor Ridge hydrothermal plume. Earth Planet. Sci. Lett. **99:** 315–335.

Kappel, E. and W. Ryan, 1986 Volcanic episodicity and a nonsteady rift valley along Northeast Pacific spreading centers: Evidence from SeaMARCI. J. Geophys. Res. **91:**

13925–13940.

Keller, G. H., S. H. Anderson, and J. W. Lavelle, 1975 Near-bottom Currents in the Mid-Atlantic Ridge Rift Valley. Can. J. Earth Sci. **12:** 703–710.

Kelley, D., J. Baross, and J. Delaney, 2002 Volcanoes, Fluids, and Life in Submarine Environments. Annu. Rev. Earth Planet. Sci. **30:** 385–491.

Kim, S. L., L. S. Mullineaux, and K. R. Helfrich, 1994 Larval dispersal via entrainment into hydrothermal vent plumes. J. Geophys. Res. **99:** 12655–12665.

Lavelle, J. W., 1994 A convection model for hydrothermal plumes in a cross flow. NOAA Technical Memorandum, ERL PMEL-102, pp. 18.

Lavelle, J. W., 1997 Buoyancy-driven plumes in rotating, stratified cross flows: Plume dependence on rotation, turbulent mixing, and cross-flow strength. J. Geophys. Res. **102:** 3405–3402.

Lavelle, J. W., E. T. Baker, and G. J. Massoth, 1998 On the calculation of total heat, salt and tracer fluxes from ocean hydrothermal events. Deep Sea Res., Part II **45:** 2619–2636.

Lavelle, J. W. and G. A. Cannon, 2001 On subinertial oscillations trapped by the Juan de Fuca Ridge, northeast Pacific. J. Geophys. Res. *106*(C11)**:** 31099–31116.

Lavelle, J. W., M. A. Wetzler, E. T. Baker, and R. W. Embley, 2001 Prospecting for hydrothermal vents using moored current and temperature data: Axial Volcano on the Juan de Fuca ridge, northeast Pacific. J. Phys. Ocean **31:** 827–838.

Lilley, M., R. Feely, and J. Trefry, 1995 Chemical and biological transformations in hydrothermal plumes. In S. E. Humphris, R. A. Zierenberg, L. S. Mullineaux, and R. E. Thomson (Eds.), *Seafloor Hydrothermal Systems: Physical, Chemical, Biological, and Geological Interactions*, pp. 369–391. American Geophysical Union.

Lister, C. R. B., 1974 On the penetration of water into hot rocks. Geophys. J. R. Astron. Soc. **39:** 465–509.

LITTLE, S. A., K. D. STOLZENBACH, and R. P. VON HERZEN, 1987 Measurements of plume flow from a hydrothermal vent field. J. Geophys. Res. **92:** 2587–2596.

LUPTON, J. E., 1995 Hydrothermal plumes: Near and far field. In S. E. Humphris, R. A. Zierenberg, L. S. Mullineaux, and R. E. Thomson (Eds.), *Seafloor Hydrothermal Systems: Physical, Chemical, Biological, and Geological Interactions*, pp. 317–346. American Geophysical Union.

LUPTON, J. E., E. T. BAKER, N. GARFIELD, G. J. MASSOTH, R. A. FEELY, J. P. COWEN, R. R. GREENE, and T. A. RAGO, 1998 Tracking the evolution of a hydrothermal event plume with a RAFOS neutrally buoyant drifter. Science **280:** 1052–1055.

LUPTON, J. E., J. R. DELANEY, H. P. JOHNSON, and M. K. TIVEY, 1985 Entrainment and vertical transport of deep-ocean water by buoyant hydrothermal plumes. Nature **316:** 621–623.

LUPTON, J. E., G. P. KLINKHAMMER, W. R. NORMARK, R. HAYMON, K. C. MACDONALD, R. F. WEISS, and H. CRAIG, 1980 Helium-3 and Manganese at the 21°N East Pacific Rise hydrothermal Site. Earth Planet. Sci. Lett. **50:** 115–127.

MCCOLLOM, T. and E. SHOCK, 1997 Geochemical constraints on chemolithoautotrophic metabolism by microorganisms in seafloor hydrothermal systems. Geochim. Cosmochim. Acta **61:** 4375–4391.

MCDOUGALL, T. J., 1990 Bulk properties of "hot smoker" plumes. Earth Planet. Sci. Lett. **99:** 185–194.

MCDUFF, R. E., 1995 Physical dynamics of deep-sea hydrothermal plumes. In S. E. Humphris, R. A. Zierenberg, L. S. Mullineaux, and R. E. Thomson (Eds.), *Seafloor Hydrothermal Systems: Physical, Chemical, Biological, and Geological Interactions*, pp. 357–368. American Geophysical Union.

MCLAUGHLIN, E. A., 1998 Microbial hydrogen oxidation associated with deep-sea hydrothermal vent environments. Ph. D. thesis, Seattle, WA, USA.

Middleton, J. H. and R. E. Thomson, 1986 Modeling the rise of hydrothermal plumes. Can. Tech. Rep. Hydrog. Ocean. Sci. **69:** 1–18.

Morton, B. R., G. I. Taylor, and J. S. Turner, 1956 Turbulent gravitational convection from maintained and instantaneous sources. Proc. R. Soc. Lond. **A234:** 1–13.

Mullineaux, L. S. and S. C. France, 1995 Dispersal mechanisms of deep-sea hydrothermal vent fauna. In S. E. Humphris, R. A. Zierenberg, L. S. Mullineaux, and R. E. Thomson (Eds.), *Seafloor Hydrothermal Systems: Physical, Chemical, Biological, and Geological Interactions*. Washington, DC: American Geophysical Union.

Murton, B., L. Redbourn, C. German, and E. Baker, 1999 Sources and fluxes of hydrothermal heat, chemicals and biology within a segment of the Mid-Atlantic ridge. Earth Planet. Sci. Lett. **171:** 301–317.

Okubo, A., 1971 Oceanic diffusion diagrams. Deep-Sea Research **18:** 789–802.

Papanicolaou, P. N. and E. J. List, 1987 Statistical and spectral properties of tracer concentration in round bouyant jets. Int. J. Heat Mass Transfer **30:** 2059–2071.

Pasquill, F., 1974 *Atmospheric diffusion: the dispersion of windborne material from industrial and other sources*. New York: Halsted Press, pp. 429.

Rao, K. S., R. M. Eckman, and R. Hosker, 1989 Simulation of tracer concentration data in the Brush Creek drainage flow using an integrated puff model. Journal of Applied Meteorology **28:** 609–616.

Rona, P. and A. Trivett, 1992 Discrete and diffuse heat transfer at ASHES vent field, Axial Volcano, Juan de Fuca Ridge. Earth Planet. Sci. Lett. **109:** 57–71.

Rona, P. A., D. R. Jackson, T. Wen, C. Jones, K. Mitsuzawa, K. G. Bemis, and J. G. Dworski, 1997 Acoustic mapping of diffuse flow at a seafloor hydrothermal site: Monolithy Vent, Juan de Fuca Ridge. Geophys. Res. Lett. **24:** 2351–2354.

Rona, P. A., D. R. Palmer, C. Jones, D. A. Chayes, M. Czarnecki, E. W.

Carey, and J. C. Guerrero, 1991 Acoustic Imaging of hydrothermal Plumes, EPR, 21°N, 109°W. Geophys. Res. Lett. **18:** 2233–2236.

Rosenberg, N. D., J. E. Lupton, D. Kadko, R. Collier, M. D. Lilley, and H. Pak, 1988 Estimation of heat and chemical fluxes from a seafloor hydrothermal vent field using Radon measurements. Nature **334:** 604–607.

Roth, S. E. and J. Dymond, 1986 Where wafts the hydrothermal plume? A moored-sensor record of lateral particle flux above Endeavour ridge. EOS Trans. AGU **67:** 1027.

Rudnicki, M. D., R. H. James, and H. Elderfield, 1994 Near-field variability of the TAG non-buoyant plume, 26°N, Mid-Atlantic Ridge. Earth Planet. Sci. Lett. **127:** 1–10.

Schey, H. M., 1992 *Div, grad, curl, and all that: An informal text on vector calculus.* New York, USA: W. W. Norton & Company, pp. 163.

Schnell, K. B. and P. R. Dey, 2000 *Atmospheric dispersion modeling compliance guide*. USA: McGraw-Hill.

Schultz, A., J. R. Delaney, and R. E. McDuff, 1992 On the partitioning of heat flux between diffuse and point source seafloor venting. J. Geophys. Res. **97:** 12299–12314.

Smith, W. H. F. and D. T. Sandwell, 1997 Global Seafloor Topography from Satellite Altimetry and Ship Depth Soundings. Science **277:** 1956–1962.

Speer, K. G., 1989 A forced baroclinic vortex around a hydrothermal plume. Geophys. Res. Lett. **16:** 461–464.

Speer, K. G. and J. Marshall, 1995 The growth of convective plumes at seafloor hot springs. J. Mar. Res. **53:** 1025–1057.

Speer, K. G. and P. A. Rona, 1989 A Model of an Atlantic and Pacific hydrothermal plume. J. Geophys. Res. **94:** 6213–6220.

STAHR, F. R., R. E. MCDUFF, and S. R. VEIRS, in preparation, 2003 Vertical heat flux at the Main Endeavour Field. Geochem. Geophys. Geosyst.

STEIN, C. A., S. STEIN, and A. M. PELAYO, 1995 Heat flow and hydrothermal circulation. In S. E. Humphris, R. A. Zierenberg, L. S. Mullineaux, and R. E. Thomson (Eds.), *Seafloor Hydrothermal Systems: Physical, Chemical, Biological, and Geological Interactions*, pp. 425–445. American Geophysical Union.

THOMSON, R., 1981 *Oceanography of the British Columbia coast*. Canada: Canadian Special Publication of Fish and Aquatic Sciences 56, pp. 291.

THOMSON, R. E., E. E. DAVIS, and B. J. BURD, 1995 Hydrothermal venting and geothermal heating in Cascadia Basin. J. Geophys. Res. **100:** 6121–6141.

THOMSON, R. E., J. R. DELANEY, R. E. MCDUFF, D. R. JANECKY, and J. S. MCCLAIN, 1992 Physical characteristics of the Endeavour Ridge hydrothermal plume during July 1988. Earth Planet. Sci. Lett. **111:** 141–154.

THOMSON, R. E., R. L. GORDON, and J. DYMOND, 1989 Acoustic Doppler Current Profiler Observations of a Mid-Ocean Ridge hydrothermal Plume. J. Geophys. Res. **94:** 4709–4720.

THOMSON, R. E., P. H. LEBLOND, and A. B. RABINOVICH, 1998 Satellite-tracked drifter measurement of inertial and semidiurnal currents in the northeast Pacific. J. Geophys. Res. *103*(C1)**:** 1039–1052.

THOMSON, R. E., S. F. MIHALY, A. B. RABINOVICH, R. E. MCDUFF, S. R. VEIRS, and F. R. STAHR, in revision, 2003 Topographically Constrained Circulation at Endeavour Ridge: Implications for the Colonization of Hydrothermal Vent Fields. Nature.

THOMSON, R. E., S. E. ROTH, and J. DYMOND, 1990 Near-Inertial Motions Over a Midocean Ridge — Effects of Topography and Hydrothermal Plumes. J. Geophys. Res. **95:** 7261–7278.

THURNHERR, A., K. RICHARDS, C. GERMAN, G. LANE-SERFF, and K. SPEER, 2002 Flow and Mixing in the Rift Valley of the Mid-Atlantic Ridge. J. Phys. Ocean. **132:** 1763–1778.

THURNHERR, A. M., 2000 Hydrography and flow in the rift valley of the Mid-Atlantic ridge. Ph. D. thesis, University of Southampton, England.

TIVEY, M. K. and J. R. DELANEY, 1986 Growth of large sulfide structures on the Endeavour Segment of the Juan de Fuca Ridge. Earth Planet. Sci. Lett. **77:** 303–317.

TURCOTTE, D. L. and G. SCHUBERT, 1982 *Geodynamics: Applications of continuum physics to geological problems*. USA: John Wiley & Sons, pp. 450.

TURNER, J. S., 1973 *Buoyancy Effects in Fluids*. Cambridge University Press. 368 pp.

TURNER, J. S., 1986 Turbulent entrainment: The development of the entrainment assumption, and its application to geophysical flows. J. Fluid. Mech. **173:** 431–471.

TURNER, J. S. and I. H. CAMPBELL, 1987 Temperature, density and buoyancy fluxes in "black smoker" plumes, and the criterion for buoyancy reversal. Earth Planet. Sci. Lett. **86:** 85–92.

VAN DOVER, C. and A. CHAVE, 1996 Light at deep-sea hydrothermal vents. Geophysical Research Letters **23:** 204–209.

VEIRS, S. R., R. E. MCDUFF, M. D. LILLEY, and J. R. DELANEY, 1999 Locating hydrothermal vents by detecting buoyant, advected plumes. J. Geophys. Res. **104:** 29239–29247.

WEISS, R. F., P. LONSDALE, J. E. LUPTON, A. E. BAINBRIDGE, and H. CRAIG, 1977 Hydrothermal plumes in the Galapagos Rift. Nature **267:** 600–603.

WESSEL, P. and W. SMITH, 1991 Free software helps map and display data. EOS Trans. AGU **72:** 441.

WETZLER, M. A., J. W. LAVELLE, G. A. CANNON, and E. T. BAKER, 1998 Variability of temperature and currents measured near Pipe Organ hydrothermal vent site. Mar.

Geophys. Res. *20*(6)**:** 505–516.

WILCOCK, W. and J. DELANEY, 1996 Mid-ocean ridge sulfide deposits: evidence for heat extraction from magma chambers or cracking fronts? Earth Planet. Sci. Lett. **145:** 49–64.

YOERGER, D., P. MURRAY, and F. STAHR, November, 2000 Estimating the Vertical Velocity of Buoyant Deep-sea Hydrothermal Plumes Through Dynamic Analysis of an Autonomous Vehicle. IEEE/RSJ IROS 2000/2001 Conference.

Appendix A

LIST OF SYMBOLS

Greek Symbols

Symbol	Units	Meaning
α	$^{\circ}C^{-1}$	thermal expansion coefficient
β	psu^{-1}	haline contraction coefficient
$\Delta\theta$	$^{\circ}C$	potential temperature anomaly; generally refers to $\Delta_S\theta$ in this thesis
$\Delta_\rho\theta$	$^{\circ}C$	isopycnal potential temperature anomaly
$\Delta_S\theta$	$^{\circ}C$	isohaline potential temperature anomaly
$\Delta_z\theta$	$^{\circ}C$	level potential temperature anomaly
Δt	m	duration of temporal averaging bin
Δx	m	horizontal displacement; width of averaging bin
Δz	m	height of averaging bin
γ		function relating ambient S and θ
ρ	kg/m^3	density
ρ_o	kg/m^3	local ambient density
ρ_{ref}	kg/m^3	reference density
σ_θ		potential density referenced to the surface
τ	s	period (of an oscillation)
θ, θ_0	$^{\circ}C$	potential temperature referenced to 0 dbar

Latin Symbols

Symbol	Units	Meaning
A	m^2	open surface, or its total area
B	m^4/s^3	buoyancy flux
C		factor relating isohaline and level H
c	m/s; n/a	speed of light; initial puff concentration
c_p	$J \cdot {}^\circ C^{-1} \cdot kg^{-1}$	specific heat capacity
c_r	$J \cdot {}^\circ C^{-1} \cdot kg^{-1}$	crustal rock specific heat capacity
F		generic flux
f	s^{-1}	Coriolis frequency
g	m/s^2	gravitational acceleration
H	W	heat flux
H_a	W	ambient, upstream heat flux
H_d	W	diffuse vent heat flux
H_f	W	focused vent heat flux
H_g	W	"grouped surface" estimate of H_h
H_h	W	horizontal heat flux
${H_h}^*$	W	horizontal heat flux (level referenced)
H_p	W	plume heat flux
H_{qs}	W	"quasi-synoptic" estimate of H_h
H_R	W/km	heat loss per km of ridge
H_v	W	vertical heat flux
${H_v}^*$	W	vertical heat flux (level referenced)
h	$J \cdot s^{-1} \cdot photon^{-1}$	Planck constant
I	$photon \cdot m^{-2} \cdot s^{-1}$	light intensity
k	m^2/s	diffusivity
L	m	length
L_r	kJ/kg	latent heat of crystallization of crust
l	m	Rossby radius of deformation

Symbol	Units	Meaning
M	m^4/s^2	momentum flux
m		generic slope of a line
N	s^{-1}	buoyancy frequency
n		summation limit; number of area elements or puffs
Q	m^3/s	volume flux
Q_R	$kg \cdot s^{-1} \cdot km^{-1}$	production rate of crust per km
$R(x, y, z)$	m^{-3}, kg^{-1}	density or concentration of an intensive property
R_ρ		water-column stability ratio
R_{ρ_o}		source fluid stability ratio
r	m	radius; half-width of initial puff
$\hat{\mathbf{n}}$		unit vector normal to surface A
S	psu	salinity
S_{SW}	psu	reference salinity of local sea water ($\sim$34.6 psu)
T	°C	temperature
t	s	time
U	m/s	horizontal cross flow
u, ($\mathbf{u}$)	m/s	horizontal velocity (vector); often across-axis component
u_r	cm/yr	full spreading rate
V	m^3	volume
v, ($\mathbf{v}$)	m/s	horizontal velocity (vector), often along-axis component
v_o	m/s	amplitude (of current oscillation)
W	m	width
w	m/s	vertical velocity
X	m	east-west distance
x	m	horizontal distance or coordinate
Y	m	north-south distance
y	m	horizontal distance or coordinate

Symbol	Units	Meaning
Z	m	vertical distance
Z_m	m	equilibration height of plume in quiescent conditions
z	m	vertical distance or coordinate
z_r	m	rise height of a plume in a cross flow
z^*	m	maximum plume rise height in quiescent conditions

Appendix B

CONVERSION TABLE FOR MODIFIED JULIAN DATES

The following table gives the range of modified Julian dates (MJD) for the Flow Mow field program, along with the corresponding range of year days and the calendar date based on coordinated universal time (UTC). Note that all of these measures of days begin at midnight.

MJD	Year day	UTC Date
51760	217	8/04/00
51761	218	8/05/00
51762	219	8/06/00
51763	220	8/07/00
51764	221	8/08/00
51765	222	8/09/00
51766	223	8/10/00
51767	224	8/11/00
51768	225	8/12/00
51769	226	8/13/00
51770	227	8/14/00
51771	228	8/15/00
51772	229	8/16/00
51773	230	8/17/00
51774	231	8/18/00
51775	232	8/19/00
51776	233	8/20/00
51777	234	8/21/00

Appendix C

SUPPLEMENTARY MATERIAL: CD-ROM

Included as supplementary material with this thesis is a CD-ROM containing animations of the advection/diffusion, or "puff" model, and a digital version of the thesis itself. The animations are provided in these formats: FLIC, or .FLI; and Quicktime, or .MOV and can be accessed via a web page (animations.html). The digital versions of the thesis are provided in these formats: Device Independent File, or DVI; PostScript, or PS; and Adobe Portable Document Format, or PDF.

The animations on the CD-ROM are intended to aid readers with slow Internet connections. Those animations are referenced via hypertext within the digital versions of the thesis can be accessed automatically via the Internet or can be opened manually from the CD-ROM. The digital version of the thesis should allow readers with capable viewing software to zoom in on figures, allowing closer examination of the content than is possible in print or microfiche media.

Finally, the CD-ROM also provides access to flat-ASCII files containing the LaTeXsource of the thesis, requisite configuration files, and the incorporated figures. My hope is that future students and interested researchers may benefit from having access to both the files needed to construct the thesis with future typesetting software and the comments that evidence thoughts, concerns, and curiosities, not included in the published version of the thesis.

The material on the CD-ROM can also be obtained via the following web sites (hopefully in perpetuity):

http://econscience.org/scott/pubs/thesis

http://www2.ocean.washington.edu/∼scottv/thesis

VITA

Scott Veirs was born Chicago, Illinois, during the spring of 1970 to Val and Leslie Veirs. At age 2 he moved to Colorado Springs, Colorado, where he learned to marvel at mountains. Upon earning a diploma from Palmer High School in 1988, he studied at Stanford University, ultimately becoming the first student to be graduated as an Earth Systems major in 1992. His experience studying deep sea sediment with Alan Mix as a REU participant at Oregon State University during the summer of 1989 marked the beginning of his interest in becoming an oceanographer. From 1992-1995, Scott was engaged in other marine endeavors: he launched balloons in the equatorial Pacific from a Chinese ship during the TOGA/COARE in 1992; he sailed aboard the Schooner Shenandoah in 1993; and he studied satellite oceanography during the 1994 NASA Graduate Student Summer Program in Earth System Sciences. Based on advice in serendipitous correspondence with James Baker, as well as visionary conversations with John Delaney, Scott became a graduate student in the School of Oceanography at the University of Washington. During his first quarter in the summer of 1995 he collected CTD data on the Mixing Zephyrs cruises, and analyzed them under the guidance of Russell McDuff and Marvin Lilley to gain a Masters degree in the fall of 1997. He then took a leave of absence to teach oceanography at San Francisco State University and the Sea Education Association. In the winter of 1999-2000, he returned to Seattle with his wife, Annie Reese, to complete his doctoral degree. His permanent email address is scott at econscience dot org.